Measurement of vector boson pair production using hadronic decays of high transverse momentum W and Z bosons at the ATLAS detector

David Peter Wallis Freeborn
University College London

Submitted to University College London in fulfilment
of the requirements for the award of the
degree of **Doctor of Philosophy**

August 10, 2016

Declaration

I, David Peter Wallis Freeborn confirm that the work presented in this thesis is my own. Where information has been derived from other sources, I confirm that this has been indicated in the thesis.

David Freeborn _____

Abstract

This thesis describes an analysis measuring the WW+WZ production cross-section and setting limits on anomalous triple gauge couplings, in the semileptonic final state, using 20.28 fb^{-1} data from the ATLAS detector at a centre of mass energy of $\sqrt{s} = 8$ TeV. Two different topologies are studied: one with two distinct jets arising from the hadronic vector boson decay, and one with the hadronic decay products merged into a single large-radius jet at high transverse momentum.

In the resolved channel, the signal cross-section is measured with 4.45 σ significance with respect to the background-only hypothesis and yielding a cross-section in the fiducial phase space of 219 pb, in agreement with the Standard Model prediction. In the boosted channel, the cross-section in the fiducial phase space was measured to be 7.6 ± 4.9 pb, lower than the expected standard model cross section of 15.3 pb, with a significance of 2.05 σ.

Limits are set on anomalous contributions to triple gauge interaction vertices. For the resolved analysis, the observed 95% CL limits are $-6.0 < c_{WWW}/\Lambda^2 < 6.0$, $-39 < c_W/\Lambda^2 < 46$ and $-6.9 < c_B/\Lambda^2 < 12.1$ TeV^{-2}. For the boosted analysis, the equivalent observed limits are $-2.54 < c_{WWW}/\Lambda^2 < 2.52$, $-15.6 < c_W/\Lambda^2 < 17.2$ and $-3.65 < c_B/\Lambda^2 < 4.94$ TeV^{-2}.

The thesis also presents a performance study of the ATLAS jet triggers, during the period of upgrade from Run 1 to Run 2. The study assesses a proposed technique to improve the performance of the HLT jet trigger algorithms, by combining selected regions of interest into a larger combined region.

Acknowledgements

In a letter to Robert Hooke, dated February 5, 1676, Isaac Newton wrote that, "If I have seen further it is by standing on the sholders of Giants" [1]. Whilst some have interpreted the remark as a sarcastic reference to Hooke's slight stature, a more generous interpretation can aptly describe the nature of the scientific enterprise, both in Newton's day, and even more so today. Modern science is a highly collaborative endeavour, and nowhere is this more true than at the forefront of contemporary high energy physics, dominated by collaborations such as ATLAS, with many hundreds or thousands of researchers. I owe a titanic debt of gratitude to the many individuals who have aided and abetted me throughout the last three and a half years. Any such list inevitably will be incomplete, but I shall endeavour to thank as many people as possible.

First and foremost, I would like to thank my supervisor, Mario Campanelli, who has tirelessly helped and guided me throughout every part of this work. Thanks must also go to Peter Sherwood, who has taught me quite literally everything I know about the aesthetics of computer programming, of particular value to the work explained in chapter 6. Thanks must also go to a number of others at University College London. Alex Martyniuk has shown inexhaustible patience, assisting me with all manner of problems, answering questions, ranging from the simple to the strictly unsolveable, and engaging in many interesting and fruitful discussions. Pauline Bernat offered considerable assistance throughout my first year. Thanks must also go to Becky Chislett, Eric Jansen, Adam Davison, Luke Lambourne and Inês Ochoa for willingly helping on several occasions.

I must also express profuse gratitude to my colleagues from the analysis described in chapters 7, 8 and 9. Fabian Spettel and Milène Calvetti have shown both great endurance and equanimity in working with me on the boosted regime of the analysis. Invaluable guidance and inspiration came from Chiara Roda and Dmitri Tsybychev;

Brian Lindquist provided crucial assistance with the setting of limits on the anomalous triple coupling, whilst Valerio Dao offered invaluable help with understanding the cross-section fits. I would also like to thank Margherita Spalla and Felix Bührer, both for their accomplishments with the resolved regime, and for aiding me in debugging my work on more than one occasion.

I must further thank the many researchers who have provided insights and answered my numerous questions on uncountably many occasions. Particular thanks must go to Chris Delitzsch, Lily Asquith and Sam Meehan for patiently advising me on the details of topics ranging from the derivation of uncertainties for large-radius jets to the application of energy correlation functions. This was vital to the work described in chapters 7, 8 and 9. Ademar Delgado and Mark Sutton gave important advice for the work explained in chapter 6.

This work was funded by the Science and Technology Facilities Council (STFC), using public money, and on behalf of the public of the United Kingdom. I would like to thank the STFC for their funding, and dedication to research into fundamental science at a time when all public institutions are facing spending cuts. I would like to thank the British public for their continued judicious support for scientific research and who I hope will ultimately benefit from this work. If it has done even a little to push further the boundaries of our collective knowledge, then I hope it has been a worthwhile endeavour.

Finally, and above all, I wish to thank my parents, Glenda and Roger, and my brother, Richard, for their unconditional support throughout the time I have spent working towards this thesis.

Contents

List of figures

List of tables

"Nature uses only the longest threads to weave her patterns, so each small piece of her fabric reveals the organization of the entire tapestry."

— Richard Feynman [15]

Chapter 1.

Introduction

Since the earliest times, man has sought to understand the cosmos, and his place within it. The ancients were fascinated by the regular movements they witnessed in the heavens, and in the structure of the most basic components of matter. What is the nature of space and time? Are there basic elements from which all matter is composed? Is the Universe governed by immutable laws? Are these laws simple or complex? This insatiable curiosity seems to be innate within us; a yearning for knowledge is present in humans from early childhood. This quest for knowledge has embodied a civilisational project, spanning the generations, and driving all human progress. Today, the search for answers to many of the most fundamental questions falls within the realm of particle physics.

The apex of our progress is currently the Standard Model of physics. This triumph of human ingenuity unifies all of the known forces of nature, except for gravity, within a single, coherent mathematical framework. The Standard Model has made predictions to incredible levels of precision, which we have seen confirmed by experiment to astonishing levels of accuracy. The most precise measurements ever made have now verified the Standard Model predictions of the electron magnetic moment and fine structure constant to an accuracy of ten parts in a billion (10^{-8}) [16]. Arguably the most advanced machines in human history, the Large Hadron Collider, and the four detectors which surround it, are now testing the Standard Model to destruction. So far, the theory has passed every test.

Yet even loftier zeniths must surely await. We know that the Standard Model cannot be a fundamental theory of nature; from gravity, the force which rules the macrocosm at its largest scales, to the dark matter and energy that account for over

95% of all mass, the Universe is replete with phenomena that the Standard Model cannot explain. It is likely that the Standard Model is merely the limiting case of some even grander, underlying theory. Today, we can only speculate about a final theory, unifying all known forces of nature and explaining all known phenomena. Were mankind to achieve such a theory, we would, in the words of Stephen Hawking, "truly know the mind of God" [17].

THe work presented here takes place within this context. It presents new measurements of the Standard Model and sets new constraints on physics from beyond the Standard Model. Data from the ATLAS experiment is used, from the 2012 runs at the Large Hadron Collider. Specifically, the analysis aims to measure the production cross section for pairs of vector bosons, WW+WZ, decaying in the semileptonic channel, and to set new limits on anomalous triple gauge couplings in this channel. Studies are also performed on the upgrade of the Large Hadron Collider during the long shutdown of 2013-2014 and on the tagging vector bosons, using more recent data from the second run of data.

Chapter 2 provides a survey of the theoretical foundation upon which this work is built. It summarises the Standard Model. The full semileptonic decay chain of vector bosons is governed by both of the main forces described in the Standard Model. The objects produced in the leptonic decay are governed by the electroweak interaction, whilst the hadronic decayproduces objects that also interact through the strong force. Attention is also paid to physics beyond the Standard Model, in particular to anomalous triple gauge couplings.

Chapter 3 discusses the machines that provide the data on which the analysis is based, the Large Hadron Collider and the ATLAS detector. Particular detail is given to the jet trigger system at ATLAS, and its upgrade during 2013-2014 to accommodate a higher rate of data-taking at an increased centre of mass energy during the second run from 2014 onwards.

The theory of the strong force, Quantum Chromodynamics, provides a particularly rich and complex phenomenology, outlined in chapter 4. The Large Hadron Collider collides protons, strongly interacting particles, and these interactions dominate the phenomena seen. Of particular importance is the physics of "jets", collimated sprays of confined, strongly interacting particles, produced in copious quantities at the Large Hadron Collider. A robust understanding of jets is a critical prerequisite to any

analysis of hadronic objects at these energy scales. Yet jets are complex objects; this chapter also discusses the emerging field of jet substructure. An accurate modelling of the complex inner properties of jets is vital to the work presented in this thesis. Details are also given of the simulation toolkits, known as "Monte Carlo" generators, utilised to model these phenomena.

The process of moving from real particles to physical objects that can be measured in a detector and studied in an analysis is known as "reconstruction", described in chapter 5. The reconstruction process is based upon a series of agreed conventions, of how to define and calibrate different physical objects, ranging from jets, to electrons and muons, as well as missing energy, not measured directly by the detectors.

Chapters 6 describes a study performed for the upgrades to the ATLAS trigger system taking place between 2013-2014. For the second run of the Large Hadron Collider, the trigger needs to cope with an increased luminosity and higher quantities of pile-up events. The study considers a new approach to the jet trigger, based on producing partial scans of events before passing these to the higher levels of the trigger system. The aim is to investigate whether this can improve the speed at which the trigger can process events without a significant loss of efficiency.

Chapters 7, 8 and 9 together describe the analysis to measure the production cross-section of vector boson pairs, WW+WZ in the semileptonic channel, and to set limits on anomalous triple gauge couplings. The analysis outline is provided in chapter 7, including the motivations and aims. A fiducial phase space is defined in which the measurement takes place, based upon a series of topological and kinematic criteria to select or reject events. Chapter 8 explains the procedures for deriving the systematic uncertainties that inevitably affect this analysis. Chapter 9 explains the sophisticated statistical procedures used to perform a measurement of the cross-section and to set limits on possible new physics, and provides the results of this analysis.

Chapter 10 summarises these findings, and presents some final thoughts about the work, its relevance and the future of the field.

The author of this work produced all of the contributions for chapter 6, in collaboration with colleagues. The author produced the majority of the work for the boosted analysis sections for chapters 7, 8 and 9, directly producing the plots for the background modelling, systematic uncertainties, cross section measurement, and

limit setting on anomalous triple gauge couplings, again with assistance of colleagues. Collaborators produced the majority of work for the resolved analysis, some aspects of the boosted analysis, including background modelling for non-resonant multijet contributions, and the overlap removal between the boosted and resolved regimes.

1.1. A brief word on units

Natural units, with $c = 1$ and $\hbar = 1$, are used throughout this thesis, unless otherwise stated. Therefore most masses, energies and momenta will all be expressed in units of energy. Despite being "unnatural", for historical reasons the GeV, or giga-electronvolt, is accepted as the most common unit of energy throughout high energy physics, and will be used throughout this thesis. One GeV is equal to 10^9 times the quantity of work done in accelerating an electron through a potential difference of one volt.

Chapter 2.

Theoretical Framework

2.1. The Standard Model

The Standard Model is our most successful theory to describe the fundamental particles of the visible Universe. Formally, the Standard Model is a gauge quantum field theory (QFT), obeying the symmetries of the unitary product group $SU(3)\times SU(2)_L\times U(1)$. The theory is described by a Lagrangian, containing 19 parameters, or 26 if we include the experimentally observed fact that neutrinos have a mass. It describes the behaviour of a set of quantised fields, corresponding to the known fundamental particles of the Universe. These particles fall into two families, according to whether they have integer spin (bosons) or half-integer spin (fermions). There are 12 fermions, four gauge bosons, and the Higgs boson. Each particle represents a degree of freedom in one of the fields, or a combination of these fields. The known elementary particles and their properties are described in table 2.1 [9].

The theory provides the most complete model of fundamental interactions, successfully describing all known physical processes except for gravity. The fields correctly present the properties of all known fundamental particles, except for the neutrino mass. The interactions of the fields accurately describe the physical processes between these particles. High precision experiments in recent decades have not lessened the descriptive power of the theory, and the predictions from the theory have been consistently verified. Most recently, the theory correctly predicted the existence of the Higgs boson, discovered in 2012 [18, 19].

	Particle		charge [e]	spin	mass [GeV]
Quarks	up	u	$+\frac{2}{3}$	$\frac{1}{2}$	0.03
	down	d	$-\frac{1}{3}$	$\frac{1}{2}$	0.006
	strange	s	$-\frac{1}{3}$	$\frac{1}{2}$	0.1
	charm	c	$+\frac{2}{3}$	$\frac{1}{2}$	1.3
	bottom	b	$-\frac{1}{3}$	$\frac{1}{2}$	4.2
	top	t	$+\frac{2}{3}$	$\frac{1}{2}$	173
Leptons	electron	e	-1	$\frac{1}{2}$	0.0005
	muon	μ	-1	$\frac{1}{2}$	0.106
	tau	τ	-1	$\frac{1}{2}$	1.75
	electron neutrino	ν_e	0	$\frac{1}{2}$	$< 2 \times 10^{-9}$
	muon neutrino	ν_μ	0	$\frac{1}{2}$	$< 1.7 \times 10^{-4}$
	tau neutrino	ν_τ	0	$\frac{1}{2}$	$< 1.55 \times 10^{-2}$
Gauge bosons	photon	γ	0	1	0
	gluon	g	0	1	0
	Weak bosons	$W^\pm$	± 1	1	80.4
		Z^0	0	1	91.2
Higgs boson		H^0	0	0	126

Table 2.1.: The set of particles described by the Standard Model. The quarks and charged leptons also have corresponding antiparticles. Neutrinos have antiparticles if they are Dirac particles, otherwise they are their own antiparticle. [9]

Noether's theorem [20] states that that every differentiable symmetry of the action of a physical system has a corresponding conservation law. Therefore, the symmetries of the Standard Model Lagrangian correspond to the conserved quantities observed in nature, such as electric charge and angular momentum. The Standard Model can be separated into two non-Abelian gauge theories. First is the unified electroweak theory, a SU(2)×U(1) Yang-Mills gauge theory which describes the electromagnetic and weak interactions. Second is Quantum Chromodynamics (QCD), an SU(3) non-Abelian gauge theory that we believe describes the strong interaction.

2.2. Electroweak Theory

The Electroweak theory is a SU(2)×U(1) Yang-Mills gauge theory, describing the unified electromagnetic and weak forces. These interactions are mediated by the $W^{\pm}$, Z^0 and γ gauge bosons. The theory explains phenomena such as beta radioactive decay, and the electromagnetic force which holds atoms together. The unification of the weak (described by the Fermi theory) and electromagnetic interactions (described by Quantum Electrodynamics, or QED), for which Sheldon Glashow, Abdus Salam, and Steven Weinberg were awarded the 1979 Nobel Prize, was one of the major theoretical accomplishments in formulating the Standard Model [21–23].

To first appearances, the electromagnetic and weak interactions seem very different. The electromagnetic interaction is described by the theory of Quantum Electrodynamics. The Lagrangian is given by

$$\mathcal{L}_{QED} = \bar{\psi}\left(i\gamma^{\mu}\partial_{\mu} - m\right)\psi - e\bar{\psi}\gamma^{\mu}A_{\mu}\psi - \frac{1}{4}F_{\mu\nu}F^{\mu\nu}\,, \tag{2.1}$$

where ψ are spin-$1/2$ Dirac spinor fields for the electron, and for the photon field, A_{μ},

$$F_{\mu\nu} = \partial_{\mu}A_{\nu} - \partial_{\nu}A_{\mu}\,. \tag{2.2}$$

The interaction is long range (mediated by the photon, a massless gauge boson), conserves parity and acts equally on particles of left-handed and right-handed chirality. By contrast, the weak interaction has a short range (and so must be mediated by massive gauge bosons) and violates parity maximally. It acts only on weakly charged left-handed particles and right-handed antiparticles.

To unify the interactions, two new uncharged massive gauge bosons were introduced, the W^0 and the B^0, alongside the $W^{\pm}$. These neutral fields mix, according to a weak mixing angle, θ_W. We can form the massless electromagnetic field A^{μ} from a linear combination of these fields. The orthogonal combination produces a new particle, which led to the prediction of a weak neutral current, the Z^0:

$$A^\mu = +B^\mu \cos\theta_W + W^{\mu,0} \sin\theta_W$$
$$Z^\mu = -B^\mu \sin\theta_W + W^{\mu,0} \cos\theta_W \,. \tag{2.3}$$

The observation of this weak neutral current in the Gargamelle Bubble Chamber in 1973 provided a major experimental verification of the theory [24].

The full electroweak Lagrangian is given by

$$\mathcal{L}_{EW} = \mathcal{L}_{\text{gauge}} + \mathcal{L}_{Higgs} + \mathcal{L}_{\text{fermion}} + \mathcal{L}_{\text{Yukawa}} \,. \tag{2.4}$$

The gauge term is the Lagrangian for the gauge fields of the weak interaction:

$$\mathcal{L}_{\text{gauge}} = -\frac{1}{4}\left(W^i_{\mu\nu} W^{\mu\nu i} + B_{\mu\nu} B^{\mu\nu}\right) \,, \tag{2.5}$$

where W^i_μ are the SU(2) gauge fields, and B_μ are the U(1) gauge fields. If g is the coupling strength to the SU(2) field, then the corresponding field strength tensors are given by

$$W^i_{\mu\nu} = \partial_\mu W^i_\nu - \partial_\nu W^i_\mu - g\epsilon_{ijk} W^j_\mu W^k_\nu \tag{2.6}$$
$$B_{\mu\nu} = \partial_\mu B_\nu - \partial_\nu B_\mu \,. \tag{2.7}$$

The Higgs term is discussed in section 2.2.1. The fermion terms describe the coupling of fermions to the weak fields. The Yukawa terms describe the coupling of fermions to the Higgs field, allowing them to acquire their masses. Their mathematical details will not be discussed here.

2.2.1. Electroweak Symmetry Breaking

The Englert–Brout–Higgs mechanism [25–27] breaks the SU(2)×U(1) symmetry of the electroweak theory. Whilst the electromagnetic force has an infinite range, mediated by a massless gauge boson, the weak force range is short, due to the high mass of the gauge bosons that mediate the interaction. This spontaneous symmetry breaking mechanism is necessary because the direct addition of boson Dirac mass terms of the form $\frac{1}{2}m^2\bar{\psi}\psi$ would break the gauge invariance of the theory. The Higgs mechanism includes an additional SU(2) double field ϕ into the Standard Model, with the Lagrangian,

$$\mathcal{L}_{Higgs} = (D_\mu\phi)^\dagger(D_\mu\phi) - \mu^2\phi^\dagger\phi - \lambda(\phi^\dagger\phi)^2\,, \tag{2.8}$$

where the covariant derivative D_μ is defined by,

$$D_\mu = \partial_\mu + \frac{1}{2}ig\bar{\tau}\bar{W}_\mu + \frac{1}{2}ig'YB_\mu\,. \tag{2.9}$$

The first term of the Lagrangian is the kinetic part; the second and third terms define the Higgs potential, a quadratic in $\phi^\dagger\phi$ with real coefficients $-\mu^2$ and $-\lambda$.

If $-\mu^2 \leq 0$, then the state of minimum energy will be at $\phi = 0$, and the potential will preserve the symmetries of the Lagrangian. Then the theory is equivalent to QED, with a massless photon and a charged scalar field ϕ of mass μ. However, if we require that $-\mu^2 > 0$, then the potential will acquire a non-zero vacuum expectation value, v,

$$\frac{v}{\sqrt{2}} \equiv |\phi_0| = \sqrt{\frac{-\mu^2}{2\lambda}}\,. \tag{2.10}$$

Without loss of generality, we can parameterise ϕ by,

$$\phi = \frac{v+h}{\sqrt{2}} e^{i2\pi\tau^a/v}\,, \tag{2.11}$$

where h and τ^a are simple scalar fields, with zero vacuum expectation, referred to as the Higgs and Goldstone fields respectively. Substituting these terms back into the Lagrangian in equation (2.8), we have terms of the form,

$$g^2\frac{v^2}{8}\left[\left(W_\mu^1\right)^2 + \left(W_\mu^2\right)^2 + \left(\frac{g'}{g}B_\mu - W_\mu^3\right)\right]\,, \tag{2.12}$$

which take the form of mass terms for the massive gauge bosons, proportional to g^2v^2. Let us apply the mixing relations from equation (2.3) and introduce a linear change of basis, $W_\mu^\pm \equiv \frac{1}{\sqrt{2}}(W_\mu^1 \mp W_\mu^2)$. If we substitute these terms in, we arrive at mass terms for the observed W, Z and γ particles of the electroweak theory:

$$\begin{aligned} m_A &= 0\,, \\ m_W &= \frac{v}{2}g\,, \\ m_Z &= \frac{v}{2}\sqrt{g^2+g'^2} = \frac{m_W}{\cos\theta_W}\,. \end{aligned} \tag{2.13}$$

Starting from a Lagrangian containing only massless bosons, the Higgs mechanism has given masses to new bosons, constructed from linear combinations of these massless fields. These mass terms originate as three out of the four original degrees of freedom of the complex Higgs doublet. The remaining degree of freedom corresponds to the Goldstone boson, which can be removed from the theory altogether by convenient choice of gauge.

We can then introduce explicit couplings between the field and the fermions to give these particles masses as well; however, in so doing, we introduce an additional degree of freedom into the Standard Model for each coupling. Moreover, since the field interacts with massive particles, it will be perturbed from the vacuum minimum when mass is present. This leads to terms corresponding to a new massive scalar

boson of mass $\sqrt{-2\mu^2}$, zero spin, no electric charge or colour charge. The discovery of this particle, referred to as the Higgs boson, in 2012 was generally interpreted as confirming the electroweak symmetry breaking model.

2.2.2. Electroweak Triple Gauge Couplings

Gauge couplings arise from the self interaction terms of the Electroweak Lagrangian, Equation (2.5). Expanding out the equation in terms of the field tensors, Equation (2.6) and Equation (2.7), terms will arise of containing three gauge fields (triple gauge couplings, or TGCs), or four gauge fields (quartic gauge couplings, or QGCs). These couplings arise due to the SU(2) symmetry of the field, and the fact that the generators of the gauge group, ϵ_{ijk}, do not commute. These terms give rise to the multi-gauge-boson interactions and are the source of electroweak diboson production.

The possible set of trilinear couplings involving the electroweak gauge bosons would be WWW, $WW\gamma$, WWZ, $ZZ\gamma$, $Z\gamma\gamma$, ZZZ and $\gamma\gamma\gamma$. However, WWW couplings are excluded by the requirement of charge conservation, whilst $\gamma\gamma\gamma$ couplings could not conserve four-momentum. Of the remaining couplings, SU(2) symmetry implies the only forms allowed are WWZ and $WW\gamma$, because the Lagrangian must be invariant under an SU(2) rotation. Figure 2.1 shows the leading order process that can produce triple gauge vertices at a proton-proton collider.

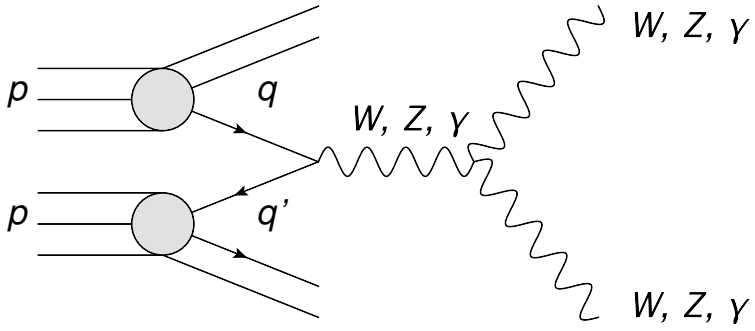

Figure 2.1.: Feynman diagram showing leading order process that can produce triple gauge vertices in proton-proton collisions, at leading order. Only two couplings are possible, WWZ, and $WW\gamma$.

Many aspects of the gauge structure of the SU(2) × U(1) electroweak theory have been tested extensively, such as the vector boson masses and their couplings to fermions. However, the non-abelian self-interactions of vector bosons, such

as the triple gauge couplings, WWZ, have been measured to a lower precision. Measurements of these couplings are potentially sensitive to new physics, as will be discussed in section 2.4.2 [28, 29].

2.3. The Strong Force and Quantum Chromodynamics

Quantum Chromodynamics (QCD) is the theory which describes the strong force in the Standard Model [30–32]. This force is responsible for binding quarks into hadrons; it is mediated by gluons, massless gauge bosons. The mathematical structure of the SU(3) theory is in some ways analogous to the U(1) QED theory that describes electromagnetism, with both quarks and gluons carrying a colour charge, fulfilling a comparable role to electric charge. A quark's colour can take one of three values or charges, labelled red, green, and blue. An antiquark can take one of three anti-colours, labelled anti-red, anti-green, and anti-blue. Gluons take a colour–anti-colour pair, such as red and anti-green. In QCD, we consider eight gluons of the possible nine colour–anti-colour combinations to be unique. However, there are important properties unique to QCD; we observe behaviours, such as asymptotic freedom and colour confinement that are not seen in QED [33].

The Lagrangian for QCD is given by

$$\mathcal{L}_{QCD} = \bar{\psi}_{q,a}\left(i\gamma^{\mu}\partial_{\mu}\delta_{ab} - m_q\delta_{ab}\right)\psi_{q,b} - g_s G^A_{\mu}\left(\bar{\psi}_{q,a}\gamma^{\mu}T^{ab}_A\psi_{q,b}\right) + \frac{1}{4}F^A_{\mu\nu}F^{\mu\nu}_A \quad (2.14)$$

where for a gluon field G^A_{μ},

$$F^A_{\mu\nu} = \partial_{\mu}G^A_{\nu} - \partial_{\nu}G^A_{\mu} - g_s f_{ABC}G^B_{\mu}G^C_{\nu}\,. \quad (2.15)$$

Note that the Lagrangian obeys SU(3) as an exact symmetry, so the strong interaction is invariant under rotations in colour space.

Here, the ψ are quark field spinors, with the sum over 6 flavours; up, down, strange, charm, bottom and top, with the corresponding masses represented by m_q

and a colour index a that runs from $a = 1$ to the number of colour charges, $N_c = 3$. The G_A correspond to the gluon fields, with A running from 1 to $N_c^{2-1} = 8$. The quarks form the fundamental representation of the group, whereas the gluons form the adjoint representation.The γ^μ are the Dirac gamma matrices, summed according to the Einstein summation convention. The T_a are the traceless, hermitian Gell-Mann matrices, which allow for rotation in colour space. g_s is related to the strong coupling constant α_s by the relation $\alpha_s = {g_s^2}/{4\pi^2}$. f_{ABC} are the structure functions of the SU(3) group. From expanding out the terms in the Lagrangian, it is clear that there are two terms in which the gluon couples to quark-antiquark pairs, analogous to the photon couplings to charged particles in QED. However, due to the nonabelian third term in the field strength tensor, there are also triplet and quartic gluon-gluon vertex interactions, to which there is no analogy in QED. This is what leads to the unique QCD behaviours, of colour confinement and asymptotic freedom.

2.3.1. Ultraviolet and Infrared Divergence

Two types of divergence are possible in QCD: infrared (IR) and ultraviolet (UV). IR divergences occur when integrals diverge because of contributions of objects with very small energy approaching zero, or, equivalently, because of physical phenomena taking place at very long distance scales. UV divergences occur when integrals diverge because of contributions from objects with very high energy or, equivalently, because of physical phenomena taking place at very short distance scales.

In the case of QCD, IR divergences occur because gluons have zero mass, and are impossible to resolve at low energies. The divergences come in two types: soft and collinear exchange, shown in figure 2.2. Soft exchanges, mediated by what are termed Coulomb gluons, occur between the incoming quarks. Collinear gluons, those with transverse momentum $k_\perp$ close to zero, will propagate parallel to the quark or gluon from which they are emitted. One way to respond to the divergence is to apply dimensional regularisation, which reduces the range of the loop integral by a particular factor, and then takes the limit of the integral as the factor is increased to infinity.

The vertices that appear in the QCD Lagrangian permit a quark or a gluon to emit a gluon, or for gluons to make quark or gluon loops. These interactions are shown in figure 2.3. Analogously to QED, the strength of these interactions

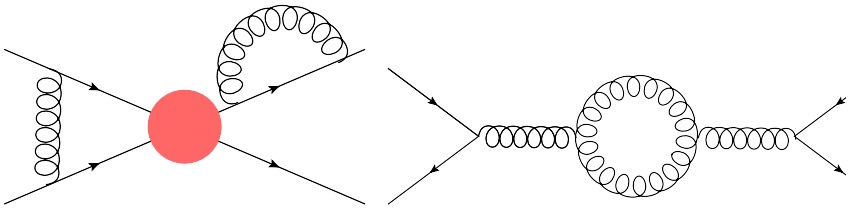

(a) Left of the interaction vertex: soft Coulomb gluon exchange; to the right: a hard collinear gluon.

(b) A simple gluon loop

Figure 2.2.: Feynman diagrams displaying (a) IR and (b) UV divergences, respectively.

is governed by the coupling constant α_s. However, in these loops, the momentum is unconstrained, resulting in an integral of divergent value. This is known as the ultraviolet divergence. One response to this is to introduce an ultraviolet cut-off at momentum transfer Q_0, a scale at which we take QCD to no longer be a valid theory. We then absorb these divergences into the definition of the parameters used, producing renormalisation parameters, valid at all orders, and yielding finite predictions for physical observables.

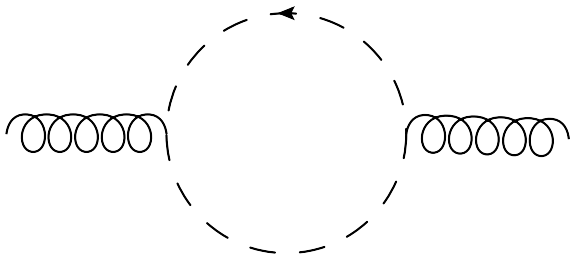

(a) Quark loop

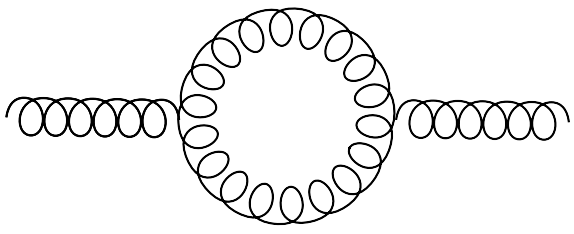

(b) Gluon loop

Figure 2.3.: Feynman diagrams displaying (a) quark and (b) gluon loops, respectively.

2.3.2. Asymptotic Freedom

Absorbing these extra diagrams into the definition of the strong coupling constant is analogous to the "electric charge screening" of QED. Through this renormalisation procedure, the sum of the perturbative series of diagrams of increasing order is mathematically equivalent to a single diagram with a "running" coupling constant,

$$\alpha_s(Q^2) \approx \frac{\alpha_s(Q_0^2)}{1 + B\alpha_s(Q_0^2)\ln\left(\frac{Q^2}{Q_0^2}\right)}\,, \tag{2.16}$$

where for N_c colours and N_f quark flavours, the constant, B, is given by

$$B = \frac{11N_c - 2N_f}{12\pi}\,. \tag{2.17}$$

Different to the coupling in QED, this coupling constant, α_s, decreases with increasing four-momentum transfer (Q^2), resulting in the anti-screening of the colour charge. In the case of QED, we can view the vacuum polarisation as "screening" the charge as the distance from it is increased; in QCD, the fact that the gluons are themselves charged and can self-interact produces this competing effect, and results in the strength of the interaction increasing with distance.

This leads to the property of asymptotic freedom: at very high energies, or very short distances, the strength of the colour field decreases, and consequently quarks behave more like free particles. This is the opposite to that seen in QED, where the charged particles behave more like free fields at low energies or long distances. Consequently, perturbation theory is only valid in QCD in the very high energy regime, where high precision tests of the theory are possible. At low energies, QCD calculations become extremely difficult to perform.

2.3.3. Colour Confinement

Experimentally, we never observe colour charged particles in isolation, i.e. free quarks or gluons. Instead, physicists have only deduced the existence of quarks from the properties of bound colour singlet states, mesons and baryons, and confirmed their

existence through deep inelastic scattering experiments (see section 2.3.5) performed on these bound states. It is therefore believed, although not yet proven, that all observable free particles must be colourless. Although no analytic proof exists that quantum chromodynamics should be colour-confining, the current best theory is that the property arises from gluon self-interactions.

As any two electrically charged particles separate, the electric fields between them diminish quickly, allowing, for example, electrons to become unbound from atomic nuclei. However, as a quark-antiquark pair separates, the gluon field is "squeezed" by the gluon self-interactions, and so forms a narrow tube of colour field between them. The cross-section of these tube remains approximately constant even as it is stretched. The number of field lines, dependent only on the number of colour sources also remains constant. Therefore, the field strength in the tube does not decrease as the distance between them increases, instead remaining approximately constant. As a result, the energy of the system increases linearly with the quark-antiquark separation. Therefore, energy injected into the hadron does not separate the quarks, but instead goes into the creation of new quark-antiquark pairs, illustrated in figure 2.4.

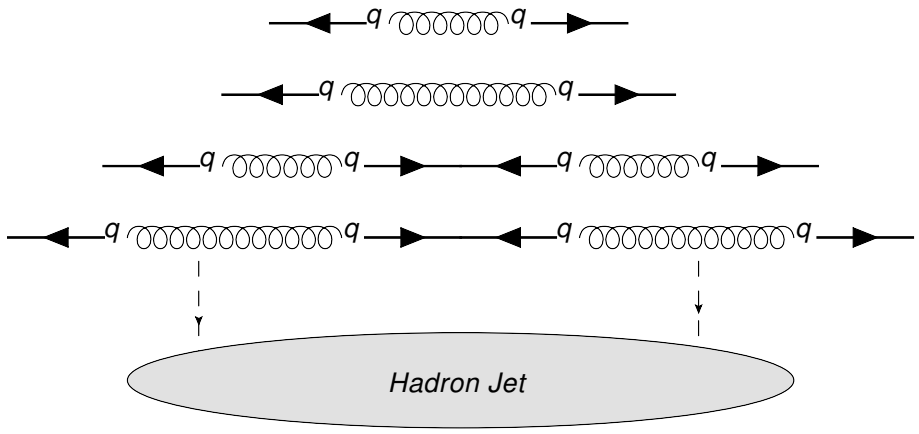

Figure 2.4.: The colour force is believed to favour confinement because it is more energetically favorable to create a quark-antiquark pair than to continue to elongate the colour flux tube.

As a consequence, highly energetic $q\bar{q}$ states, such as those produced in hadron-hadron collisions, will continue to produce more pairs until a stable ground state is reached. This process, known as hadronisation, or fragmentation, results in the formation of many hadronic final states.

2.3.4. Hadronisation and Jets

As discussed in section 2.3.3, coloured quarks may be produced as a final state of a collision, and can be described by perturbative QCD calculations, but due to colour confinement, we only observe colourless hadrons as final states in experiments. The process by which quarks form hadronic final states is known as hadronisation; both this and the showering processes are inherently non-perturbative: consequently they must be described using phenomenological models. In practice, at detector level, we observe collimated showers of hadrons, with an implicit non-perturbative component. Hence, instead of individual hadrons, particle showers are typically enveloped into ensembles known as "jets".

The concept of jets originates in cosmic ray studies in 1952 [34]. When sufficiently energetic cosmic rays interacted with nuclei in an emulsion plate, physicists recorded a shower of particles. The experiment operated by finding tracks in emulsion plates by eye, aided by scanning machines. As the momentum of the cosmic particles increased, the showers became increasingly directional, but also more complex. All tracks originating from a single observed interaction point were then grouped as a jet.

The first evidence of jets arising from quarks was obtained in $e^+e^- \to q\bar{q}$ events at the SPEAR collider in 1975 [35]. Hadrons are composed of constituents known as partons (quarks and gluons). However, it is fundamentally impossible to measure the properties of partons: they are not physical objects but rather propagators, and their representation may vary depending on the model being used. On the other hand, jets are well-defined objects, and so provide a means to measure the parent particles: many properties of quarks and gluons can be deduced from jet analyses. The phenomenology of jets will be discussed extensively in chapter 4.

2.3.5. Deep Inelastic Scattering

Deep inelastic scattering, the interaction of leptons, such as electrons, muons or neutrinos with individual partons, is used to probe the structure of hadrons. It provided the first first convincing evidence that quarks were a real phenomenon, rather than simply a mathematical device. Let us look at the example of $e^{\pm}p$ scattering. When at high enough energy to resolve the parton structure of the

hadron, the probing particle, will interact with a quark, carrying a fraction x of the proton's four-momentum, p. The cross-section for the process is

$$\frac{d^2\sigma}{dxdQ^2} = \frac{4\pi\alpha^2}{Q^4}\left[\left(1 - y - \frac{m_p^2 y^2}{Q^2}\right)\frac{F_2(x,Q^2)}{x} + y^2 F_1(x,Q^2)\right]. \tag{2.18}$$

where $Q^2 = -q^2$ is related to the momentum transfer between the quark and electron, $y = \frac{P_p \cdot q}{p_p \cdot p_c}$ is the fraction of the electron's energy transferred to the proton in the proton's rest frame, m_p is the proton mass, and $F1(x,Q^2)$ and $F2(x,Q^2)$ are, respectively, the pure magnetic and electromagnetic proton structure functions, describing the momentum distribution of the quarks and the proton. In the high energy limit, $Q^2 \gg m_p^2 y^2$, the expression for the cross-section simplifies to

$$\frac{d^2\sigma}{dxdQ^2} = \frac{4\pi\alpha^2}{Q^4}\left[(1-y)\frac{F_2(x,Q^2)}{x} + y^2 F_1(x,Q^2)\right]. \tag{2.19}$$

In 1969, it was predicted that the structure functions, $F_1(x,Q^2)$ and $F_2(x,Q^2)$, should be approximately independent of Q^2 in the deep inelastic limit, $Q^2 \to \infty$, while x remains finite [36]. This has been experimentally verified over a large range of x; however, at very low values of x, $F_2(x,Q^2)$ will rise with increasing Q^2, whereas at high values of x, $F_2(x,Q^2)$ will fall with increasing Q^2. Nonetheless, structure functions are more dependent on the kinematic quantity x, than on the four-momentum transfer of the collision, Q^2. In addition, we have experimentally observed that the structure functions $F_1(x,Q^2)$ and $F_2(x,Q^2)$ obey the Callan-Gross relation:

$$F_2(x) = 2xF_1(x). \tag{2.20}$$

The differential cross-section for elastic scattering between an electron and a quark of charge q_i carrying a fraction, x, of the proton's four-momentum is given by

$$\frac{d^2\sigma}{dxdQ^2} = \frac{2\pi\alpha^2}{Q^4}\left[1+(1-y)^2\right] . \tag{2.21}$$

Inside a hadron, the parton distribution function (PDF), $f_q(x_0, Q^2)\delta x$, expresses the fraction x between x_0 and $x_0 + \delta x$ [37]. So multiplying equation (2.21), by the relevant PDF, we can arrive at the cross-section for electron scattering with a particular quark type in the proton:

$$\left.\frac{d^2\sigma}{dxdQ^2}\right|_{x\to x+\delta x} = \frac{4\pi\alpha^2}{Q^4}\left[(1-y)+\frac{y^2}{2}\right] q_i^2 f_q(x_0, Q^2)\delta x\,, \tag{2.22}$$

leading to an equation for the total differential cross-section between the electron and the proton, from summing over all the quark and antiquark types in the proton:

$$\frac{d^2\sigma}{dxdQ^2} = \frac{4\pi\alpha^2}{Q^4}\left[(1-y)+\frac{y^2}{2}\right] \sum q_i^2 f_{q,i}(x_0, Q^2)\,. \tag{2.23}$$

Comparing equation (2.23) to equation (2.19) leads to equation (2.24) for the proton structure functions in electron scattering,

$$F_2(x) = 2xF_1(x) = \sum_i x f_{q,i}(x_0, Q^2) + x\bar{f}_{q,i}(x_0, Q^2)\,. \tag{2.24}$$

This provides evidence for the parton picture of hadrons; the four-momentum of the hadrons is carried by constituent particles (quarks and gluons) known as partons. Currently, f_q cannot be calculated analytically because perturbation theory is only valid in QCD in the very high energy regime. However, physicists have managed to measure experimentally the PDFs of the partons across a wide range of x and Q^2. Key measurements of PDFs have taken place at experiments like H1 and ZEUS, at the HERA lepton–proton collider [38–41]. The evolution of PDFs can be determined

using splitting functions, derived from the DGLAP equations [41–44]. They are usually assumed to be process-independent, so PDFs measured from deep inelastic scattering experiments may then be applied when modelling other processes.

2.3.6. Factorisation

In practice, calculations of cross-sections for real QCD processes can be technically difficult. Quark and gluon splitting can continue until the four-momentum of the partons is very low. Theoretically, $g \to gg$ splitting can continue even as the massless gluon 4-momenta approaches the limit of zero. Thus, perturbative QCD cannot in general be used when considering the parton structure of hadrons in calculations for real processes.

The process of factorisation splits QCD into two regimes, which can be determined separately. The procedure only works exactly for processes with 0 or 1 incoming quarks or gluons — hence for hadron collider experiments, it must currently be applied in approximation only due to contributions from multiparton interactions. We write the process cross-section as a convolution of a perturbative coefficient function, which can be calculcated as a series in terms of the coupling constant α_s, and a non perturbative parton distribution function, usually determined from experiments. This is shown schematically for proton-proton collisions in Equation (2.25).

As in the case of the renormalisation procedures discussed in section 2.3.3, a choice must be made about the scale, called the factorisation scale, μ_f, at which Q and α_s are chosen. Below this scale, emissions are included as part of the PDFs, whilst above it, emissions are included in the coefficient function calculation. We usually take μ_f to be of the order of the typical four-momentum transfer for the process being considered, $\mu_f^2 \sim Q^2$. In the example of proton–proton collisions, the factorisation of the expression for the cross-section takes the form,

$$\sigma_{pp\text{ scattering}} = \iint dx_1 dx_2 \sum_a \sum_b \overbrace{f_a(x_1, \mu_F^2) f_b(x_2, \mu_F^2)}^{\text{PDFs}} \overbrace{\hat{\sigma}_a, b\left(p_{p,1} p_{p,2} \alpha_s(\mu_R^2), \frac{Q^2}{\mu_F^2} \frac{Q^2}{\mu_R^2}\right)}^{\text{Hard scatter}} . \tag{2.25}$$

where, μ_F is the chosen factorisation scale, while μ_R is the renormalisation scale. Q^2 is the hard scale that characterises the parton–patrton interaction. The 4-momenta of the two interacting partons is given by $p_{p,1,2}$; f_a and f_b are their PDFs. The form of the convolution is analogous for other scattering processes involving hadrons.

Since the perturbation series is an asymptotic expansion, in practice there is a limit to the precision we can calculate theoretical quantities in QCD. We provide indications of the uncertainties on these theoretical predictions by varying renormalisation and factorisation scales away from their chosen values, usually by a factor of 2.

2.4. Physics beyond the Standard Model

The Standard Model remains our most successful model of fundamental physics, its predictions verified from decades of high energy experiments and subjected to intense scrutiny. Nonetheless, the Standard Model cannot be a complete description of nature, and is subject to certain theoretical and experimental limitations. The search for physics beyond the Standard Model (BSM) is an active, ongoing area of research, with proposed models including supersymmetry and loop quantum gravity. Some current of the problems within the Standard Model are outlined below.

1. **Gravity**
   The most significant limitation of the standard model is the lack of a description of gravity. The Standard Model does not explain gravity. The approach of simply adding a new gauge boson, a "graviton", to the Standard Model does not recreate experimental observations without other modifications, as yet undiscovered, to the model. No renormalisable quantum field to describe gravity has ever been formulated that is compatible with the tenets of general relativity. The unification of gravity with the other forces of nature may require an altogether different approach [45].

2. **Dark matter and energy**
   Cosmological observations tell us the standard model explains only around 5% of the energy present in the universe. Astronomical observations currently suggest that the matter is dominated by an invisible "dark matter", comprising about 26% of the Universe's energy. Presumably, this matter does not interact

electromagnetically, as it does not seem to absorb or emit light. Nor does it decay into known hadronic states and so presumably does not interact with the strong force. However, it does interact gravitationally, for example by influencing the rotation curves of observed galaxies, and through gravitational lensing. The properties of this dark matter, if this is the correct inference from these observations, are not well understood. Although neutrinos could fit the profile, their mass is insufficient to provide an explanation. The Standard Model is therefore missing a candidate to explain this dark matter [46, 47].
Meanwhile, cosmological models suggest that about 69% of the Universe's energy should be dark energy, a constant energy density for the vacuum. Attempts to explain dark energy in terms of vacuum energy of the standard model lead to a mismatch of 120 orders of magnitude [48].

3. **Neutrino masses**
   In the Standard Model, neutrinos are defined as massless. However, recent experiment evidence of neutrino oscillations suggests that they do indeed have masses, albeit much smaller than any other observed massive particles. The exact mechanism by which neutrinos obtain mass is not known; they may be Dirac particles like other fermions; however, the small scale could hint that they have a Majorana mass, meaning that the neutrinos are their own antiparticle. The theoretical appeal of this comes from the Seesaw Mechanism [49, 50].

4. **Matter-antimatter asymmetry**
   The observed universe consists almost entirely of matter rather than antimatter. In existing cosmological models, the baryon and lepton numbers at the beginning of the universe were zero. Given this, the standard model would predict that matter and antimatter should have been created in almost equal amounts. The Standard Model does contain some CP violation in the weak interaction, leading to a small asymmetry in the decays of matter and antimatter; however, this is insufficient to explain most of the scale of the imbalance [51].

5. **Mass hierachy problem**
   There is a large disparity between the masses of the lightest and heaviest observed quarks and leptons, with the top quark having a mass forty times greater than the next heaviest, the bottom quark. The Higgs mechanism itself makes no prediction for the masses of fermions; these are determined by Yukawa

couplings of the fermion fields to the Higgs scalar field, which are currently input as free parameters. This feels unnatural to many physicists [52].

6. **Hierachy problem**
   More significantly, the Higgs mass parameter μ receives very large quantum corrections due to loop diagrams, especially those involving virtual top quarks. These are cut off at the scale λ of the Standard Model, assumed to be valid up to around the Planck mass scale, $M_p l = \sqrt{\hbar c / 8\pi G}$, at which point hypothetical particles like gravitons may become important. Given that the Higgs mass is 126 GeV, the scale $\mu^2 \approx -10^4$ GeV; if the cut-off is at the Planck scale this would lead to higher order corrections of around 10^{31} GeV. These corrections are much larger than the actual mass of the Higgs, meaning that the bare mass parameter of the Higgs in the Standard Model requires an enormous amount of fine-tuning, in order to almost completely cancel the quantum corrections. Again, to many physicists, this feels very unnatural [53].

7. **Strong CP problem**
   There are no known theoretical restrictions to prevent the strong force Lagrangian from containing terms that break CP symmetry. Experimentally, no CP violation has been found in the strong sector, suggesting that any such terms must have a coefficient close to zero. This also seems to require unnatural fine tuning [54].

8. **Number of parameters**
   The Standard Model has 19 free parameters; or 26 if neutrino masses are included. Having so many free parameters in a fundamental theory seems unsatisfactory [55].

2.4.1. The Effective Field Theory approach

If BSM physics exists, then we expect that the Standard Model must be an effective field theory, valid at low energies, but breaking down somewhere above the energy scales that have so far been experimentally probed. We call this the scale of new physics, Λ. Given the current lack of experimental evidence for new physics, it often makes sense to use model-independent Lagrangian parametrisations of any BSM physics as far as possible [56]. An effective Lagrangian can take the form,

$$\mathcal{L}_{\text{eff}}[\phi] = \sum_n \frac{1}{\Lambda^n} \sum_i \alpha_i^n \mathcal{O}_i^n \,, \tag{2.26}$$

where $L_{\text{eff}}[\phi]$ is the effective Lagrangian, and the operators $\mathcal{O}_i^n$ have the dimensions $[\text{mass}]^{n-4}$ are functions of the fields ϕ. We can approximate the expansion with a finite number of terms, using the assumption that all particle masses and momenta fall well below the new physics scale, Λ. However, such an effective Lagrangian will fail at energy scales close to Λ because all terms in the expansion of n become approximately equally significant. So it makes no sense to test the unitarity of such a theory at arbitrarily large energies. At the scale close to Λ, a better, underlying high energy theory is needed to make predictions [56, 57].

2.4.2. Anomalous Triple Gauge Couplings in the Electroweak Sector

BSM physics is likely to modify the self-interactions of vector bosons, in particular the TGCs. If the new physics occurs at an energy scale, Λ, then the terms in equation (2.26) can be integrated out, and the result expressed as a set of anomalous (non-Standard Model) interaction vertices, such as anomalous triple gauge couplings (aTGCs) [56].

We would expect BSM physics to lead to large deviations for Standard Model predictions on gauge boson self-interactions. In certain models, one-loop contributions from aTGCs to measured parameters could turn out to be quadratically or even quartically divergent. At the scale of new physics, and for sufficiently large Λ, the value of the quantum corrections would become much larger than lower order effects. These problems imply that the Lagrangian of the effective field theory for the Electroweak interaction becomes inconsistent at large Λ: to avoid such an unphysical situation, significant deviations for the triple gauge couplings must occur at a lower physics scale, or alternatively, extra parameters are needed to cancel the apparent divergences. Measurements of these triple gauge couplings could therefore provide a particularly clear search for new physics [28, 57].

If we assume that Λ is large, so we can cut off operators of dimension 8 or greater, then the most general set of Lagrangian terms for WWV, $V\varepsilon\{Z,\gamma\}$ are

$$\begin{aligned}\frac{\mathcal{L}_{WWZ}}{g_{WWZ}} &= ig_1^Z\left(W^\dagger_{\mu\nu}W^\mu Z^\mu - W^\dagger_\mu Z_\nu W^{\mu\nu}\right) + i\kappa_Z W^\dagger_\mu W_\nu Z^{\mu\nu} \\ &+ i\frac{\lambda_Z}{m_W^2}W^\dagger_{\lambda\mu}W^\mu_\nu Z^{\nu\lambda} - g_4^Z W^\lambda_{\mu\nu}W_\nu\left(\partial^\mu Z^\nu + \partial^\nu Z^\mu\right) \\ &+ g_5^Z\epsilon^{\mu\nu\lambda\rho}\left(W^\dagger_{\mu\nu}\partial_\lambda W_\nu - \partial_\lambda W^\dagger_{\mu\nu}W_\nu\right)Z_\rho \\ &+ i\tilde{\kappa}_Z W^\dagger_{\mu\nu}W_n u\tilde{Z}^{\mu\nu} + i\frac{\tilde{\lambda}_Z}{m_W^2}W^\dagger_{\lambda\mu}W^\mu_\nu\tilde{Z}^{\nu\lambda}\,, \end{aligned} \tag{2.27}$$

where $g_{WWZ} = -e\cot(\theta_W)$ and $\tilde{X}_{\mu\nu} \equiv \frac{1}{2}\epsilon_{\mu\nu\lambda\rho}X^{\lambda\rho}$. For the Standard Model Lagrangian, all couplings are zero except for $g_Z = \kappa_Z = 1$.

We generally express deviations from the standard model in terms of λ_X, $\Delta g_1^X \equiv g_1^X - 1$, and $\Delta\kappa_1^X \equiv \kappa_1^X - 1$. If we assume gauge invariance of the electromagnetic fields, then Δg_1^γ will be zero, leaving five parameters remaining: λ_Z, $\Delta\kappa_Z$, Δg_1^Z, λ_γ, and $\Delta\kappa_\gamma$. In general, we assume that the new terms do not introduce any additional charge conjugation violation or parity violation, referred to as the "LEP constraints" [58]:

$$\begin{aligned}\Delta\kappa_Z &= \Delta g_1^Z - \Delta\kappa_\gamma\tan^2\theta_W\,, \\ \lambda_Z &= \lambda_\gamma\,. \end{aligned} \tag{2.28}$$

The LEP model leaves us with $5-2=3$ free parameters, which we choose as $\lambda = \lambda_\gamma = \lambda_Z$, $\Delta\kappa_Z$ and Δg_1^Z. Applying the LEP constraints will greatly simplify the effective Lagrangian;

$$\frac{\mathcal{L}_{WWZ}}{g_{WWZ}} = ig_1^Z\left(W^\dagger_{\mu\nu}W^\mu Z^\mu - W^\dagger_\mu Z_\mu W^{\mu\nu}\right) + i\kappa_Z W^\dagger_\mu W_\nu Z^{\mu\nu} + i\frac{\lambda_Z}{m_W^2}W^\dagger_{\lambda\mu}W^\mu_\nu Z^{\nu\lambda}\,. \tag{2.29}$$

The aTGC amplitudes have a non-trivial dependence on the total energy of the TGC vertex, $\hat{s}$ (equivalent to the invariant mass of the diboson system). The κ_Z term will be linear in $\sqrt{\hat{s}}$, whilst the other two, g_1^Z and λ_Z will be linear in $\hat{s}$. The $\hat{s}$ dependence means that variables dependent on $\hat{s}$, such as the cross-section and the p_T of the leading jets from vector boson decays. Moreover, the gauge boson p_Ts will be particularly sensitive to the aTGCs due to the derivative terms in the effective Lagrangian, which translates to gauge momentum dependence [59].

The implications of this are that studies of TGCs could provide a particularly sensitive field in searches for new physics. Measurements of diboson decays can provide a particularly useful channel, with high sensitivity to aTGCs. This sensitivity will be particularly high for systems with high Lorentz boosts, i.e. with objects carrying high p_T [60, 61].

2.4.3. An Effective Theory Interpretation of Triple Gauge Vertices

Some theorists prefer to employ an effective field theory interpretation of aTGCs. We can relate the parameters of effective field theories to those used to parametrise the aTGCs in section 2.4.2. Let us consider an effective field theory model in the form given in equation (2.26), and apply the demand that it reduces to the Standard Model in the limit that $\sqrt{s}$ is well below Λ. The dimension-4 operators will simply be the terms of the Standard Model Lagrangian, whilst higher order terms will represent new physics. If we restrict ourself to dimension-6 operators, there are 3 such operators that contribute to triple-gauge-boson interactions. Dimension-8 operators would be suppressed by an additional factor of $1/\Lambda^2$.

One useful paramaterisation [62] of these operators is

$$\begin{aligned} \mathcal{O}_{WWW} &= \mathrm{Tr}\left[W_{\mu\nu}W^{\nu\rho}W_{\rho}^{\mu}\right], \\ \mathcal{O}_{W} &= (D_{\mu}\Phi)\dagger W^{\mu\nu}(D_{\nu}\Phi), \\ \mathcal{O}_{B} &= (D_{\mu}\Phi)\dagger B^{\mu\nu}(D_{\nu}\Phi), \end{aligned} \tag{2.30}$$

where Φ is the Higgs doublet, and $W^{\mu\nu}$, $B^{\mu\nu}$ are as defined in equations (2.6) and (2.7). We name the coefficients of these operators c_{WWW}, c_W and c_B respectively. If we apply the LEP constraints, then matching the effective field theory Lagrangian terms to those in equation (2.29), we arrive at a simple linear relationship between the effective field theory parameters and the aTGC parameters:

$$\begin{aligned} \frac{c_{WWW}}{\Lambda^2} &= \frac{2}{3g^2 m_W^2}\lambda \ , \\ \frac{c_W}{\Lambda^2} &= \frac{2}{m_Z^2}\Delta g_1^Z \, , \\ \frac{c_B}{\Lambda^2} &= \frac{2}{m_W^2}\Delta\kappa_\gamma - \frac{2}{m_Z^2}\Delta g_1^Z \, , \end{aligned} \tag{2.31}$$

where g is the Electroweak coupling constant. The linear relationship means that by searches for limits on aTGC parameters can also be used to set limits on effective field theories for BSM physics. Several analyses at the ATLAS and CMS experiments described in chapter 3, have searched for anomalous couplings by looking at the decays of vector bosons [14, 63, 64].

Chapter 3.

The Large Hadron Collider and the ATLAS Detector

3.1. The Large Hadron Collider

The Large Hadron Collider (LHC) [65] is by far the largest synchrotron proton accelerator ever built. It is located around 100m underground, in a roughly circular, 27km circumference tunnel, based at the European Centre for Nuclear Research (CERN), near Geneva, Switzerland. The purpose of the LHC is to deliver proton-proton collisions at the highest energy ever explored, to provide the opportunity to make precision tests of the Standard Model and to search for new physics, beyond the Standard Model.

A chain of accelerators provide the proton beams for the LHC. First is LINAC2, a linear accelerator using a duoplasmatron ion source to deliver pulses of 50 MeV protons. These are accelerated to successively higher energies by a set of circular synchrotron accelerators. The Proton Synchrotron Booster accelerates them to 1.4 GeV, then the Proton Synchrotron accelerates them to 26 GeV, then the Super Proton Synchrotron accelerates them to 450 GeV. Finally, the protons enter the LHC itself, the largest synchrotron accelerator, which in Run 1 (2009-2013) accelerated protons up to an energy of 4 TeV in each beam, for a centre of mass energy $\sqrt{s} = 8$ TeV, by far the highest ever achieved [1]. Figure 3.1 shows the CERN accelerator complex.

[1] The previous highest centre of mass energy achieved was $\sqrt{s} = 1.96$ TeV at the Tevatron accelerator.

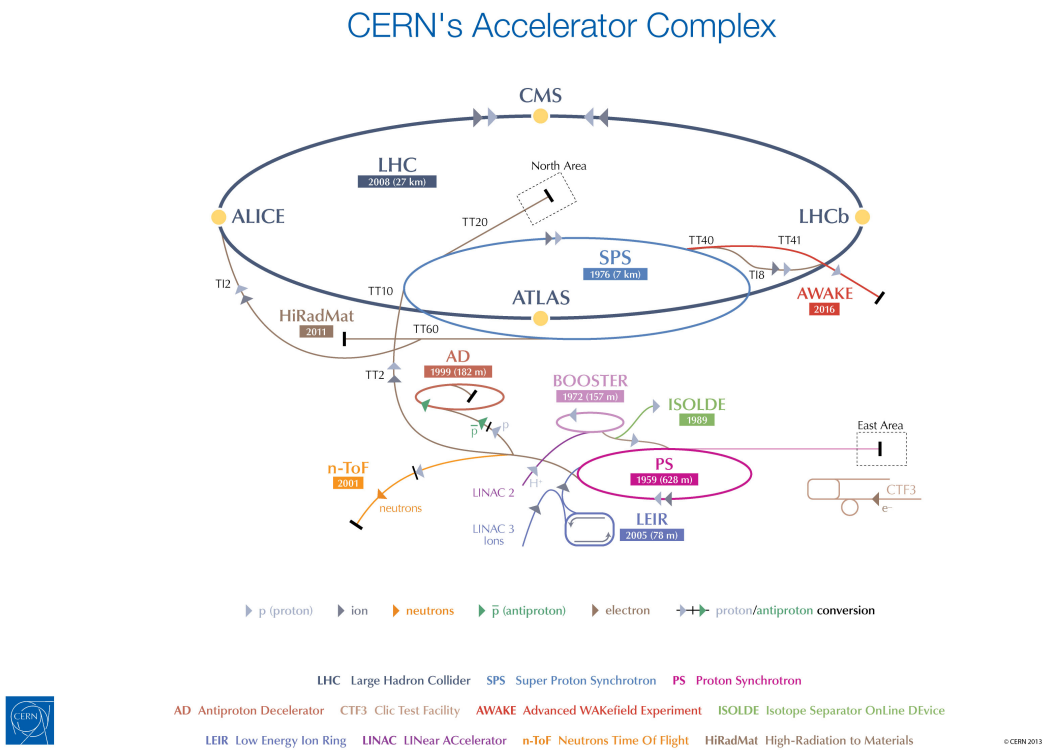

Figure 3.1.: The layout of the accelerator structures and experiments present at CERN [2].

The LHC itself consists of two separate evacuated beam pipes, contained within a series superconducting electromagnets, cooled to 1.9 K by a bath of liquid Helium. The magnetic fields keep the high energy protons within the confined space of the synchrotron. The beam pipes each have their own radio frequency (RF) cavities, which accelerate the protons using a standing wave electromagnetic field, whose frequency is timed to give the protons a small kick of energy each time they pass by. Two main types of magnet are used within the LHC; large superconducting dipoles to guide the beams round the curvature of the machine, and quadrupoles, used to focus and squeeze the beam size.

The bunches of protons inside the LHC circulate continuously, in opposite directions, crossing at a set of fixed interaction points around the ring. The bunches must be sufficiently spaced such that they are in time with the rise of the RF cavities to allow acceleration, ramping up the energy from 450 GeV to the full beam energy, up to 4 TeV in Run 1. In addition, the bunches need to be positioned to collide at each of the four interaction points. The optics of the machine squeezes the beams

size at these points. Four main experiments take place at the interaction points; CMS (Compact Muon Solenoid), and ATLAS (A Toroidal LHC ApparatuS), which are general purpose detectors, ALICE, which focuses on heavy ion physics, LHCb, which focuses in particular on flavour physics, such as that of particles containing a b quark. As the beam energy is increased, the magnetic fields of the dipole magnets must be synchronously ramped from 0.53 T at injection to around 4 T at the full beam energy, in order to continue to bend the beam around the LHC.

Many of the processes that we want to study will typically happen only very rarely in proton collisions. The number of events we expect in a particular time will depend upon the cross-section, σ, and on the instantaneous luminosity of the collider, $\mathscr{L}$:

$$\frac{dn}{dt} = \mathscr{L}\sigma = \frac{f n_b n_p^2}{A} \times \sigma = \frac{f n_b n_p^2}{4\pi\sigma_x\sigma_y} \times \sigma \,. \tag{3.1}$$

Here the instantaneous luminosity, $\mathscr{L}$, is defined, for a machine like the LHC with symmetric beams in terms of f, the rotation frequency of the beams, n_b, the number of bunches per beam, n_p, the number of protons for each bunch, and A, the transverse area of the beam. σ_x and σ_y characterise the Gaussian transverse beam profiles in the horizontal and vertical directions; we assume that the bunches are identical in transverse profile, that the profiles are independent of the position along the bunch, and that the particle distributions are not altered during the collision. Generally, accelerators aim for the highest possible luminosity, to enable the study of rarer processes with smaller cross-sections. The total luminosity delivered over a period of time is called the integrated luminosity.

3.2. Pile-up and the Underlying Event

A typical proton-proton collision is highly complex process. As discussed in chapter 2, protons are composite objects with complex internal structures. To first order, we can consider a "hard process" in which an individual pair of quarks or gluons inside the incoming protons interact and exchange momentum; however, in addition to this, one would expect interactions between the remnants of the protons whilst they are

still close to the direction of the beam, and in addition initial or final state radiation (ISR or FSR) from the incoming or outgoing quarks and gluons, respectively. The particles from these processes are known as the underlying event. Furthermore, when bunches of protons cross, it is possible that other protons in each bunch will interact in inelastic collisions, known as pile-up collisions.

In order to increase the luminosity, it is desirable to maximise the number of protons per bunch, and to keep the transverse area of the beam as small as possible. However, when n_p^2/A is very large, each bunch crossing produces more inelastic proton-proton scatters, known as in-time pile-up. Similarly, to increase luminosity, it is desirable to maximise n_b. However, as n_b rises, the time between collisions at an interaction point falls, so that a particular collision can be contaminated from particles from other bunch crossings. This is known as out-of-time pile-up.

In Run 1, the LHC delivered 25 fb^{-1} integrated luminosity, at centre of mass energies 7 and 8 TeV. This enabled studies of processes with cross-sections as low as a few fb at these energies. In order to achieve this, beams circulated with bunches composed of approximately 10^{11} protons. When colliding, these bunches were squeezed into a transverse diameter of around 20 μm. As a result, there were of order O(20) in-time pile-up events for each measured interesting event. The beams had up to around 1400 bunches each. The revolutionary frequency was approximately 11kHz. This led to delivered instantaneous luminosities of around 10nb s^{-1}. Beams are optimally circulated for 12 hours at a time, their lifetimes limited by the amount of scattering taking place in collisions, and by interaction with the residual gas in the beam pipe.

3.3. ATLAS coordinates

The ATLAS coordinate system defined here will be used throughout the thesis. The origin of the coordinate system is defined as the nominal interaction point at the centre of the detector. The beam direction defines the z-axis, and the x–y plane is the plane transverse to the beam direction. The positive x-axis points towards the centre of the LHC ring, and the positive y-axis points directly upwards from the interaction point. The positive z axis points down the beam pipe, towards the LHCb detector on the LHC ring.

The detector has a roughly symmetrical geometry, so it makes more sense in most cases to apply cylindrical coordinates. The azimuthal angle, ϕ , is measured in the x–y plane, and the polar angle, θ is measured between the z-axis and the x–y plane.

In a hadron collider the centre-of-mass frame of the hadrons is not usually the same as the centre-of-mass frame of the interacting partons. Energy and angular separations are not invariant under Lorentz boosts and, for a detector constructed in the hadronic centre-of-mass frame, particles will appear more collimated or dispersed, depending on their boost.

It is therefore particularly important when dealing with a range of different boosts, to choose variables which are longitudinally Lorentz invariant with which to classify events. It is frequently useful in collider experiments to use the quantity, rapidity, which depends on the amount of energy and z-axis momentum that a particle possesses. Differences in rapidity are invariant under Lorentz transformations. Rapidity is defined as

$$y = \frac{1}{2} \ln \left(\frac{E + p_z}{E - p_z} \right) . \tag{3.2}$$

We define the related quantity, pseudorapidity, as

$$\eta = - \ln \tan \left(\frac{\theta}{2} \right) . \tag{3.3}$$

and is only dependent on the polar angle of a particle's trajectory, not its energy. In terms of momentum, the pseudorapidity is given by

$$\eta = \frac{1}{2} \ln \left(\frac{|\vec{p}| + p_z}{|\vec{p}| - p_z} \right) . \tag{3.4}$$

Pseudorapidity differs from true rapidity, y, by taking the relativistic approximation that the particle's mass is negligible. Whilst rapidity has a stronger physical motivation, by mapping uniquely onto the polar angle , θ, pseudorapidity is often

more useful in practice. We usually take pseudorapidity to define the polar angle in the detector. As with rapidity, differences in pseudorapidity are invariant under Lorentz boosts along the z-axis.

Transverse momentum, p_T, is defined along the x–y plane as

$$p_T = \sqrt{p_x^2 + p_y^2}\,, \tag{3.5}$$

and all other transverse objects such as transverse energy, E_T, are defined in a similar fashion.

It is often useful to define the distance ΔR between two particles in terms of η, ϕ coordinates,

$$\Delta R^2 = \Delta\eta^2 + \Delta\phi^2\,. \tag{3.6}$$

3.4. The ATLAS detector

The ATLAS detector [4], shown in Figure 3.2, is a multi-purpose detector, aiming for complete coverage in η and ϕ, and able to detect and distinguish a broad range of physics signatures. Its first incarnation was first proposed in 1994, with the first data from pp collisions at $\sqrt{s} = 900$ GeV collected in November 2009. The length of the detector is around 46 m, the diameter around 25m, and the total weight is approximately 7000 tonnes.

The interactions that physicists wish to study take place over extremely small distances and times. To provide an idea characteristic time scales, consider the lifetime of a W boson, of order 10^{-25} s, or a B meson, of order 10^{-12} s. A W boson could travel up to around 10^{-17}m before decaying. The most powerful microscopes available today can only explore relatively static structure, on atomic distance scales (around 10^{-10} m). However, a few short lived particles travel easily measurable distances, such as the B meson, which could travel around 10^{-3} m, discussed in section 3.4.2.

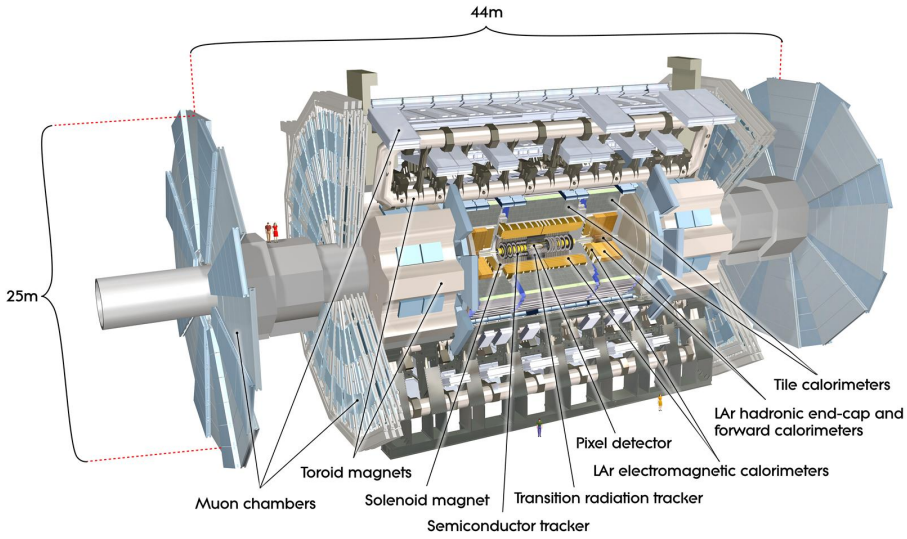

Figure 3.2.: A schematic of the ATLAS detector at the LHC [3].

For the most part, the study of particle physics must utilise indirect observation techniques. A decay chain eventually produces more stable particles, which will travel further and are easier to detect. By measuring their kinematics, and by identifying the type of particle we are observing, we can deduce information about the fundamental processes that took place to produce them. The detector was designed with physically interesting processes in mind, with a focus on getting the best possible resolution for relevant quantities, whilst using radiation-hard materials and electronics, and allowing for distinction between various kinds of particles.

As such, ATLAS consists of many concentric layers, of different kinds of detector, each with a different main purpose. The overall geometry is roughly cylindrical, with each sub-detector having a barrel and an endcap region to provide central and forward coverage. A solenoid provides magnetic field for the inner detector, while three air-core toroid magnets provide the bending in the outer part of the detector. The design resolution and η coverage of the detector components is shown in table 3.1.

Sub-detector	Design resolution	η coverage
Tracking	$\sigma_{p_T}/p_T = 0.05\% p_T \oplus 1\%$	$\|\eta\| < \pm 2.5$
Electromagnetic Calorimeter		
Barrel and end-caps	$\sigma_E/E = {}^{10\%}/\sqrt{E} \oplus 0.7\%$	$\|\eta\| < \pm 3.2$
Forward calorimeter	$\sigma_E/E = {}^{100\%}/\sqrt{E} \oplus 3.5\%$	$3.1 < \|\eta\| < 4.9$
Hadronic Calorimeter		
Barrel and end-caps	$\sigma_E/E = {}^{50\%}/\sqrt{E} \oplus 3\%$	$\|\eta\| < \pm 3.2$
Forward calorimeter	$\sigma_E/E = {}^{100\%}/\sqrt{E} \oplus 10\%$	$3.1 < \|\eta\| < 4.9$
Muon spectrometer	$\sigma_{p_T}/p_T = 10\%$ at $p_T = 1$ TeV	$\|\eta\| < \pm 2.7$ (± 2.4 for trigger)

Table 3.1.: Design resolutions and η coverage of the ATLAS sub-detectors; $\oplus$ refers to addition in quadrature [4].

3.4.1. Magnet Systems

The magnet systems at ATLAS are superconducting, cooled to around 4.5K by liquid helium from a dedicated cryostat system. There are two main magnet systems incorporated into the ATLAS detector, a central solenoid (CS) and air core toroids. The CS surrounds the inner detector and provides it with a 2 T magnetic field to bend charged particles within the inner detector. The air core toroids are arranged as two endcap toroids (ECT) and one central barrel toroid (BT), providing on average 1.0 and 0.5 T fields respectively, to the muon spectrometers.

3.4.2. Inner Detector

The Inner Detector, shown in figure 3.3, is comprised of three tracking detectors, the pixel detector, the semiconductor tracker (SCT) and the transition radiation tracker (TRT). Each provides multiple space points, or hits, from which to form particle tracks, together providing an average of 48 hits per particle. Each detector consists of two endcaps and one barrel, giving almost full hermetic coverage around the interaction point.

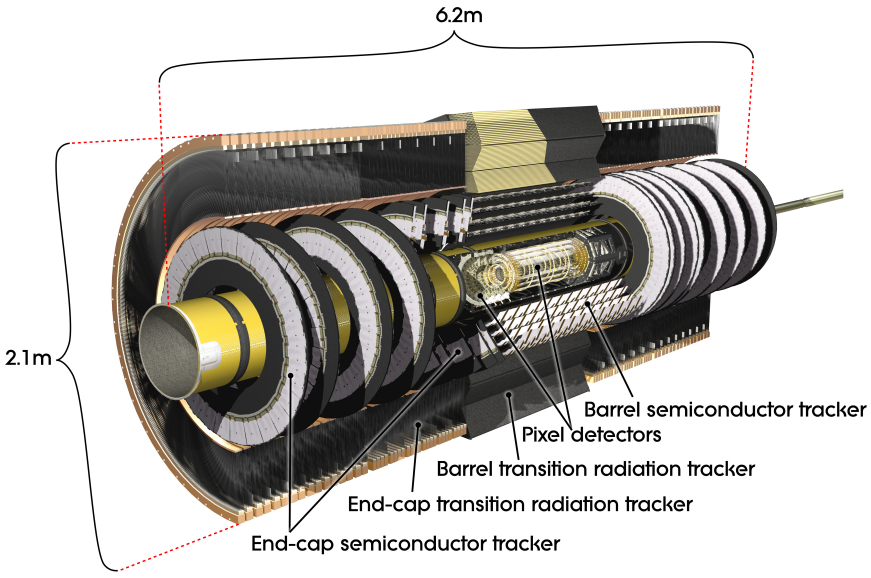

Figure 3.3.: The ATLAS inner detector [4].

Together, these detectors aim to minimise the amount of material used, in order to reduce the number of coloumb-scattering interactions and photon conversions. The thickness varies between around 0.5 to 2 radiation lengths, depending on the position in η.

One of the main functions is to provide high-resolution momentum measurements of charged particle tracks. It is immersed in the solenoid's 2T magnetic field, curving the tracks of charged particles to allow a momentum measure from their curvature. It is also used for the identification of primary and secondary interaction vertices, caused from decaying particles such as a B meson, and so can be used for particle identification in these cases. The detector provides full azimuthal coverage, and reaches an eta range of $|\eta| < 2.5$.

Pixel Detector

The pixel detector forms the innermost layer of the inner detector, and is also the most finely segmented of the inner detector subsystems, with around 80 million readout channels. It is composed of three cylinders and six rings of flat, silicon-based position detectors, of radi 4, 9 and 12 cm in the barrel region, and three endcap discs extending radially from 9 to 15 cm at different points in z. The pixel detector begins

approximately 4.5 cm from the beam, extending to a radius of 24cm and a z of 65 cm. In total, the pixel detector contains 1744 pixel modules, 1456 in the barrel and 288 modules between the two endcaps. Each module contains 47232 pixel elements, providing an active area of 60.8×16.4 mm^2.

This allows for extremely precise spatial resolution, as small as 10 by 115 μm. It provides three high precision space point measurements per track. It is also useful, by being situated so close to the interaction point, in the reconstruction of secondary vertices, helping to tag short lived particles such as B hadrons or τ leptons.

Semiconductor Tracker

The semiconductor tracker (SCT) is a silicon strip detector, with the strips aligned with the beam axis in cylinders around it, and aligned radially in the end disks. It is possible for a strip sensor to provide a position in only one direction. Hence, the 6.4 cm long strips attach back-to-back, together with a pitch of about 80 μm. To improve the accuracy of the position measurement, the strips are arranged in pairs, with layers tilted at an angle of 40 mrad, solving any ambiguities and providing a full space point. This results in an accuracy of 17 μm in R–ϕ and 580 μm in z. There are 4 layers of these pairs in the barrel, and 9 disks at each end, with a size of about 3 m in z and 0.5 m radially. The barrel contains 2112 identical modules, whilst the two endcaps have 1976 modules, of 3 different types depending on the posiiton. In total, there are 63 m^2 of silicon detectors. Both the SCT and pixel detectors operate at temperatures between 0 and -7 $^\circ$C, maintained by an environment of dry nitrogen gas.

Transition Radiation Tracker

The Transition Radiation Tracker (TRT) forms the outermost layer of the tracking system. It consists of straw drift tubes, aligned with the beam axis in the barrel, and in a fan at the ends. The tubes are about 4 mm in diameter, with thin tube walls containing 31 μm thick gold-coated tungsten anode wires. They are filled with a Xe–CO_2–O_2 gas mixture. This gas is ionised when a charged particle passes through. The negative electrons drift to the wire running down the centre of each tube, producing a current. The accurate timing measurement of the pulses leads to

a precision of about 130 μm in R–ϕ. In the barrel, the tubes are up to 144 cm long, and offer no information on the z position. Similarly, at the ends, no information is given on the R position. This is less precise than the silicon detectors, but the number of hits is much higher. Each charged particle passing through can cause around 35-40 hits. Furthermore, the TRT provides a significant extension to the track length. A flow of CO_2 surrounds the TRT system, keeping it at a temperature of 20°C.

The volume between the tubes is filled with polypropylene foil or fibres, which creates transition radiation when highly relativistic charged-particles cross it, in an amount dependent on the Lorentz boost of the particles. This helps with the identification of electrons, because they are much lighter than other particles and thus typically have a higher Lorentz boost.

3.4.3. Calorimeters

The ATLAS calorimetry system, shown in figure 3.4, provides energy and position measurements of electromagnetic (EM) and hadronic showers. Unlike the tracking detectors, they measure both charged and electrically neutral particles. They are designed to give accurate energy measurements over the full range of ϕ and up to $|\eta| < 4.9$, such that the full energy of the event is recorded, and an accurate determination of missing energy can be made, used for identifying neutrinos, which pass straight through the entire detector system without interacting.

Crucial to the calorimeter system is the fact that hadrons penetrate further and have broader showers than electrons and photons. Thus, the electromagnetic calorimeter, used for measurements of electron and photon showers, lies closer to the beam line than the hadronic calorimeter, which surrounds it. Quite different technologies and materials are used in the different calorimeters and regions. It is important that the electromagnetic calorimeter captures as much as possible of the electromagnetic showers. Therefore, the material is chosen for the electromagnetic calorimeter with the intention of minimising the radiation length, X_0 of electromagnetic showers, whilst maximising the nuclear interaction length, λ of hadronic showers.

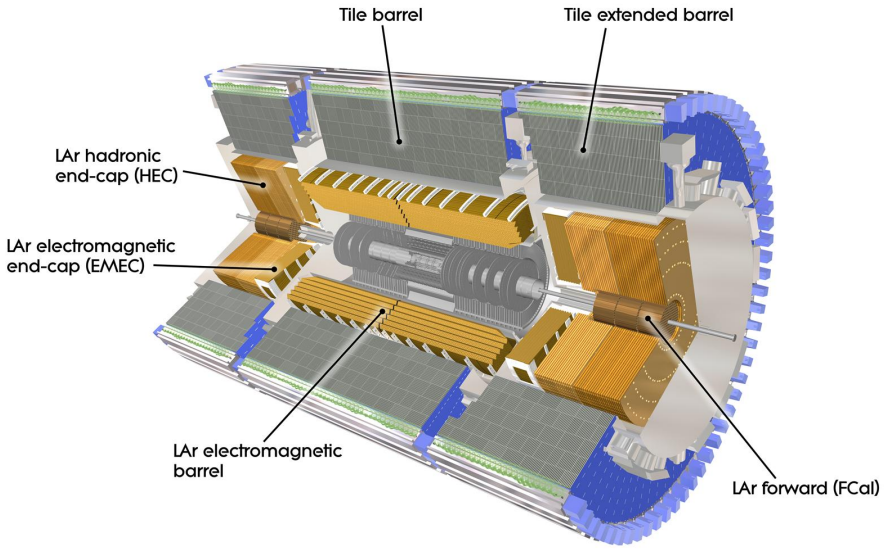

Figure 3.4.: The ATLAS calorimetry system [4].

Electromagnetic Calorimeter

The electromagnetic calorimeter (ECAL) is a liquid argon (LAr) sampling calorimeter. Its function is to measure the position and energy of electrons and photons incident on it. However, it can also measure the neutral component of hadronic jets and τ lepton decays, via the decay $\pi^0 \to \gamma\gamma$: these photons then deposit energy in the calorimeter, as with photons from other processes.

Liquid argon is the active material, while thin layers of lead are used as absorbers, which initiate electromagnetic showers when electrons and photons hit. Electromagnetic showers are a cascade of electromagnetic interactions, mainly Bremsstrahlung for electrons and electron pair-production for photons. The sampling layers of LAr are sandwiched between the absorbers; electrons in the shower ionise the argon, and this charge is collected by layers of copper electrodes.

The ECAL offers fine granularity, allowing precision measurements of electrons and photons to be made. It is divided into a barrel region, covering $|\eta| < 1.475$ and two endcaps, for $1.375 < |\eta| < 3.2$, each in their own cryostat. The barrel is split into two identical half barrels, seaprated by a small gap of 4mm at $\eta = 0$. The end caps each consist of two coaxial wheels, the one one covering $1.375 < |\eta| < 2.5$, the outer covering $2.5 < |\eta| < 3.2$. To reduce the amount of material, and hence improve

the performance, the LAr calorimeter and central solenoid are located inside the same vacuum vessel.

A presampler detector covers the region $|\eta| < 1.8$, which consists of a layer of liquid argon, 1.1 cm thick in the barrel region, and 0.5 cm in the end caps. It is used to correct for energy lost by electrons and photons before they reach the calorimeter itself.

The lead plates and copper electrodes are arranged in an accordion geometry, to ensure complete ϕ symmetry, without any cracks. In the barrel region, it is separated by three longitudinal layers, reaching out to 22 X_0. In the end caps, the calorimeter reaches up to 24 X_0, with the first wheel separated into three layers, and the outer wheel two, having a coarser granularity.

Hadronic Calorimeter

The hadronic calorimeter (HCAL) measures the position and energy of hadronic showers. Two different technologies are used.

The HCAL in the barrel region ($|\eta| < 1.7$) is a sampling tile calorimeter with steel absorbing layers and plastic scintillator sampling layers as the active material. These are read out through wavelength-shifting fibres on each side of the scintillating tiles, to photomultiplier tubes. Charged particles passing through the scintillator cause it to emit ultraviolet light. The scintillator contains fluors that then shift the wavelength of this light towards the visible spectrum. It is then collected by wavelength-shifting fibres at the end of each tile, which transmit the signal to a set of photomultiplier tubes at the module edges, where incident photons can be measured and an energy deposit determined.

The barrel region HCAL is further subdivided, into a central barrel region ($|\eta| < 1.0$), with three radial layers of 1.5, 4.1 and 1.8 λ thickness, and two extended barrles ($0.8 < |\eta| < 1.7$), with three radial layers of 1.5, 2.6 and 3.3 λ thickness. Each of these components is divided azimuthally into 64 modules in ϕ.

The hadronic endcap users LAr technology, similar to that used in the ECAL, and with a similar segmentation. It covers $1.5 < |\eta| < 3.2$. There are 2 wheels per end cap, with 32 wedges in ϕ, each wheel divided into two layers. It uses copper as

an absorber (unlike the lead used in the ECAL end caps), with 25 mm sheets in the first layer and 50 mm sheets in the second, separated by 8.5 mm of LAr, which provides the active medium.

Forward Calorimeter

The Forward Calorimeter (FCAL) consists of one module at either end of the detector, approximately 10 λ deep, to provide coverage for the region $3.2 < |\eta| < 4.9$. They are integrated into the end cap cryostats, although recessed by about 1.2 m from the electromagnetic calorimeter. The depth available is limited, so it requires a high density design. The two FCALs each contain three modules, a copper calorimeter, optimised for electromagnetic measurements, and two tungsten calorimeters, designed primarily for hadronic measurements. Each module has a matrix form, with regularly spaced longitudonal channels filled with concentric tubes, parallel to the beam axis. Each tube contains a rod, and is otherwise filled with LAr, providing the active medium. The gaps left for LAr are as small as 0.25 mm, in order to avoid ion build-up in the high radiation environment close to the beam line.

3.5. Muon Spectrometer

The muon spectrometer (MS), shown in figure 3.5, is the outermost of the ATLAS subdetectors, and defines the overall size of the ATLAS detector. It provides accurate measurements of the position and momentum of muons, relying on the fact that they are the only particles that pass through the calorimeter without stopping (except for neutrinos, which are highly unlikely to interact at all with any part of the detector). The three barrel and two endcap air core toroid magnets provide a magnetic field that is roughly perpendicular to the muon momentum across the whole of the muon detector. To minimise multiple scatterings, the detector covers a large volume, but is of low density.

The muon spectrometer employs two precision measurement chamber designs: monitored drift tubes (MDTs) in the barrel and encap, covering the range $|\eta| < 2.7$, and cathode strip chambers in the inner endcaps, covering $2.0 < |\eta| < 2.7$. The muon spectrometer also uses faster detectors for triggering purposes, with resistive

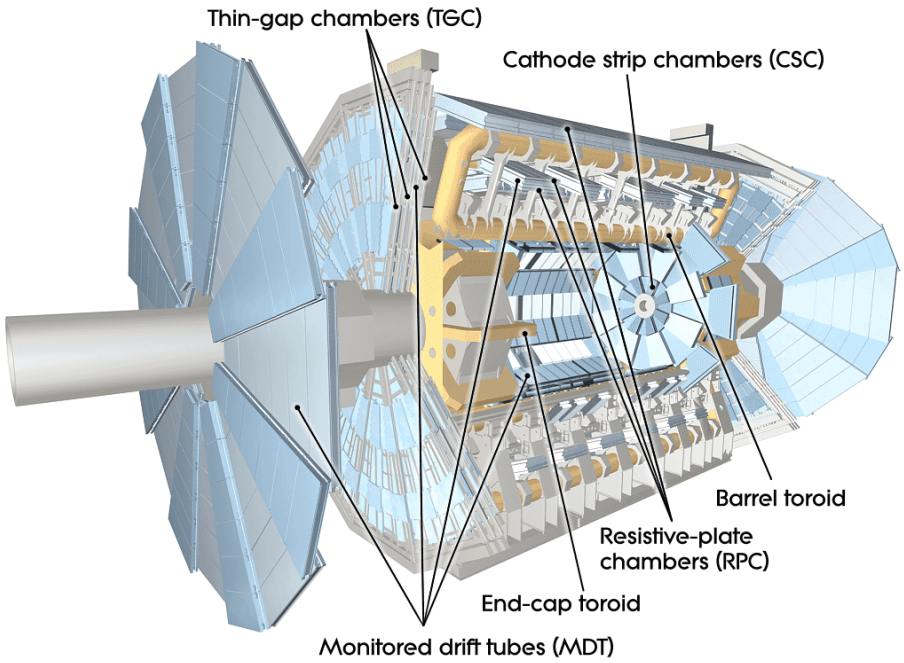

Figure 3.5.: The ATLAS Muon detector system [4].

plate chambers in the barrel, for $|\eta| < 1.05$ and thin gap chambers (TGC) in the endcaps, $1.05 < |\eta| < 2.4$.

The precision tracking MDT chambers consist of pressurised drift tubes, of radius 15 mm, filled with an Ar–CO_2 gas mixture. A gold plated 50 μm anode wire runs along the centre of each tube and collects the charge from gas ionisations caused by muons passing through the tube. The MDTs form cylindrical shells, at radii of 5, 7.5 and 10 m in the barrel region, and four wheels at 7.4, 10.8, 14 and 21.5 m from the interaction point in the z direction. In the very far forward region, cathode strip chambers (CSC) are used to cope with the high particle fluxes present. These are multi-wire proportional chambers, with radially aligned anode wires and perpendicular cathode strips. They are filled with a different Ar–CO_2 gas mixture to the MDTs, and record hits by interpolating the charge induced on adjacent cathode strips.

The trigger chambers provide fast triggering information from the muon spectrometer, providing a region of interest and a fast estimate of the transverse momentum of the muons. Resistive plate chambers are used in the barrel. There are three trigger stations between the MDTs, each containing two resistive plate chambers,

which provide measurements in η and ϕ. Thin gap chambers are used in the end caps, based on a similar technology to the CSCs. This system provides coverage only up to $|\eta| < 2.4$, providing fast p_T information for initial trigger decisions.

3.6. Trigger system

The LHC is designed to deliver collisions at a rate of 40 MHz at an instantaneous luminosity of 10^{34} cm^{-2}s^{-1}. The data storage systems available can only store events at a rate of a few hundred events per second. The vast majority of physically interesting events that take place at ATLAS have a small cross-section, typically of order $\sim$ pb, so they are extremely rare, forming only a marginal fraction of the total events that take place. A triggering system is therefore essential, in order to select physically interesting events to be stored, reducing the event rate to manageable levels. Substantial upgrades to the trigger system were made between Run 1 and Run 2.

3.6.1. The Trigger in Run 1

The ATLAS trigger system, shown in figure 3.6, is designed to reduce the rate of data-taking by a factor of around 10^5, by excluding uninteresting events. However, decisions on which events to select must be made extremely quickly, due to the fast rate of events taking place and the large quantities of data being stored. During Run 1, ATLAS tackled this using a three-level trigger system, designed to optimise between rapid selection and reliable event identification. The fastest trigger, Level 1 (LVL1) was hardware based; the other two, Level 2 (LVL2) and the event filter (EF) were software-based, together forming the high level trigger (HLT). Table 3.2 of the trigger levels gives the input and output frequencies.

During Run 1, the LVL1 trigger made a decision with a latency of approximately 2μs. The central trigger processor (CTP) determined the rate at which it took readings, defining the ATLAS internal clock frequency (usually 40 MHz). The LVL1 calorimeter trigger obtained inputs from the read-outs of the electromagnetic and hadronic calorimeter, while the LVL1 muon trigger system processed information

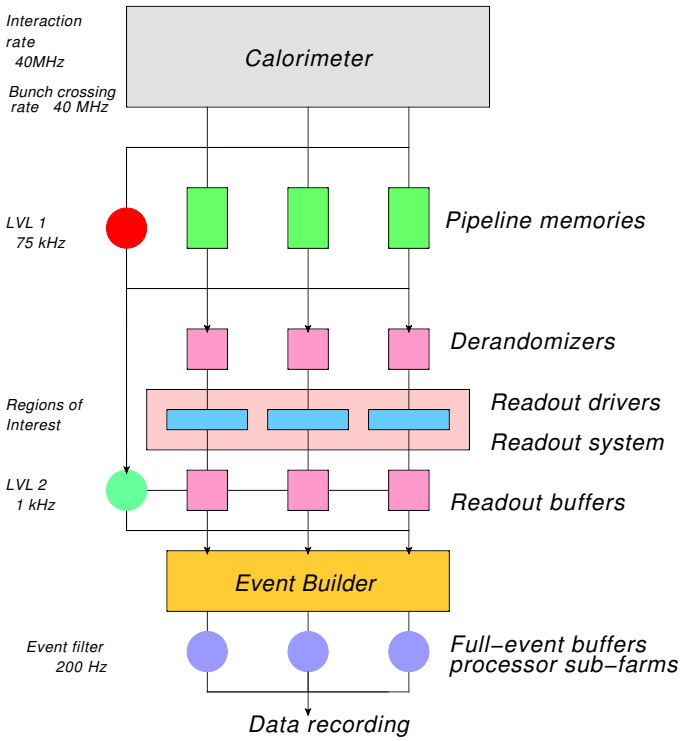

Figure 3.6.: Schematic of the ATLAS trigger system

	LVL1	LVL2	HLT
Input rate	40 MHz	75 kHz	1 kHz
Output rate	75 kHz	1 kHz	500 Hz
Execution time	2.2 μs	40 ms	1 s
Location	On detector	Counting room	Counting room

Table 3.2.: Characteristics of the trigger levels and offline analysis.

read-out from the muon detectors and identified the bunch crossing in which they were produced.

The Run 1 LVL1 trigger identified areas known as regions of interest (RoIs) that contained the most interesting fraction of a given event. These RoIs formed rectangular-based pyramid in the η–ϕ plane, opened in the z-direction. The RoIs were selected according to whether particular objects passed a particular energy threshold. The LVL1 trigger system made a decision to pass events or not based

on a required multiplicity of RoIs. A typical RoI contained only around 10% of the detector information.

Run 1 events accepted by the LVL1 trigger decision were stored in read-out buffers (ROBs), whilst the LVL2 trigger took its decision. ROBs connected to read-out systems (ROS), which sent signals to the LVL2 trigger networks.

For Run 1, the LVL2 software-based trigger took decisions with a latency of order 10 ms. The more sophisticated LVL2 algorithms took input data from the ROS corresponding to the data elements inside each selected RoI. The algorithms reconstructed data considering only those slices defined by the RoI. Therefore, at this stage, events were selected on the basis of a partial reconstruction: this allowed for a high selection efficiency, while avoiding the huge bandwidth that would be required for complete event reconstruction.

The decision from LVL2 was sent to data-flow managers. These distributed the data from the read-out servers (ROS's) to the Event Builder (EB), in which each data were processed to construct a full event structure. The event data were then sent to the EF for the final trigger analysis.

During Run 1, the EF software-based trigger made decisions with a latency of order 1 s. As input, it took the RoIs of events passed at LVL2. The EF algorithms were similar to their offline counterparts, running a full reconstruction of the RoI on processor sub-farms. This allowed for a more refined alignment and calibration. Those events that passed the EF were written to tape.

At LVL1, the trigger menu consisted of a list of thresholds for particular objects (for example, "J15" refers to a 15 GeV threshold for jets) and items, which were logical combinations of these thresholds (for example "3J15" refers to a threshold of 15 GeV for three jets). The central trigger processor counted objects passing these trigger items. The majority of items in the LVL1 menu were prescaled, only recording a certain proportion of otherwise acceptable events.

For the HLT, the trigger menu consisted of a list of algorithms, and sequences of these algorithms. Trigger chains consisted of a full series of required trigger signatures that need to pass, including LVL1 inputs, a list of sequences of algorithms, and prescales associated at each level. Trigger chains were labelled by the physics objects that they required (for example, "L1_J15" refers to a chain requiring an event to

have at least one jet candidate at LVL1, with a p_T of at least 15 GeV, while"EF_j40" requires a jet candidate at the EF level, with a p_T of at least 40 GeV). Upper case lettering of objects refers to the LVL1 definition, lower case to the HLT definition.

Prescales were typically applied to reduce the rate associated with such triggers. This is because some types of event are useful to maintain for analyses, but are so common that the rates would be prohibitive without a high prescale. Another use for prescales is to test new triggers before placing them into the system at potentially higher rates. "Passthrough" of a trigger can also be defined to force a set fraction of events be accepted by the trigger, still recording the decision but not removing any events.

If an event passed through a full trigger chain, from Level 1 through to the Event Filter, it is was recorded along with information of all of the triggers that it has passed. An event was placed into data-streams defined by the triggers it passed. There were a set of physics streams which take events from groups of physics triggers, the main physics streams are; egamma for electron and photon triggers, muon, jet (which includes triggered τ objects) and E_T^{miss}. There was a small amount of overlap between the streams. There were also express, calibration and debug streams which take small samples for testing and debugging purposes.

The trigger system was configured consistently and coherently over all of its levels. In order to do this, ATLAS used a trigger configuration system. During Run 1, this configured the complete trigger menus and chains consistently, from LVL1 through to the EF. It also stored information for future usage in the production and analysis of simulated events.

If the trigger system made decisions that data from a collision should be kept, then the raw detector data were written to disk in a format known as Raw Data Object (RDO). The ATLAS offline software package, Athena, was then used to process this data; the output is called Event Summary Data (ESD). This data then underwent a second processing step where some of the data not needed for analysis was removed, to produce smaller, more manageable files known as Analysis Object Data (AOD). These files contained high level objects, such as electron or muon candidates.

3.6.2. Trigger Upgrade for Run 2

During the Run 1 period, between 2009 and 2013, the ATLAS trigger system operated highly successfully. It selected events with high efficiency at centre-of-mass energies $\sqrt{s}$ up to 8 TeV, for a wide range of physics processes including TeV-scale particle searches.

The first LHC upgrade took place at the end of Run 1, during the 2013-2014 (called "Long Shutdown 1" or LS1). During Run 2, the LHC is running with a centre of mass energy $\sqrt{s} \sim 13$ TeV, with luminosities peaking at around 10^{34} cm^{-2}s^{-1}. Trigger rates for a Run 1 type system would be expected to increase by a factor of roughly five in total: a factor of around 2 from the increase in energy, and a factor of 2.5 from the peak luminosity increase. In addition to the increase in luminosity, at these higher energies, ATLAS events will experience much higher average levels of pile-up.

Furthermore, the peak number of interactions per bunch crossing (μ_{peak}), which was 40 during the 2012 run, has increased to 50. The bunch spacing reduction from 50 ns to 25 ns will help to decrease the in-time pile-up, but will increase both out-of-time pile-up, and beam-induced fake trigger rates, particularly in the muon system.

These changes are summarised in table 3.3. They demanded significant upgrades to the trigger system in order to respond to the increased challenges of Run 2. The improvements help to reduce the trigger rates down to acceptable levels, while maintaining efficiencies in the challenging LHC conditions [66].

Period : year	Bunch spacing	$\sqrt{s}$	Peak Luminosity ($\times 10^{33}$cm^{-2}s^{-1})	Peak number of collisions per bunch
Run 1 : 2012-2013	50 ns	8 TeV	8	40
Run 2 : 2015-2018	25 ns	13 TeV	10–20	25–50

Table 3.3.: The LHC running conditions during Run 1 and Run 2.

The upgraded trigger system for Run 2 replaces the three stage trigger system with one composed of two stages. The Run 2 trigger system consists of a hardware

Level 1 (L1) and a single software-based high-level trigger (HLT), replacing the previous LVL2 and EF. This new two-stage system will reduce the event rate from the bunch-crossing rate of 40 MHz to 100 kHz at L1 and to an average recording rate of 1 kHz at the HLT.

The LVL1 is very similar to that applied in Run 1. At LVL1, fast custom-made electronics find regions of interest (RoI) using the calorimeter and muon data with coarse information within a latency of 2.5 μs. The LVL1 system in Run 2 consists of the LVL1 calorimeter trigger system (L1Calo), the LVL1 muon trigger system (L1Muon), new LVL1 topological trigger modules (L1Topo) and the CTP. At the HLT, fast algorithms accessing data from an RoI, or offline-like algorithms using the full-event information run with a processing time of 0.2 s on average. At the end of 2016, a hardware track finder (FTK) is planned to be fully integrated and will provide tracks to the HLT at the L1 rates.

The Level 1 Calorimeter trigger system (L1Calo) processes signals from the ECAL and HCAL in a pipeline, and provides trigger signals to the CTP. During Run 1, one of the most severe problems of the L1Calo system was the high LVL1 rates of missing transverse energy triggers, which were strongly affected by pile-up near the start of the bunch train. This resulted from an unbalanced overlap of bipolar signal shapes in the LAr calorimeter.

The solution adopted for Run 2 is to use a more flexible signal processing, in the new Multi-Chip Modules (nMCM). This allows the L1Calo system to use an auto-correlation filter and dynamical pedestal subtraction based on global cell occupancy and a bunch position in each LHC bunch train. Run 2 can achieve significant rate reduction for the missing transverse energy triggers. For instance, in the case of a 70 GeV threshold, the rate may be reduced by a factor of around 50. Furthermore, the number of thresholds to be applied to the different LVL1 trigger objects are are roughly double that in Run 1, from 12 to 25 for jets and forward jets, and from 8 to 16 for both electromagnetic and τ clusters [67, 68].

Chapter 4.

The Phenomenology of Quantum Chromodynamics

4.1. Jets at Hadron Colliders

As described in chapter 2.3.4, quark and gluons at high energies will undergo a process of showering, creating a spray of further quarks and gluons. The first (high energy, small distance scale) part of this process will be mostly perturbative. However, parton showering at larger distance scales and lower energies will be inherently non-perturbative. Eventually, these particles will undergo hadronisation, becoming confined in hadrons. This hadronisation process is non-perturbative and so cannot be calculated analytically. In practice, we observe the hadrons in collimated showers, which we envelope into ensembles called jets. Unlike the partons, which are propagators, these jets are physical objects, although their representation may be dependent on the model being used [69, 70].

Individual hadrons themselves provide little information about the hard process we are interested in studying. Ideally we want to group them in some way that provides information about the hard process. To do this, we use some particular jet algorithm (these will be discussed in 4.2), clustering individuals particles into jets. These "particles" may be any objects that we can represent as four-vectors; in practice we may choose partons produced at a fixed order from a perturbative QCD calculation or final state particles from a Monte Carlo model (see section 4.8), or alternatively could be detector level objects, such as calorimeter towers or tracks. Regardless

of the input, the output should be clustered jets, only minimally dependent on hadronisation models and detector effects that are often only understood empirically.

In some sense, the clustering of jets can be thought of as an attempt to reverse the fragmentation process; the jet kinematic properties such as momentum and energy should correspond to those of the original quark or gluon. However, in practice, reversal of the fragmentation is often not possible, or even physically well defined. It is more realistic to consider a jet algorithm as a way of usefully grouping the large amount of information found within an event. At ATLAS, collisions might produce thousands of particles, so this task of grouping these particles is highly non trivial [71].

In 1990, physicists established the "Snowmass accord" [72], stating the desirable properties that a jet algorithm should have. According to the accord, a jet algorithm should be:

1. Simple to implement in an experimental analysis;
2. Simple to implement in theoretical calculation;
3. Defined at any order of perturbation theory;
4. Yielding finite cross-sections at any order in perturbation theory;
5. Yielding a cross-section that is relatively insensitive to hadronisation;

Jet algorithms must be mathematically well-behaved in two critical respects, known as infrared and collinear safety (together known as IRC) [73]. Infrared safety is the property that if one modifies an event by a addition of a soft emission, the set of hard jets that we identify in the event must remain unchanged. Collinear safety is the property that if one modifies an event with a collinear splitting, travelling almost parallel to the particle from which it split, then the set of hard jets that we identify in the event must also remain unchanged. There are three main reasons why jet algorithms must obey IRC:

1. Without the IRC requirements, perturbative QCD calculations become impossible. In fixed-order perturbative QCD calculations, soft emissions and collinear splittings are associated with divergent tree-level matrix elements, as discussed in chapter 2.3.1. Normally, there are corresponding loop matrix elements that enter with the opposite sign and cancel these divergences; however, for IRC

unsafe jet algorithms, the tree-level splittings may lead to one set of jets, while the loop diagrams may lead to another, breaking the cancellation and leading to infinite cross-sections in perturbation theory.

2. Experimental detectors have a finite resolution and momentum threshold, and they cannot resolve the full infrared or collinear structure of an event. If the jet algorithms in use vary greatly based on these unmeasured infrared or collinear emissons, then it may not be possible to consistently connect experimentally measured jets to the expectations at hadron level.

3. Ultimately, failure to meet the IRC conditions breaks the relationship between the partonic structure of the hard event and the jets that we observe. It is precisely this relation that a jet algorithm is intended to codify. Fundamentally, collinear splittings and soft emissions are statistical occurrences are hard to predict because they will always occur in large numbers in QCD events, both through perturbative and non-perturbative effects. It makes no sense for the structure of a jet that may have an energy of several hundred GeV to change radically because of a difference in a random QCD emission of order 1 GeV. The motivation for constructing jets is precisely that we want to establish a way of viewing events that is insensitive to all these effects.

4.2. Jet Algorithms

When we cluster energy deposits into jets, we intend for these jets to approximately represent the decay products of the hard collision. However, it is crucial to realise that this choice is somewhat arbitrary, and the use of different jet algorithms could lead us to group the energy deposits in a different way. Ultimately, our choice of clustering algorithm depends on convention. It is therefore necessary to understand the implications of different algorithms for jet clustering.

We can distinguish two main classes of jet algorithm. Originally, the most commonly used were cone algorithms, which group all particles within some radius. These algorithms rely on the fact that QCD branching and hadronisation mostly leave the bulk features of an event's energy flow unchanged, keeping the shape roughly

conical in η–ϕ space. In practice, it has been difficult to create cone algorithms that are infrared and collinear safe (the exception being the SISCone algorithm) [74].

Today, clustering algorithms are far more common. These algorithms combine particles sequentially, based on a particular distance function, and stop when the distance function exceeds some particular threshold. The three most commonly used clustering algorithms are the $k_\perp$, Cambridge-Aachen and anti-$k_\perp$, all of which are closely related [73]. They are defined by the two distance functions, given by

$$\begin{aligned} d_{ij}^2 &= \min\left(p_{T,i}^{2p}, p_{T,j}^{2p}\right) \frac{\Delta R_{ij}^2}{R^2} \\ d_{iB}^2 &= p_{T,i}^{2p}\,, \end{aligned} \tag{4.1}$$

where,

$$\Delta R_i j^2 = \left(y_i - y_j\right)^2 + \left(\phi_i - \phi_j\right)^2\,. \tag{4.2}$$

Clustering proceeds by first calculating d_{iB} and d_{ij} for all particles, i and j. These values are then sorted from smallest to largest. If the smallest value is d_{iB}, then i is declared to be a jet and removed from the clustering procedure. If the smallest value is d_{ij}, then i and j are combined into a new k (through vector addition of their four momenta), and the process repeats.

The three algorithms are defined by the value of p that they take:

$$p = \begin{cases} 1 & k_\perp \text{ algorithm} \\ 0 & \text{Cambridge-Aachen algorithm} \\ -1 & \text{anti-}k_\perp \text{ algorithm}\,. \end{cases} \tag{4.3}$$

The dominant step in these algorithms is scanning the table in search of the minimal d_{iB} and d_{ij}. This step is of order $O(n^2)$ and must be done n times, where n is the number of particles. So, at first glance, it would appear that these algorithms would be of $O(n^3)$. However, the application of computational geometry techniques can

reduce this to $O(n\log(n))$ [75]. Today, these methods are widely applied by means of the FastJet software package [76].

In sequential recombination algorithms, the absolute number of jets is not infrared safe, because soft jets can be identified near the beam remnant; however, if we institute a p_T threshold, the number of jets above the threshold will become infrared safe.

The $k_\perp$ algorithm [77] forms clusters from pairs of low p_T objects. The method of combining objects in this way is inherently collinear safe. However, it has the disadvantage that $k_\perp$ jets can have irregular shapes, which are complicated to deal with experimentally, especially when trying to correct for the effects of underlying event and pile-up. The Cambridge-Aachen [78] algorithm clustering is dependent only on angle, leaving it sensitive to the distribution of soft objects and producing irregularly shaped jets. However, it is useful when studying the substructure of a jet, allowing studies on a range of angular scales. Today, anti-$k_\perp$ [5] is the default for both the ATLAS and CMS experiments. It builds clusters between pairs of high p_T particles, disfavouring clustering between soft objects. It produces roughly circular jets, starting with a hard seed and accumulating the softer objects within radius R of the jet centre.

Figure 4.1 shows a comparison between between four different jet algorithms. The jets produced by $k_\perp$, Cambridge-Aachen, anti-$k_\perp$ and SISCone are shown, with the same input distribution of particles and the same parameter R in each case. The circular shapes of the anti-$k_\perp$ jets and the irregular outline of the $k_\perp$ jets are clearly visible. The four algorithms generally agree about the hardest jets, although combine different soft constituents into them. The p_T-ordering of the softest jets does not agree between the four algorithms.

4.3. Jet Construction in ATLAS

The many hadrons produced from quarks and gluons are detected as energy deposits in the various ATLAS calorimeters (including both the electromagnetic and hadronic calorimeters). However, energy deposits are unlikely to correspond to the hadrons directly, due to the finite resolution of the detectors, as well as electronic noise. Some hadrons may also be undetected, for example if they are scattered from other

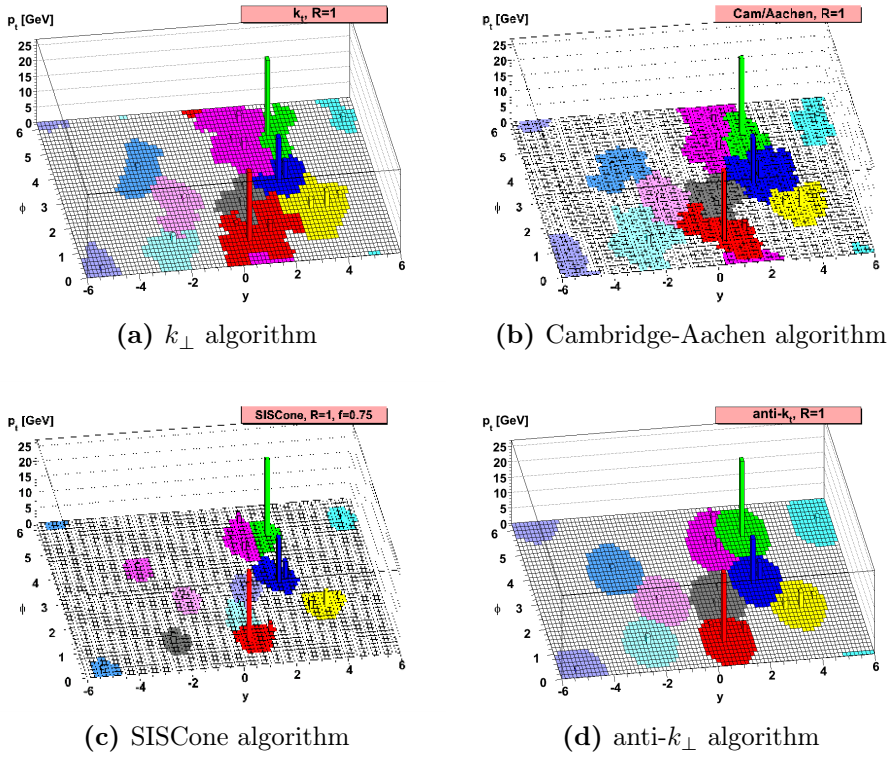

(a) $k_\perp$ algorithm **(b)** Cambridge-Aachen algorithm

(c) SISCone algorithm **(d)** anti-$k_\perp$ algorithm

Figure 4.1.: A sample Herwig (see Section 4.8.2) generated parton level event, shown in y–ϕ space, overlaid with random soft particles, clustered with four different jet algorithms, illustrating the shapes and sizes of the resulting hard jets [5].

material before reaching the calorimeters. Jet clustering algorithms group these hadron-like objects, as described in section 4.2. To facilitate this, the calorimeter is divided into towers, groups of calorimeter cells that form blocks of 0.1×0.1 in η – ϕ [79].

The most common inputs for jet reconstruction are "topoclusters" [79], formed through topological clustering. These are 3 dimensional energy deposits in the calorimeter, which are intended to roughly correlate to hadrons. Topological clustering aims to automatically suppress uncorrelated calorimeter noise, whilst giving the closest possible representation of individual particles in the calorimeter. Furthermore, it allows for a faster reconstruction of jets than directly constructing them from individual cells. To form topoclusters, we start by taking as a seed cell, with energy $E_{\text{cell}} > 4\sigma_{\text{cell}}$, where σ_{cell} is the standard deviation of the noise in that cell. We iteratively combine any neighbouring cell into the topocluster, if it meets the requirement energy $E_{\text{cell}} > 2\sigma_{\text{cell}}$, until there are no more neighbouring cells satisfying

the condition. Finally, we add one further layer of neighbouring cells, satisfying $E_{\text{cell}} > 0$.

Once topoclusters have been formed, we define local maxima within them. These are any cells with an energy larger than 500 MeV, and with no neighbouring cell of a larger energy. If local maxima are found, we apply a splitting algorithm to divide the topocluster in two. The splitting algorithm combines neighbouring cells as before, but cells lying at the border between two clusters can have their energy shared.

Finally, we take topoclusters as the inputs for clustering with a jet algorithm, with the mass taken to be 0 and the position taken as the energy-weighted centre of the cluster.

One alternative to using calorimeter deposits is to form jets using tracks from the tracking detectors. The tracking detectors are only sensitive to charged particles, so they cannot give a full reconstruction of the jet; nevertheless, it may be useful to compare the track jets to the calorimeter jets to give an estimate of systematic uncertainties (see further discussion in section 8.1). Tracks are required to pass some quality cuts before they are used. In particular, they must have to a $p_T > 500$ MeV, a minimum of 7 hits in the pixel and silicon detectors, the χ^2 per degree of the freedom for the track must be no greater than 3, the impact parameter of the track from the beam spot must be less than 2 mm, and the track must satisfy the relation $z \sin\theta < 2$ mm. The tracks are then taken as inputs directly into the jet clustering algorithm.

4.4. Boosted Jets

In the high energy interactions taking place at the LHC, many jets will be produced at energies of several hundred GeV or even a few TeV. This is many times greater than the characteristic masses of these jets, which will typically be under 100 GeV. Thus, some of the jets produced will have a large Lorentz boost, and it is important to understand the characteristics of the highly boosted jets [80–82].

The study of boosted jet properties will help to shed light on QCD showering mechanisms, and provides one of the best possible environments for probing perturbative QCD. Moreover, the LHC is likely to produce many hadronically decaying

boosted W bosons, Z bosons, Higgs bosons and top quarks. For example, around two thirds of all decays of W and Z bosons will be hadronic. The highly boosted regime, holds some advantages for the study of these objects, because the background falls off faster than the signal, so this boosted regime will often have more manageable initial signal/background (S/B) ratios. The study of boosted decays may also provide a test of the Standard Model under new, extreme conditions. In addition, boosted objects such as W and Z Bosons would be expected from the decay of new heavy particles beyond the Standard Model, such as a W' and Z' bosons [83, 84]. Studies of boosted objects may provide the first hints of beyond Standard Model physics.

If the Lorentz boost is high enough, the opening angles between the decay products of a heavy object, such as a W or Z boson, or a top quark, may become so small, in the rest frame of the detector, that the jets become highly collimated and cannot be independently resolved, as shown in figure 4.2. In this case, it is better to try to capture the entire decay within the area of a single large-radius jet, such as an anti-$k_\perp$ jet of radius 1.0 in η and ϕ. In order to distinguish the jets from these decays from other boosted jets, one must look at the internal structure of the jets, referred to as their substructure [85–87].

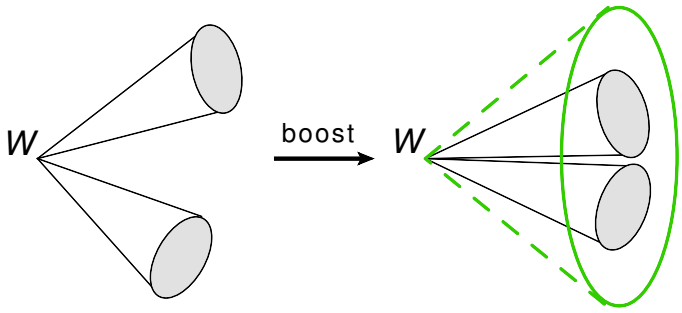

Figure 4.2.: With a high Lorentz Boost in the rest frame of the detector, hadronic decay products will become highly collimated. When the boost is sufficiently large, the entire hadronic decay of a heavy object may be captured within the radius of a single large-radius jet.

4.5. Jet Grooming

As a jet's radius increases, it becomes more likely to be contaminated by pile-up, multi-parton interactions from the underlying event, and initial and final state radiation, problems discussed in section 3.2. For large-radius, boosted jets, this is

likely to be particularly significant, obscuring the jet's substructure, and tending on average to skew the mass of the jet upwards. One might hope to reduce the radius of the jet, but this still needs to be sufficiently large to pick up the full decay of the hadronically decaying object. A crude solution, known as area subtraction [88], is to assume a roughly isotropic and unform distribution of the radiation that does not correspond to the hard scatter, and simply to subtract a fixed contribution of four momentum to each jet, in proportion to its area.

A more sophisticated approach is to look inside a jet, and attempt to systematically remove soft radiation components, either through a modification of the sequential clustering procedure, or through the identification of subjets. This relies on the fact that we expect usually only one hard scattering per event: the other sources of radiation, whether from the underlying event or from pile-up, are likely to be much softer. These techniques are known as jet grooming, and through their implementation, we can significantly improve jet reconstruction. Three important grooming algorithms are trimming, pruning and filtering.

4.5.1. Jet Trimming

A larger jet radius would be preferable to properly capture all of the products of a decaying particle, whereas a smaller jet radius would be preferable in order to mitigate the effects of the underlying event and pileup. The jet trimming algorithm [7] is designed to keep the advantages of a large jet radius whilst reducing the undesirable effects. To do this, we start with a large-radius jet and then sequentially remove the calorimeter cells corresponding to softer contributions, leaving behind those cells which correspond to the hard scatter.

The jet trimming algorithm works by reclustering each large-radius jet into smaller jets of radius R_{sub}, using the $k_\perp$ algorithm, to produce a number of subjets. A subjet i is discarded if it fails to satisfy the relation,

$$\frac{p_{T,i}}{p_{T,\text{jet}}} < f_{\text{cut}} \,, \tag{4.4}$$

where f_{cut} is a chosen trimming parameter, typically about 5%.Finally, we group the remaining subjets to form the final jet. Figure 4.3 shows the trimming procedure.

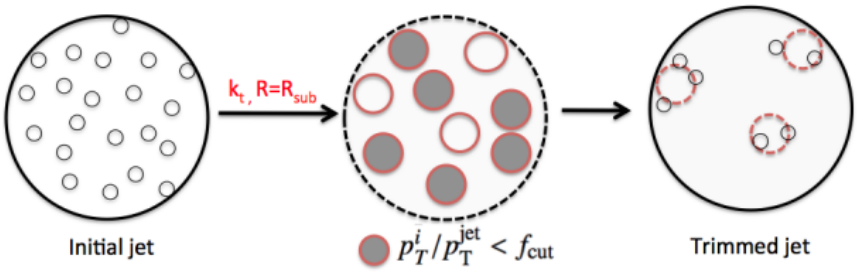

Figure 4.3.: A cartoon of the trimming procedure [6].

The $k_\perp$ algorithm is particularly suitable for the reclustering because it forms jets starting with the softest and ending with the hardest clusters. This leads to more equal sharing of energy between the subjets, so if the final state radiation from the hard scatter cannot be contained within a single subjet, it will be split more evenly between several. Hence the algorithm is less likely to accidentally discard components from the hard scatter.

Low-mass jets (< 100 GeV) from a light quark or gluon will typically lose about 30–50% of their mass in the trimming procedure, while jets containing the decay products of a boosted object lose a smaller proportion, with most of the reduction coming from the removal of clusters from pile-up or the underlying event.

4.5.2. Jet Pruning

The jet pruning algorithm [89, 90] is similar to jet trimming, removing the lowest p_T constituents, but also vetoing wide angle radiation. This is based on the fact that radiation from the hard collision itself is most likely to lie closest to the jet centre. Further out from the jet centre, soft calorimeters are most likely to correspond to the underlying event or pile-up.

Unlike trimming, we do not need to identify particular subjets. Instead we recluster the large-radius jets (using the k_T or Cambridge-Aachen algorithm), invoking the pruning criteria at each successive recombination step. At each step of the jet reconstruction, a decision is made on whether to merge constituents i and j into the jet, based upon two critera:

$$\frac{\min(p_{T,i}, p_{T,j})}{p_{T,\text{jet}}} > z_{\text{cut}} \tag{4.5}$$

and

$$\Delta R_{i,j} < R_{\text{cut}} \times \frac{2m_{\text{jet}}}{p_{T\text{jet}}}\,, \tag{4.6}$$

where, again, z_{cut} and R_{cut} are parameters which we choose. In other words, for a constituent to be merged, it needs to have a sufficiently high p_T fraction of the final jet, and must not be at too an wide-angle from the jet. If either of these two conditions are not met, the softer of these constituents is removed, otherwise they are merged. Then the clustering continues. Figure 4.4 illustrates the pruning procedure.

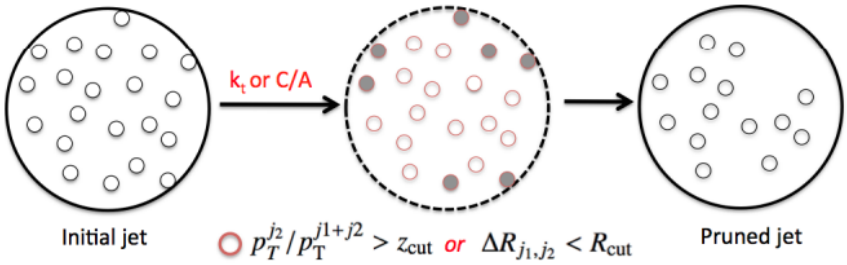

Figure 4.4.: A cartoon of the pruning procedure [6].

4.5.3. Jet Splitting and Filtering

The splitting and filtering procedure [91] is quite different from the other two grooming algorithms described. It seeks to isolate concentrations of energy within a jet by identifying relatively symmetric subjets, each with a significantly smaller mass than that of the original jet. These symmetric energy concentrations are assumed to correspond to the partons from the hard scatter. The procedure was originally developed and optimised using Cambridge-Aachen jets in the search for the Higgs Boson in the decay channel $H^0 \to bb$. The Cambridge-Aachen algorithm was applied because it provides an angular-ordered shower history that begins with the widest

combinations when reversing the cluster sequence. This provides useful information regarding the presence of potentially large splittings within a jet.

Although the procedure is not explicitly based on identifying and removing soft components, by attempting to keep only those parts of the event that correspond to the hard scatter due to their internal structure, unwanted information from pileup and the underlying event are removed. We can divide the algorithm into two stages, the splitting and filtering. The splitting attempts to identify jets which have a two-body-like structure, whilst the filtering throws out unwanted contributions to the reconstructed jet.

1. The splitting procedure uses iterative decomposition of the jet looking to identify a symmetric splitting which could be caused by a boosted heavy particle decay. We begin by undoing the last stage of the Cambridge-Aachen algorithm. Thus, the jet is split into two subjets, i and j such that the mass of i is larger, $m_i > m_j$. We then require the two subjets to pass two criteria:

$$m_1/m_2 < \mu_{\text{frac}} \tag{4.7}$$

and

$$\frac{\min(p_{T,i}^2, p_{T,j}^2)}{p_{T\text{jet}}^2} \times \Delta R_{i,j}^2 > y_{\text{cut}}\,, \tag{4.8}$$

where μ_{frac} is a parameter we define to represent the mass symmetry between the two subjets, and y_{cut} is a parameter we define to represent the energy sharing between the two subjets. Together these requirements demand that the two subjets are sufficiently symmetric in energy and mass. The requirement arises precisely because we expect the two hard partons to have, on average, roughly equal masses and energies, whereas these should be significantly lower for the soft components from the pile-up or underlying event.

If the criteria are not passed, we take i to be the new jet, undo the previous step of the clustering and repeat the procedure. If the criteria are passed, then we move onto the filtering stage.

2. For the filtering stage, the constituents of i and j are reclustered using the Cambridge-Aachen algorithm. Then, we discard all of the constituents except for the three (or occasionally two) hardest subjets. The choice of three is designed to capture a hard two body decay, whilst allowing for the possibility of one additional parton from final state radiation.

Figure 4.5 illustrates the two processes of jet splitting and filtering.

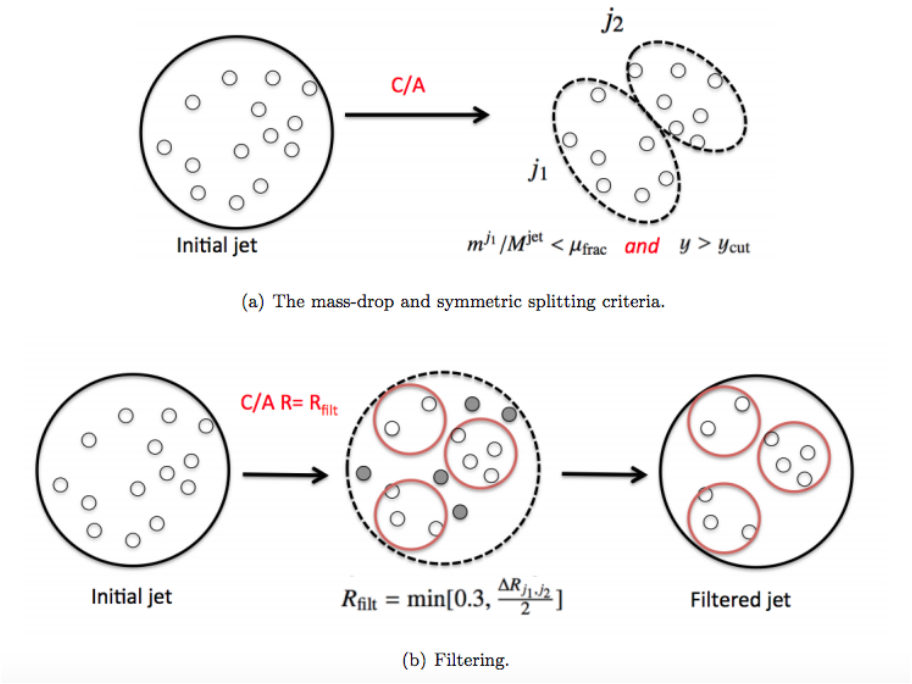

Figure 4.5.: A cartoon of the two stages of (a) the splitting procedure and (b) the filtering procedure [6].

To decide on a choice of μ_{frac}, one needs to consider that, to allow for additional gluon radiation, $V \to qqg$, we would expect μ to be of order $1/\sqrt{3}$. The standard value (0.67) is chosen to be slightly higher than this. Choices of y_{cut} are motivated by studies to optimise the ratio of signal against background; a typical value would be of order 0.1.

4.6. Jet Substructure

The flow of energy within a jet can contain a significant amount of interesting physics. In particular, information about QCD processes taking place at values of p_T higher

than the hadronisation scale, but well below the p_T scale of the hard scatter will be lost by jet algorithms, but we can learn about them by studying the internal structure of the jet. In particular, as shown in figure 4.6, jets coming from a heavy object decay are expected to have a very different internal structure as compared to more common jets produced from non-resonant QCD processes [87, 92].

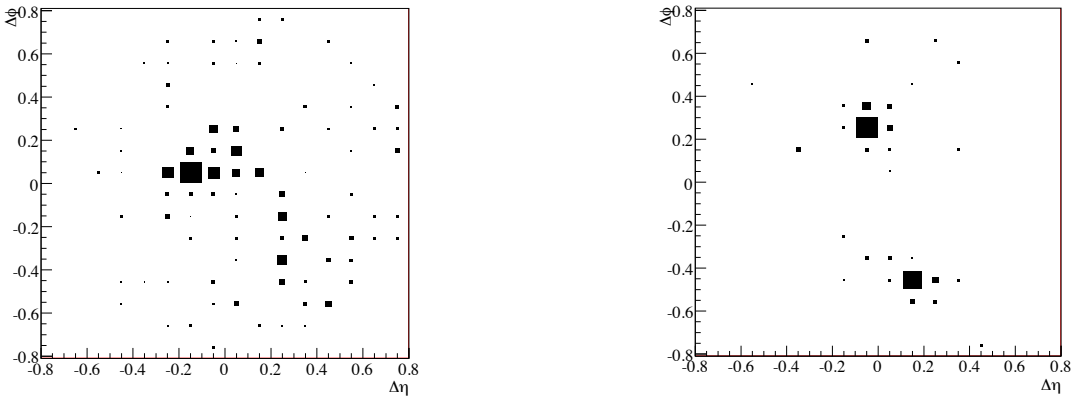

(a) Jet produced from non-resonant QCD processes.

(b) Jet from boosted heavy boson decay.

Figure 4.6.: Schematics of typical jets produced by two different processes, shown on an $\eta - \phi$ detector layout [7].

It is useful to parametrise the substructure of jet within a single function that contains much of the significant information about the layout of energy deposits within the jet. Three such groups of functions are the $k_\perp$ splitting scales, n-subjettiness and energy–energy correlation (EEC) functions [93].

4.6.1. $k_\perp$ splitting scales

The $k_\perp$ splitting scales [85, 92] are defined by reclustering the constituents of a jet with the $k_\perp$ recombination algorithm, discussed in section 4.2. This tends to cluster the hardest constituents last. Before any step of the recombination procedure, the clusters we are grouping will be grouped into two subjet components. The $k_\perp$ distance measure, d_{ij} between these two components is used to define a splitting scale,

$$\sqrt{d_{ij}} = \min(p_{T,i}, p_{T,j}) \times \Delta R_{ij}\,, \tag{4.9}$$

where ΔR_{ij} is the distance between the two subjects in $\eta - \phi$ space. $\sqrt{d_{12}}$ characterises the distance scale between the two subjet components before the final clustering step; similarly, $\sqrt{d_{23}}$ characterises the distance scale between the two subjet components before the second-to-last clustering step. These two parameters can together be used to distinguish between heavy particle decays, which tend to be relatively symmetric in the decay to light-mass particles, whereas the splittings from non-resonant multijet radiation are likely to be less symmetric. From a two-body heavy boson decay, we expect $\Delta R_{12} \sim {}^{m}/_{p_T}$; jets from non-resonant processes will tend to see smaller values. By studying the ratio of ΔR_{12}, and ΔR_{23}, we can also distinguish between two-body and three-body decays.

4.6.2. N-subjettiness

N-subjettiness [94], τ_N is used to characterise the substructure of a particle as being typical of a number, N, of typical subjets. It is calculated by clustering the constituents of the jet, using the $k_\perp$ algorithm, in order to find N subjets candidates. With these subjets in hand, τ_N is defined iby,

$$\tau_N = \frac{1}{d_0} \sum_k p_{T,k} \min\left(\Delta R_{1,k}, \Delta R_{2,k}, \ldots, \Delta R_{N,k}\right)\,, \tag{4.10}$$

where,

$$d_0 = \sum_k p_{T,k} R_0\,. \tag{4.11}$$

Here, k runs over the constituent particles in the jet, and the Δ_R are defined in the $\eta - \phi$ space. τ_N can be thought of as showing the degree to which jet constituents are aligned along the axes of the number N of subjets. Using this definition, τ_N gives one possible measure of how well we can characterise the jet as being composed

of N or fewer $k_\perp$ subjets, for a given hypothesis of the subjet number, N. Then, we can use the ratio $\tau_{21} = {}^{\tau 2}/_{\tau 1}$ to discriminate between jets formed from two body decays to jets formed from non-resonant QCD processes, and the ratio $\tau_{32} = {}^{\tau 3}/_{\tau 2}$ to distinguish between jets formed from two and three-body decays.

4.6.3. Energy–Energy Correlation Functions

We can use generalised energy correlation functions [95,96] to identify a jet's N-prong substructure. Ratios of these functions will have two great advantages. First, there is no requirement for a separate (and computationally expensive) subjet-finding procedure, as is needed for both splitting scales and N-subjettiness. These correlators depend only on information about the energies and pair-wise angles of components within a jet. Second, we can parametrise the angular components of these correlation functions for the best discrimination power. The energy correlation functions (ECFs) are defined by

$$\mathrm{ECF}(N,\beta) = \sum_{i_1<i_2<\ldots<i_{N\varepsilon\mathrm{jets}}} \left(\prod_{a=1}^{N} p_{T,i_a}\right)\left(\prod_{b=1}^{N-1}\prod_{c=b+1}^{N} \Delta R_{i_b i_c}\right)^{\beta} \tag{4.12}$$

where ΔR_{ij}s are defined as usual on the η–ϕ plane. The angular part of this correlation, can be adjusted through the parameter β, in order to optimise the discrimination power of the correlators. We can set β to any value consistent with collinear safety (that is, $\beta > 0$). At small values of β, correlators will more effectively probe small-scale collinear splittings, useful for quark–gluon discrimination. Then, the first few ECFs are defined,

$$
\begin{aligned}
\mathrm{ECF}(0,\beta) &= 1 \\
\mathrm{ECF}(1,\beta) &= \sum_{i\varepsilon\mathrm{jets}} p_{T,i} \\
\mathrm{ECF}(2,\beta) &= \sum_{i<j\varepsilon\mathrm{jets}} p_{T,i}p_{T,j}\left(\Delta R_{ij}\right)^{\beta} \\
\mathrm{ECF}(3,\beta) &= \sum_{i<j<k\varepsilon\mathrm{jets}} p_{T,i}p_{T,j}p_{T,k}\left(\Delta R_{ij}\Delta R_{jk}\Delta R_{ki}\right)^{\beta} .
\end{aligned} \tag{4.13}
$$

These ECFs have several useful properties. They are defined such that $\mathrm{ECF}(N,\beta) \to 0$ in the soft and collinear limits of the particle configuration. Furthermore, the ECFs are recoil-insensitive, that is, they are insensitive to displacement of the hardest particle from the jet momentum axis, due to soft and wide-angle radiation. Recoil-sensitivity would reduce the sensitivity of an observable to the structure of the jet around its hard core.

However, the key observation is that the $(N+1)$ point correlators tend towards zero if there are only N (or fewer) particles in the jet. More generally, if a system has N subjets, then $\mathrm{ECF}(N+1,\,\beta)$ should be significantly smaller than $\mathrm{ECF}(N,\,\beta)$. It would then be natural to consider the ratio,

$$
r_N^{\beta} \equiv \frac{ECF(N+1,\beta)}{ECF(N,\beta)} . \tag{4.14}
$$

We can think of this ratio analogous to N-subjettiness: for a system of N hard partons and soft radiation, the ratio will be linear with the energy of the soft radiation. However, the clearest demarcation in phase space between 1-prong and 2-prong jets is in fact given by dimensionless ratios called C_2^{β} and D_2^{β}, given by,

$$
C_2^{\beta} \equiv ECF(3,\beta) \times \frac{ECF(1,\beta)}{ECF(2,\beta)^2} \tag{4.15}
$$

$$
D_2^{\beta} \equiv ECF(3,\beta) \times \frac{ECF(1,\beta)^3}{ECF(2,\beta)^3} . \tag{4.16}
$$

A wide-ranging study to search for an optimal vector boson tagger, at centre of mass energy $\sqrt{s} = 8$ TeV, looking at multiple jet algorithms, grooming techniques and jet substructure variables, found that the optimal tagger was $D_2^{\beta=1}$, with anti-$k_\perp$ jets of radius 1.0, trimmed with grooming parameters $f_{\text{cut}} = 0.05$ and $R_{\text{sub}} = 0.2$ in η–ϕ [97].

4.7. B-Tagging

The process of identifying jets arising from B-hadron decays (known as "b-jets") is known as b-tagging [98]. The key fact exploited by b-taggers is that B mesons typically have a comparatively long lifetime, of order 10^{-12} s; during which they may travel up to of order 10^{-3} m (due to relativistic time dilation). We can therefore hope to identify a secondary vertex, and we proceed by first identifying tracks which have momentum pointing to within some $\Delta R \sim 0.4$ of the jet axis. There are several approaches to identifying tracks originating from b-hadron decay.

1. **Jet Probability discrimination** Jet probability algorithms combine information from all the selected tracks in the jet to compute a probability that tracks originated at the primary interaction vertex. The shortest distance between a track and the primary vertex is known as the impact parameter. If many of the tracks do not cross the jet axis at the primary vertex, then this implies the presence of a displaced decay;

2. **Secondary vertexing** If several tracks intersect at a point other than the primary vertex, then this implies a displaced decay;

3. **Lepton tagging** b-hadrons somtimes produce leptons when decaying: the presence of a lepton may indicate a b-hadron;

4. **Track Counting** Jets containing b-hadron decays tend to contain higher numbers of charged particles: counting these may be used to indicate this;

In practice, we can produce a combined algorithm from these techniques, using multivariate neural networking methods. For collisions with a centre of mass energy $\sqrt{s} = 8$ TeV, the most optimal tagger was found to be the MV-1 (multivariate-1) tagger, applied with a 70% b-tagging efficiency. At this efficiency, jets from c-decays

correspond to about $^2/_3$ of mis-tags (20% of all b-tagged events); jets from light hadrons correspond to only a few percent of b-tagged events [99].

4.8. Monte Carlo Generators

Monte Carlo (MC) methods are a tool for performing numerical integrations, based on random sampling within a defined space. In particle physics, Monte Carlo generators aim to make numerical calculations of physical quantities such as cross-sections, corresponding to particular physical processes is defined kinematic regions of phase-space. To do this, we use a random number generator to produce a large number of simulated events, which can reproduce the sorts of yields and distributions one would expect from real data.

As well as the calculating the hard event, usually these combine models of the parton distribution functions, as well as modelling various non-analytic processes, such as the underlying event, fragmentation and hadronisation. Typically, different programs will be used for different aspects: one program will generate the hard process, whilst another evolves it through a parton shower algorithm, and another could perform hadronisation. Different Monte Carlo generators often make use of different physics models, especially for those parts which we cannot calculate analytically. Therefore, we can use comparisons between different Monte Carlo models to provide an indication of the compatibility of different theories with experimental results [100].

The complete event generation involves several steps [101]. First the hard process is calculated from the matrix elements and convoluted with the parton distribution functions as described in section 2.3.6. Final and initial state radiation branches are added, and then parton showering is modelled. Next, the partons are hadronised and the decays are simulated. Finally, we add the proton remnants and the underlying event.

The final state particles simulated by the event generation are then passed through a full detector simulation. At ATLAS, this is based on GEANT4 [102], which simulates the interaction of these hadrons with material in the detector. For

example, it models ionisation in the trackers, energy deposition in the calorimeters and decays and radiation that take place en route.

After a Monte Carlo generator has produced particle-level predictions, and passed these through the ATLAS simulation, we treat the simulated events in the same way as data. For example, the same jet calibration and reconstruction is implemented on both simulated and real events. This allows as direct as possible a comparison between data and theory.

Monte Carlo generators used in the analysis and studies presented here are PYTHIA, HERWIG, ALPGEN, SHERPA, MC@NLO and POWHEG.

4.8.1. PYTHIA

PYTHIA [103, 104] uses perturbative QCD at leading order (LO) to compute matrix elements for $2 \to 2$ processes. It applies p_T ordered parton showers. Finally, the Lund string model [105] is applied for the hadronisation. For the underlying event, PYTHIA interleaves multi-parton interactions with the initial state parton shower.

The non-perturbative parts of the event generation can be tuned to different data. At ATLAS, PYTHIA usually generates samples using the ATLAS Minimum Bias Tune 1 (AMBT1) set of parameters. For this, the non-diffractive model is turned to a set of ATLAS measurements for charged particle production at $\sqrt{s} = 900$ GeV and at $\sqrt{s} = 7$ TeV. The AMBT1 uses Martin-Roberts-Stirling-Thorne (MRST) LO* PDFs [106].

4.8.2. HERWIG

HERWIG [107, 108] uses the same leading order matrix elements as PYTHIA. However, unlike PYTHIA, HERWIG implements an angular-ordered parton shower, and uses a clustering model for hadronisation. For the underlying event, HERWIG 6 is linked to JIMMY, to provide multi-parton interactions. The latest version of HERWIG, HERWIG++ directly implements a JIMMY-like approach to the underlying event. Like PYTHIA, events can be generated using the MRST LO*PDF set. It uses the LHC Underlying Event (LHC-UE7_2) tune for the underlying event.

4.8.3. Alpgen

Alpgen [109] provides leading order matrix elements with up to six partons in the final state. It is able to make corrections to the matrix element from several (not only one) hard emissions. Configurations in which the emitted partons' pT falls below a certain threshold are described with a pure parton shower approach, while configurations in which some partons are above the threshold are described with the Matrix Element.

The samples can be generated using the CTEQ6L1 PDF set, produced by the Coordinated Theoretical-Experimental Project [110]. Then these are passed through another generator, such as Pythia to provide the non-perturbative parts of event generation: the parton showering, hadronisation and multi-parton interactions. At ATLAS, samples are generated using the ATLAS Minimum Bias Tune 1 (AMET1) set of parameters.

4.8.4. Sherpa

sherpa [111] implements leading order matrix elements. As with Alpgen, it can make corrections to the matrix element from several different hard emissions; however, the matrix element corrections used for matching to the parton shower are calculated in a different way. The procedure implemented by sherpa is known as CKKW matching. This calculates cross-sections up to a fixed number of additional partons in the final state matrix element. A Sudakov weight is then applied, accounting for the probability that no further emission will be computed in the parton showering.

4.8.5. MC@NLO

MC@NLO [112, 113] was the first widely used Monte Carlo generator to calculate the hard process at next-to-leading order (NLO). This means that the matrix element can include the emission of an additional parton, as well as all internal loop diagrams at next-to-leading order. For leading order generators, the emission of an additional parton is instead included only in the (non-analytic) parton shower modelling. As a result, modelling of third jets in events is overall performed better by MC@NLO than when simply applying leading order generators.

However, a possible double counting problem arises: the emission of an additional parton is being modelled both at next-to-leading order for the matrix element, and in the parton showering procedure. To solve this problem, MC@NLO derives additional NLO terms in the matrix element, of negative weight, and allows these to cancel out the equivalent terms in the parton shower model. These cancellations lead to some undesirable consequences. MC@NLO generated events will be linked to one specific parton shower model, and cannot be used by a different one. Moreover, these cancellation terms must be calculated by hand and then implemented in the MC@NLO code.

4.8.6. POWHEG

Like MC@NLO, POWHEG [114–116] performs NLO calculations. However, unlike MC@NLO, in the POWHEG method the hardest radiation is generated first, with a technique that yields only positive weights. This has the advantage that it can then be combined these with a different parton shower generator, such as PYTHIA or HERWIG. Because it calculates the hard event at a higher order than Pythia and Herwig, this means that the emission of an additional hard parton will be included in the matrix element calculation.

Chapter 5.

Reconstruction and Calibration

Reconstruction is the process of interpreting signals in detectors as physical objects, such as electrons, muons and jets. Event reconstruction is a necessary component of any physics analysis, providing a means for converting the detector outputs into final results and distributions, which can be compared to theoretical predictions. Ultimately, the procedures used for identifying a particular signal depend upon convention, and in each case there is the possibility for errors in identification or measurement. Consequently, each step of the reconstruction process will introduce a source of systematic uncertainty into the physics analysis. We apply similar reconstruction steps to Monte Carlo events and data. With Monte Carlo events, we can distinguish between "truth-level" particles (i.e. simulated real particles) and "detector-level" reconstructed objects [117].

5.1. Data Quality

Before any event is considered for any analysis, it must pass certain generic cuts to ensure data quality. First, we demand that the event belongs to a Good Runs List (GRL), which detail those luminosity blocks where all the relevant parts of the detector are performing correctly. The luminosity blocks are sections of data of around 2 minutes in length. Second are the LAr hole requirements. During certain runs of data-taking, a crate in the ATLAS LAr calorimeter failed, so that any jets falling into this region have been mismeasured. The failure is replicated in Monte Carlo simulations, so as not to affect comparisons between Monte Carlo simulations

and real detector data. Furthermore, events with noise bursts in the LAr calorimeters, as well as events with data corruption in either the tile or LAr calorimeters must be rejected. These events are flagged during data-taking and so can be easily rejected.

5.2. Jet Reconstruction

Jet reconstruction in ATLAS is described in detail in section 4.3. We reconstruct jets from energy deposits (topological clusters) in the calorimeter using a jet-clustering algorithm, the standard being anti-$k_\perp$. Jets can be constructed with small or larger radius, such as anti-$k_\perp$ jets with radius parameters 0.4 or 1.0.

Jets that are constructed without accounting for the difference responses between the electromagnetic and hadronic calorimeters are described as being at the electromagnetic (EM) energy scale. Jets at this scale correctly account for the energy deposited in the calorimeter by electromagnetic showers, as has been validated using test-beam measurements with electrons and muons of known energy. However, hadrons have a lower response that is not well accounted for, so a series of calibration steps is needed to bring the jet from the EM scale to the hadronic energy scale. The hadronic scale should give a better description of the real energy of the jets. Jets which fall below a reconstruction threshold of 7 GeV are discarded altogether before calibration [118, 119].

Jet calibration is divided into three steps: the pileup correction, the origin correction and finally the Jet Energy Scale (JES) correction.

5.2.1. Pile-up Correction

The pile-up described in section 3.1 will add extra energy deposits to calorimeter cells. These energy deposits are in general softer than the hard interaction of interest. To assess the level of pile-up in a collision, we can look at the number of primary interaction vertices (N_{PV}) and the average number of interactions that take place per bunch crossing (μ) in an event. We then calculate an average pile-up contribution to E_T, as a function of N_{PV}, and the η of the jets and subtract it from each jet.

5.2.2. Jet Origin Correction

When reconstructing the jets, we assume that the jet originated from the geometrical centre of the detector. In reality, this will rarely be the case. We correct jet origins by instead pointing back to the primary vertex with the highest $\sum p_T^{\text{track}}$ of the event. If there is no primary vertex, the beam spot is used instead.

The kinematics of calorimeter cluster are then recalculated using the direction from the primary vertex to the centre of the cluster. This correction leads to a small improvement in the angular resolution and p_T resolution.

5.2.3. Jet Energy Scales

The final correction accounts for the lower response of hadrons in the calorimeters, as compared to EM objects (electrons, positrons and photons).

We perform Monte Carlo simulations to produce reconstructed jets at particle level, using the same jet clustering algorithm as is run on the topoclusters, but using all Monte Carlo particles (rather than topoclusters) as four-vector inputs. We include all stable particles except for muons (which are minimally interacting) and neutrinos (which the calorimeters will not detect). These Monte Carlo jets are known as "truth jets", and are geometrically matched to the reconstructed jets produced from the topoclusters. By comparing the energy of the reconstructed jets and the truth jets, a correction factor is applied to the reconstructed jets, generally given as a function of the jets' η and energy, because the calorimeter response is energy-dependent, and the technology of the calorimeter varies with the η direction.

Finally, we apply a small η-dependent correction to account for a bias in the reconstructed η of the jets. This occurs in poorly instrumented regions of the calorimeter, which have a lower response than other parts. There is therefore a small bias in the directions of reconstructed jets; when reconstructing jets there will be a tendency for the jets to be pulled away from such regions of lower calorimeter response. The correction is given as a function of jet energy and η, it is typically very small, of order $\delta\eta < 0.01$ in most of the detector, and $\delta\eta = 0.07$ in crack regions [120].

5.3. Jet Cleaning

Reconstructed ATLAS jets need to pass some basic quality requirements before they can be used in analyses [10]. These are designed to remove fake jets that are artefacts of detector effects, are produced by noise or out-of-time energy deposits, which are flagged as "bad jets", or those which are not well measured due to detector problems with the calorimeter, which are flagged as "ugly jets" [10, 121].

There are three main types of bad jets. First are those which arise from noise bursts in the HEC: the signature of such jets is that most of the energy comes from a single calorimeter cell. Second are those which arise from noise bursts in the EM calorimeter, which again have most the energy arising in a single calorimeter cell. Finally, there are out-of-time jets, which appear with large out-of-time energy deposits in the calorimeter, incompatible with the event time. They may be caused by photons from cosmic rays. The variables used to identify bad jets are shown in table 5.1. The ATLAS Jet/ETmiss Working Group [10, 122] has designated three different levels of criteria for bad jet removal termed "loose", "medium" and "tight". These cuts are summarised in table 5.2.

EM_f	fraction of energy deposited in the EM calorimeter
$f_{\max}$	maximum fraction of energy deposited in a single calorimeter layer
HEC_f	fraction of energy deposited in the HEC
LAr_Q	fraction of energy deposited in the LAr cells with a cell quality factor > 4000
HEC_Q	fraction of energy deposited in HEC cells with a cell quality factor > 4000
E_{neg}	negative energy in the jet
t	the mean timing difference between cells in the jet and event timing
η	jet η given at the EM scale
Chf	The charged fraction of the jet, given by $\Sigma p_T^{\text{track}} / p_T^{jet}$

Table 5.1.: Variables for jet cleaning criteria [10].

Ugly jets are defined as those which have more than half of their energy coming from either the transition region between the barrel and end-cap of the calorimeters, or from known dead cells, which are assigned an energy value based on the values of their neighbouring cells. Ugly jets are rejected from analyses.

	Loose	Medium (includes loose)	Tight (includes medium)
HEC spikes	$HECf > 0.5$ & $\mid HECQ \mid > 0.5$ OR $\mid NegE \mid > 60\ GeV$	$HECf > 1 - \mid HECQ \mid$	
EM coherent noise	$EMf > 0.95$ & $\mid LAr_Q \mid > 0.8$ & $\mid \eta \mid < 2.8$	$EMf > 0.9$ & $\mid LAr_Q \mid > 0.8$ & $\mid \eta \mid < 2.8$	$EMf > 0.98$ & $\mid LAr_Q \mid > 0.05$ OR $\mid LAr_Q \mid > 0.95$
Cosmics and background	$\mid t \mid < 25$ ns OR $EMf < 0.05$ & $Chf < 0.05$ & $\mid \eta \mid < 2$ OR $EMf < 0.05$ & $\mid \eta \mid \geq 2$ OR $F_{\max} > 0.99$ & $\mid \eta \mid < 2$	$\mid t \mid < 10$ ns OR $EMf < 0.05$ & $Chf < 0.1$ & $\mid \eta \mid < 2$ OR $EMf > 0.95$ & $Chf < 0.1$ & $\mid \eta \mid < 2$	$\mid \eta \mid < 2$ OR $EMf > 0.90$ & $Chf < 0.02$ & $\mid \eta \mid < 2$ OR $EMf < 0.1$ & $\mid \eta \mid \geq 2$

Table 5.2.: ATLAS cuts for jet cleaning. The medium cuts comprise the loose cuts with the additional criteria given. The tight cuts comprise this full set of medium cuts, with the additional criteria given. Therefore, any jet that considered bad by a looser of cuts will automatically be considered bad under tighter cuts as well [10].

5.4. Electron Reconstruction

To reconstruct an electron's energy, we must sum the entire energy of the electromagnetic shower that it produces in the EM calorimeter, as described in 3.4.3. A sliding window algorithm searches for, and then clusters, the energy deposited by electrons. There are three steps; tower building, pre-clustering and cluster-filling.

First, the calorimeter is divided into a grid of calorimeter elements, of dimensions $\eta \times \phi = 0.025 \times 0.025$. We use a window of 5×5 of these units in $\eta \times \phi$. The energy deposited in cells within the calorimeter is summed across the calorimeter layers to form a tower. If the shower lies across multiple towers, the energy is split between the towers in accordance with the fraction of the cell which overlaps each tower. The transverse energy of the towers within the window is summed to provide the transverse energy of the window. We scan the window over the calorimeter, accepting as preclusters those windows for which the transverse energy lies above a threshold of 3 GeV. If two preclusters overlap by an area of 3×3 towers, then we remove precluster with the lower transverse energy.

Once we have the preclusters, we use them to seed a secondary sliding window algorithm, forming clusters that represent the full EM showers. This will produce a cluster of cells formed from the preshower through to the back of the EM calorimeter. The solenoid-induced magnetic fields will bend charged particles in ϕ, so the windows are allowed to be wider in the ϕ direction. In general, the window size depends on the EM calorimeter layer and whether we are assuming a photon or electron particle, with photon showers tending to be narrower than electron showers.

To distinguish electron clusters from photon clusters, we match the tracks from the inner detector. To do this, we extrapolate the fitted track and declare a match if a calorimeter cluster lies within $\Delta\eta < 0.05$ and $\Delta\phi < 0.1$ of the tracks of the inner detector. The track with the closest match is considered to be the electron and we use it to make momentum and charge measurements. In those cases where no track is identified, we assume that the cluster arose as an unconverted photon, that is, a photon which did not yet produce electron-positron pairs prior to arriving at the calorimeter. Photons which undergo conversion before the calorimeter may be misidentified as electrons; we reduce this by making requirements on the track found, requiring at least a minimum number of hits in the pixel and SCT detectors to indicate the presence of an electron.

Cluster and track measurements are accepted as electrons if they pass a series of pre-selection cuts, which reject likely photons and fake electrons. These cuts are shown in table 5.3. Once again, various sets of cuts are defined as "loose", "medium" and "tight". Tight electrons must have an $E_T > 20$ GeV and to be found within $| \eta | < 2.47$, the fiducial region of the EM calorimeter. In addition, we reject electrons

that lie in the poorly instrumented region of overlap, between the calorimeter barrel and endcap, given by $1.37 <| \eta |< 1.52$ [123, 124].

Type	Description
	Loose criteria
Detector acceptance	$\mid \eta \mid < 2.47$ and $1.37 < \mid \eta \mid < 1.52$
Hadron leakage	Ratio of E_T in the first sampling of the hadronic calorimeter to the EM cluster
Second layer of EM calorimeter	Ratio in η of cell energies in 3×7 versus 7×7 cells
	Lateral width of the shower
	Medium criteria (includes loose)
First layer of EM calorimeter	Total shower width
	Ratio of energy difference associated with the largest and second largest energy deposit over the sum of these energies
Track quality	Number of hits in the pixel detector ≥ 1
	Number of hits in the pixel and SCT ≥ 7
	Transverse impact parameter < 5 mm
Track matching	$\Delta\eta$ between the cluster and track < 0.01
	Tight criteria (includes medium)
b-layer	Number of hits in the b-layer ≥ 1
	$\Delta\phi$ between the cluster and the track < 0.02
Track matching	Ratio of the cluster energy to the track momentum
	Tighter $\Delta\eta$ cut < 0.005
Track quality	Tighter transverse impact parameter cut < 1 mm
TRT	Total number of hits in the TRT ≥ 15
	Ratio of the number of high-threshold hits to the total number of hits in the TRT
Conversions	Electron candidates matching to reconstructed photon conversions are rejected

Table 5.3.: Variables used for ATLAS pre-selection cuts for electron identification [11]. The medium cuts comprise the loose cuts with the additional criteria given. The tight cuts comprise this full set of medium cuts, with the additional criteria given. Therefore, any jet that considered bad by a looser of cuts will automatically be considered bad under tighter cuts as well.

5.5. Muon Reconstruction

We reconstruct muon candidates using the information from the muon spectrometer described in section 3.5. Whilst the MS alone is sufficient for stand-alone muon reconstruction, we can use information from other detector parts to improve muon identification efficiency. We classify three types of reconstructed muons.

1. **Stand-alone muons**
   These use only information from the MS. Tracks are reconstructed using the Moore algorithm [125] and are then extrapolated to the beam line.

2. **Combined Muons**
   These use stand-alone muons found in the MS, matched to ID tracks using algorithms such as STACO [125]. Muon properties are evaluated by combining the information from both detector components. A muon trajectory is reconstructed in the inner detector and the muon spectrometer separately at first, then combined by a statistical combination approach into a combined track.

3. **Tagged Muons**
   We produce tagged muons by starting the reconstruction from suitable ID tracks and extrapolating them to the MS. We use the MuTag or MuGirl algorithms [125] to search for hits in nearby MS segments.

Well-reconstructed muons need to pass a series of pre-selection cuts. Combined muons found by the STACO algorithm are required to have a $p_T > 20$ GeV and $|\eta| < 2.5$ [126–128].

5.6. Missing Transverse Energy Reconstruction

If our events contain missing transverse energy (E_T^{miss}), this indicates the presence of particles which have escaped the detector without being detected. Most often, these particles are neutrinos. We reconstruct E_T^{miss} using the "RefFinal" definition, as the negative transverse vector sum of calorimeter energy deposits and of the p_T of muons reconstructed in the inner detector or muon spectrometer. Knowledge of the gaps in detector coverage, calorimeter shielding by the cryostat, and dead regions are also taken into account when calculating E_T^{miss}. Additional corrections come from

identified photons, electrons, muons and jets, using the definitions for these objects given in the previous sections. Any corrections applied to such objects must also be propagated to the E_T^{miss} calculation. The calibrations of specific objects are generally better than generic calibrations of individual cells, so by using the final objects with their full calibrations, we can usually improve the E_T^{miss} resolution. Noise from the calorimeters can cause a mis-measurement of E_T^{miss}; we can only alleviate this by using topoclusters that already take noise suppression into account [127, 129].

Chapter 6.

Performance Studies on the Jet Trigger

The ATLAS trigger system underwent a series of upgrades during the LS1 period, in order to cope with the Run 2 environment, as discussed in section 3.6.2. The Run 2 luminosity peaks at around 10^{34} $cm^{-2}s^{-1}$, average levels of pile-up increase, and the number of expected interactions per bunch crossing rises from around 40 to 50. Trigger rates allowed by the new system increased by a factor of approximately 2 over the Run 1 system.

In addition to a multitude of upgrades to the trigger system, efforts were made to improve the speed of the reconstruction algorithms. This study investigates one possible scheme for improving the algorithmic efficiency of the higher level jet triggers, known as partial scan (PS), focussing on the potential improvements to algorithm performance times and trigger efficiencies. PS is compared against an existing data loading scheme known as full scan (FS). This chapter will explain the partial and full scan approaches, present the study, its results and conclusions, and discuss the implications for the upgrade of the jet trigger system.

6.1. Full scan and Partial scan

An important change to the jet trigger is the merging of LVL2 and the EF, such that HLT becomes a single trigger level, pooling the computing resources of the two levels and minimising data transfers. Faster readout boards enable more frequent accessing

cell information across the whole calorimeter system. In practice this allows the computationally intensive step of building topoclusters (explained in section 4.3) to be performed for all events passing first trigger level. Topoclusters are inherently noise-suppressed, so provide a higher resolution than other types of input. [68, 130].

During Run 1, the HLT used two distinct data loading schemes:

- **Full scan (FS)** uses the complete calorimeter data load. The FS scheme allows for precise event reconstructions, but is computationally expensive and is more difficult to integrate into the HLT time constraints.
- **RoI scheme** takes in data only from the selected RoIs (described in section 3.6. This is less computationally demanding, but the sliding window algorithm used to select RoIs has a lower efficiency to identify close-by jets. In addition, any overlap between selected RoIs will be processed multiple times, as each RoI is treated independently, shown in figure 6.1.

Although simulations showed that the new trigger design should respect the latency constraints of the Run 2 online environment, a fallback approach was designed [131], intermediate between FS and the RoI scheme:

- **Partial scan (PS)** runs as if in a single-pass full scan over the full calorimeter, but with the data suppressed outside of the RoIs selected at LVL1. In effect, all of the RoIs are grouped into a single region, removing any overlap between regions. This still suppresses low activity regions of calorimeters, whilst avoiding processing energy deposits multiple times if they lie in overlap regions covered by more than one RoI, shown in figure 6.1.

The partial scan is particularly interesting for the improved HLT due to its lighter event processing, which reduces the overall computational power required by the system. The degree to which computational power is reduced will depend on the size of the RoI windows. On one hand, if the window size is too small, part of the jet may lie outside of the window, resulting in lower reconstructed jet energy, which may reduce the trigger efficiency. On the other hand, too large a region will not improve the selection, but will severely penalise the processing time. In the limit where the RoIs stretch across the entire calorimeter, the PS scheme becomes identical to FS. Studies found the optimal size to be around 1×1 in η–ϕ; this size is used throughout the study [131].

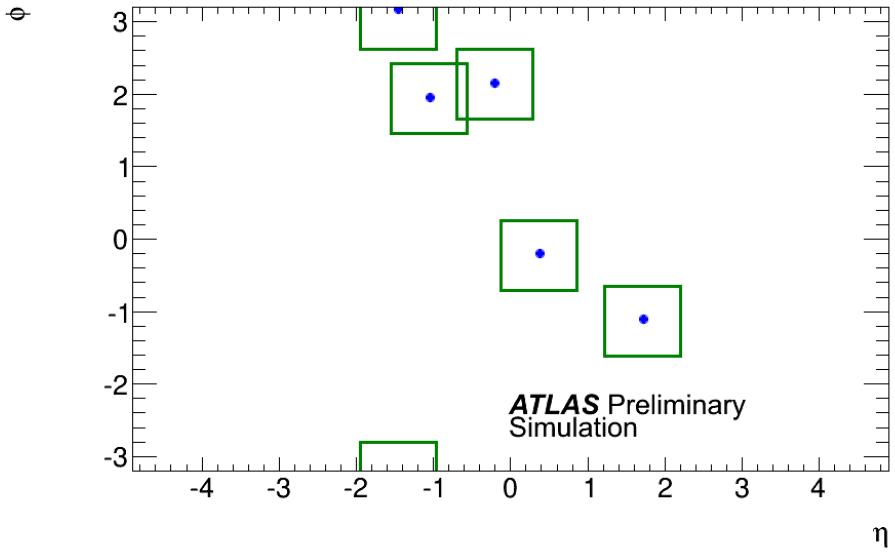

Figure 6.1.: Calorimeter partial scan data readout scheme for a simulated event. Blue dots represent the Level 1 jet positions in a particular simulated event. Green rectangles represent RoIs of size 1×1 in the η–ϕ plane, selected at LVL1. An overlap is seen between two RoIs, which would be processed twice in the Run 1 RoI scheme. In the PS scheme, the jet finding algorithms at the HLT run as if in a single pass scan over the full calorimeter, but with data suppressed outside the regions defined by Level 1 jet positions. The PS removes any overlap between regions [8].

6.2. Trigger Efficiencies and Turn-on Curves

The efficiency of a higher level trigger, ε, is given by the ratio of the number of jets passing the trigger, with an E_T threshold, to the total number of jets reaching the trigger, i.e. those jets passing the selection cuts and the seed trigger,

$$\varepsilon = \frac{\text{Number of jets passing trigger}}{\text{Number of jets arriving at trigger}} \,. \tag{6.1}$$

For an n-jet trigger, efficiencies are measured as a function of the n^{th}-highest E_T offline jet to pass to the trigger, referred to as the "trigger jet". For example, the efficiency of the 3j50 jet trigger is measured as a function of the E_T of the jet third highest in E_T. The profile of the trigger efficiency against the E_T of the trigger jet is described as the "turn on curve" of the trigger. The characteristic shape has a

turn-on region where the efficiency increases quickly, and a plateau region, at which maximum efficiency is reached and no longer varies. The triggers are considered to be fully efficient at the plateau region, once $\varepsilon \geq 99\%$.

6.3. Event Selection

The study makes use of 40,000 PYTHIA8 Monte Carlo simulated events for the maximal Run 2 centre-of-mass energy $\sqrt{s} = 14$ TeV, and a high average pile-up of 80 simultaneous interactions per bunch-crossing. We reconstruct offline jets using the anti-$k_\perp$ algorithm, with jet radii of 0.4 in η–ϕ space. To obtain events with a high jet multiplicity, in which enough jet energies lie close to the trigger thresholds, we consider non-resonant multijet events with an offline leading jet p_T between 500 and 1000 GeV and $|\eta| < 2.8$. Non-leading jets will typically have much lower energies than this.

We consider only those offline jets that are matched to a trigger jet at each level. First, the offline jet is geometrically matched to an EF jet by finding the closest jet within a $\Delta R < 0.3$ in the η–ϕ plane. The EF jet is matched to the closest LVL2 jet within a $\Delta R < 0.3$. Finally, the LVL2 jet is matched to LVL1 using RoI information stored at LVL1 and LVL2. Providing that a jet is found at each of these levels the jet is used to calculate the trigger efficiencies. Studies have found these values of ΔR to be highly efficient for identifying whether a LVL1 jet corresponds to an offline jet [132].

Events are required to pass the ATLAS GRL, discussed in section 5.1 , and must have at least one primary vertex with at least 4 tracks. The standard jet cleaning requirements described in section 5.3 are applied, and we implement the tightest criteria for removing bad jets.

Four different multijet triggers are considered for the study. Table 6.1 lists the triggers considered for the study. Jets are passed through each trigger separately, under both the FS and PS schemes. In the Monte Carlo sample used, the leading five jets were found to match to within a $\Delta R < 0.1$ between FS and PS in over 99% of events.

Jets passed to a HLT trigger must pass a LVL1 seed trigger, also shown in table 6.1. These seed triggers have a lower E_T threshold and apply to one fewer jets than the corresponding HLT triggers. This is to ensure that they are fully efficient at the E_T range considered for the turn-on curves. We consider range of multijet triggers, to assess the performance of partial scan in as wide a range of different scenarios as possible.

LVL1 Seed Trigger	HLT Trigger
L1_J50	j110
L1_J20	3j50
L1_3J50	4j100
L1_4J20	5j85

Table 6.1.: The multijet triggers considered for the study on partial scan performance. The corresponding LVL1 seed triggers are also shown.

6.4. Results and Conclusions

Figure 6.2 shows the times for the cell-making algorithm to run for PS and FS. The PS sees a much broader peak than FS, expected to be dependent on the number of the RoIs selected for the event. The mean times were around 15-20% lower for the PS than FS. Figure 6.3 shows the corresponding times for the cluster-making algorithm. FS shows a narrow peak; PS shows a similar peak but with a substantially longer tail, again probably dependent on the number of RoIs selected for the event. The average times for partial scan were typically around one fifth or lower than those seen for FS. Combined, PS sees improvements of around a factor of five compared to full scan, because the cluster-maker times dominate over the cell-maker. The average timings for each trigger are summarised in table 6.2.

It is likely that the longer tails observed in PS arise from algorithms for "fetching" the detector elements. If the fullscan flag is passed, then the algorithms simply retrieve the complete collections and processes them, with no additional checks. However, if the fullscan flag is not passed, then the algorithms scan across all regions

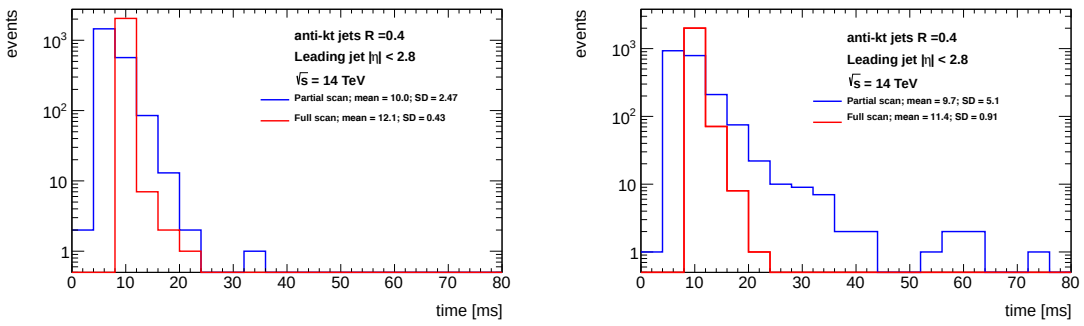

(a) j110 **(b)** 3j50

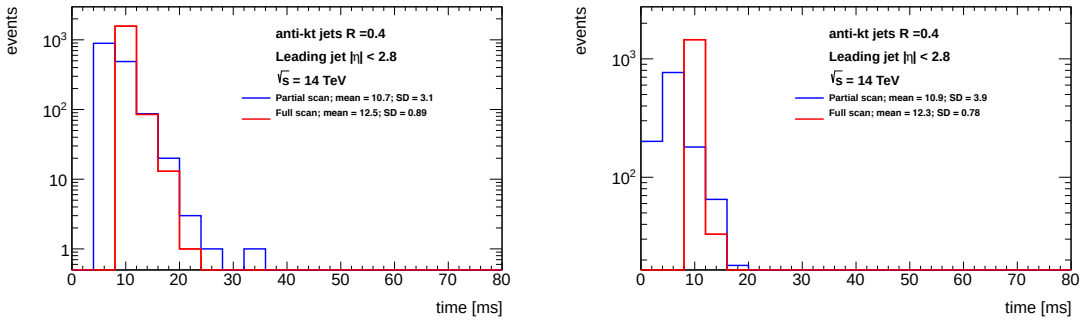

(c) 4j100 **(d)** 5j85

Figure 6.2.: Timings of the cell-maker algorithm, for multijet triggers, compared between full scan and partial scan for a variety of HLT multijet trigger algorithms. All timings are given in units of ms.

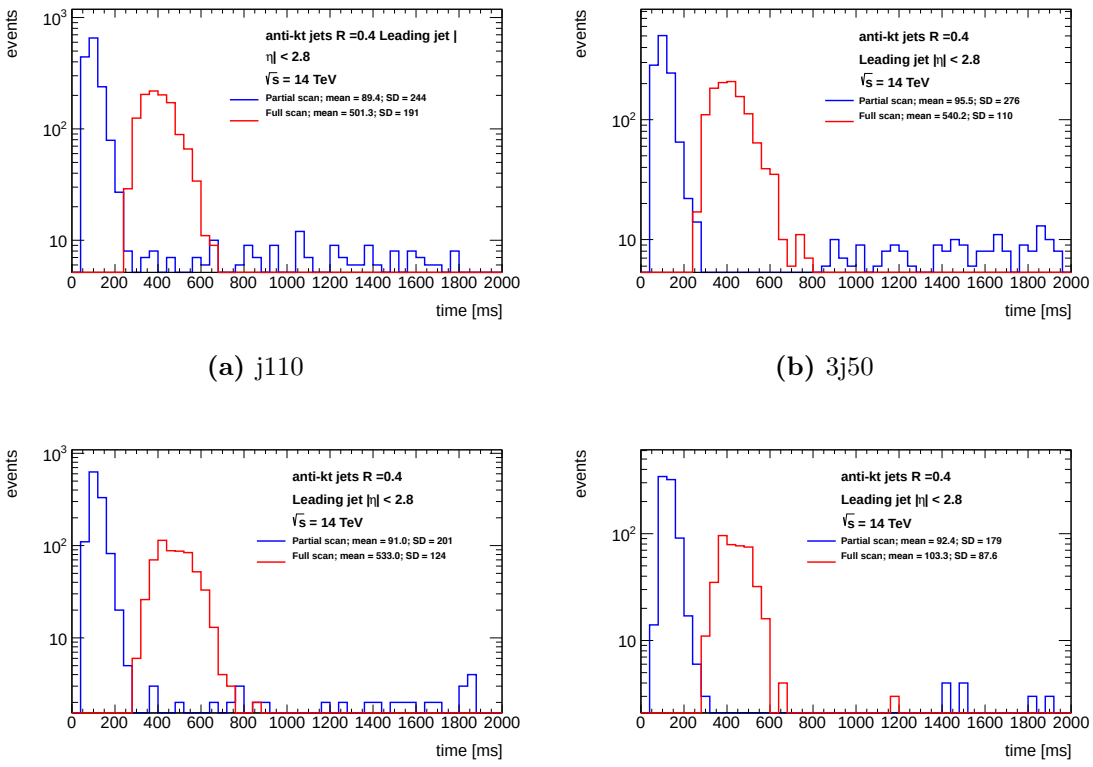

(a) j110 **(b)** 3j50

(c) 4j100 **(d)** 5j85

Figure 6.3.: Timings of the cluster-maker algorithm, for multijet triggers, compared between full scan and partial scan for a variety of HLT multijet trigger algorithms. All timings are given in units of ms.

	j110		3j50		4j100		5j85	
	PS	FS	PS	FS	PS	FS	PS	FS
cell maker $\langle t \rangle$	10.0	12.1	9.7	11.4	10.7	12.5	10.9	12.3
cluster maker $\langle t \rangle$	89.4	501.3	95.5	540.2	91.0	533.0	92.4	544.3
total $\langle t \rangle$	99.4	512.4	104.5	551.6	101.7	545.5	103.3	556.6

Table 6.2.: The mean timings for the cell-maker and cluster-maker algorithms, as well as total timings, for each trigger, considered for PS and FS. The timings of the cluster-maker dominate, and overall timings reveal a substantial improvement for PS, compared to FS. All timings are given in units of ms.

and fetch the collections independently in the regions specified. In practice, this means separately checking the list of cells or clusters to identify whether they lie within the selected RoIs, rather than simply using a cached list of all detector elements. For events with very large numbers of RoIs, this can substantially increase the total algorithm timings.

Figure 6.4 shows the efficiency curves for FS and PS for each of the four triggers considered, plotted against the matched offline E_T of the n^{th} jet. For each trigger, the PS is seen to have a slower turn-on than FS. Typically, with PS samples reached 100% efficiency at about 2 or 3 GeV higher than with FS; this effect was slightly greater for the highest E_T threshold triggers, the 4j100 and j110.

In conclusion, PS shows the potential to improve the algorithm timings substantially, compared to FS. However, the less steep turn-on curves indicate a signficant fall in the E_T resolution. Further studies [130, 131] of the E_T resolution found a significant difference between PS and FS at low E_T; whilst this could be mitigated with larger RoIs, the effect remained, shown in figure 6.5. Therefore, ultimately PS was not adopted for the Run 2 trigger.

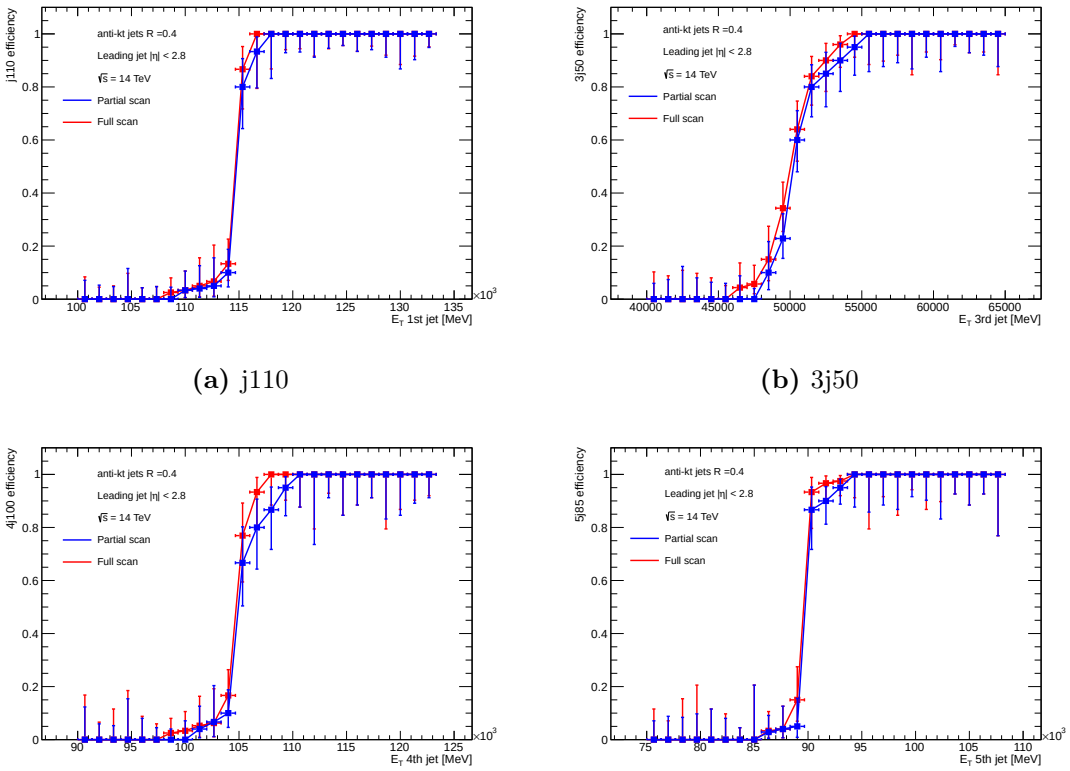

(a) j110 **(b)** 3j50

(c) 4j100 **(d)** 5j85

Figure 6.4.: Efficiencies of the multijet trigger algorithms. For an n-jet trigger algorithm, the efficiency is plotted as a function of the E_T of the n^{th} leading jet. Full scan and partial scan efficiencies are shown for each HLT multijet trigger algorithm considered.

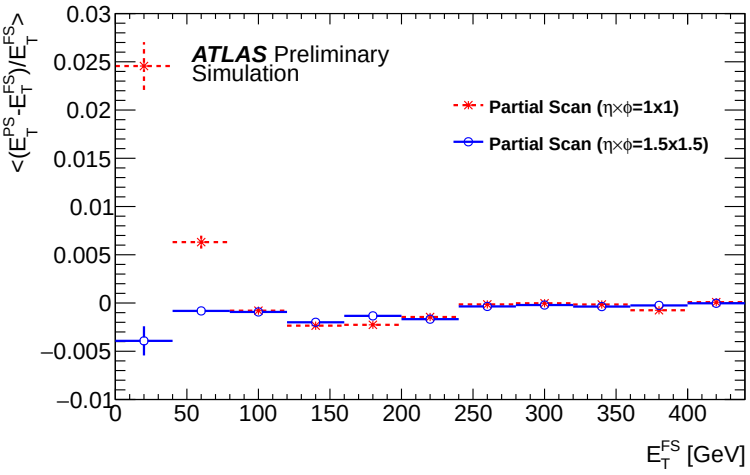

Figure 6.5.: Relative transverse energy difference between jets reconstructed using the PS and FS calorimeter readout schemes, represented versus the Full scan jet transverse energy, for HLT jets matching jets identified at LVL1 (within a radius 1 around the LVL1 jet in the η–ϕ plane). The error bars represent the standard error on the mean. The data sample used consist of non-resonant di-jet events with leading-jet transverse momentum above 20 GeV and 40 simultaneous interactions per bunch-crossing. [8].

Chapter 7.

Semileptonic Decays of Vector Boson Pairs

7.1. Introduction

In this analysis, we study inclusive vector boson pair (WW, WZ) production, decaying in the semileptonic channel. In this channel, one vector boson decays leptonically to $l\nu$, where $l = e, \mu$, while the other decays hadronically to qq, shown in figure 7.1. The production takes place at centre of mass energy $\sqrt{s} = 8$ TeV, and with an integrated luminosity of 20.3 ± 0.6 fb^{-1} using LHC Run 1 data collected by the ATLAS experiment in 2012. There are two distinct aims. First is to measure the diboson production cross-section in the semileptonic channel. Second is to use the transverse momentum distributions to set limits on anomalous contributions to the triple gauge coupling vertices (aTGCs), which are described in chapter 2.4.2.

The finite resolution of measurements of jet mass leads to considerable overlap between peaks arising from the hadronic decays of W and from Z bosons. Given the expected uncertainities and the relatively small contribution from the WZ (of order 10% of the total signal yield in each channel), no effort is made to distinguish separate WW and WZ results.

In this chapter, the analysis purpose and detail the design are explained, including the choice of Monte Carlo generators, the data used, the conventions used for object identification, the selection of events and choice of phase space, and the modelling of the Monte Carlo samples. Chapter 8 describes the estimation of the sources

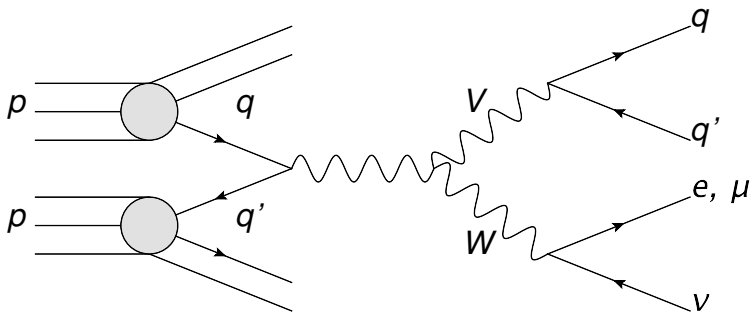

(a) s-channel

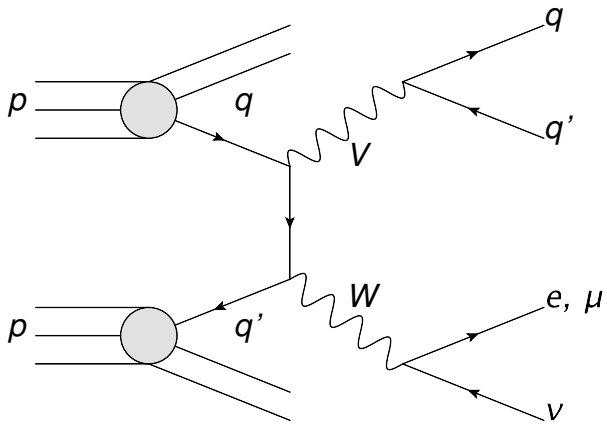

(b) t-channel

Figure 7.1.: Feynman diagrams for WV (V=W,Z) production and semileptonic decay processes, $WV \to l\nu qq$, at the LHC, at leading order.

of systematic uncertainty for the analysis. Chapter 9, explains the details of the cross-section measurement and aTGC limit-setting procedure, and discusses the results of the analysis.

In physics analyses, we generally aim to study specific phenomena (in this case the diboson production cross-section, and the aTGCs), defined in a particular region of phase space. The region of phase space is defined to optimise the statistical significance of the quantity we intend to measure; this involves a trade-off between improving the ratio of signal events against background, and having higher overall numbers of events. Generally, the phase space is defined through a series of selections, or "cuts", on kinematic observables, and the event topology; the phase space is chosen to enhance the signal and reduce backgrounds. We call this signal-enriched region the "signal region". Section 7.4 details the cuts to define the signal region phase space.

To estimate the background processes that contaminate the signal region, we apply data-driven reweighting to the Monte Carlo samples. To do this, we define "control regions" in which particular backgrounds have a very high purity, and use these to reweight background samples to data. Section 7.5 outlines the control regions used for the background modelling procedure.

Measurement of the diboson production cross-section remains an important test of the Standard Model. Vector boson production provides important backgrounds in Higgs measurements and studies, as well as in searches for physics beyond the Standard Model. In particular, high energy decays of W and Z bosons are very useful in the search for new physics, as they would be likely products from the decay of heavy hypothetical particles such as a W' or Z' [83, 84].

The majority of ATLAS and CMS measurements of vector boson pair production have been done in the fully leptonic decay channels, which provide a significantly larger ratio of signal against background, and are affected by lower overall systematic uncertainties. However, semileptonic channels have the potential to provide around a factor of 6 improvement in statistics, because the hadronic decay branching ratios are higher than the leptonic for W and Z bosons. There are no other 8 TeV measurements for the semileptonic process, however fully leptonic results already exist at this centre of mass energy for the WW and WZ channels [12, 13, 64, 133]. However, searches at 7 and 8 TeV centre of mass energies have used the $WV \to l\nu jj$ channel to search for heavy resonances such as the W' [83, 84].

Analyses in ATLAS and CMS previously performed measurements of inclusive vector boson pair production in the semileptonic decay channel at the lower centre of mass energy of $\sqrt{s} = 7$ TeV [14, 63]. The higher centre of mass energy used in this analysis provides better discrimination between signal and background, due to the larger vector boson production cross-sections at higher energies. Moreover, the sensitivity to aTGCs increases with higher transverse momenta. Furthermore, the higher centre of mass energy opens up the possibility to exploit a boosted topology for some events, where the hadronic decay products have a sufficiently high Lorentz boost for them to merge, so as to be captured within a single large-radius jet. As explained in section 4.4, boosted channels have the potential to provide especially good sensitivity to aTGCs.

From henceforth, we will distinguish between two channels, characterised by different event topologies. The first, in which we expect the boson decay products to be captured by a single, merged jet of large-radius, will be referred to as the "boosted channel". The second, in which we expect the boson decay products to be captured by two distinctly resolved small-radius jets will be referred to as the "resolved channel". We implement a different event selection for the two channels, requiring that the two channels are fully orthogonal, i.e. that no event may pass the event selections for both channels. Figure 7.2 shows a schematic of the two topologies.

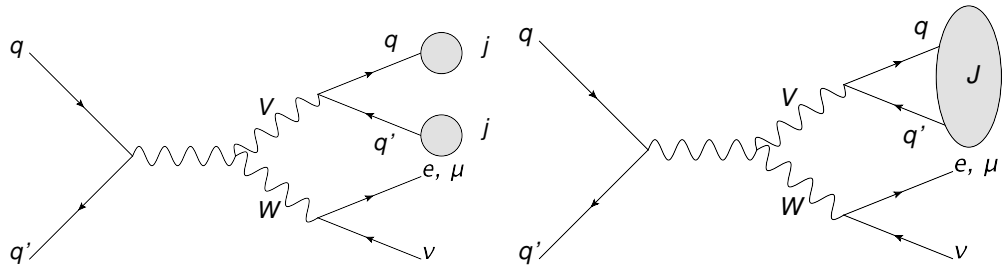

(a) resolved topology **(b)** boosted topology

Figure 7.2.: Feynman diagrams showing the signal process in the boosted and resolved channels. J refers to a large-radius jet, whilst j refers to a small-radius jet. Only the leading order s-channel diagrams are shown.

The WV production cross-section is measured within the defined fiducial volume, corresponding to the process we wish to measure. The precise definition of this fiducial volume is given in section 9.1.2. For the resolved topology, the process it corresponds to is $WV \to l\nu jj$, where j represents a small-radius jet arising from the hadronic decay of a vector boson. For the boosted topology, the fiducial volume corresponds to the process $WV \to l\nu J$, where J represents a single large-radius jet, intended to capture entire hadronic decay of a vector boson. Processes in which electrons or muons originate from the $W \to \tau\nu \to \ell\nu\nu$ decay chain are accounted for in the analysis, but are not part of the fiducial phase space definition, as is explained in section 9.1. We extract the WV signal using a binned maximum likelihood (ML) fit to the dijet mass distribution. A glossary of terms used in the fit is provided in Appendix B.

aTGCs typically enhance the cross-sections for diboson production at high transverse momenta. Hence, physics analyses normally obtai limits on aTGCs by fitting

the p_T distribution of the lepton or vector boson. In the semileptonic diboson analysis at $\sqrt{s} = 7$ TeV, the most sensitive channels for the aTGC fit were investigated. It found that the optimal variable to choose for the fit was the p_T of the dijet system, corresponding roughly to the p_T of the hadronically-decaying V boson [14]. Following from these results, in this analysis, aTGC limits are determined from a fit to $p_T(jj)$ in the resolved channel, and $p_T(J)$ in the boosted channel.

7.2. Data and Monte Carlo Samples

7.2.1. Data Samples

Data for the analysis comes from pp collisions at centre of mass energy $\sqrt{s} = 8$ TeV, collected by the ATLAS detector in 2012, corresponding to an integrated luminosity of 20.3 ± 0.6 fb^{-1}, and passing the GRL described in section 5.1.

7.2.2. Monte Carlo Samples

Signal processes, WW and WZ, are modelled using Monte Carlo simulated samples, while the contributions from various Standard Model backgrounds are estimated using a combination of Monte Carlo samples and control samples from the data. For the Monte Carlo samples, the particle interactions with the ATLAS detector are modelled using GEANT4. We reconstruct Monte Carlo events using the same software that is used for data reconstruction.

Signal processes

The nominal signal samples are $q\bar{q} \to WW/WZ$ events generated using MC@NLO v4.07 with NLO calculations, interfaced with Herwig and Jimmy to model the parton showering, hadronisation and underlying event. Initial parton momenta are modelled using the CT10 set for the PDFs [110]. Samples are generated for both the Standard Model and for the aTGC point parametrised by $\Delta g_1^\gamma = 0$, $\Delta g_1^Z = -0.3$, $\Delta\kappa_Z = 1$, $\Delta\kappa_\gamma = 0$, $\lambda_Z = 0.3$, $\lambda_\gamma = 0$. The events produced using MC@NLO contain on-shell W and Z bosons; they are subsequently decayed by Herwig.

We also generated additional diboson signal processes, WW, $WZ/\gamma*$, for studies of systematic uncertainities. We used SHERPA 1.4.3 and POWHEG v2.1, both using the CT10 PDFs. The SHERPA samples model the diboson production at LO, but consider up to 3 additional partons in the matrix element. The POWHEG samples describe the processes at NLO, and are interfaced with PYTHIA8 for the parton shower. The WW sample was generated to be inclusive, whilst $WZ/\gamma*$, we considered only specific decay modes. The full signal samples generated for the analysis are summarised in table A.1 in Appendix A.

V+jets processes

The largest background is formed from states which contain a single leptonically decaying vector boson and additional jets from non-resonant processes (referred to henceforth as W+jets, Z+jets or as V+jets). Such processes can look like the semileptonic decay of a WV, if there is a dijet pair with a mass close to the mass of a vector boson. These processes are modelled using SHERPA v1.4.1, using the CT10 PDF set. The Monte Carlo samples were generated using schemes with massive c and b quarks, and containing up to 4 partons in the initial matrix element. Samples were generated in slices of vector boson p_T, in order to generate the higher number of events needed at higher p_T. The full W+jets processes generated are summarised in tables A.2 and the Z+jets in A.3 in Appendix A.

To cover regions with lower transverse momenta, samples inclusive in $p_T(V)$ are used, with a $p_T < 40$ GeV cut applied at truth particle level in order to remove overlap with the p_T slice samples.

$t\bar{t}$ and Single-top processes

Another important background comes from events with a top quark; almost all top quarks will decay to a b-quark and a W boson, which may decay leptonically. The full set of generated Monte Carlo samples is shown in table A.4 in Appendix A.

We generated $t\bar{t}$ samples using POWHEG at NLO using the CT10 PDF set, assuming a top quark mass of 172.5 GeV. This was interfaced with PYTHIA6.425 with the CTEQ61L PDF set, and the Perugia 2011C underlying event tune [134]. The sample was normalised to the cross section obtained from theoretical calculations.

These were performed at NNLO in QCD, including resummation of next-to-nex-to-leading logarithmic (NNLL) soft gluon terms, with top++2.0, yielding a cross-section of 253^{+15}_{-16} pb for the centre of mass energy $\sqrt{s} = 8$ TeV [135–141].

Systematic uncertainties for these $t\bar{t}$ processes arise from the choices of PDF and α_s, as well as from knowledge of the top quark mass. The PDF and α_s uncertainties were calculated using the PDF4LHC prescription [142]. To provide the uncertainties, the maximal envelope was taken from the following PDF sets and their errors: the MSTW2008 68% CL NNLO [106, 143], CT10 NNLO [110, 144] and NNPDF2.3 five flavour PDF sets [145].

Samples containing a single top quark were generated at NLO using POWHEG with the CT10 PDF set. They were generated in the t-channel, s-channel and Wt production mechanisms. All samples were interfaced with PYTHIA6.425, the CTEQ61L PDFs, and the Perugia2011C underlying event tune. Overlaps between the $t\bar{t}$ and Wt final states were removed using the diagram subtraction approach. The single-top quark samples were normalised to the appropriate theoretical NNLO cross-sections, using the MSTW2008 NNLO PDF set [106, 143].

ZZ processes

One possible small background arises from ZZ processes. We modelled this using HERWIG v6.520.2, at LO, using the CTEQ6L1 PDFs plus JIMMY. Events were generated taking into account all possible decays of the two Z bosons, and normalised to NLO predictions.

Non-resonant multijet processes

Another small background can arise from non-resonant multijet processes. We did not model these using Monte Carlo simulations, but instead estimated this background using a data-driven technique, described in section 7.5.1.

7.3. Object Identification

In order to identify events in the semileptonic WV decay channel, we need rigorous definitions of the physical objects to be identified. In the resolved channel we expect to identify two small-radius reconstructed jets, which we shall henceforth refer to as "signal small-radius jets". In the boosted channel, we expect to identify a single reconstructed large-radius jet, which we shall refer to as the "signal large-radius jet". In both states, we expect the presence of a reconstructed muon or electron, which we shall refer to as the "signal muon" or "signal electron" respectively. We also expect to see missing transverse energy, lost from an undetected neutrino.

In section 7.4 we shall also discuss the removal of events that contain certain unwanted objects. We shall refer to such particles as "veto muons", "veto electrons" and "veto jets".

In addition, the evaluation of non-resonant multijet events, which will be described in section 7.5.1, requires the identification of specific "fake" muon and electron signals. We shall refer to these as "fake muons" and "fake electrons" respectively.

7.3.1. Electron Definitions

Electron candidates are defined as clusters of energy deposited in the electromagnetic calorimeter associated to a track reconstructed in the Inner Detector. All electron candidates are required to satisfy the ATLAS MediumPP identification criteria, as outlined in section 5.4.

In order to reduce backgrounds from leptonic decays from within heavy flavour jets (such as $b \to ce\nu$), we make isolation cuts around the electron candidates. To do this, we draw cones around the electron candidate, and sum the energy or transverse momentum found in these cells. Cells that have already been included in the electron are not included as part of the cone energy or transverse momentum. We then require that the energy of transverse momentum in these cones is less than a certain proportion of the energy or transverse momentum of the electron candidate.

We label the E_T in a calorimeter cone in η–ϕ space of radius R = 0.3 around an electron candidate by 'etcone30'. imilarly, we label p_T in such a cone by 'ptcone30'.

We label the p_T in a calorimeter cone of radius R = 0.2 around an electron candidate by 'ptcone20'.

Signal and veto electron candidates lying within a cone in the η–ϕ plane with a radius of 0.2 and 0.4 of a signal or veto jet are removed (having already removed jets that lie within a radius of 0.2 of the electron candidates). This is in place to remove electrons that arise from leptonic decays within heavy flavour (c, b) jets.

To ensure that the electron originates in the hard scatter of interest, the electron track must have a longitudinal impact parameter, that is the shortest distance between the track and the primary vertex in the longitudonal direction, $|z_0 \sin\theta|$, along the beam axis less than 0.5 mm from the primary vertex. This applies to signal, veto and fake electron candidates.

Specific criteria for selecting electrons are outlined below.

Signal electron selection

- $p_T > 30$ GeV
- Pass Tight ID requirements
- etcone30/$p_T < 0.07$
- ptcone30/$p_T < 0.14$
- $\Delta R_{\text{electron-jet}} \geq 0.4$

Veto electron selection

- $p_T > 15$GeV
- Pass Medium ID requirements
- ptcone20/$p_T < 0.1$
- $\Delta R_{\text{electron-jet}} \geq 0.4$

Fake electron selection

- $p_T > 30$ GeV
- pass MediumPP and fail TightPP
- ptcone20/$p_T < 0.1$
- 2 GeV< etcone30 < 20 GeV
- Require b-layer hit

7.3.2. Muon Definitions

Muons are reconstructed using the STACO combined muon reconstruction algorithm, as described in 5.5.

Similarly to the electron case, we make isolation cuts around the muon candidates to reduce backgrounds from leptonic decays within heavy flavour jets (such as $b \to c\mu\nu$). We draw cones around the muon candidates, and require the sum of energy and transverse momentum in these cells to be less than a certain proportion of the energy or transverse momentum of the muon candidate, with different criteria in the cases of signal and veto muons. Once again, cells that have already been included in the muon are not included as part of the cone energy or transverse momentum.

We label the E_T in a calorimeter cone in η, ϕ space of radius R = 0.3 around an muon candidate by 'etcone30'. We label p_T in such a cone by 'ptcone30'. We label the p_T in a calorimeter cone of radius R = 0.2 around an muon candidate by 'ptcone20'.

We label the transverse impact parameter of the Inner Detector by 'd_0'. This is used to remove muons whose tracks lie far away from the interaction point: such muons could arise from background cosmic rays or out-of-time events.

Signal and veto muon candidates lying within a cone in the η–ϕ plane with a radius of 0.2 and 0.4 of a signal or veto jet are removed (having already removed jets that lie within a radius of 0.2 of the electron candidates). This is in place to remove muons that arise from leptonic decays within heavy flavour (c, b) jets.

To ensure that the muon comes from the hard scatter of interest, the muon track must have a longitudinal impact parameter, that is the shortest distance between the track and the primary vertex in the longitudonal direction, $|z_0 \sin\theta|$, along the beam axis less than 0.5 mm from the primary vertex. This applies to signal, veto and fake muon candidates.

Specific criteria for selecting muons are outlined below.

Signal muon selection

- $p_T > 30$ GeV
- $|\, {}^{d_0}/_{\sigma_{d_{0,track}}} | < 3$
- etCone30$/p_T < 0.07$
- ptcone30$/p_T < 0.07$
- $\Delta R_{\text{muon-jet}} \geq 0.4$

Veto muon selection

- $p_T > 15$ GeV
- $|\, {}^{d_0}/_{\sigma_{d_{0,track}}} | < 3$
- ptcone20$/p_T < 0.1$
- $\Delta R_{\text{muon-jet}} \geq 0.4$

Fake muon selection

- $p_T > 30$ GeV
- $|\, {}^{d_0}/_{\sigma_{d_{0,track}}} | > 4$
- ptcone20$/p_T < 0.1$

7.3.3. Small-Radius Jet Definitions

We identify small-radius jets as described in section 5.2 using the anti-$k_\perp$ algorithm, with the radius of 0.4 in the η–ϕ plane. The jet calibraton is performed as an average shift (to correct for pile-up) and multiplicative correction factor, obtained from Monte Carlo simulations in bins of η and p_T, as outlined in section 5.2.3. For signal jets, we use only central jets within the range $|\eta| < 2.5$, because these have lower uncertainties arising from the calibration, and are affected to a lesser extent by pile-up. Veto jets may take any value of η up to the limits of the detector.

To discriminate between jets arising from the hard scatter and those originating in pile-up, we define the jet vertex fraction (JVF), which measures the probability that a jet originated from a particular vertex. This can be obtained by comparing calorimeter jets to jet tracks in the inner dector and the primary vertices.

To reduce the contribution of jets produced from pile-up interactions, jets with $p_T < 50$ GeV and $|\eta| < 2.4$ are rejected if the absolute value of the jet vertex fraction (JVF) is lower than 0.5 (i.e. they do not satisfy $|\text{JVF}| \geq 0.5$). From henceforth, these will be referred to as the 'JVF requirements'. In addition, small-radius jets are required to lie at least 0.2 away from veto or signal electron candidates in η–ϕ space, as such jets are likely to be artefacts arising from energy deposits from the electron.

The effects of systematic uncertainties arising from the jet energy scale and jet energy resolution, as well as possible discrepancies between the data and Monte Carlo samples due to mis-modelling of pile-up, are taken into account in the systematic uncertainty estimations, as described in chapter 8.

Specific criteria for selecting jets are outlined below.

Small-radius signal jet selection

- $p_T > 30$GeV
- $|\eta| < 2.5$
- Pass JVF requirements
- $\Delta R_{\text{jet-electron}} \geq 0.2$

Small-radius veto jet selection

- $p_T > 15$GeV
- Pass JVF requirements
- $\Delta R_{\text{jet-electron}} \geq 0.2$

7.3.4. Large-Radius Jet Definition

We identify large-radius jets as described in section 5.2 using the anti-$k_\perp$ algorithm, with the standard ATLAS large radius 1.0 in the η–ϕ plane. The jet calibration is performed as an average shift (to correct for pile-up) and multiplicative correction factor, obtained from the Monte Carlo simulation in bins of η and p_T, as outlined in section 5.2.3. We restrict large radius jets to the region $|\eta| < 2.0$. Any wider range in η would allow a large proportion of the jet to fall outside of the central region, where the uncertainties would be higher and the contamination from pile-up greater.

Large-radius jets are required to have a high transverse momentum of at least 250 GeV in order to be sufficiently boosted to capture the entire hadronic boson decay. In addition, we only study jets with a mass greater than 50 GeV; large-radius jet masses are not calibrated in the low mass region. In order to account for the high level of pile-up contamination in jets of this radius, jet grooming is essential. We apply jet trimming using the procedure explained in section 4.5.1, applying the parameters $R_{\text{sub}} = 0.3$ and f_{cut} at 5%. A previous study found that these parameters maximise signal/background discrimination for boosted W and Z vector bosons [97].

Large-radius jets are required to pass the same JVF requirements as small-radius jets. As with small-radius jets, we require large-radius jets to lie at least 0.2 away from veto or signal electron candidates in η–ϕ space.

As with small-radius jets, the effects of systematic uncertainties arising from the jet energy and mass scale and jet energy and mass resolution, as well as possible discrepancies between the data and Monte Carlo due to mis-modelling of pile-up are taken into account in the systematic uncertainty estimations, as described in chapter 8.

7.3.5. Missing Transverse Energy Definition

We expect large missing energy in the transverse plane to arise from the neutrino in the final state. We use the RefFinal definition for reconstructing the missing energy, as explained in section 5.6. We refine our estimate of the energy deposited in the calorimeter by associating the calorimeter energy deposits with reconstructed objects (such as jets, electrons and muons) and by replacing the calorimeter energy estimate by that of calibrated objects. The smearing, energy corrections, and calibrations applied to the identified objects are propagated into the E_T^{miss} calculation.

7.4. Event Selection

To select WW, WZ events decaying in the semileptonic channel, we employ a series of kinematic and topological criteria, on the data, and then impose these same cuts on our Monte Carlo samples.

Let us conceive of three general purposes of these cuts. First, are cuts to select a leptonic W boson decay, by requiring a suitable lepton candidate passes the ATLAS triggers, and carries sufficient energy, as well as requiring sufficient missing transverse energy, from the neutrino. These first cuts will be the same in both the resolved and boosted channels. Second, are cuts to select for the hadronic vector boson decay, which should be captured by jets. By definition, these cuts are different in the resolved and boosted channels. Finally, there are cuts to remove specific backgrounds, some of which may have been shaped by the earlier cuts and now peak at similar points in the mass distribution to the signal. In particular, we introduce specific cuts to remove non-resonant multijet background from the resolved channel, and to remove events containing a $t\bar{t}$ pair from the boosted channel.

7.4.1. Resolved Channel Selection

1. **Preselection cuts**
   We employ the preselection cuts detailed in chapter 5, requiring data events to pass a GRL, and discarding any events that contain a reconstructed jet with a $p_T > 20$ GeV that is flagged as 'badLoose'. We require the primary vertex with

the highest sum of track p_T^2 to have at least three associated tracks. We require that the event passes the ATLAS single lepton triggers:

- electron channel: e24vhi_medium1 OR e60_medium1,
- muon channel: mu24i_tight OR mu36_tight.

Once we have a selected signal lepton, it must be must be matched to a trigger object fulfilling the respective event trigger.

2. **Lepton selection**
   We require the event to contain precisely one signal lepton (electron or muon).

3. **Lepton veto**
   We remove any events containing one or more veto leptons (electrons or muons), other than the signal lepton.

4. **Missing transverse energy requirement**
   We require the event to have sufficiently high missing transverse energy, given by $E_T^{\text{miss}} > 40$ GeV.

5. **Transverse mass cut**
   We require the transverse mass of combined selected lepton and E_T^{miss} to be greater than 40 GeV. We expect these objects to arise from the leptonic decay of a W boson, so the transverse mass should be sufficiently close to the W boson mass. Heavy flavour background jets could decay to a virtual (i.e. away from the mass shell) W boson which could then decay leptonically. This could look similar to the signal, but we would expect a lower transverse mass. Hence, this cut will greatly to reduce the background from non-resonant multijet events.

6. **Angular separation between jets and missing transverse energy**
   We make a cut on the azimuthal separation between the leading jet and the E_T^{miss} ($\Delta\phi(j_1, E_T^{\text{miss}}) > 0.8$) to further reduce the non-resonant multijet background, where high missing transverse energy can only arise from a mis-measured object.

7. **Exactly two signal jets**
   We require precisely two signal jets, designed to capture the hadronic W boson decay. By discarding events with more than two signal jets, we greatly reduce the background from events containing a $t\bar{t}$, which we expect to have a high jet multiplicity.

8. **Signal jet separation**
   We require a separation between selected jets satisfying $|\Delta\eta(j,j)| < 1.5$ in order to increase the ratio of signal/background. Figure 7.3 shows the comparison between the $\Delta\eta(j,j)$ distributions for the signal and background samples.

9. **Transverse momentum requirements**
   We require the dijet and the lepton-E_T^{miss} pairs each to have $p_T > 100\text{GeV}$[1] to improve the separation between signal and background peaks, shown in figure 7.4.

10. **dijet mass cut**
    We restrict the dijet invariant mass for the fit to the range $40\text{GeV} < m_{jj} < 200\text{GeV}$. The Monte Carlo samples were found to model the individual jet masses poorly, so we perform this calculation setting small-radius jet masses to zero.

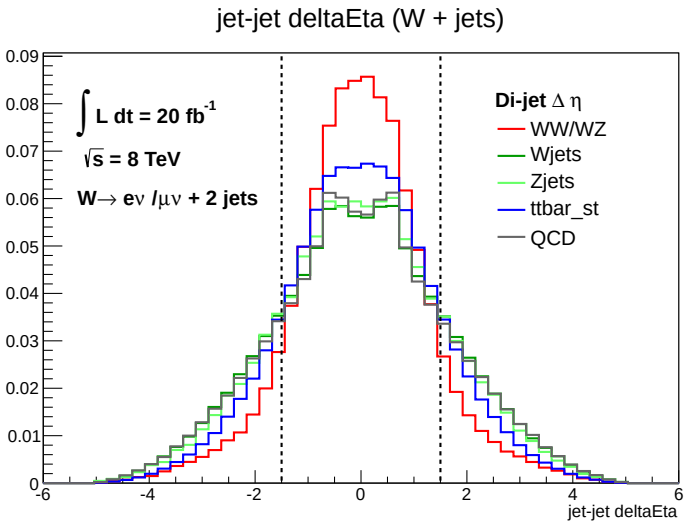

Figure 7.3.: Distribution of $\Delta\eta(j,j)$ for signal (red) and main background processes. The non-resonant multijet background sample (QCD) is extracted from the data, all other samples are Monte Carlo simulations. Events pass the full event selection except the $\Delta\eta(j,j) < 1.5$ cut.

[1] When we refer to the p_T of the lepton-E_T^{miss} pair, we mean the p_T of the W boson decaying to lepton-neutrino, as reconstructed by summing the transverse momenta of lepton and neutrino: $p_T(l, E_T^{\text{miss}}) \equiv p_T(W) \equiv |\vec{p}_{\text{T}_l} + \vec{E}_{\text{T}}^{\text{miss}}|$.

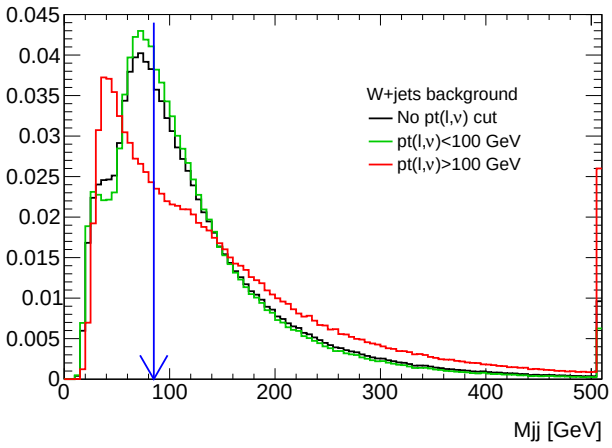

Figure 7.4.: Dijet invariant mass for W+jets simulated events passing the full leptonic selection. The full event sample is compared to the two sub-samples with $p_T(W) > 100$ GeV and $p_T(W) < 100$ GeV. All distributions are normalized to unity; the last bin includes overflows. The blue arrow marks the centre point of the signal peak. The cut on $p_T(W)$ has the effect of shifting the background peak to lower masses.

7.4.2. Boosted Channel Selection

1. **Preselection cuts**
   We employ the preselection cuts detailed in chapter 5, requiring data events to pass a GRL, and discarding any events that contain a reconstructed jet with a $p_T > 20$ GeV that is flagged as 'badLoose'. We require the primary vertex with the highest sum of track p_T^2 to have at least three associated tracks. We require that the event passes the ATLAS single lepton triggers:

   - electron channel: e24vhi_medium1 OR e60_medium1,
   - muon channel: mu24i_tight OR mu36_tight,

   Once we have a selected signal lepton, it must be must be matched to a trigger object fulfilling the respective event trigger.

2. **Lepton selection**
   We require the event to contain precisely one signal lepton (electron or muon).

3. **Lepton veto**
   We remove any events containing one or more veto leptons (electrons or muons).

4. **Missing transverse energy requirement**
   We require the event to have sufficiently high missing transverse energy, given by $E_T^{\text{miss}} > 40$ GeV.

5. **Exactly one large-radius jet**
   We require precisely one large-radius jets, designed to capture the full boosted hadronic W boson decay.

6. **Jet veto**
   We remove any events with one or more veto jets that are sufficiently separated from the selected large-radius jet. This separation is given by $\Delta R_{jj} > 0.8$ in dimensions of η–ϕ. Jets that lie closer to the large-radius jet than this are assumed to be partly or fully reconstructed using energy from this jet and so can be considered part of the hadronic W decay.

   Top quarks will almost always decay to a W boson and a b quark, which will in turn form a b-jet, and so $t\bar{t}$ events can have a very similar appearance to signal events, especially after applying the previous selection criteria. However, we would expect a high jet multiplicity from these decays. Hence we use this cut to greatly reduce the background from such events.

7. **Vector boson tagging**
   To improve discrimination of signal against background, we apply vector boson tagging using the energy-energy correlation functions. As explained in section 4.6.3, the $D_2^{\beta=1}$ variable has the potential to make a particularly powerful for boosted vector bosons. It was found to be an optimal W boson tagger in an extensive previous study [97]. We follow the recommendations of the study, requiring that the $D_2^{\beta=1} < 1.2$ for the large-radius jet, which corresponds to approximately 50% efficiency. Figure 7.5 shows the distribution of the tagging variable for the data and Monte Carlo samples used.

8. **Jet mass cut**
   We restrict the jet mass for the fit to the range $50 < m_J < 170$ GeV. Jets below this mass are poorly calibrated. We found there to be no events in the data above this range.

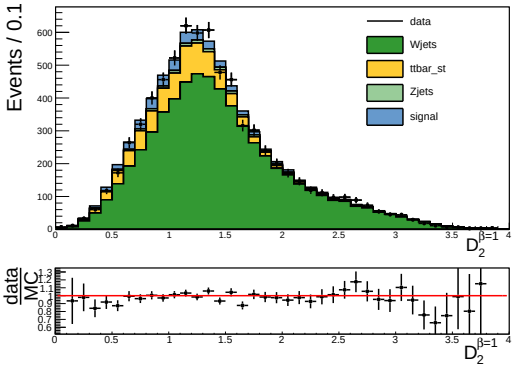

(a) Data and Monte Carlo comparison

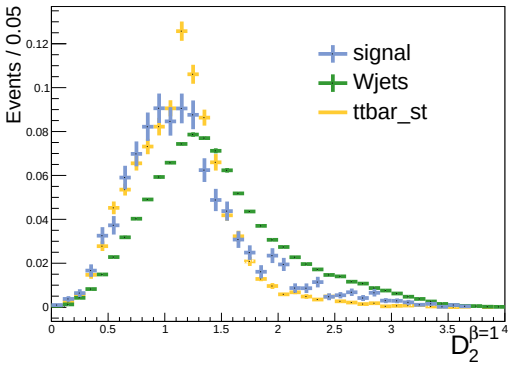

(b) Monte Carlo shape comparison (each process normalised to unity)

Figure 7.5.: The $D_2^{\beta=1}$ variable for the selected large-radius jet in the data and Monte Carlo processes passing the full boosted selection. The Monte Carlo distributions are shown after applying reweighting procedures discussed in section 7.5.

7.5. Background Modelling

7.5.1. Non-resonant Multijet Background Estimation

Non-resonant multijet backgrounds, produced from various QCD processes can pass the event selection in cases where one jet is misidentified as a lepton. In the resolved analysis, we estimate this background using data-driven techniques, whilst in the boosted analysis, we demonstrate that contributions from non-resonant multijet events are negligible.

Resolved analysis

To model non-resonant multijet processes, we apply apply the usual selection but replace the signal lepton requirements with those for fake leptons, detailed in sections 7.3.1 and 7.3.2, in order to reduce the contribution from real, isolated leptons. These lepton selection criteria are orthogonal to the ones used for the signal region, so no events can pass both sets of criteria. After applying the kinematic and topological requirements of the signal region, this "inverted" lepton selection reveals the contamination from processes containing real leptons to our estimated of the multijet backgrounds.

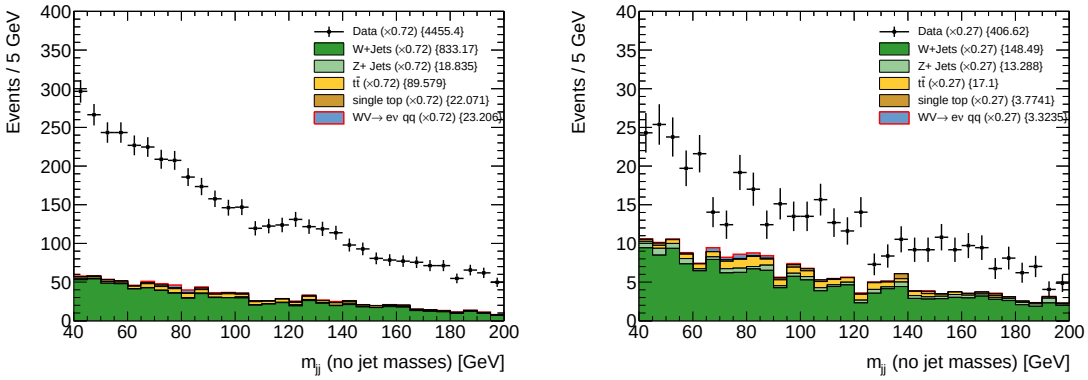

(a) electron channel **(b)** muon channel

Figure 7.6.: Dijet mass (m_{jj}), spectrum in the resolved analysis, for data and Monte Carlo events in the electron and muon channels. Events pass the full event selection with "inverted" cuts on the lepton.

The normalisation is then determined from a likelihood fit to the E_T^{miss} distribution in data, shown in figure 7.7. This variable provides the best discrimination between multijet backgrounds and the dominant W+jets background because non-resonant multijet processes will not contain a real source of missing energy. The fit is performed in the region where all selection criteria are applied, except the cut on E_T^{miss} and $\Delta\phi(j_1, E_T^{\text{miss}})$, and additionally no cut on $\Delta\eta(j, j)$ or transverse mass in the muon channel. The fit is performed in the region $5 < E_T^{\text{miss}} < 130$ GeV, shown in figure 7.8.

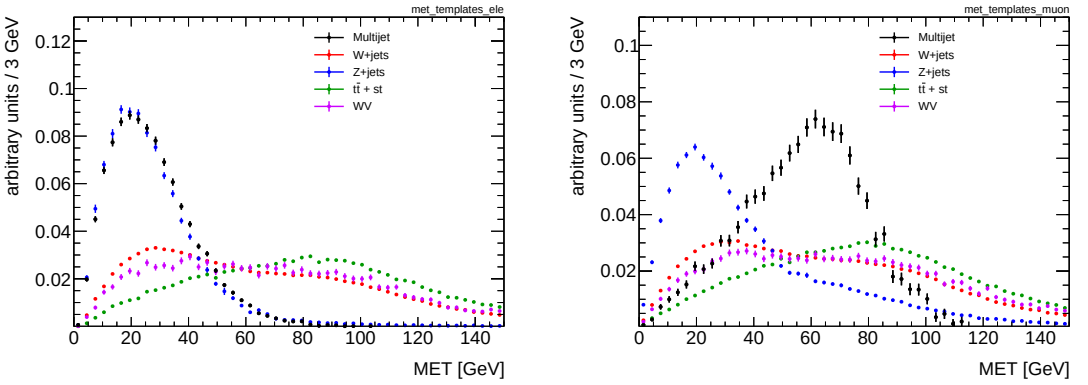

(a) electron channel **(b)** muon channel

Figure 7.7.: Resolved channel E_T^{miss} template distribution for considered processes in the electron and muon channel.

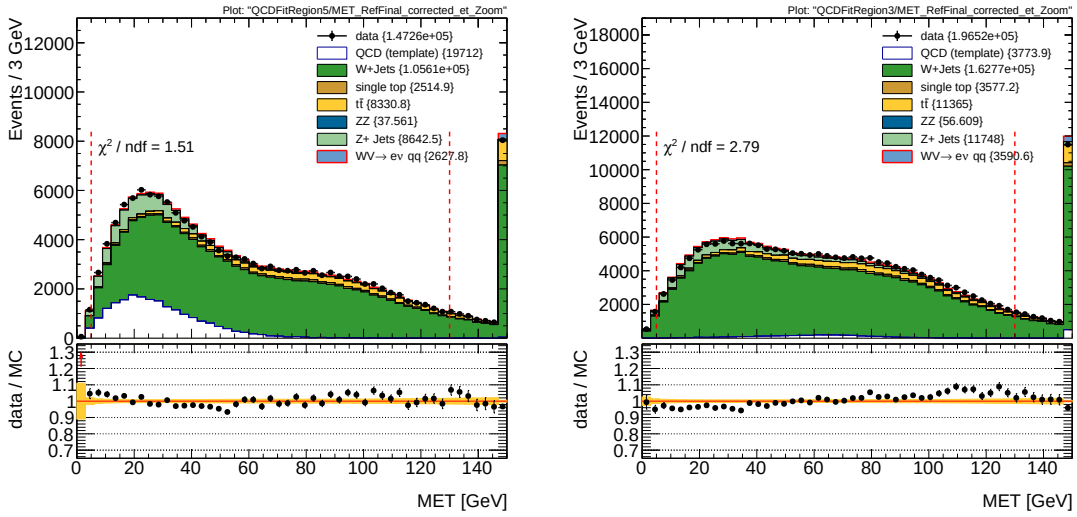

(a) electron channel **(b)** muon channel

Figure 7.8.: Nominal result of the fit to the resolved channel E_T^{miss}-distribution for the electron and muon channels. The red lines indicate the fit range.

Boosted analysis

The contributions from non-resonant multijet backgrounds in the boosted analysis are negligible, removed by the E_T^{miss}, and large-radius jet p_T requirements. To estimate contributions, data and background are compared with systematically lower E_T^{miss} cuts at 20 and 30 GeV; data and Monte Carlo disagreement rises in the lowest bins of jet mass, presumably corresponding to non-resonant multijet contributions. This disagreement is not visible when the E_T^{miss} cut is in place.

7.5.2. Top Backgrounds Modelling

Top-contributions, i.e. contributions from events containing a single top quark or $t\bar{t}$, are expected to form the second largest backgrounds in both the resolved and boosted regimes. We define specific control regions, different in the two analysis regimes, in order to study the top backgrounds.

Resolved analysis

In the resolved analysis, contributions containing a top quark are enhanced by the event selection cuts on $p_T(W)$ and $p_T(jj)$. Figure 7.9 shows that this is dominated by the $t\bar{t}$. The distribution has two large-scale features: a broad peak at around 110 GeV and a peak at around 80 GeV, corresponding to the W boson mass. The former originates mostly from dileptonic decays, in which one selected jet likely contains a b quark; however, the latter originates mostly from events in which one W decays hadronically, and neither of the two b-jets originating from the top decay meet the acceptance criteria. Thus the two selected jets are unlikely to contain b-quarks. We do not employ a cut to remove b-tagged jets (described in section 4.7), because it would be likely only to minimally reduce the peak at around 80 GeV, shaping the overall top-background to become more signal-like.

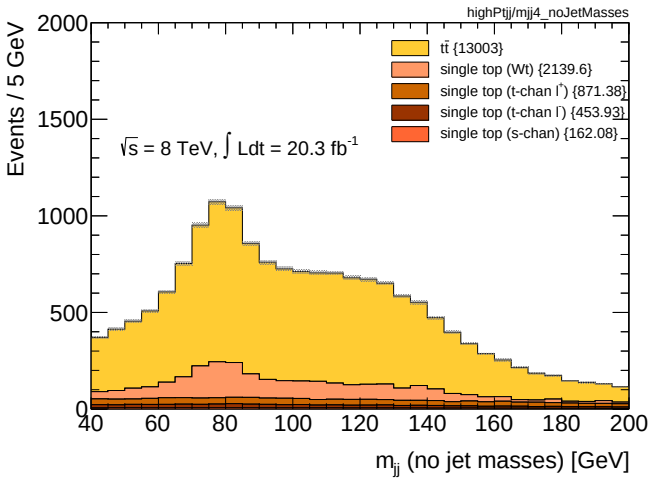

Figure 7.9.: m_{jj} distribution for Monte Carlo generated single-top and $t\bar{t}$ events in the resolved channel signal region split into the contribution of all subprocesses.

We construct a control region for backgrounds containing a top quark with the following criteria:

- exactly 3 selected jets;
- exactly 1 b-tagged jets, tagged using the MV1 tagger 70% working point;
- the invariant mass of the three jets falls within the range $150 < m_{jjj} < 200$ GeV;
- the pair of untagged jets fulfilling the same list of cuts as the signal region.

As shown in figure 7.10, the agreement between data and Monte Carlo generated events is already good in this control region. Hence, we use the control region only to validate the modelling and not to constrain the backgrounds containing top quarks.

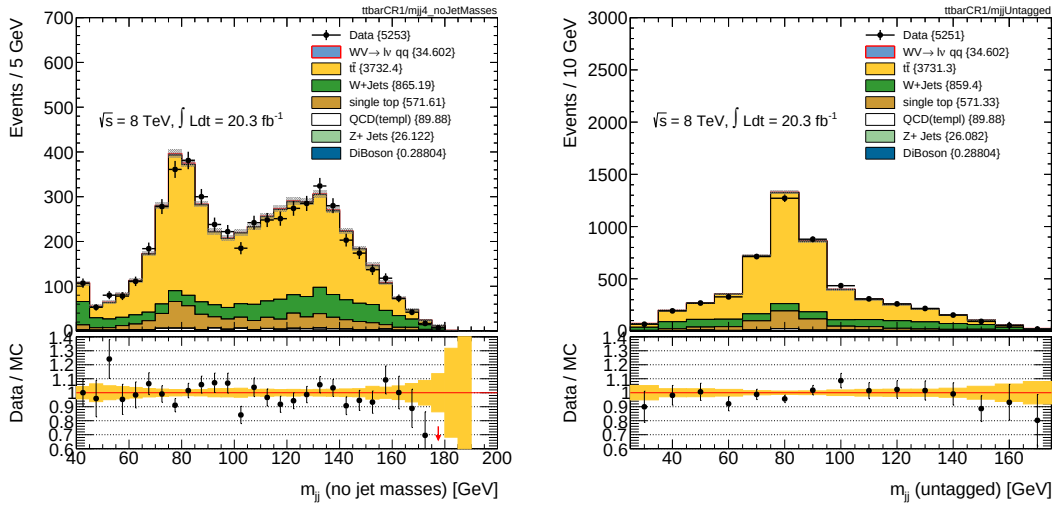

(a) m_{jj} (two closest jets) **(b)** m_{jj} (untagged jets)

Figure 7.10.: Resolved analysis data and Monte Carlo events comparison for events in the top control region for the resolved analysis. Electron and muon channel are considered together.

Boosted analysis

In the boosted analysis, contributions containing a top quark are greatly enhanced by the event selection, including the requirement of a boosted jet, and the application of the $D_2^{\beta=1}$ tagger for W bosons. The distribution is even more dominated by the $t\bar{t}$ contributions than in the resolved analysis. Once again, application of a b-tagger would shape the background to become more signal-like.

We construct a control region for backgrounds containing a top quark with the following criteria:

- the usual boosted channel requirement of exactly 0 additional jets is dropped;
- the $D_2^{\beta=1}$ tagging requirement is dropped;
- at least 1 b-tagged jet, with the veto-jet criteria, tagged using the MV1 tagger 70% working point;

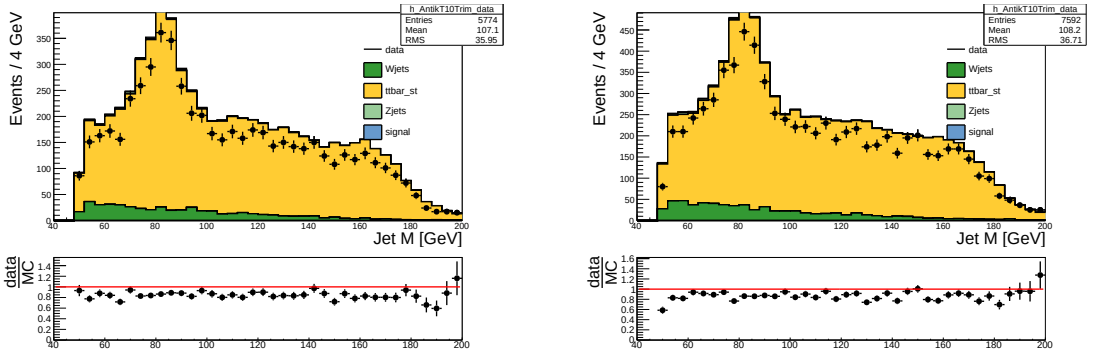

(a) Electron channel **(b)** Muon channel

Figure 7.11.: Boosted analysis jet mass distributions in the electron and muon channels, in the top control region before applying reweighting. Statistical uncertainties are shown. A significant discrepency is seen between data and Monte Carlo simulated events.

We see significant differences between data and Monte Carlo events, shown in figure 7.11.

We apply a single reweighting function, derived by comparing the Monte Carlo events containing a single top quark or $t\bar{t}$ against data with the other backgrounds and signals subtracted from it. The function is obtained separately for the electron and muon channels. We derive it by fitting a first order polynomial to the $p_T(J)$ distribution, the transverse momentum of the large-radius jet. We apply these reweighting functions as individual weights to each generated event. The functions are obtained by fitting polynomials to the mismodelling histograms. Figure 7.12 shows the reweighting histograms and fitted functions; figure 7.13 and 7.14 show the the fully reweighted Monte Carlo simulated events and data, in the electron and muon channels respectively.

7.5.3. Vector Boson with Jets Modelling

The dominant background for both the resolved and boosted analyses is V+jets, as shown in 7.15 and 7.16. This is dominated overwhelmingly by W+jets, with Z+jets contributing only around 2% in both the resolved and boosted cases. We study the two backgrounds together, because they originate in similar physical processes and are modelled using the same Monte Carlo generator (SHERPA). We study enhanced-

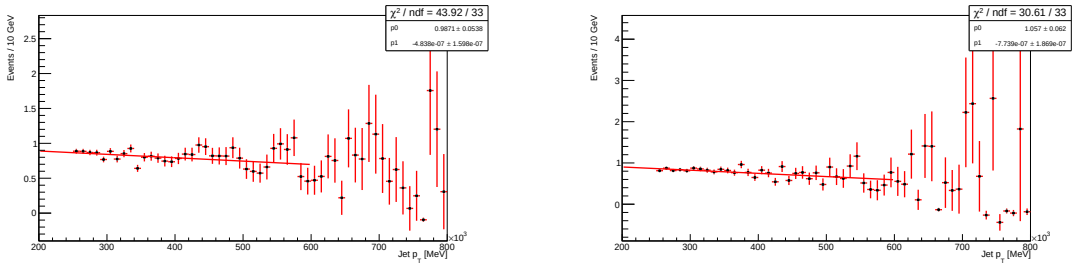

(a) electron channel **(b)** muon channel

Figure 7.12.: Boosted analysis distributions used to obtain the top-contributions reweighting functions with different reweightings applied to the top Monte Carlo samples. On the left, is shown the electron channel, on the right the muon channel.

purity samples of V+jets generated events passing the selections by defining control regions. In the boosted analysis, this takes place after having already applied the reweighting for the top-backgrounds modelling.

Resolved analysis

For the resolved analysis, the control region is defined by a dijet invariant mass range $m_{jj} < 65$ || $m_{jj} > 95$ GeV. We identify several systematic differences between data and Monte Carlo predictions in the control region, shown in figures 7.17. To improve the Monte Carlo description, we use two reweighting functions, derived by comparing the V+jets Monte Carlo events against data with the other backgrounds and signals subtracted from it. For $p_T(j)$, the transverse momentum of the leading jet, we use a first order polynomial, whereas for $\Delta\phi(jj)$, the difference in ϕ between the two leading jets, we use a second order polynomial, to account for the flattening of the relation at higher values of $\Delta\phi(jj)$. To account for any correlations between the reweightings, we first reweight the Monte Carlo using the $p_T(j)$ functions, and then apply the $\Delta\phi(jj)$ to these fitted events. As a closure-check, the order is reversed. Figure 7.18 shows the reweighting histograms and fitted functions; The fully reweighted Monte Carlo simulated events and data are shown in figure 7.19.

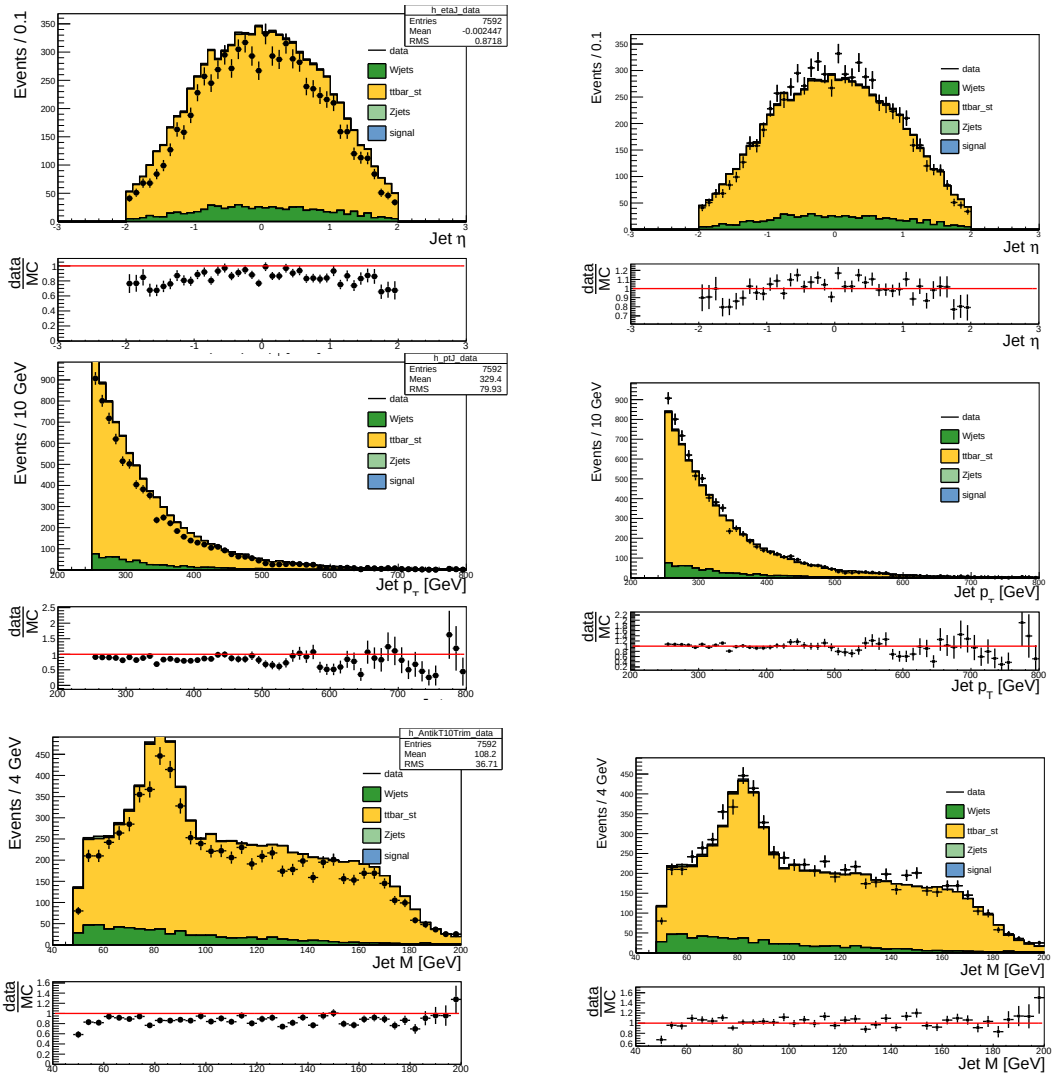

(a) before reweighting **(b)** after reweighting

Figure 7.13.: Boosted analysis distributions in the electron channel before and after applying reweighting in the top-contributions control region. Statistical uncertainties are shown.

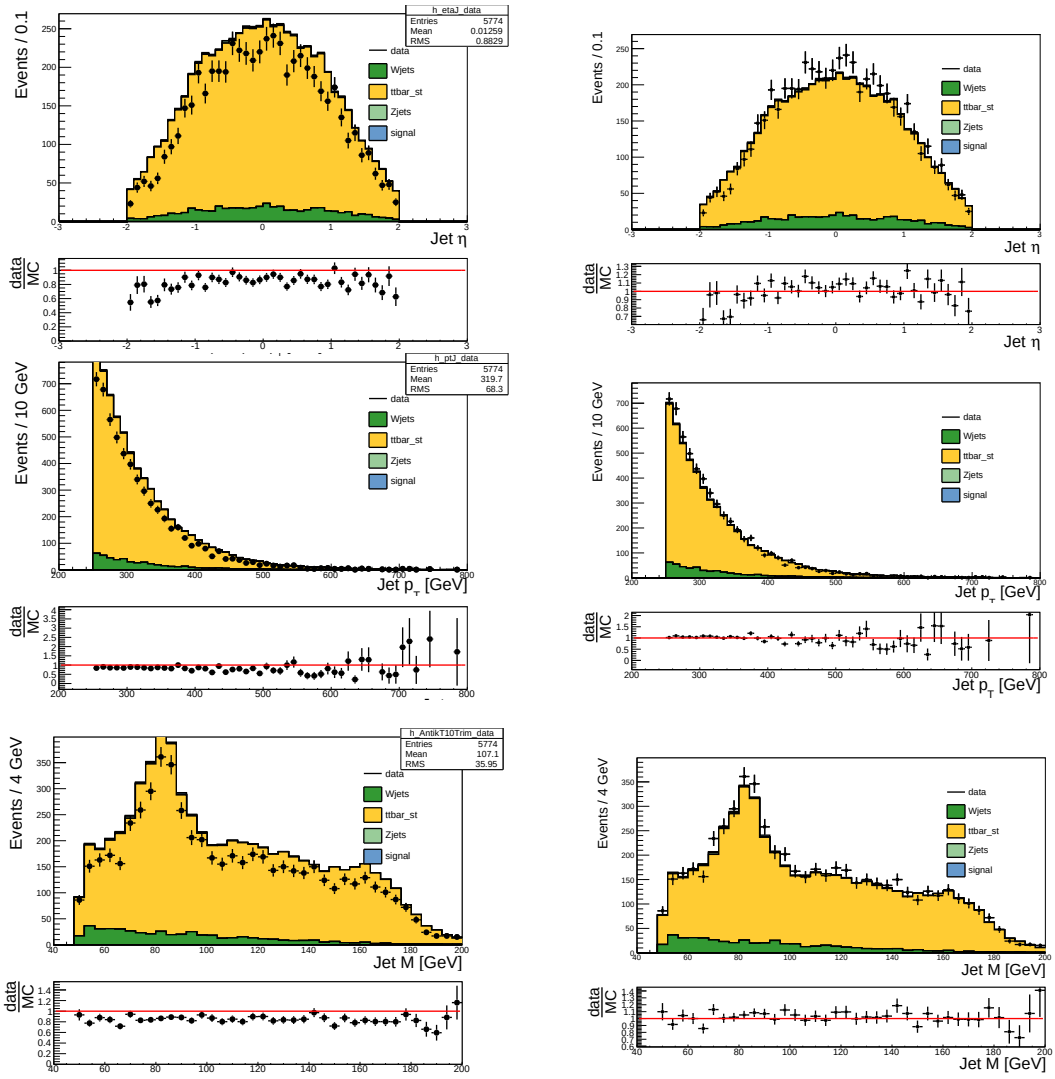

(a) before reweighting **(b)** after reweighting

Figure 7.14.: Boosted analysis distributions in the muon channel before and after applying reweighting in the top-contributions control region. Statistical uncertainties are shown.

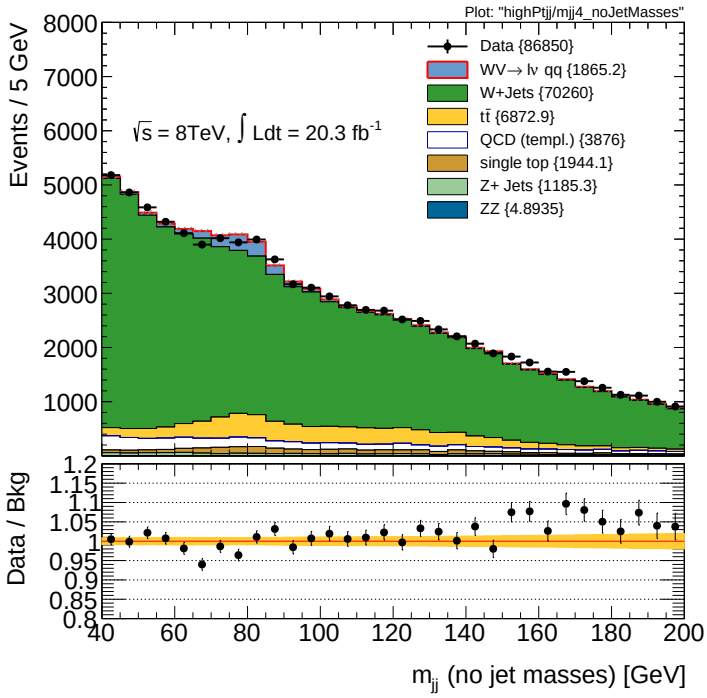

Figure 7.15.: Resolved m_{jj} distribution for data and Monte Carlo for all processes and subprocesses. The background processes can be seen to be dominated by W+jets contributions in both cases.

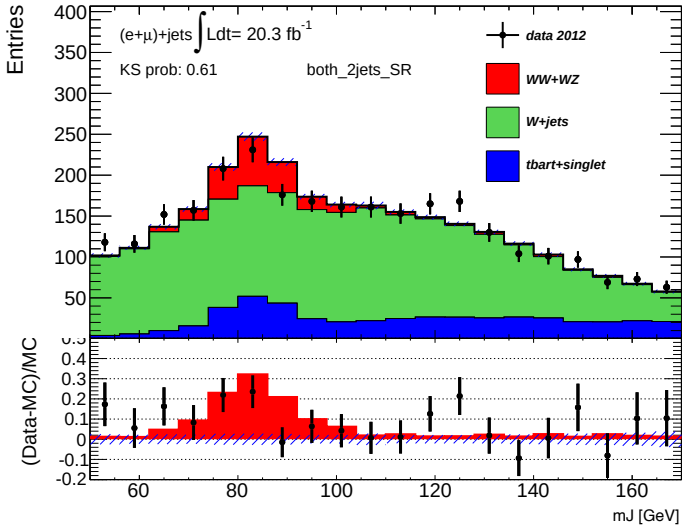

Figure 7.16.: Boosted m_J distribution for data and Monte Carlo for all processes and subprocesses. The background processes can be seen to be dominated by W+jets contributions in both cases.

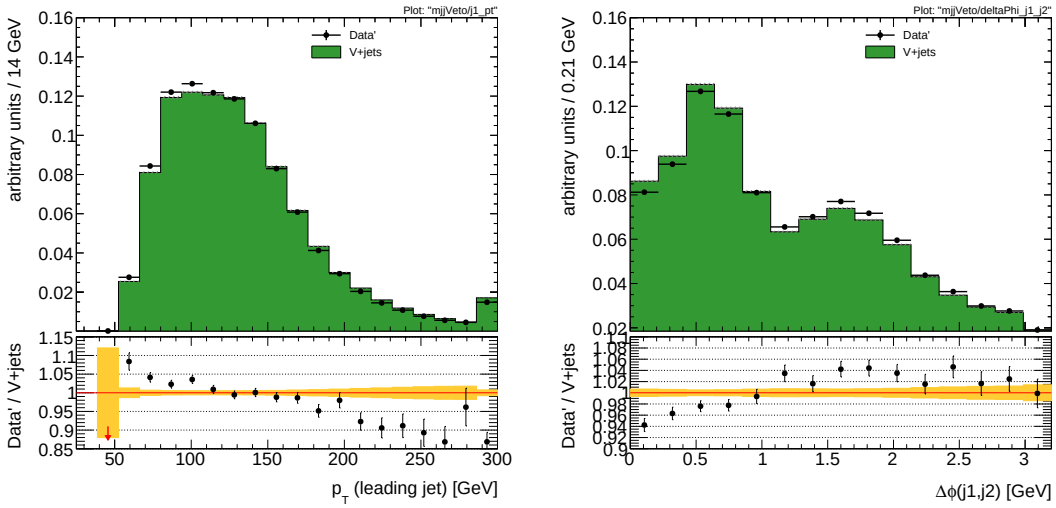

(a) $p_T(j_1)$ **(b)** $\Delta\phi(jj)$

Figure 7.17.: Resolved analysis distributions used to derive the reweighting, shown in the control region defined by $m_{jj} < 65$ || $m_{jj} > 95$ GeV. Data$'$ denotes data with all other (non V+jets) contributions subtracted.

Boosted analysis

In the boosted analysis, we use a method analogous to that in the resolved case to reweight the V+jets Monte Carlo events. The control region is defined by a leading large-radius jet mass range $m_J < 60$ || $m_J > 100$ GeV. In addition, the $D_2^{\beta=1}$ W-tagging requirement is dropped. We apply the reweighting after having already performed the reweighting on the Monte Carlo events containing top quarks.

We apply a single reweighting function, derived by comparing the V+jets Monte Carlo events against data with the other backgrounds and signals subtracted from it. The function is derived separately in the electron and muon channels. The function is obtained by fitting a first order polynomial to the $p_T(J)$ distribution, the transverse momentum of the large-radius jet, shown in figure 7.20. The reweighting histograms and fitted functions are shown in figure 7.21. The fully reweighted Monte Carlo simulated events and data are shown in figure 7.22.

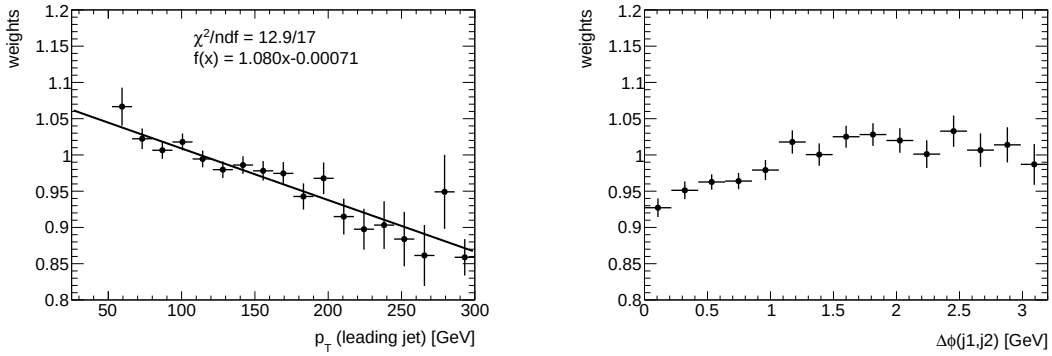

(a) No reweighting applied

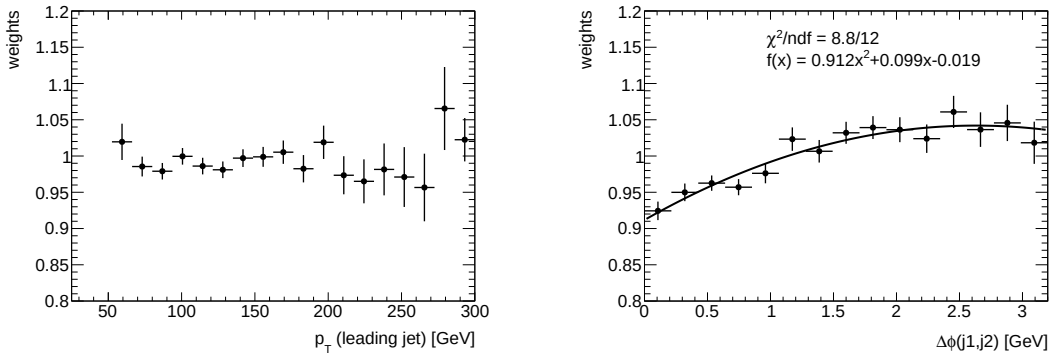

(b) $p_T(j_1)$ reweighting applied only

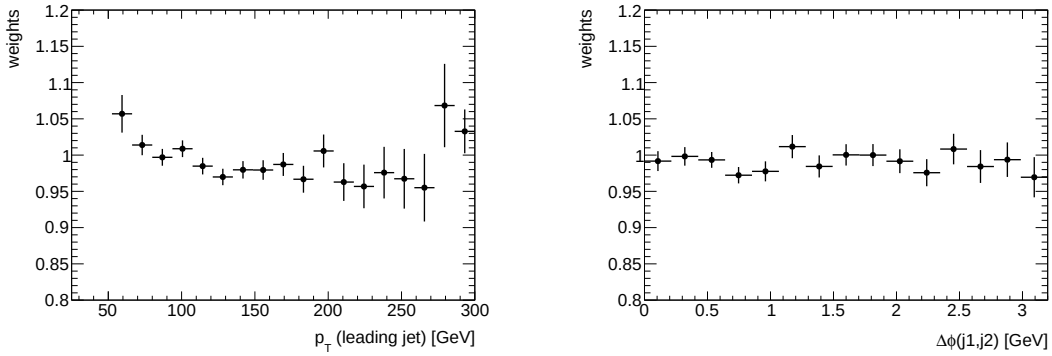

(c) Full reweighting applied

Figure 7.18.: Resolved analysis distributions used to obtain the V+jets reweighting functions, with different reweightings appplied to the V+jets Monte Carlo events.

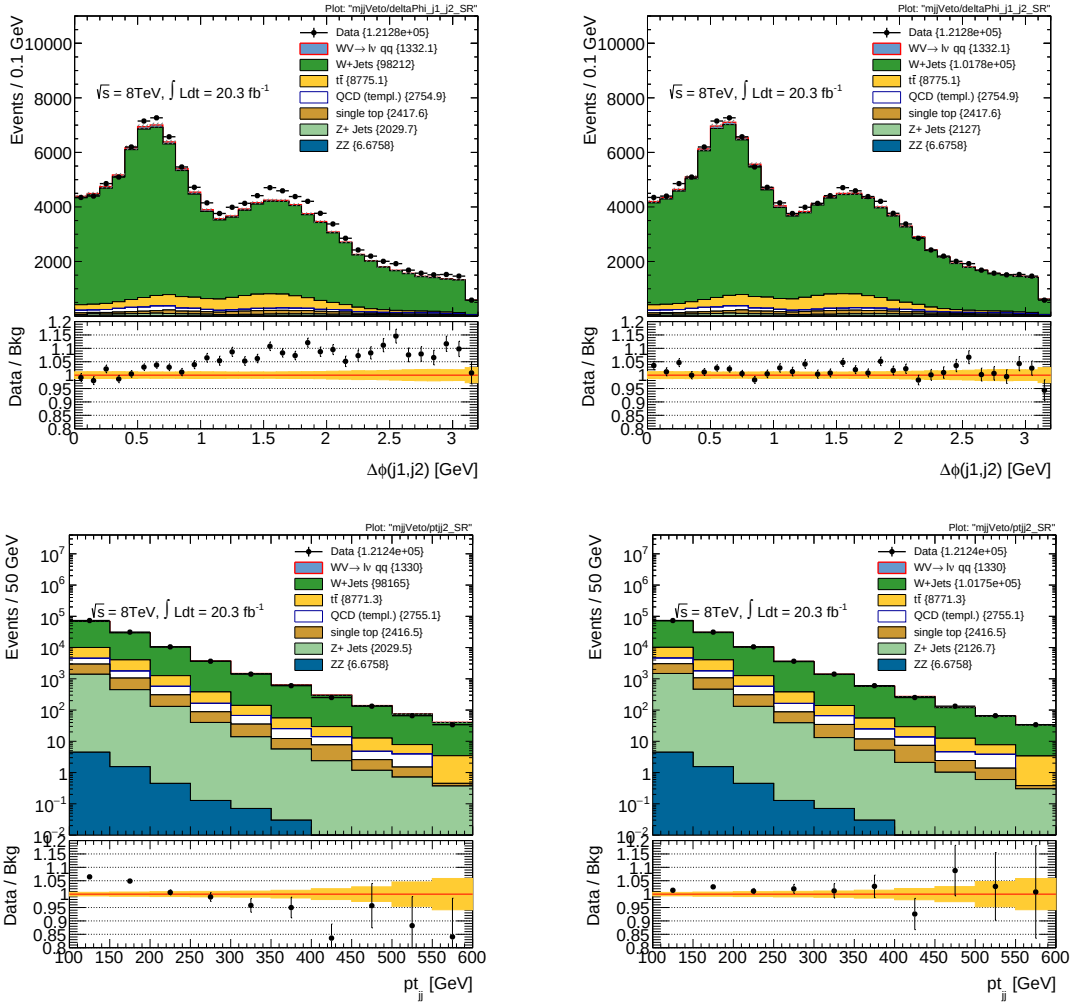

(a) before reweighting **(b)** after reweighting

Figure 7.19.: Resolved analysis distributions before and after applying reweighting in the $m_{jj} < 65 \,||\, m_{jj} > 95$ GeV control region. Statistical uncertainties are shown.

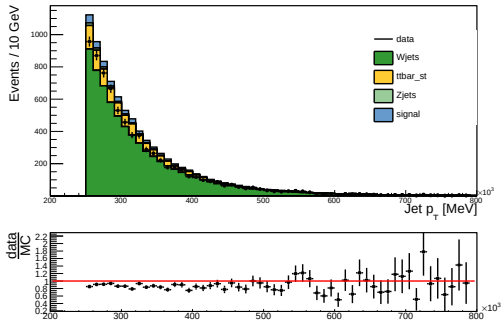

(a) $p_T(j_1)$

Figure 7.20.: Boosted analysis jet p_T distribution, used to derive the reweighting, shown in the control region defined by $m_J < 60$ || $m_J > 100$ GeV. Data$'$ denotes data with all other (non V+jets) contributions subtracted.

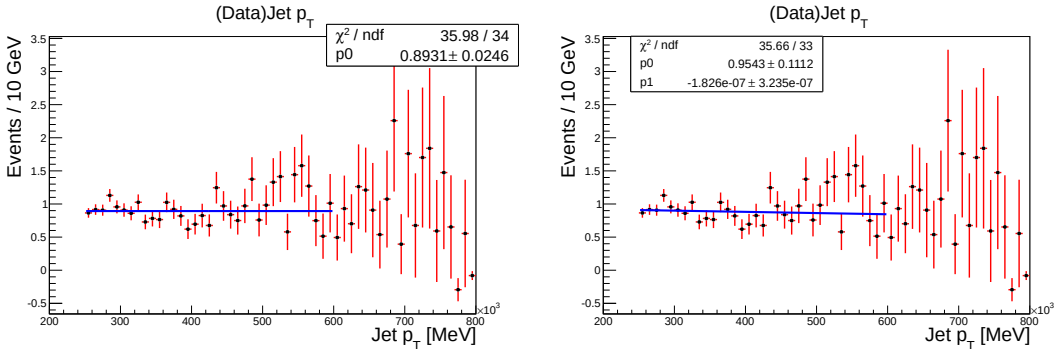

(a) electron channel **(b)** muon channel

Figure 7.21.: Boosted analysis distributions used to obtain the V+jets reweighting functions with different reweightings appplied to the V+jets Monte Carlo events.

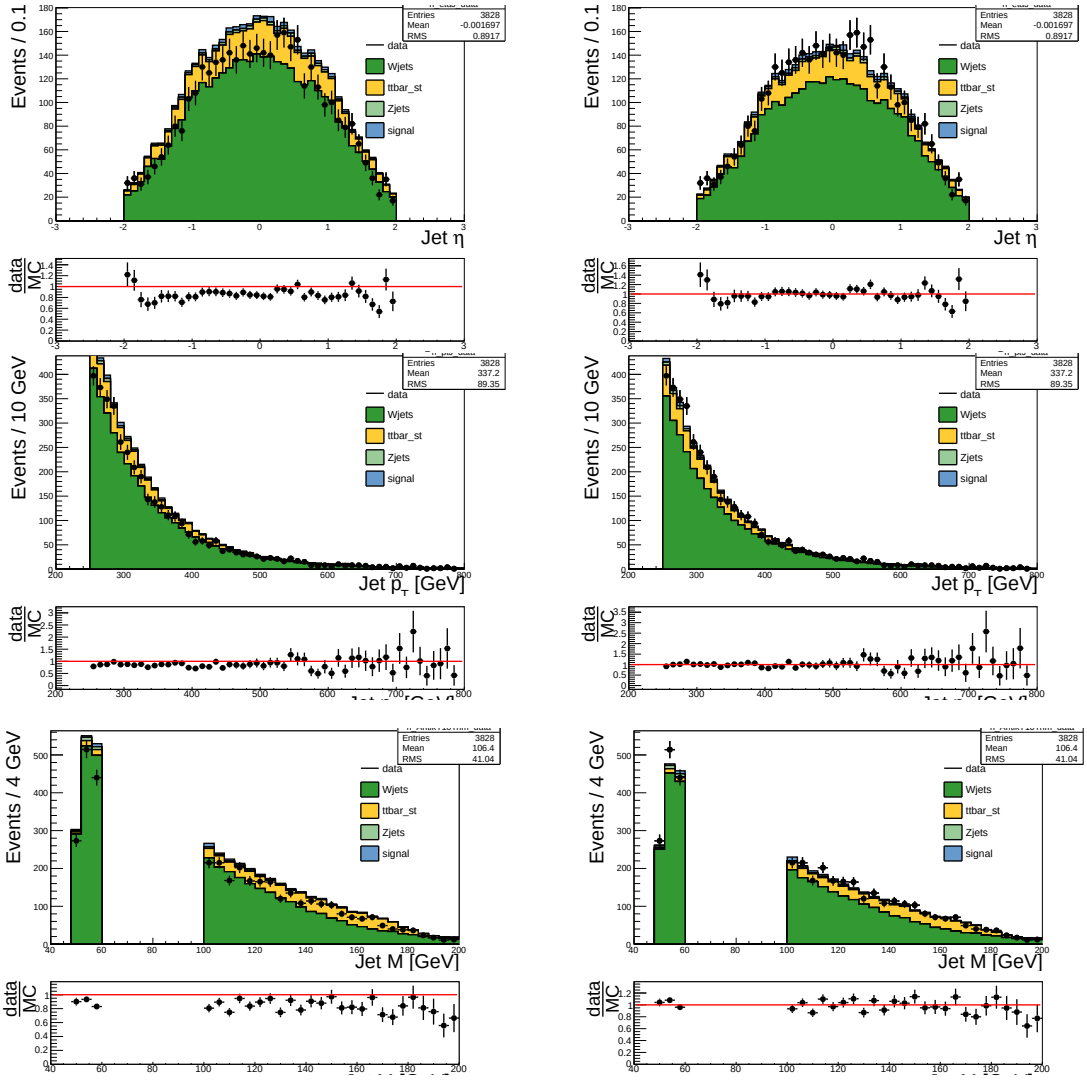

(a) before reweighting **(b)** after reweighting

Figure 7.22.: Boosted analysis distributions before and after applying reweighting in the $m_J < 60 \,||\, m_J > 100$ GeV control region, shown in the combined electron and muon channel. Statistical uncertainties are shown.

7.5.4. Charge Subtraction Modelling

At the LHC, W+jets production is mostly initiated from quark-quark interactions. As a consequence, one would expect a higher production rate for positively charged W bosons, compared to negatively charged.

This charge asymmetry can be exploited to cross-check the Monte Carlo modelling of the W+jets against data. We can look at the difference between the number of events with positive and negative leptons,

$$\Delta N = N^{+} - N^{-} . \tag{7.1}$$

The beneit of calculating this charge difference is that most other processes passing the event selection, such as the multijet background, are expected to give rise to equal numbers of positive and negative leptons, thus leaving the charge difference highly dominated by W+jets events, and providing a high-purity sample with which to check the modelling.

This comparison is shown in figure 7.23 for the resolved and figure 7.24 boosted analyses. We see that the charge-difference is indeed dominated by the W+jets background. The charge-subtracted plots confirm that the W+jets background is well-modelled, with agreement of at least 10% in both cases.

7.6. Overlap Removal between the Two Regimes

It is essential to keep the resolved and boosted regimes orthogonal, to ensure that no single event is analysed for both channels. A list of event numbers is printed for the both analyses, and any event that is seen to pass the event selections in both regimes is directly removed from the boosted analysis. This results in a loss of 37 signal events, around 18% of the total, and around 367 background events, around 14% of the total, from the boosted regime.

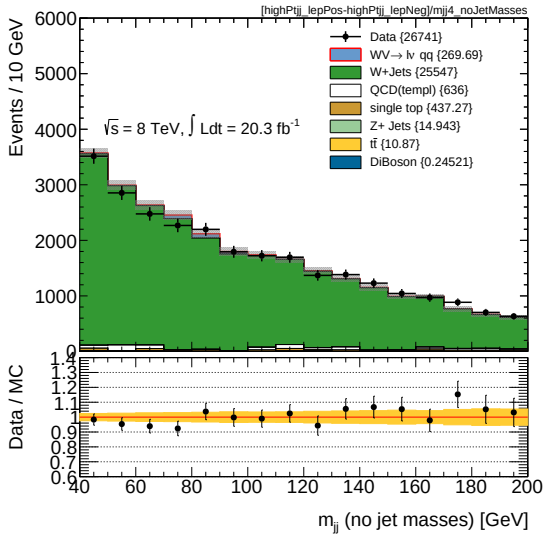

Figure 7.23.: Comparison between data and Monte Carlo simulations for events in the resolved analysis signal region, after the charge subtraction procedure.

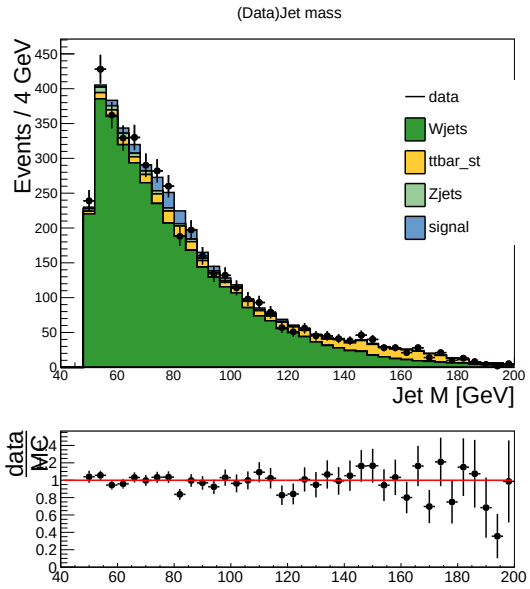

Figure 7.24.: Comparison between data and Monte Carlo simulations for events in the boosted analysis signal region, after the charge subtraction procedure.

Chapter 8.

Evaluation of Systematic Uncertainities

In this chapter, we will consider the sources of systematic uncertainty on the background and signal samples discussed in chapter 7. These systematic uncertainties are included as parameters in the fit for the cross-section measurement and procedure for setting limits on the anomalous triple gauge couplings. The methodology for including these systematic uncertainties within the statistical fits is discussed in section 9.1.6 for the cross-section fit, and section 9.3.1 for the limit setting procedure.

Systematic uncertainties may affect both the shape and normalisation of our Monte Carlo templates. In both cases, the systematic uncertainties are included as nuisance parameters within the fit. To evaluate the systematic uncertainties, we produce new Monte Carlo templates by running the analysis code under varied conditions. In each case, we produce two templates, representing the variations of $\pm 1\sigma$ within the constraints of the systematic uncertainty, and compare these to the nominal template.

In the case of the V+jets background (in both the resolved and boosted analyses), and the top contributions (in the boosted analysis), the uncertainties are allowed only to vary the template shape, because the normalisation is left as a floating factor within the fit.

It is necessary to smooth some of the systematic uncertainties, in order to reduce the impact of statistical fluctuations due to limited numbers of Monte Carlo generated events, thereby avoiding the problems of overfitting. However, inevitably

the smoothing adds a layer of arbitrariness to the evaluation of the uncertainties so it is only applied when necessary to stabilise the fit. The steps used to apply the smoothing procedure are:

1. Average the $\pm 1\sigma$ variations, or symmetrise one-sided uncertainties;
2. Smooth the varied templates. This requires us to:
    - Normalise the varied templates to same integral as the nominal template;
    - Smooth the ratio of the varied templates and nominal template using the 353QH algorithm [146] in 3 passes;
    - Produce a second iteration with 4 passes;
    - Multiply the nominal histogram by the smoothed ratio;
    - Normalise the smoothed, varied templates back to the original normalisation.

In the following sections, when smoothing is applied to the systematic uncertainty, each plot showing the effect of the systematic contains the original distribution with a dashed line and the final, smoothed distribution with a solid line. Statistical errors in the original distribution are shown by a yellow band around zero. A full list of systematic uncertainties is given in table 8.1. The details of these systematic uncertainties are explained in the following sections.

8.1. Uncertainties on Physics Objects

Each of the object types reconstructed (electrons, muons, jets and missing transverse energy) in the analysis carry systematic uncertainties, associated with their kinematic variables, identification, reconstruction or triggering. In both the resolved and boosted analyses, those systematic uncertainties associated with jet measurements are found to be greater than those associated with lepton measurements.

- **Electrons**
  Sources of uncertainty associated with electrons arise from the efficiency correction factors, associated with the reconstruction and identification of the electron,

Systematic uncertainty	Type	components	topology
Luminosity	N	1	RB
Physics Objects			
electron energy scale/resolution	SN	4	RB
electron efficiency(reco/ID/iso/trig)	N	4	RB
muon momentum scale/res	SN	3	RB
muon efficiency (reco/trig)	N	2	RB
Small-radius Jet energy scale/resolution	SN	18	RB
Large-radius Jet energy scale/resolution	SN	2	B
Large-radius Jet mass scale/resolution	SN	2	B
Large-radius Jet W-tagging uncertainty	SN	1	B
Jet vertex fraction	SN	1	RB
E_T^{miss} scale/resolution	SN	2	RB
Background Model			
V+jets: scale variations	S	3	RB
V+jets: parton shower	S	1	RB
V+jets: generator	S	1	RB
V+jets: data-reweighting	S	2	RB
W/Z ratio	S	1	RB
$t\bar{t}$ cross-section	N	1	RB
$t\bar{t}$ modelling: generator	SN	1	RB
$t\bar{t}$ modelling: parton shower	SN	1	RB
$t\bar{t}$ modelling: ISR/FSR	SN	1	RB
single-top cross-section (single-top/$t\bar{t}$ ratio)	SN	1	RB
Multijet normalisation	N	2	R
Multijet shape	S	3	R
ZZ cross-section	N	1	R
Signal Model			
$W + V$: scale variations	SN	2	RB
$W + V$: generators	SN	2	RB
$W + V$: PDF	SN	1	RB

Table 8.1.: Sources of systematic uncertainty. The column labelled "Type" specifies whether the uncertainties affect only the normalisation (N), shape (S) or both (SN) for affected processes. Some of the uncertainties are split into several components for a more accurate treatment, indicated under the column labelled "Components". The final column denotes whether the uncertainty affects the resolved (R), boosted (B) or both (RB) topologies.

as well as the electron trigger and the isolation of a single electron. We derive these uncertainties using the prescription described in [11]; these uncertainties are found to be of order a percent or lower in both analyses. In addition, there are uncertainties from the measurement of the electron energy scale and resolution, described in [11, 124]. These originate from uncertainty about the amount of material in the simulation, as compared to the true detector, as well as uncertainty in the sampling of the electromagnetic calorimeter. These uncertainties are also found to be of order a percent or lower. Figure 8.1 shows the total effect of the largest of the electron uncertainty components for the top, V+jets and signal templates, in the boosted and resolved channels.

- **Muons**

  Analogous sources of systematic uncertainty are associated with the muons. We associate uncertainties with the reconstruction and identification of the muon, as well as the muon trigger and isolation. There are also uncertainties associated with the measured muon energy scale and resolution, arising from uncertainties in the measurement from the muon spectrometer. We derive these uncertainties following the scheme prescribed in [126, 128]. Again, these uncertainties are found to be of order a percent or lower. Figure 8.1 shows the total effect of the largest of the muon uncertainty components for the top, V+jets and signal templates, in the boosted and resolved channels.

- **Small-radius jets**

  The evaluation of the uncertainty of the small-radius jet energy scales (JES) is taken from detailed studies using data and Monte Carlo samples, and involving uncertainties from many sources [120]. Jet response was studied with various theoretical conditions (such as the hadronic shower model), as well as detector configurations. Sources of uncertainty include the calorimeter energy scale, the description of dead material, the reconstruction of clusters, the modelling of fragmentation, the underlying event and pile-up, and the modelling of interactions between close-by jets, in a multijet environment. In total, there are 56 sources of uncertainty that enter the full jet energy scale uncertainty; however, many of these are correlated, and so this number can be reduced. We invoke a scheme comprising of 18 components for the JES uncertainties: 14 from the calorimeter, 3 from jet-flavour (especially pertaining to the modelling of heavy flavour quarks within the jets), 1 for punch-through.

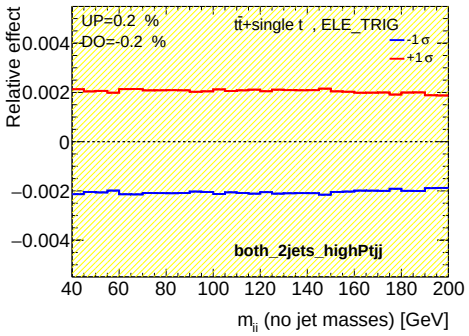

(a) ELE_TRIG uncertainty for top samples, resolved regime

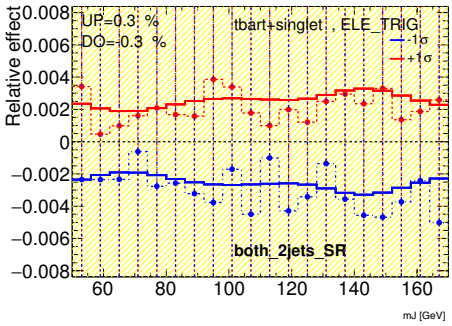

(b) ELE_TRIG uncertainty for top samples, boosted regime

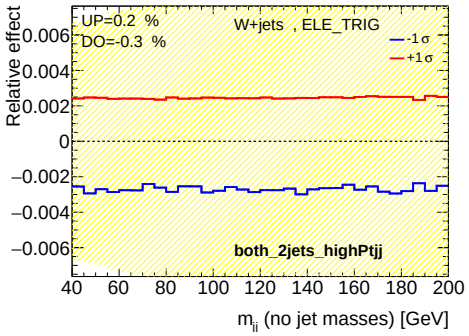

(c) ELE_TRIG uncertainty for V+jets samples, resolved regime

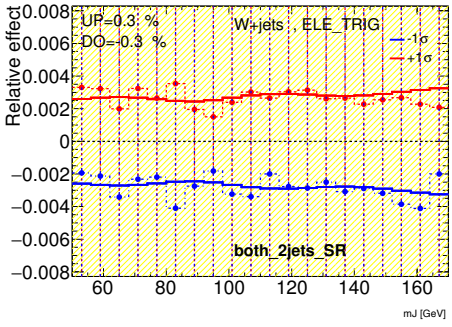

(d) ELE_TRIG uncertainty for V+jets samples, boosted regime

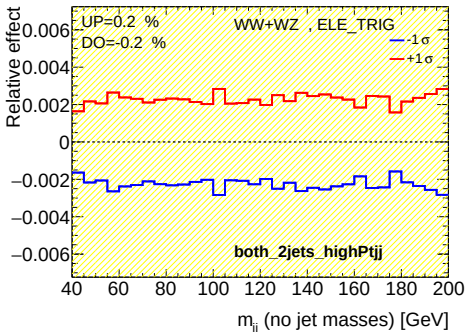

(e) ELE_TRIG uncertainty for signal samples, resolved regime

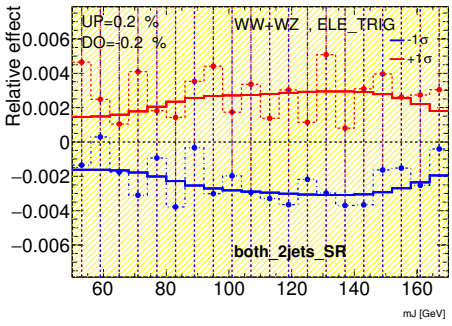

(f) ELE_TRIG uncertainty for siganl samples, boosted regime

Figure 8.1.: Relative effect of the electron uncertainties on the top, V+jets and signal templates, in resolved and boosted channels. Uncertainties are shown for the largest uncertainty component only (labelled ELE_TRIG) for the resolved regime and boosted regimes. The size of the statistical uncertainty is shown in yellow.

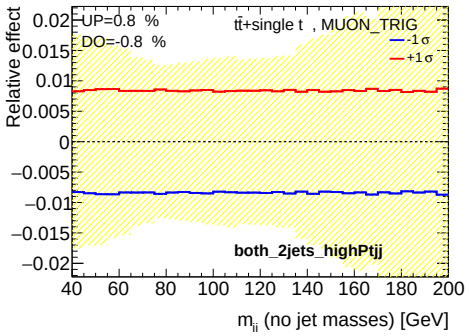

(a) MU_TRIG uncertainty for top samples, resolved regime

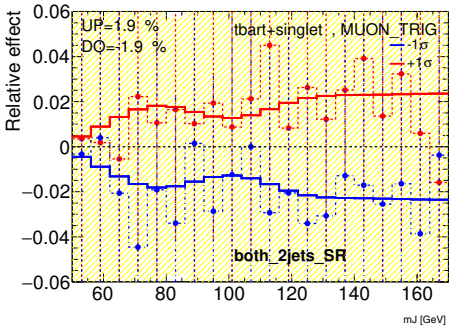

(b) MU_TRIG uncertainty for top samples, boosted regime

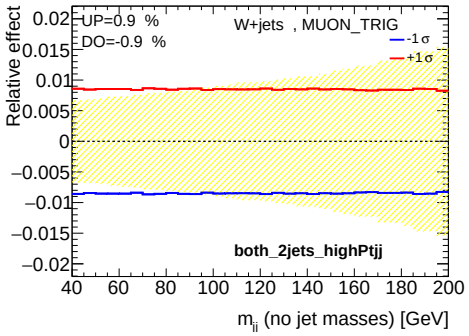

(c) MU_TRIG uncertainty for V+jets samples, resolved regime

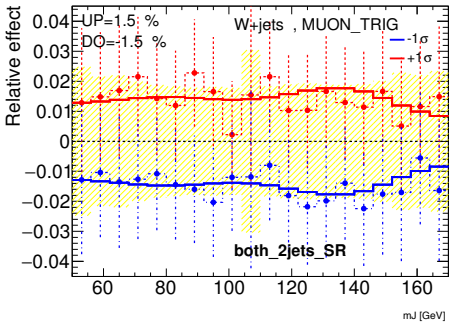

(d) MU_TRIG uncertainty for V+jets samples, boosted regime

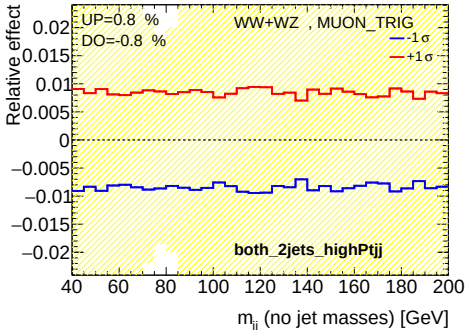

(e) MU_TRIG uncertainty for signal samples, resolved regime

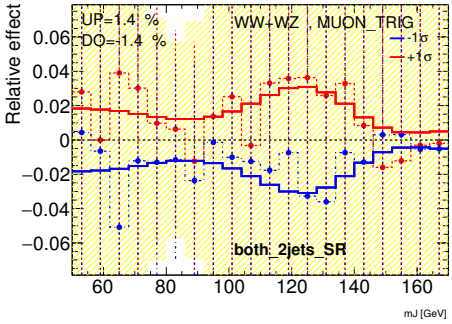

(f) MU_TRIG uncertainty for signal samples, boosted regime

Figure 8.2.: Relative effect of the muon uncertainties on the top, V+jets and signal templates, in the resolved and boosted channels. Uncertainties are shown for the largest uncertainty component only (labelled MU_TRIG) for the resolved regime a ndboosted regimes. The size of the statistical uncertainty is shown in yellow.

The jet energy resolution uncertainty is applied as a symmetric Gaussian smearing to the jet energies. It is also propagated to the calculation of E_T^{miss}.
The total uncertainty on the energies of small-radius jets ranges from around 3-5%, depending on the jet p_T and η. The total effect of the uncertainties on small-radius jets is proportionally greater in the resolved analysis, where small-radius jets are used to capture the hadronic boson decay; however, they are still important in the boosted analysis, where they are relevant for the jet veto. Figure 8.3 shows the total effect of the largest of the small-radius jet uncertainty components for the top, V+jets and signal templates, in the boosted and resolved channels.

- **Large-radius jets**
  In the boosted analysis, three measured quantities are used from the large-radius jets, each resulting in a particular source of systematic uncertainty. A cut at 250 GeV is employed on the transverse momentum of the jet, to define the boosted analysis phase space; we perform boson-tagging cut on the variable $D_2^{\beta=1}$; and we use the jet mass distribution itself as the input to the fit.

  We take uncertainties on these measurements from a study of boosted boson tagging [97], following from a method proposed in [6]. Consider some particular variable, p (for example, it could be the jet mass, p_T, or $D_2^{\beta=1}$). We define the single ratio as the ratio of p, measured using topolcusters from the calorimeter, against the same variable measured using tracks from the inner detector,

$$\text{single ratio } S_p = \frac{p_{\text{calo jet}}}{p_{\text{track jet}}} \quad . \tag{8.1}$$

  We define the double ratio as the ratio of the single ratios found using data and Monte Carlo simulations,

$$\text{double ratio } D_p = \frac{S_p^{\text{data}}}{S_p^{\text{MC}}} \, . \tag{8.2}$$

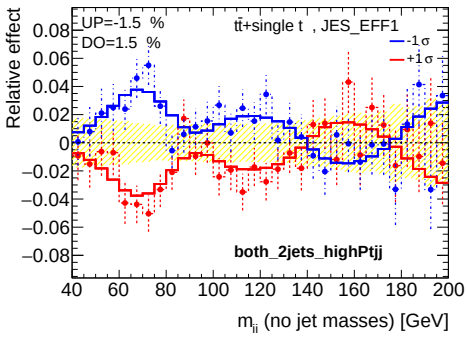

(a) JES1 uncertainty for top samples, resolved regime

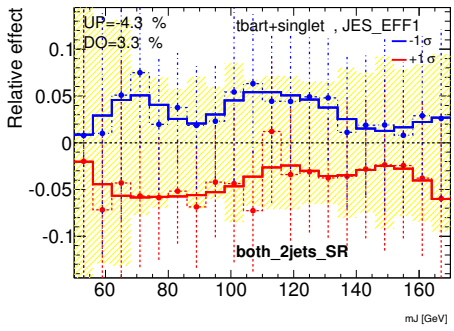

(b) JES1 uncertainty for top samples, boosted regime

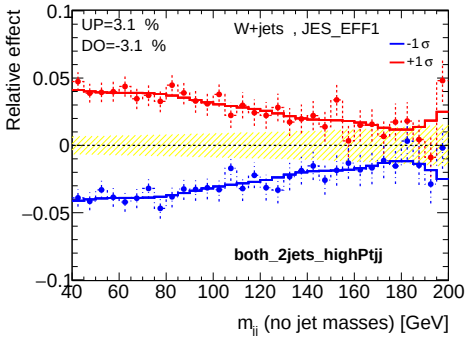

(c) JES1 uncertainty for V+jets samples, resolved regime

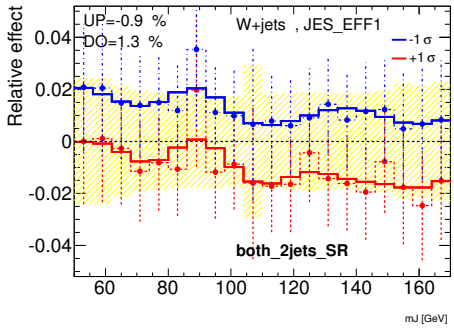

(d) JES1 uncertainty for V+jets samples, boosted regime

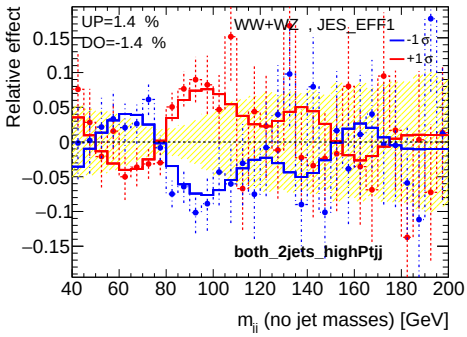

(e) JES1 uncertainty for signal samples, resolved regime

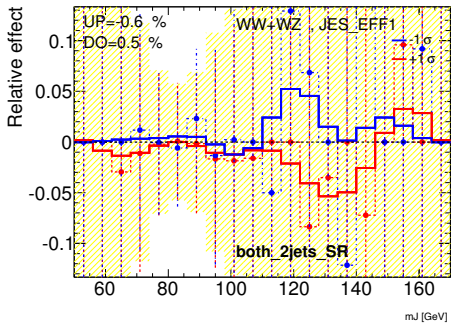

(f) JES1 uncertainty for siganl samples, boosted regime

Figure 8.3.: Relative effect of the small-radius jet uncertainties on the top, V+jets and signal templates, in the boosted channel. Uncertainties are shown for the largest uncertainty component only (labelled JES1), in the resolved and boosted regimes. The size of the statistical uncertainty is shown in yellow.

We obtain the uncertainties from these double ratios. In effect, we compare the same object, measured in two separate detector subsystems; a comparison of the two measurements can elucidate any systematic mis-modelling that takes place in the Monte Carlo. We make two main assumptions in this approach. First, we assume that the the systematic uncertainties associated with the tracking measurements will be essentially uncorrelated with those associated with the calorimeter. Second, we assume that any theoretical uncertainties (such as in the parton showering model), will affect the track and calorimeter measurements in a fully correlated way, so the effects will then cancel in the ratio. However, there is no inherent assumption that either the track jet properties or calorimeter jet properties are better measured than the other.

The estimation of the systematic uncertainties is taken as the maximum deviation from unity, for various Monte Carlo models, considered in [97], and weighted by the statistical uncertainty in each bin. The estimated uncertainty, δ, is given by,

$$\begin{aligned} \delta^{MC} &= \frac{\sum_{\text{bins}} w_{\text{bin}}(D_p - 1)}{\sum_{\text{bins}} w_{\text{bin}}} \\ \delta &= \max\left[\delta_1^{MC}, \delta_2^{MC}, \cdots, \delta_N^{MC}\right], \end{aligned} \tag{8.3}$$

where N is the number of Monte Carlo samples, and δ_i^{MC} is the weighted uncertainty for the ith Monte Carlo sample. For the uncertainties derived in [97], two Monte Carlo generators were considered, PYTHIA and HERWIG++.

This uncertainty must be added in quadrature with an uncertainty associated with the tracking component. In order to evaluate the latter, tracks are randomly removed from the set of track jets, according to the probability that they are missed, and a ratio is taken to data [147]. Figure 8.4 shows the total effect of these three systematics for the top, V+jets and signal templates.

Scale variations on the jet mass and tagging variable are found to be large. The uncertainty on jet energy resolution and mass resolution are not directly measured; however, studies of the W boson mass peak observed in high transverse momentum samples of events containing a $t\bar{t}$ indicate that the resolution is

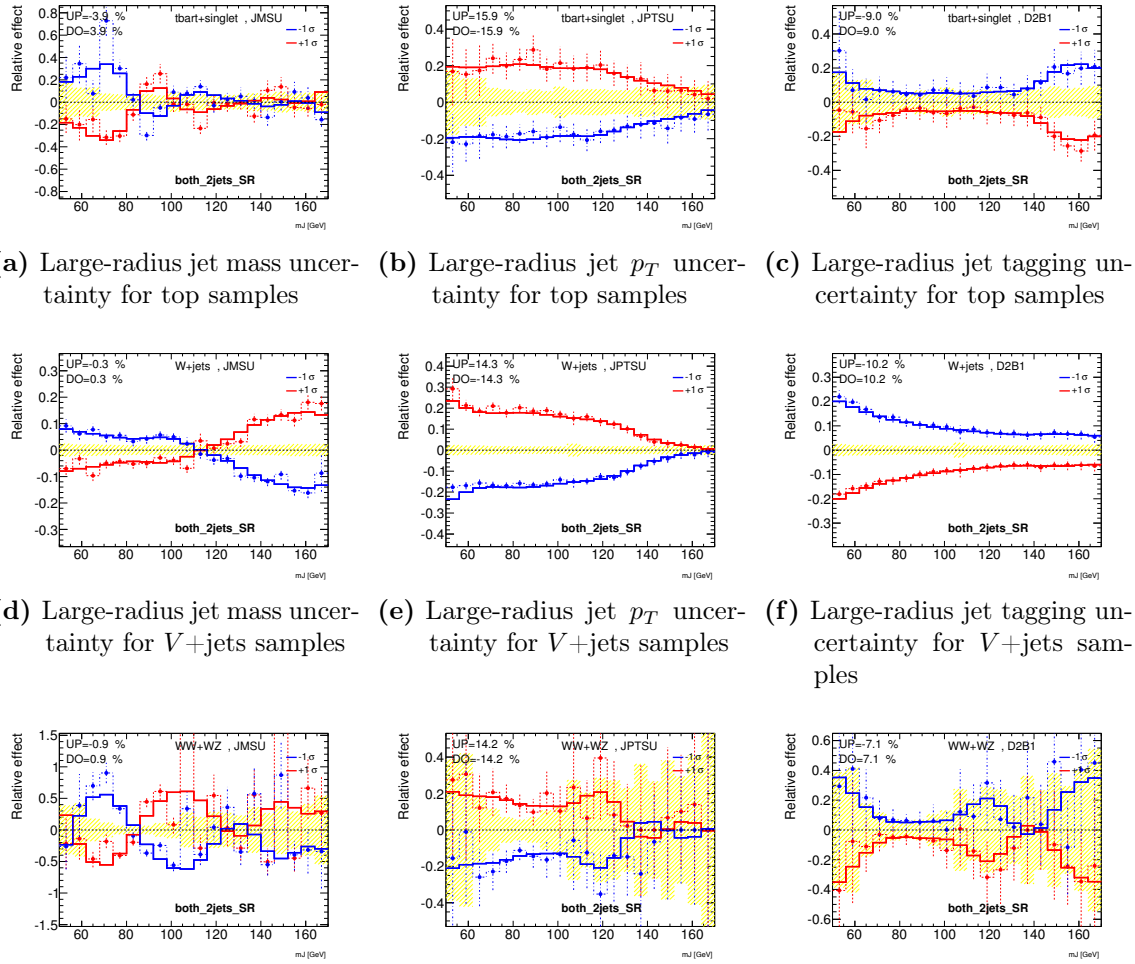

(a) Large-radius jet mass uncertainty for top samples **(b)** Large-radius jet p_T uncertainty for top samples **(c)** Large-radius jet tagging uncertainty for top samples

(d) Large-radius jet mass uncertainty for V+jets samples **(e)** Large-radius jet p_T uncertainty for V+jets samples **(f)** Large-radius jet tagging uncertainty for V+jets samples

(g) Large-radius jet mass uncertainty for signal samples **(h)** Large-radius jet p_T uncertainty for signal samples **(i)** Large-radius jet tagging uncertainty for signal samples

Figure 8.4.: Relative effect of the large-radius jet uncertainties on the top, V+jets and signal templates, in the boosted channel. Uncertainties are shown for the jet mass scale, the jet p_T scale and the $D_2^{\beta=1}$ tagging variable of the large-radius jet. The size of the statistical uncertainty is shown in yellow.

well-described by Monte Carlo simulation; estimated resolution uncertainties are found to be signficiantly lower than a percent [97].

- **Jet vertex fraction**

  The jet vertex fraction, discussed in section 7.3.3, is used to distinguish jets arising from the hard-scatter from those originating in pile-up. The inputs for the JVF algorithm are reconstructed tracks, jets, and primary vertices. Uncertainties are taken from studies of the variation of the measured jet p_Ts

with the number of primary vertices and the level of pile-up, $\Delta^{\partial p_T}/_{\partial NPV}$ and $\Delta^{\partial p_T}/_{\partial \langle \mu \rangle}$. The uncertainties were taken as the maximal differences between simulated dijet, photon+jet and Z+jet events and data was evaluated [148].

- **Missing Transverse energy**
  The derivation of the uncertainties on the missing transverse energy scale and resolution is analagous to the treatment for the small-radius jet uncertainties. For the resolution uncertainty, a Gaussian smearing is applied to the evaluated E_T^{miss}; the variance of the smearing is taken from independent studies of $Z \to \mu\mu$ processes in which no genuine E_T^{miss} is expected [129]. The uncertainties are calculated without applying smearing to the other physics objects. We assume that the scale and resolution uncertainties are uncorrelated.

8.2. Uncertainties from Normalisation and Modelling

- ***V*+jets samples**
  For the V+jets processes, we consider uncertainties arising from the data-driven correction factors, described in section 7.5.3, as well as variation of the Monte Carlo generator parameters and comparisons between other generators. The W+jets and and Z+jets processes are treated together, and considered correlated due to the similarity of the processes and the fact that we use the same Monte Carlo generators in both cases.

  We include the full effects from the data-driven reweighting as a source of systematic uncertainties. The uncertainties arising from the reweighting are treated independently. The reweighting with resepct to p_T had minimal effect, whereas the reweighting with respect to $\Delta\phi jj$ in the resolved channel introduced a signficiant uncertainty.

  We also make comparisons with other Monte Carlo generators to estimate the theoretical uncertainties on the V+jets samples. To estimate uncertainties on the modelling of the parton showering, we compare samples generated with Alpgen, interfaced with Pythia to samples generated with Alpgen, interfaced with Herwig. We also consider an additional uncertainty, from comparison

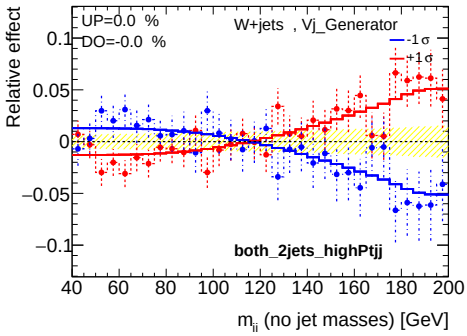

(a) V+jets Generator uncertainty, resolved channel

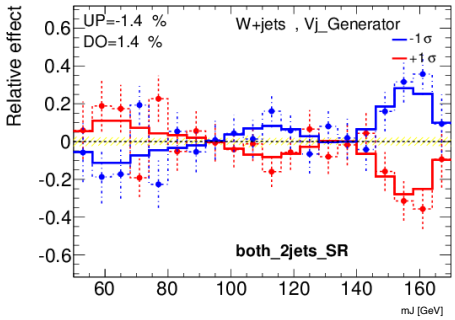

(b) V+jets Generator uncertainty, boosted channel

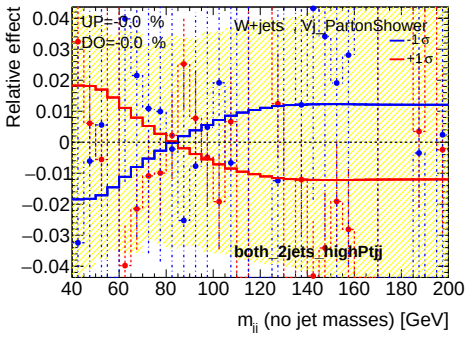

(c) V+jets PS uncertainty, resolved channel

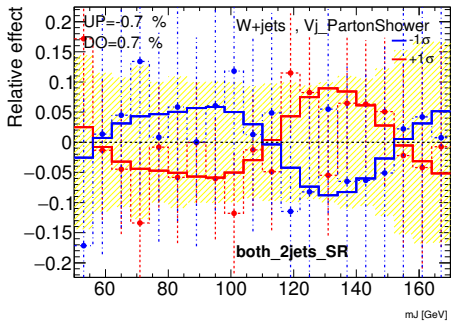

(d) V+jets PS uncertainty, boosted channel

Figure 8.5.: Relative effect of the generator uncertainties on the V+jets template for the resolved and boosted channels. The size of the statistical uncertainty is shown in yellow.

of the residual difference between the nominal Sherpa samples against the Alpgen+Pythia samples. Due to a bug in the generated Alpgen samples, the phase space corresponding to $0.4 < \Delta R < 0.7$ in η–ϕ between the partons was incorrectly modelled. To correct for this, the samples were reweighted to the Sherpa $\Delta R(jj)$ distribution, where j refers to the two selected jets in the resolved channel, and to the two highest p_T subjets within the selected large-radius jet in the boosted channel. Figure 8.5 shows the size of these generator uncertainties for each channel.

The Monte Carlo generation of the V+jets samples is dependent on many parameters. These include the factorisation scale, renormalisation scale and CKKW matching scale, each of which carries a systematic uncertainty. To estimate these uncertainties, vary each scale up and down by a factor of two. We produce truth-level samples for each variation, and pass these through the event

selection for the fiducial phase space described in section 9.1.2. We pass the nominal samples through the same event selection. We then apply the difference between each varied template and the nominal to the reconstruction-level nominal templates, under the reasonable assumption of a strong resemblance between the reconstruction-level and truth-level templates. Figure 8.6 shows size of these systematic uncertainties in the boosted and resolved channels.

- **Top samples**
  The uncertainty on the dominant $t\bar{t}$ template normalisation, amounting to 6%, is obtained from the most precise theoretical cross-section calculation [9]. We apply a conservative estimate of 10% for the templates for samples with a single top quark, combining together all single-top processes.

  In addition, we consider uncertainties on the Monte Carlo modelling $t\bar{t}$ processes. To estimate uncertainties from the parton shower modelling, we compare the nominal sample generated with POWHEG interfaced with PYTHIA to an alternative sample, generated with POWHEG interfaced HERWIG. To estimate uncertainty on the matrix element calculated at NLO, we compare the POWHEG+HERWIG sample to a sample generated with MC@NLO, showered using HERWIG, and then apply this difference to the nominal template. To estimate the uncertainty from the modelling of initial and final state radiation, two samples were generated using POWHEG, interfaced with PYTHIA, with the amount of initial and final state radiation varied, and apply this difference to the nominal template. Figure 8.7 shows the size of the uncertainties in the boosted and resolved channels. The normalisation effects from modelling uncertainties are of the order of 5-8% and completely dominate over the detector effects.

- **Non-resonant multijet samples**
  This uncertainty is relevant only to the resolved analysis. We use two nuisance parameters to summarise the normalisation uncertainties of the multijet template, one for the electron and muon channels (which have independent data-driven estimates), with three more to implement shape variations within the template. The overall effect of these uncertainties is small.

- **ZZ production**
  The contribution from ZZ processes is small, so only a normalisation uncertainty of 30% is considered for this analysis. This number is conservative

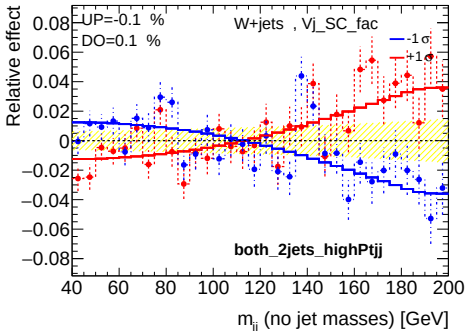

(a) fact. scale uncertainty, resolved channel

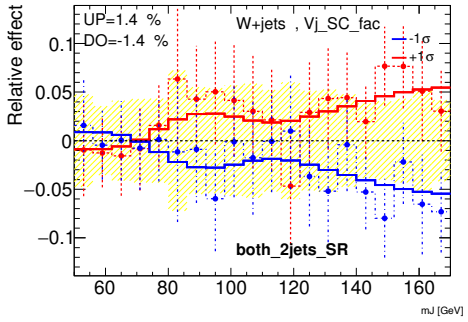

(b) fact. scale uncertainty, boosted channel

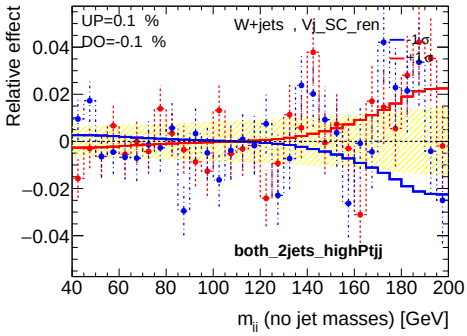

(c) ren. scale uncertainty, resolved channel

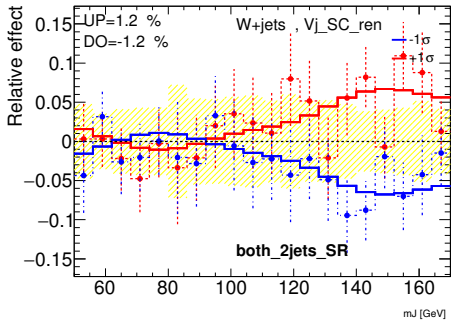

(d) ren. scale uncertainty, boosted channel

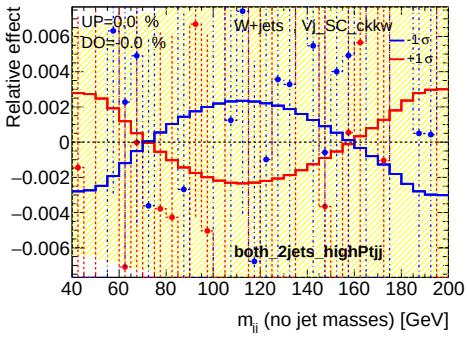

(e) matching scale, resolved channel

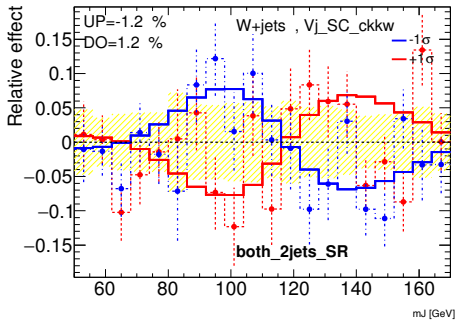

(f) matching scale, boosted channel

Figure 8.6.: Relative effect of the scale uncertainties systematic uncertainties on the W+jets template for the resolved and boosted channels. The size of the statistical uncertainty is shown in yellow.

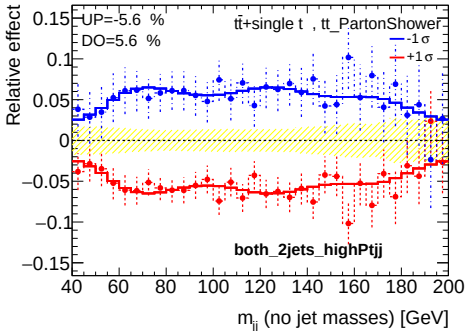

(a) PS uncertainty resolved

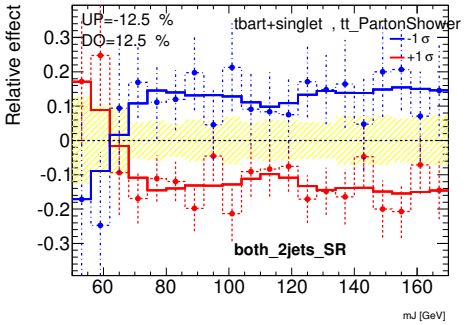

(b) PS uncertainty boosted

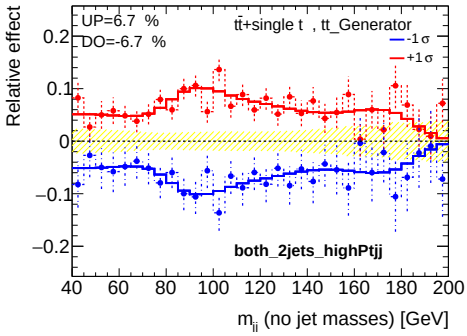

(c) NLO uncertainty resolved

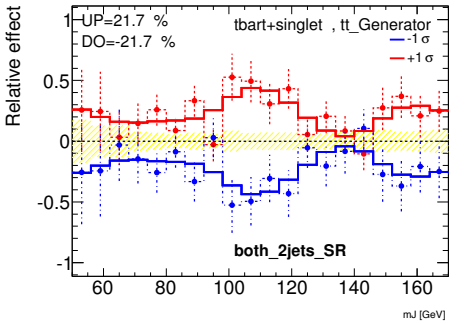

(d) NLO uncertainty boosted

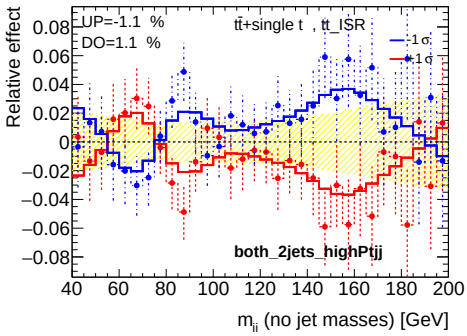

(e) IFSR uncertainty resolved

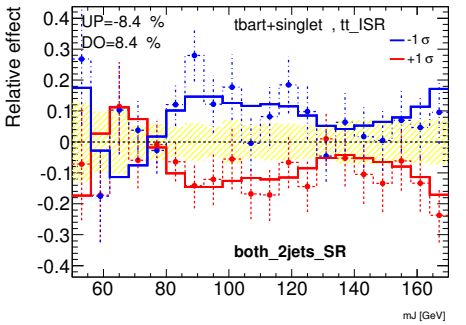

(f) IFSR uncertainty boosted

Figure 8.7.: Relative effect of the modelling systematic uncertainties on the $t\bar{t}$+single top templates. "PS" refers to the uncertainty from the parton shower modelling, "NLO" refers to the uncertainty from the modelling of next-to-leading order contributions. "ISFR" refers to the uncertainty from modelling the effects of initial and final state radiation. The size of the statistical uncertainty is shown in yellow.

enough to cover theoretical uncertainties on the inclusive cross-section and the extrapolation of these uncertainties to the signal region.

- **Signal modelling**
  The generation of the signal samples using the MC@NLO generator depends on the choice of renormalisation and factorisation scales, each of which carries a systematic uncertainty. To estimate these uncertainties, we generate samples with the parameters varied by a factor of 2 and $1/2$. The effect on these scale variations was found to be negligible compared to other sources of uncertainty.

  To consider the uncertainties from the Monte Carlo generator, we generated samples of signal events with POWHEG+PYTHIA8 and SHERPA. The three generators differ in the matrix element implementation, as well as in the parton shower and hadronisation models. Moreover, whilst MC@NLO only generates on-shell bosons with the zero decay width approximation, PYTHIA and SHERPA correctly take into account the natural decay width of massive bosons. The POWHEG sample lacks some of the WZ decay channels ($l\nu\nu\nu$ and $l\nu ll$), and so the effects of the Sherpa against Powheg comparison is only considered as a source of uncertainty on the dominant WW component of the signal. Figure 8.8 demonstrates the effects of the systematic variations on the signal templates.

Table 8.2 provides of the sizes of the normalisation effects for some of the main uncertainties for the considered resolved analysis. Table 8.3 provides of the equivalent information for the boosted analysis. However, the V+jets normalisation is freely floating in the final cross-section fit, so its normalisation uncertainty is not directly relevant to the cross-section measurement. The signal uncertainties are also given, although the normalisation uncertainties are not directly implemented in the fit for the cross-section measurement.

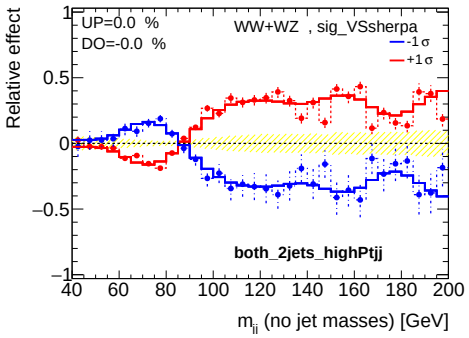

(a) MC@NLO v.s. Sherpa resolved

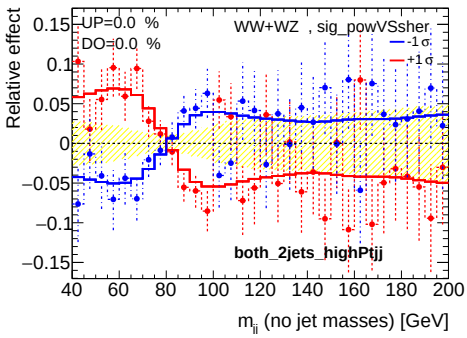

(b) Powheg v.s. Sherpa resolved

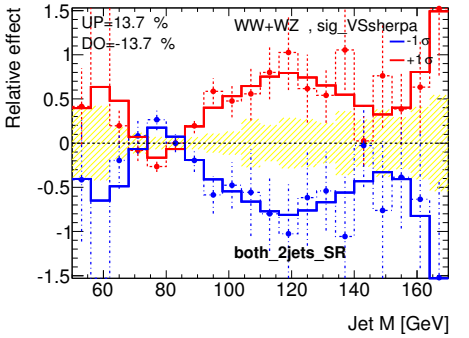

(c) MC@NLO v.s. Sherpa boosted

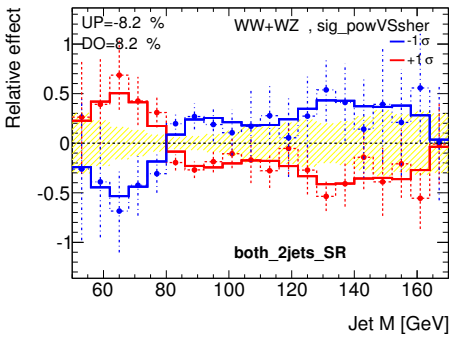

(d) Powheg v.s. Sherpa boosted

Figure 8.8.: Relative effect of the generator uncertainties on signal templates, for the boosted and resolved regimes. Uncertainties are derived from a comparison between the nominal textscMC@NLO simulated samples against SHERPA and POWHEG samples against SHERPA. The size of the statistical uncertainty is shown in yellow.

sample	WW+WZ	V+jets	$t\bar{t}$+single t	Multijet
stat.	0.7 %	0.2 %	0.3 %	1.6 %
ELE_ID	0.5 % / -0.5 %	-0.5 % / 0.5 %	0.4 % / -0.4 %	–
ELE_ISO	0.2 % / -0.2 %	0.2 % / -0.2 %	-0.2 % / 0.2 %	–
ELE_RES	-0.2 % / 0.2 %	0.0 % / -0.0 %	0.0 % / -0.0 %	–
ELE_SF_PS	0.1 % / -0.1 %	0.0 % / -0.0 %	0.0 % / -0.0 %	–
ELE_SF_R12	0.6 % / -0.6 %	0.0 % / -0.0 %	0.1 % / -0.1 %	–
ELE_SF_Zee	0.2 % / -0.2 %	-0.1 % / 0.1 %	0.0% / -0.0 %	–
ELE_TRIG	0.4 % / -0.4 %	0.2 % / -0.3 %	0.2 % / -0.2 %	–
JER	-0.4 % / 0.4 %	-2.3 % / 2.3 %	-0.0 % / 0.0 %	–
JES_AF2NC	-0.0% / 0.0%	-0.3 % / 0.3 %	1.4 % / -1.4 %	–
JES_EFF1	-1.4% / 1,4 %	-3.1 % / -3.1 %	-1.5 % / 1.5 %	–
JES_EFF2	0.5 % / -0.5 %	0.5 % / -0.5 %	0.7 % / -0.7 %	–
JES_EFF3	-0.6 % / 0.6 %	-0.5 % / 0.5 %	-0.6 % / 0.6 %	–
JES_EFF4	0.4 % / -0.4 %	0.4 % / -0.4 %	0.4 % / -0.4 %	–
JES_EFF5	0.5 % / -0.5 %	0.2 % / -0.2 %	0.2 % / -0.2 %	–
JES_EFF6	0.2 % / -0.2 %	-0.3 % / 0.3 %	-0.1 % / 0.1 %	–
JES_ETAModel	0.5 % / -0.5 %	-0.6 % / 0.6 %	-0.3 % / 0.3 %	–
JES_ETAStat	-0.5 % / 0.5 %	-0.7 % / 0.7 %	-0.5 % / 0.5 %	–
JES_OFFMU	1.8 % / -1.8 %	0.1 % / -0.1 %	0.2 % / -0.2 %	–
JES_OFFPT	-1.8 % / 1.8 %	0.2 % / -0.2 %	0.2 % / -0.2 %	–
JES_PUPT	-0.4 % / 0.4 %	0.4 % / -0.4 %	0.3 % / -0.3 %	–
JES_PURHO	0.7 % / -0.7 %	-1.9 % / 1.9 %	-0.0 % / 0.0 %	–
JVF	0.1 % / -0.1 %	0.5 % / -0.3 %	0.9 % / -0.9 %	–
MUON_ID	0.1 % / -0.1 %	0.1 % / -0.1 %	0.3 % / -0.3 %	–
MUON_RESID	0.4 % / -0.4 %	0.0 % / -0.0 %	0.1 % / -0.1 %	–
MUON_RESMS	0.4 % / -0.4 %	0.0 % / -0.0 %	0.0 % / -0.0 %	–
MUON_SCALE	-0.2 % / 0.2 %	0.1 % / -0.5 %	0.0 % / -0.0 %	–
MUON_TRIG	0.8 % / -0.8 %	0.9 % / -0.9 %	0.8 % / -0.8 %	–
QCD_COMB	–	–	–	28.9 % / -28.9 %
Vj_Generator	–	-0.3 % / 0.3 %	–	–
Vj_PartonShower	–	-0.1 % / 0.1 %	–	–
Vj_SC_ckkw	–	5.0 % / -0.4 %	–	–
Vj_SC_fac	–	3.0 % / -1.4 %	–	–
Vj_SC_ren	–	48.6 % / -26.7 %	–	–
sig_VSsherpa	-0.2 % / 0.2 %	–	–	–
sig_powVSsher	-15.0 % / 15.0 %	–	–	–
tt_Generator	–	–	6.7 % / -6.7 %	–
tt_ISR	–	–	-2.1 % / 2.1 %	–
tt_PartonShower	–	–	-5.6 % / 5.6%	–
total sys	15.4 %	49.2 %	9.5 %	28.9 %

Table 8.2.: Effect of the main systematic uncertainties for all the samples in the resolved analysis. The V+jets normalisation is freely floating in the final cross-section fit, so its normalisation uncertainty is not directly relevant to the cross-section measurement. The signal uncertainty in this table gives the uncertainty on the prediction, but this does not affect the cross-section measurement.

sample	WW+WZ	V+jets	$t\bar{t}$+single t
stat.	3.0 %	0.5 %	1.7 %
D2B1	-7.1 % / 7.1 %	-10.2 % / 10.2 %	-9.0 % / 9.0 %
ELE_ID	0.4 % / -0.4 %	-0.6 % / 0.6 %	0.4 % / -0.4 %
ELE_ISO	0.2 % / -0.2 %	-0.2 % / 0.2 %	-0.1 % / 0.1 %
ELE_RES	-0.2 % / 0.2 %	-0.1 % / 0.1 %	0.2 % / -0.2 %
ELE_SF_PS	0.1 % / -0.1 %	0.0 % / -0.0 %	0.0 % / -0.0 %
ELE_SF_R12	0.2 % / -0.2 %	0.1 % / -0.1 %	0.1 % / -0.1 %
ELE_SF_Zee	0.3 % / -0.3 %	-0.1 % / 0.1 %	0.1% / -0.1 %
ELE_TRIG	0.4 % / -0.4 %	0.3 % / -0.3 %	0.3 % / -0.3 %
JER	-1.0 % / 1.0 %	-2.2 % / 2.2 %	-1.7 % / 1.7 %
JES_AF2NC	0.1 % / -0.1 %	0.5 % / -0.5 %	0.6 % / -0.6 %
JES_EFF1	-0.6 % / 0.6 %	-1.2 % / 1.2 %	-3.9 % / 3.9 %
JES_EFF2	0.3 % / -0.3 %	0.9 % / -0.9 %	1.4 % / -1.4 %
JES_EFF3	0.1 % / -0.1 %	-0.5 % / 0.5 %	-0.6 % / 0.6 %
JES_EFF4	0.1 % / -0.1 %	0.4 % / -0.4 %	0.6 % / -0.6 %
JES_EFF5	0.2 % / -0.2 %	0.5 % / -0.5 %	0.6 % / -0.6 %
JES_EFF6	0.2 % / -0.2 %	-0.2 % / 0.2 %	-0.1 % / 0.1 %
JES_ETAModel	0.1 % / -0.1 %	-0.5 % / 0.5 %	-1.0 % / 1.0 %
JES_ETAStat	-0.2 % / 0.2 %	-0.6 % / 0.6 %	-0.9 % / 0.9 %
JES_OFFMU	0.4 % / -0.4 %	0.3 % / -0.3 %	0.4 % / -0.4 %
JES_OFFPT	0.1 % / -0.1 %	0.4 % / -0.4 %	0.3 % / -0.3 %
JES_PUPT	-0.1 % / 0.1 %	0.3 % / -0.3 %	0.3 % / -0.3 %
JES_PURHO	-0.7 % / 0.7 %	-1.0 % / 1.0 %	-2.8 % / 2.8 %
JES_SinglePart	0.1 % / -0.1 %	0.4 % / -0.4 %	0.6 % / -0.6 %
JMSU	-0.9 % / 0.9 %	-0.3 % / 0.3 %	-3.9 % / 3.9 %
JPTSU	14.2 % / -14.2 %	14.3 % / -14.3 %	15.9 % / -15.9 %
JVF	0.2 % / -0.2 %	0.5 % / -0.5 %	1.0 % / -1.0 %
MUON_ID	-0.1 % / 0.1 %	-0.1 % / 0.1 %	-0.4 % / 0.4 %
MUON_RESID	0.4 % / -0.4 %	0.0 % / -0.0 %	0.1 % / -0.1 %
MUON_RESMS	0.2 % / -0.2 %	0.0 % / -0.0 %	0.0 % / -0.0 %
MUON_SCALE	-0.4 % / 0.4 %	0.3 % / -0.3 %	0.2 % / -0.2 %
MUON_TRIG	0.9 % / -0.9 %	1.0 % / -1.0 %	0.9 % / -0.9 %
Vj_Generator	–	-1.4 % / 1.4 %	–
Vj_PartonShower	–	-0.7 % / 0.7 %	–
Vj_SC_ckkw	–	-1.2 % / 1.2 %	–
Vj_SC_fac	–	17.1 % / -14.1 %	–
Vj_SC_ren	–	4.5 % / -4.5 %	–
sig_VSsherpa	13.7 % / -13.7 %	–	–
sig_powVSsher	-8.2 % / 8.2 %	–	–
tt_Generator	–	–	21.7 % / -21.7 %
tt_ISR	–	–	-8.4 % / 8.4 %
tt_PartonShower	–	–	-12.5 % / 12.5 %
total sys	23.6 %	27.1 %	35.6 %

Table 8.3.: Effect of the main systematic uncertainties for all the samples in the boosted analysis. The V+jets normalisation is freely floating in the final cross-section fit, so its normalisation uncertainty is not directly relevant to the cross-section measurement. The signal uncertainty in this table gives the uncertainty on the prediction, but this does not affect the cross-section measurement.

Chapter 9.

Cross-section Measurement and Limit-Setting on Anomalous Triple Gauge Couplings

In this chapter, we discuss the methodology and results for the cross-section fit and limit-setting on aTGCs, for the analysis explained in chapter 7. We implement the sources of systematic uncertainty, detailed in chapter 8 into these fits. The fitting procedures are based on frequentist methods. Appendix B provides a glossary of the statistical terminology used.

9.1. Cross-section Defitions and Fitting Procedure

9.1.1. Fiducial Cross-Section Definition

We measure the fiducial cross-section, i.e. the cross-section in the fiducial phase space. The fiducial phase space is defined precisely in section 9.1.2. The fiducial cross-section is given by,

$$\sigma_{\text{fid}} = \frac{N_{\text{obs}}}{\mathscr{L} \cdot D_{\text{fid}}}\,, \tag{9.1}$$

where $\mathscr{L}$ represents the integrated luminosity and D_{fid} gives a factor to correct for the difference between the number of $WV \to l\nu qq$ events produced in the fiducial phase space compared to the number of reconstructed events that passes the event selection. A full definition of D_{fid} is given in section 9.1.3. Correction by D_{fid} will account for false positives (events that pass the event selection but which do not originate as truth $WV \to l\nu qq$ events), but not for true negatives (truth $WV \to l\nu qq$ events that are rejected at some point in the event selection).

We do not attempt to extrapolate the fiducial cross-section to the total cross-section in this analysis.

9.1.2. Fiducial Volume Definitions

We define the fiducial phase space by applying a selection as close as possible to the analysis selection described in section 7.4 to truth particle level objects. There are two separate fiducial volumes for the two channels: resolved and boosted. As explained in section 7.6, when performing the limit-setting, these two channels are designed to be completely orthogonal, by directly removing those events which are found to pass the boosted event selection from the resolved channel.

The fiducial phase space requires a WV event, in which the V decays hadronically and the W decays leptonically, to $e\nu$ or $\mu\nu$. We exclude events that contain a decay to $\tau\nu$ from the fiducial phase space; however, such decays will still contribute to measured 'signal' events if they pass the reconstruction level cuts; this is taken into account through the calculation of D_{fid} in section 9.1.3.

For the leptonic decay, we require exactly one truth-level electron or muon with a $p_T > 30$GeV and and $\mid \eta \mid < 2.47$ in both the resolved and boosted channels. The lepton p_T is obtained by summing together the lepton transverse momentum and the transverse momenta of all photons within $\Delta R = 0.1$ in η–ϕ of the selected lepton and not produced by hadron decays. We require the truth E_T^{miss}, calculated by considering all non-interacting particles, to be greater than 40 GeV. In the resolved channel, we also require the transverse mass of the leptonically decayed W boson, calculated from the truth lepton p_T and the E_T^{miss} to be greater than 40 GeV.

For the hadronic decay, for the resolved channel we require precisely two particle level jet of radius 0.4 with $p_T > 25$ GeV and $\mid \eta \mid < 2.5$. Jets that lie within $\Delta R = 0.2$

in η–ϕ of a selected lepton are discarded. Subsequently, leptons that are within $\Delta R = 0.4$ of a remaining jet are discarded. Finally, the two selected jets, the lepton and the E_T^{miss} are required to satisfy the following requirements:

$$\begin{aligned} \Delta\phi(j_1, E_T^{\text{miss}}) &> 0.8 \\ \Delta\eta(j,j) &< 1.5 \\ p_T(j,j) &> 100 \text{ GeV} \\ p_T(l, E_T^{\text{miss}}) &> 100 \text{ GeV} \\ m_{jj} &\epsilon [40, 200] \text{ GeV}\,. \end{aligned} \tag{9.2}$$

For the boosted, channel, we require exactly one particle level jet of radius 1.0, trimmed with parameters $R_{\text{sub}} = 0.3$ and f_{cut} at 5%, and with $p_T > 250$ GeV and $|\eta| < 2.0$. Anti-$k_\perp$ jets of radius 0.4, with $p_T > 25$ GeV and $|\eta| < 2.5$ that lie within $\Delta R = 0.2$ in η–ϕ of a selected lepton are discarded. Subsequently, leptons that are within $\Delta R = 0.4$ of a remaining jet are discarded. Finally, we discard events with remaining anti-$k_\perp$ jets of radius 0.4 that do not overlap the selected large-radius jet by $\Delta R = 0.8$.

The fiducial phase space definitions are summarised in table 9.1.

9.1.3. Calculation of D Factors

The diboson fiducial cross-sections in the resolved and boosted topologies are extracted using the number of observed events in each channel. We use factors D_{fid}^R and D_{fid}^B, in the resolved and boosted channels respectively, to account for the fact that the two processes, $WW \to l\nu jj$ and $WZ \to l\nu jj$, will contribute to the total signal yield by different amounts, due to the different process cross-sections, acceptances, and correction factors. We define the D_{fid} factors by

$$D_{\text{fid}} = f^{WW} \cdot C^{WW} + (1 - f^{WW}) \cdot C^{WZ}\,, \tag{9.3}$$

$W \to l(e,\mu)\nu$ **selection**	
Must contain a $W \to (e,\mu)\nu$ decay	
Exactly one e or μ with $p_T > 30$ GeV and $\mid \eta \mid < 2.47$	
$E_T^{\text{miss}} > 40$ GeV	
resolved:	**boosted:**
$M_T > 40$ GeV	
hadronic W/Z **selection**	
Must contain an hadronically decayed W or Z	
resolved:	**boosted:**
Exactly 2 selected jets (R=0.4)	Exactly 1 selected large-radius jet (R=1.0)
with $p_T > 25$GeV and $\lvert\eta\rvert < 2.5$	with $p_T > 250$GeV and $\lvert\eta\rvert < 2.0$
lepton-jet overlap removal	lepton-jet overlap removal
$\Delta\phi(j_1, E_T^{\text{miss}}) > 0.8$	Exactly 0 veto jets (R=0.4)
$\Delta\eta(j,j) < 1.5$	
$p_T(j,j) > 100$ GeV	
$p_T(l, E_T^{\text{miss}}) > 100$ GeV	
40 GeV $< m_{jj} <$ 200 GeV	50 GeV $< m_J <$ 170 GeV
Overlap removal with boosted channel	

Table 9.1.: Summary of the fiducial volume definition in the resolved channel. All the specified selections are applied at the truth-particle level as specified in the text.

where f^{WW} is the ratio of the WW process cross-section to the total cross-section of $WW + WZ$:

$$f^{WW} = \frac{\sigma_{WW} \cdot BR^{WW}_{l\nu qq} \cdot A^{WW}}{\sigma_{WW} \cdot BR^{WW}_{l\nu qq} \cdot A^{WW} + \sigma_{WZ} \cdot BR^{WZ}_{l\nu qq} \cdot A^{WZ}} \,. \tag{9.4}$$

A^{WV} is the acceptance within the fiducial phase space, which was defined in section 9.1.2. A^{WV} is given by

$$A^{WV} = \frac{N^{WV}\ [WV \to l\nu qq \text{ in Fiducial space}]}{N^{WV}\ [WV \to l\nu qq]}\,. \tag{9.5}$$

C^{WW} is the ratio of N_{exp}, the expected number of signal events measured at detector level, estimated from Monte Carlo, to the number of truth-level $WV \to l\nu qq$ events, where V may be a W or Z boson, within the defined fiducial phase space, given by

$$C^{WW} = \frac{N_{\text{exp}}}{N^{WV}\ [WV \to l\nu qq \text{ in Fiducial space}]}\,. \tag{9.6}$$

As explained in section 7.1, we make no attempt to distinguish between the two processes, $WW \to l\nu jj$ and $WZ \to l\nu jj$. We assume that the ratio between the cross-sections in equation (9.5) follows the prediction of the Standard Model, calculated using MC@NLO.

The D factors for the two channels, D^R_{fid} and D^B_{fid}, are given in Table 9.2.

9.1.4. Theoretical Fiducial Cross-Section

Finally, we can calculate the theoretical cross-section, defined in the fiducial phase space, using values for the acceptance from table 9.2 and the Standard Model branching ratios. We calculate the fiducial cross-section separately in the resolved and boosted channels. The fiducial cross-section definition is given in equation (9.1.4) and the computed values were found to be 225 fb for the resolved analysis and 15.3 fb for the boosted analysis.

$$\sigma_{fid} \;=\; (\sigma_{qq\to WW} + \sigma_{gg\to WW}) \cdot BR^{WW}_{l\nu qq} \cdot A_{WW} + \sigma_{WZ} \cdot BR^{WZ}_{l\nu qq} \cdot A_{WZ} \tag{9.7}$$

Resolved Channel	Boosted Channel
***D* factors**	
$D^R_{\text{fid}} = 0.90 \pm 0.04(\text{stat})$	$D^B_{\text{fid}} = 0.86 \pm 0.10(\text{stat})$
C factors	
$C^{WW} = 0.90 \pm 0.02(\text{stat})$	$C^{WW} = 0.88 \pm 0.4(\text{stat})$
$C^{WZ} = 0.91 \pm 0.04(\text{stat})$	$C^{WZ} = 0.82 \pm 0.9(\text{stat})$
Acceptance and f^{WW}	
$f^{WW} = 0.84 \pm 0.03(\text{stat})$	$f^{WW} = 0.83 \pm 0.09(\text{stat})$
$A^{WW} = 0.0114 \pm 0.0002(\text{stat})$	$A^{WW} = 0.000775 \pm 0.00004(\text{stat})$
$A^{WZ} = 0.0124 \pm 0.0004(\text{stat})$	$A^{WZ} = 0.000815 \pm 0.00002(\text{stat})$

Table 9.2.: D_{fid} factors and the terms used for their computation. D_{fid} is computed separately for the resolved and boosted channels. Systematic uncertainties are evaluated recalculating the A^{WV}, C^{WV}, f^{WW} and D_{fid} factors for each systematic variation, as described in Chapter 8. Systematic uncertainties are then not evaluated separately for A^{WV}, C^{WV} and f^{WW} factors: the quoted uncertainties for these factors are statistical only.

where $l = e, \mu$.

9.1.5. Templates and Parameter of Interest

We measure the combined $WW+WZ$ signal yields by performing a binned maximum likelihood fit, separately in the resolved and boosted channels. Details of the fit are provided in section 9.1.6. The parameter of interest for the fit is the signal strength, μ, a multiplicative factor that we apply to the theoretical signal event yield;

$$N_{\text{obs}} = \mu N_{\text{theo}} \,, \tag{9.8}$$

where N_{obs} is is the measured signal event yield and N_{theo} is the expected signal yield predicted from the Standard Model.

In the resolved channel, we fit to the invariant mass distribution of the selected dijet system. In the boosted channel, we perform a fit to the mass of the selected large-radius jet. In both cases, we choose the variable that closest represents the invariant mass of the hadronically decaying W boson. T variable has been found to be the single most powerful variable for discrimination between the signal and the background.

We perform the fit over a much larger range than that of the signal peak (around 65-95 GeV in both analyses). In the resolved case, we fit over an invariant mass range between 40 and 200 GeV. In the boosted case, we fit over the mass range between 50 and 170 GeV. Fitting over these larger ranges allows for sidebands, nearly free of the signal, to constrain the range of the W+jets and top background processes. We allow a common scale factor for the W+jets and Z+jets normalisation to float freely in the fit. The templates for the fit arise either from the Monte Carlo simulation or from data-driven estimates in the case of the non-resonant multijet background, as detailed previously.

Because of the finite resolution of dijet and large-radius jet mass, in both analyses, there is considerable overlap between decays arising from W and from Z bosons, Given the expected uncertainties and the relatively small contribution from the WZ (of order 10% of the total signal yield in each channel), no effort is made to distinguish the WW and WZ results. Instead, we fix the ratio between the WW and WZ cross-sections to the Standard Model value.

We exploit the difference between the distribution shapes of the different background and signal processes to disentangle the signal from the large underlying background. Figure 9.1 shows the templates for each signal and background process.

9.1.6. Binned Maximum Likelihood Fit

As described in section 9.1.5, we determine the signal event yield in the fiducial-volume through a binned maximum likelihood fit to the m_{jj} and m_J distributions in the resolved and boosted channels respectively.

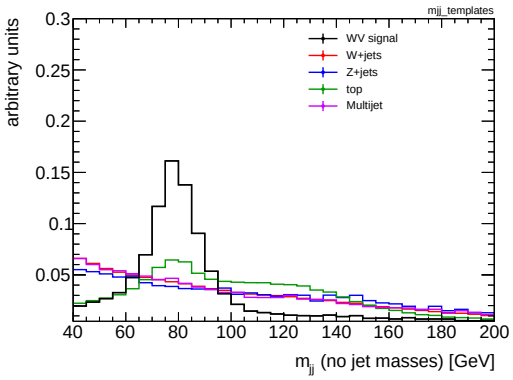

(a) Templates for all processes considered in the resolved analysis

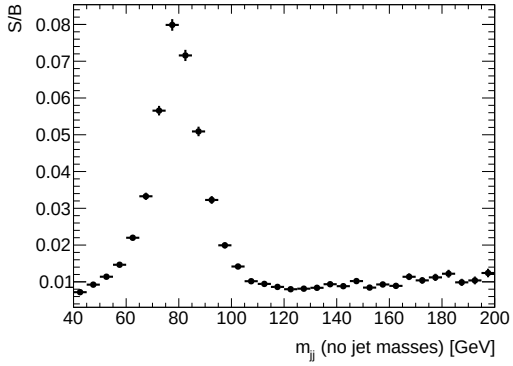

(b) Combined WV signal / total expected background for the resolved analysis

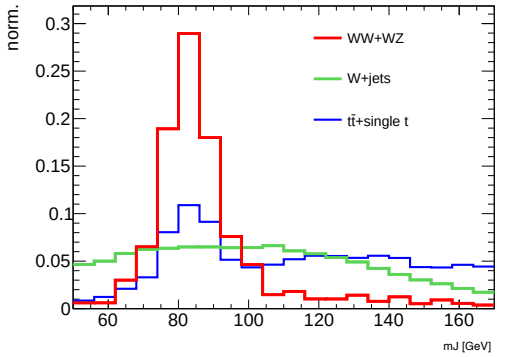

(c) Templates for all processes considered in the boosted analysis

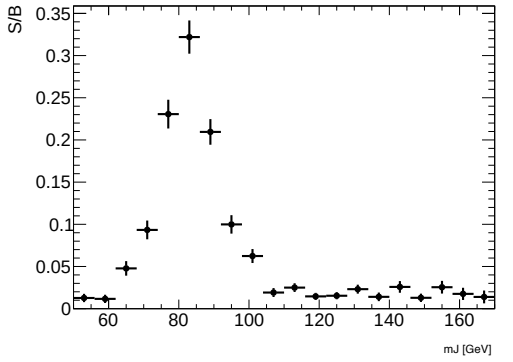

(d) Combined WV signal / total expected background for the boosted analysis

Figure 9.1.: Invariant mass nominal templates for candidates hadronically decayed bosons. The templates for WW/WZ, V+jets and top quarks production, are obtained from Monte Carlo simulations, while the multijet template is obtained using a data-driven method. All templates are normalised to unit area.

For the fit, we use a binned likelihood function, $L(\mu, \vec{\alpha})$, with the signal strength, μ, defined in equation (9.8) and α representing the nuisance parameters included to address the effects of systematic uncertainties. In each bin, b_k represents the expected number of background events, resulting from the sum of all of the background templates; s_k represents the number of signal events, resulting from the signal Monte Carlo samples.

To model the effect of the systematic uncertainties on the normalisation of the background samples, we write $N_i = N_i^{\text{nominal}} \prod \eta_{ij}$ for each background sample, i, where N_i is the sample normalisation for the ith background sample, N_i^{nominal} is the

normalisation before applying any variation from the uncertainties, and the scale factor η_{ij} represents the effect of the jth systematic of the ith background sample. η_{ij} will fluctuate with a Gaussian distribution of mean 1 and standard deviation σ_{ij}, estimated from the studies on the sources of the systematic uncertainties, described in Chapter 8.

To model the effect of systematic uncertainties on the shapes, we use an analagous approach. we must now evaluate σ_{ij} bin-by-bin to describe different shape variations in each different bin, k. This then leads to a likelihood function of the form,

$$L(\mu, \vec{\alpha}) = \prod_k \text{Poisson}(N_k^{\text{data}} | (b_k^{\text{bkg}} + \mu s_k^{\text{sig}})(\vec{\alpha})) \cdot \prod_p f_p(\alpha_p)\,, \tag{9.9}$$

where N_k^{data} is the measured number of data events in each bin, and f_p are Gaussian constraints on α_p, the p nuisance parameters.

We allow the V+jets and top Monte Carlo templates to float freely within this fit, whereas the normalisation of the other background templates are small and are treated as nuisance parameters. The parameters are left unconstrained in order to avoid any bias originating from prior assumptions on the Monte Carlo normalisation.

9.2. Fiducial Cross-sections Measurements

We can create estimates for the sensitivity of the analysis by performing a fit using an Asimov dataset (explained in Appendix B), built from the Monte Carlo simulations, defined such that the maximum likelihood estimators are set equal to the true values, following the methodology set out in [149].

From the Asimov datasets, we calculate an expected uncertainty on the signal strength, μ, of 24% in the resolved channel, and 47% for the boosted channel. We calculate a sensitivity of 5.1σ in the resolved channel and 2.3σ in the boosted channel.

Figure 9.2 shows the constraints on the nuisance parameters from the Asimov fit. In an Asimov fit, the central values of all nuisance parameters are definitionally 0. We introduce a ranking procedure to evaluate the relative importance of different sources

of systematic uncertainty (in which those nuisance parameters which have the biggest impact on the signal strength are ranked highest). This involves performing fits to the Asimov datasets for each nuisance parameter, in which we hold that nuisance parameter constant at $\pm 1\sigma$ whilst the others are allowed to vary. The ranking of the systematic uncertainties is shown in figure 9.3 for the resolved regime, and in figure 9.4 for the boosted regime.

In figure 9.5 we show comparisons of the data and Monte Carlo distributions before performing the fitting procedure, the m_{jj} distribution for the resolved channel, and the m_J distribution for the boosted channel. The full statistical and systematic uncertainties from section 8 are shown.

Performing the fit to the data in the resolved channel yields a signal strength of $\mu = 0.97 \pm 0.28$, corresponding to an observed significance of 4.45σ. In the boosted channel, the fit to the data yields a signal strength of $\mu = 0.49 \pm 0.31$, corresponding to an observed significance of 2.05σ. The results for the fits to Asimov data and real data are summarized in table 9.4. For each channel, the yields after the fit to the data are summarised in table 9.3.

	Resolved					
Sample	Signal	W+jets	top	Z+jets	non-resonant multijet	ZZ
Yield	3600	138400	16000	2790	3700	15
Uncertainty (±)	1000	1900	1700	280	1000	4
	Boosted					
Sample	Signal	V+jets	top			
Yield	205	2169	452			
Uncertainty (±)	90	300	100			

Table 9.3.: Yields after the fit to the data for all processes used in the analyses. The quoted uncertainties are the sum in quadrature of statistical and total systematic uncertainties on the yields, computed taking into account correlations among nuisance parameters and among processes.

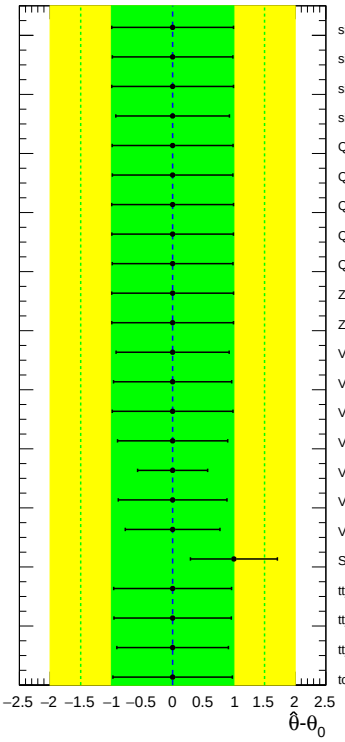

(a) modelling uncertainties in the resolved regime

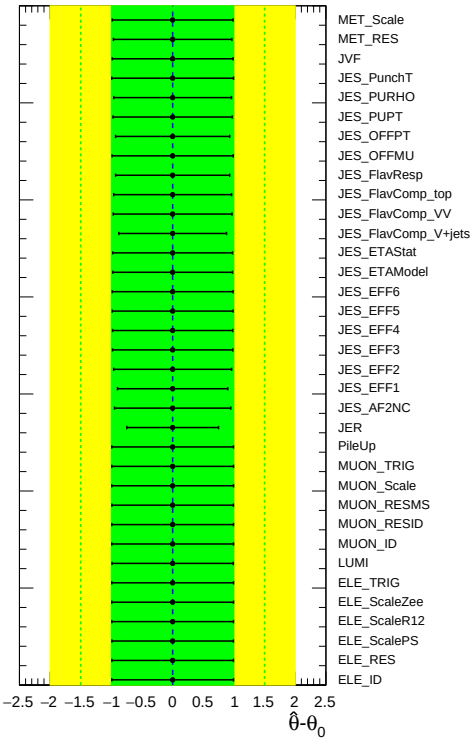

(b) detector uncertainties in the resolved regime

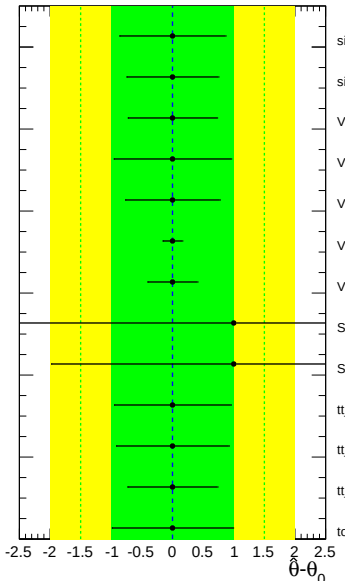

(c) modelling uncertainties in the boosted regime

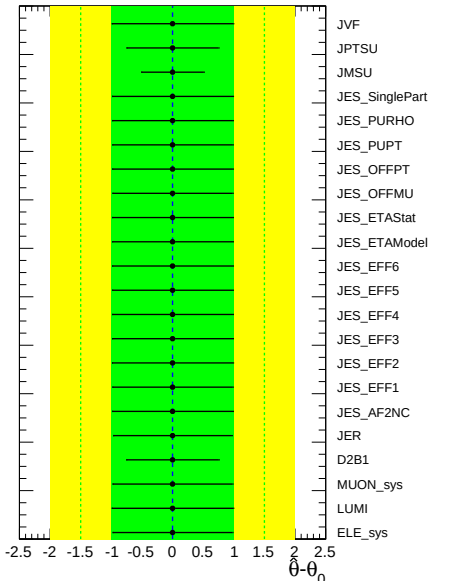

(d) detector uncertainties in the boosted regime

Figure 9.2.: Constraints on systematic uncertainties from fit to Asimov dataset, including uncertainties from background modelling and detector uncertainties, for the boosted and resolved regimes. The normalization factor on the V+jets template (labeled SF_SF_V+jets) is not a nuisance parameter in the fit, so the expected value is 1. The normalization factor is shown for demonstration purpose only. By definition, an Asimov fit gives pulls of zero for each nuisance parameter.

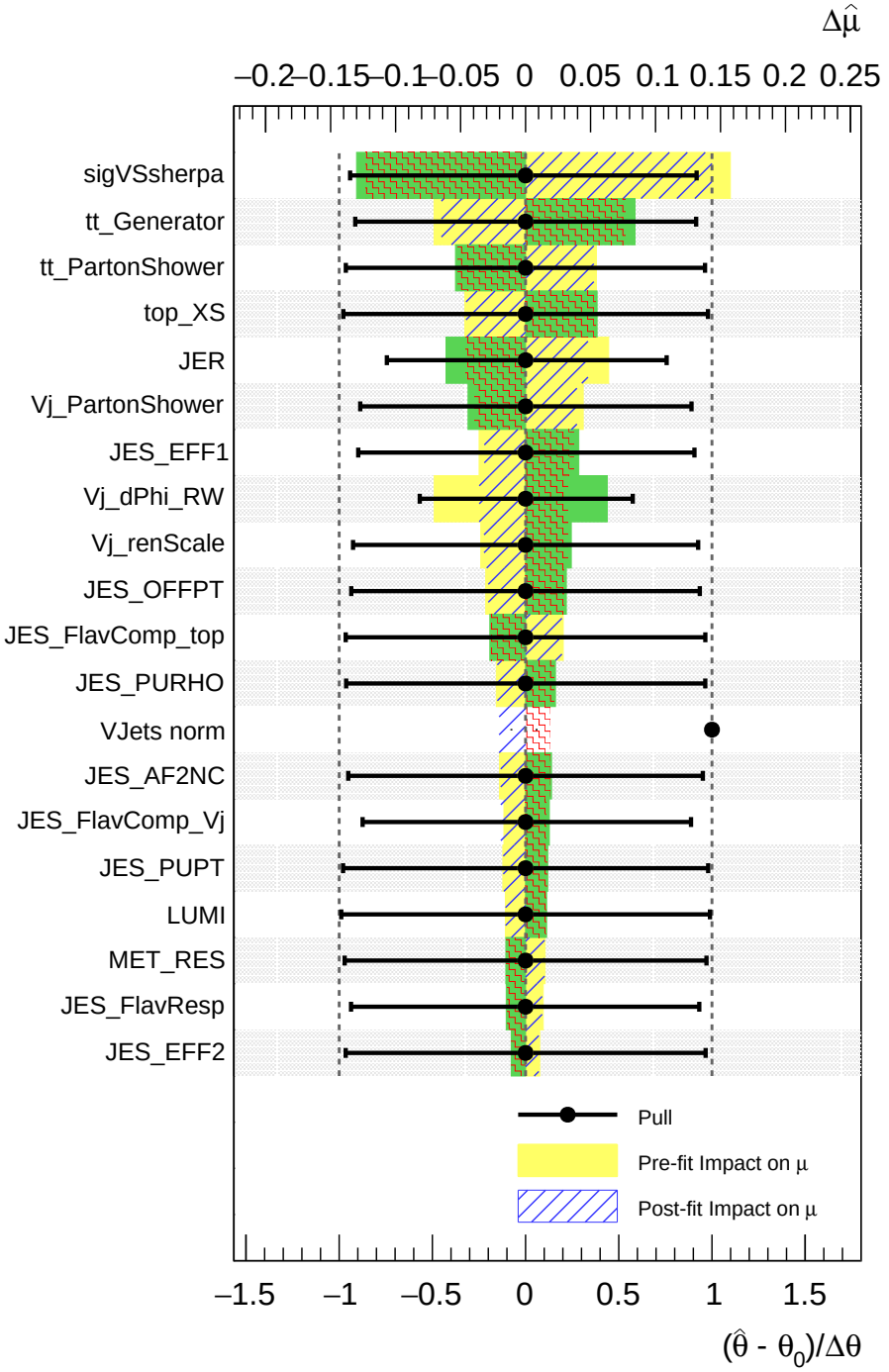

Figure 9.3.: Ranking of the systematic uncertainties for the fit to Asimov data in the resolved regime, with the largest uncertainties shown highest. The impact of each source of uncertainty on the measured signal efficiency is shown, before and after the fitting procedure, as well as the pulls on each nuisance parameter. The normalization factor on the V+jets template (labelled Vjets norm) is not a nuisance parameter in the fit, and so is set to unity.

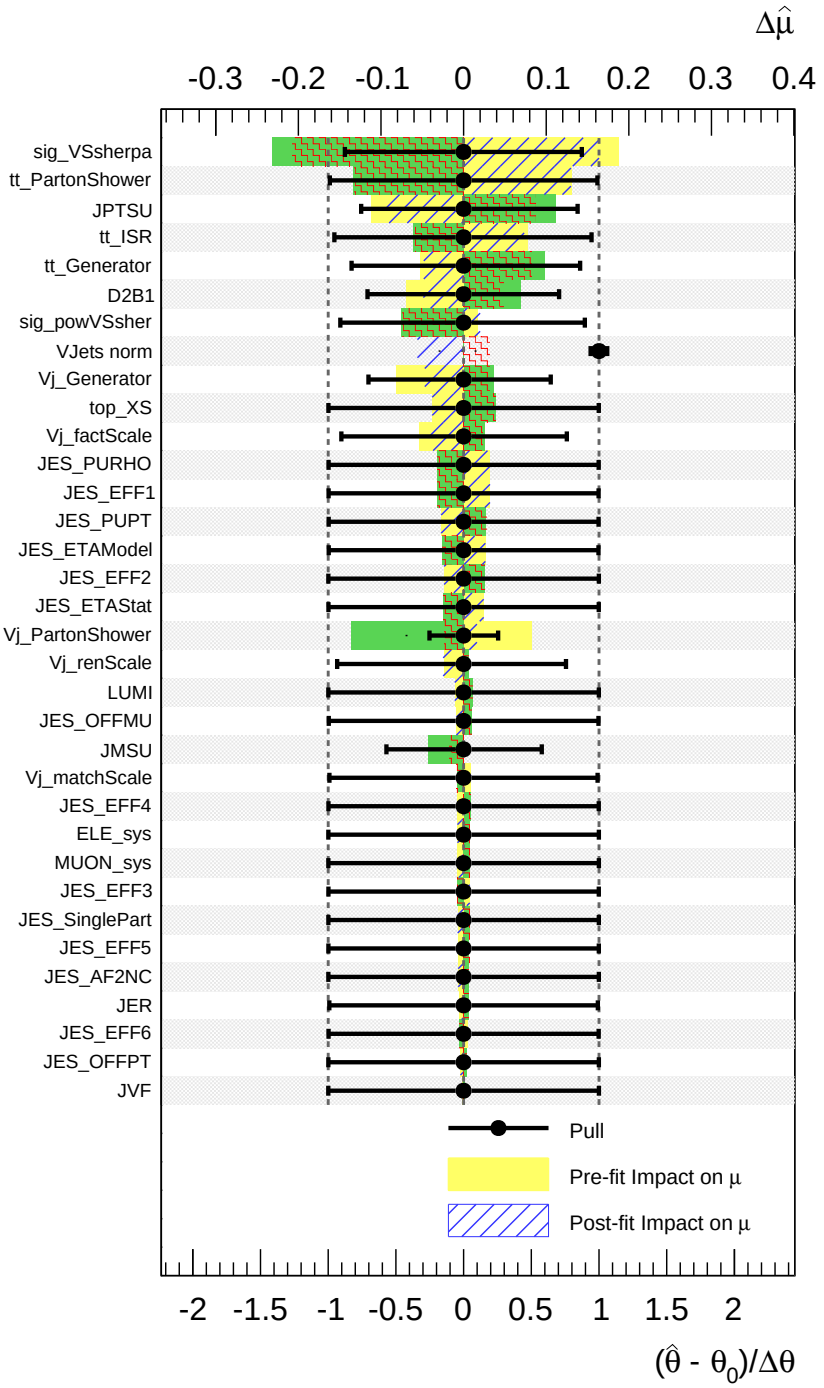

Figure 9.4.: Ranking of the systematic uncertainties for the fit to Asimov data in the boosted regime, with the largest uncertainties shown highest. The impact of each source of uncertainty on the measured signal efficiency is shown, before and after the fitting procedure, as well as the pulls on each nuisance parameter. The normalization factor on the V+jets template (labelled Vjets norm) is not a nuisance parameter in the fit, and so is set to unity.

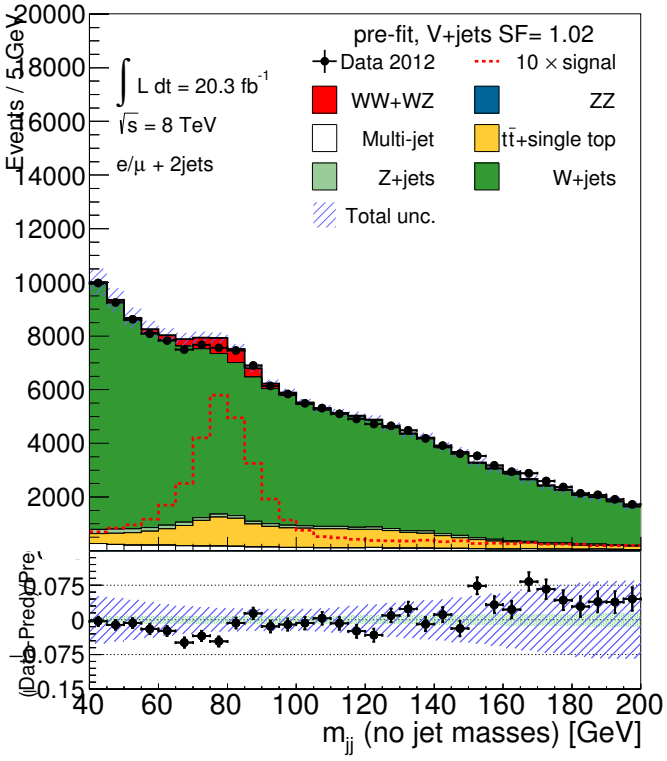

(a) Mass of the dijet system in the resolved regime

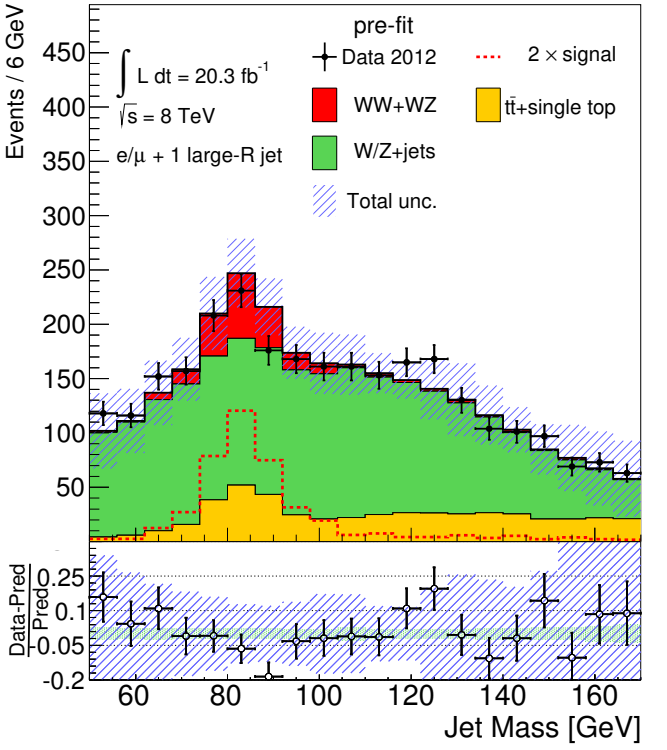

(b) Mass of the jet in the boosted regime

Figure 9.5.: Distributions of data and Monte Carlo events before performing the fit. Full statistical and systematic uncertainties are shown.

	Resolved		**Boosted**	
	Expected	Observed	Expected	Observed
μ	1	0.97	1	0.49
Error on μ	24%	28%	47%	63%
Significance	5.1σ	4.5σ	2.3σ	2.1σ

Table 9.4.: Results of the fits to Asimov and real data in the resolved and boosted channels. The errors shown are combined statistical and systematic errors.

Figure 9.6 shows the best-fit results for the nuisance parameters, for the resolved and boosted channels. We show two sets of fits; first are unconditional fits, in which we leave the signal strength, μ, floating; second are background-only hypothesis fits, in which we set the signal strength to $\mu = 0$. We see some small pulls on the nuisance parameters in the free-floating fits; however, the background-only hypothesis generates large pulls on the nuisance parameters associated with the top backgrounds. These pulls are needed to enhance the peak from real W bosons. Figure 9.7 shows the ranking of the systematic uncertainties with data in for the resolved regime, whilst figure 9.8 shows the ranking for the boosted regime.

We can also see that the fit generates correlations between the nuisance parameters, shown in figure 9.9.

Finally, figure 9.10 provides comparisons of the data and Monte Carlo distributions after performing the fitting procedure for the two different fits: after the unconditional fit, with μ free-floating, and after the conditional fit, with $\mu = 0$. The m_{jj} distribution for the resolved channel, and the m_J distribution for the boosted channel are shown for each fit. The full statistical and systematic uncertainties from section 8 are shown.

9.3. Limits on Anomalous Triple Gauge Couplings

We study the aTGC parameters,c_{WWW}/Λ^2, c_W/Λ^2, and c_B/Λ^2, in the effective field theory framework (discussed in section 2.4.3). aTGCs enhance the diboson cross-sections at high boson transverse momenta. Therefore, we calculate the limits from a binned maximum likelihood fit to the p_T of the dijet system in the resolved analysis, and to

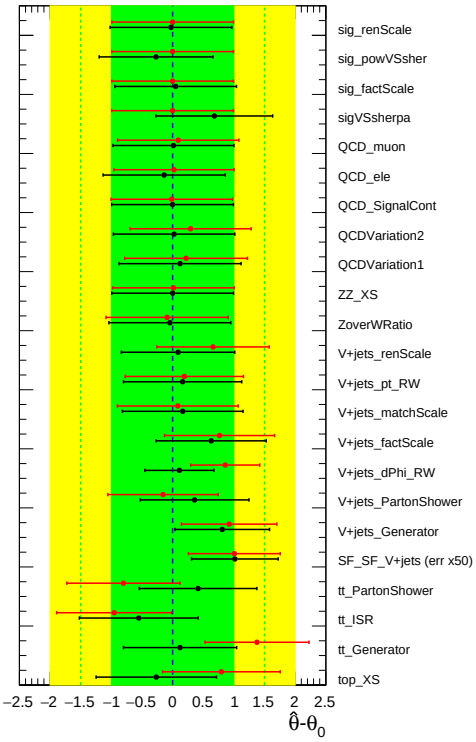

(a) modelling uncertainties in the resolved regime

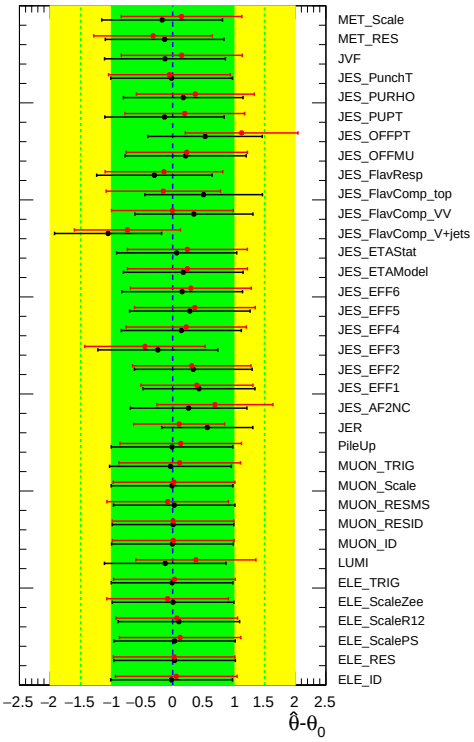

(b) detector uncertainties in the resolved regime

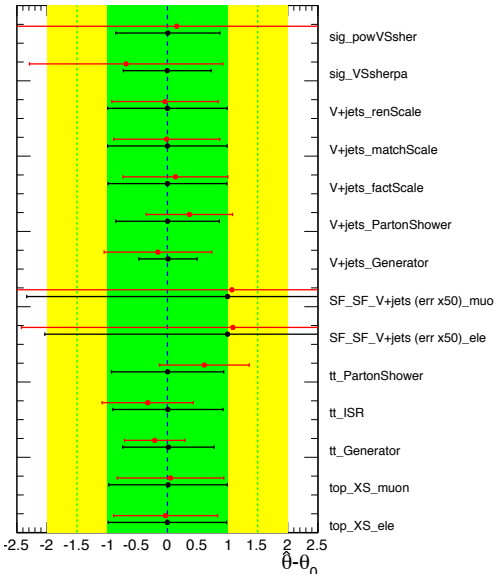

(c) modelling uncertainties in the boosted regime

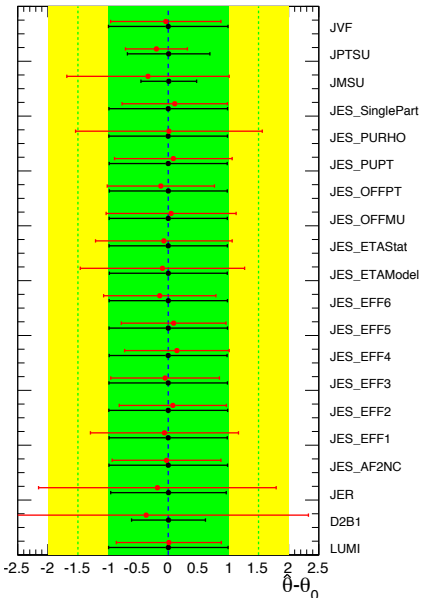

(d) detector uncertainties in the boosted regime

Figure 9.6.: Constraints on systematic uncertainties from fit to the data, split up in uncertainties from background modelling and detector uncertainties and shown for the boosted and resolved regimes. Two different fits are shown: an unconditional fit (signal normalization μ floating) in black and background-only fit ($\mu = 0$) in red. The normalization factor on the V+jets template (labeled SF_SF_V+jets) is not a nuisance parameter in the fit, so the expected value is at 1. The normalization factor is shown for demonstration purpose only.

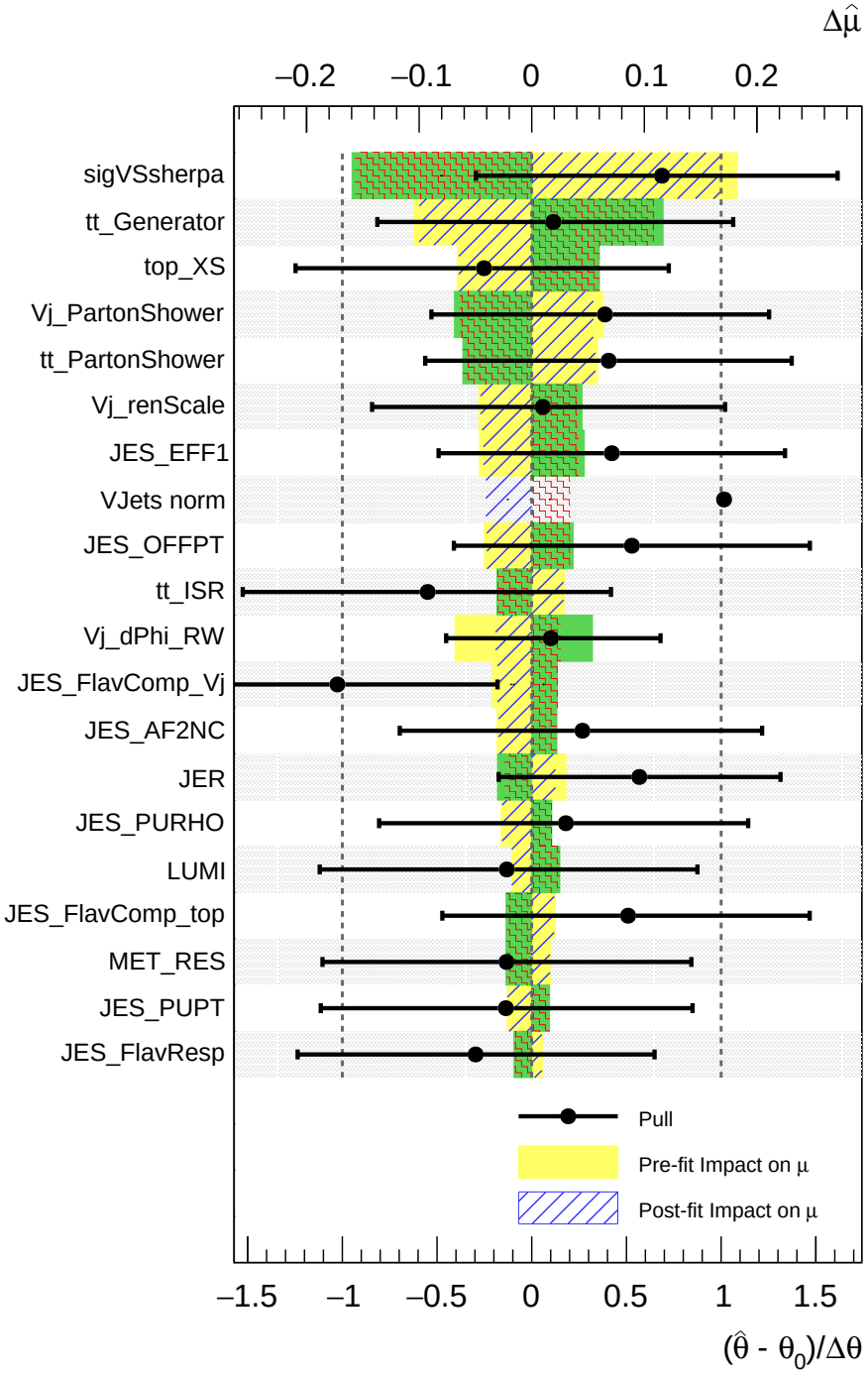

Figure 9.7.: Ranking of the systematic uncertainties for the fit to data in the resolved regime, with the largest uncertainties shown highest. The impact of each source of uncertainty on the measured signal efficiency is shown, before and after the fitting procedure, as well as the pulls on each nuisance parameter. The normalization factor on the V+jets template (labelled Vjets norm) is not a nuisance parameter in the fit, and so is set at 1.

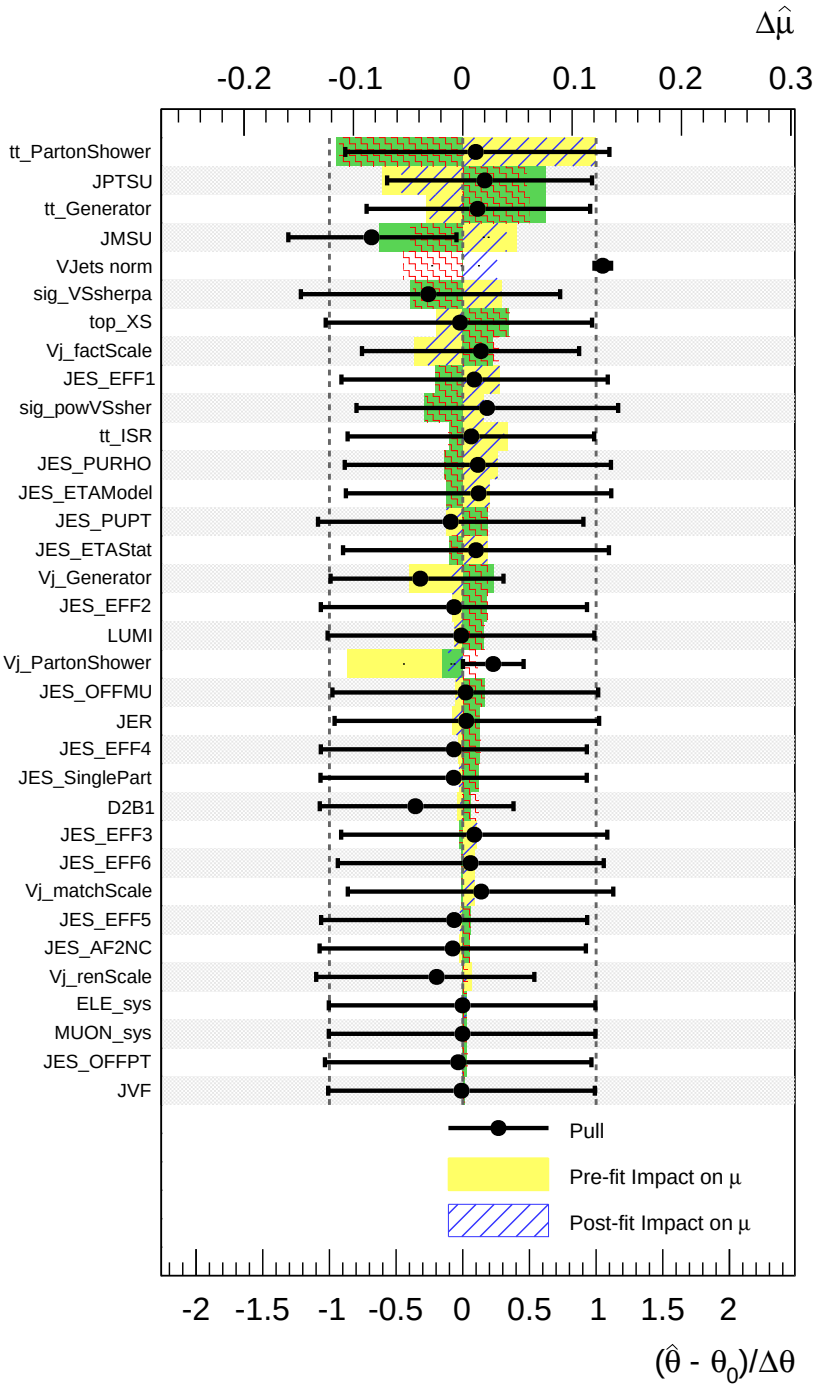

Figure 9.8.: Ranking of the systematic uncertainties for the fit to data in the boosted regime, with the largest uncertainties shown highest. The impact of each source of uncertainty on the measured signal efficiency is shown, before and after the fitting procedure, as well as the pulls on each nuisance parameter. The normalization factor on the V+jets template (labelled Vjets norm) is not a nuisance parameter in the fit, and so is set at 1.

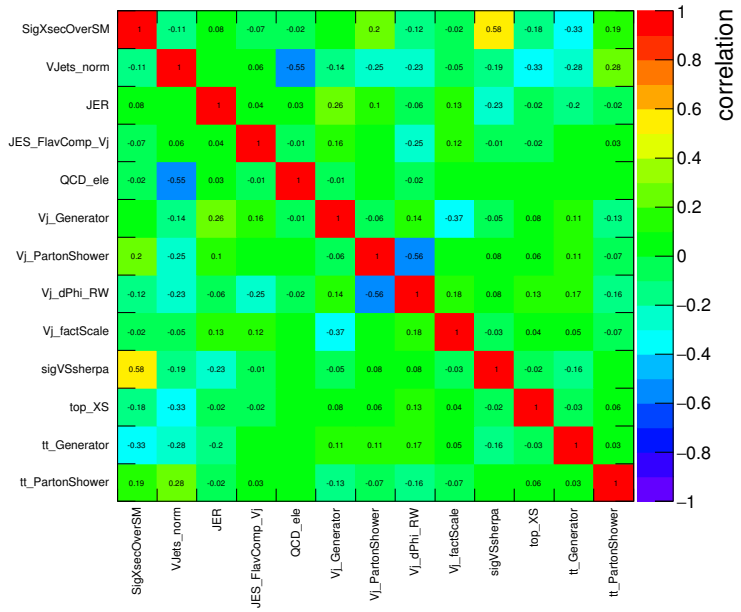

(a) largest correlations in the resolved regime

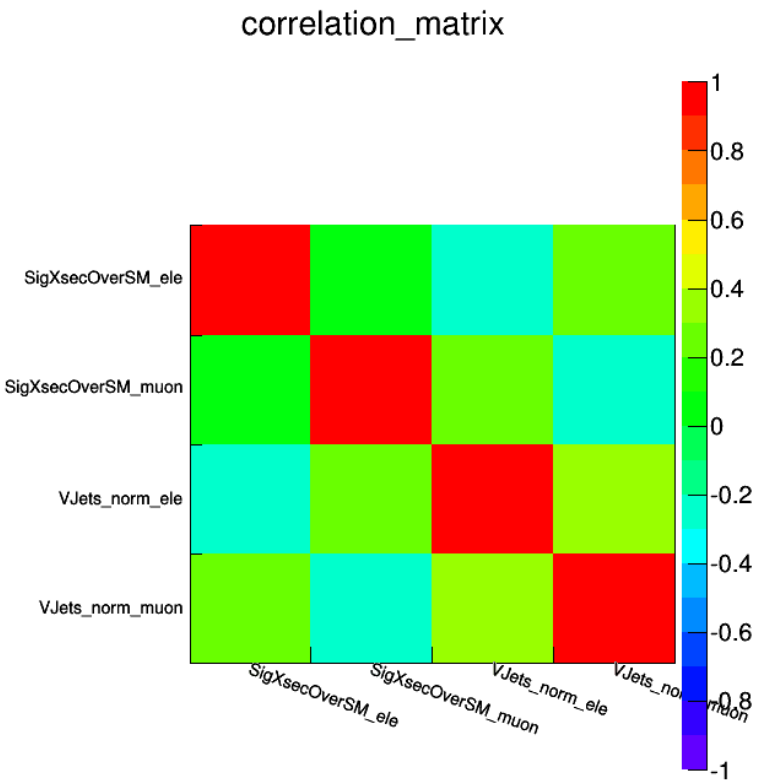

(b) largest correlations in the boosted regime

Figure 9.9.: Correlation coefficients for the nuisance parameters used in the fit. Only uncertainties for which correlations exist greater than 30% are shown.

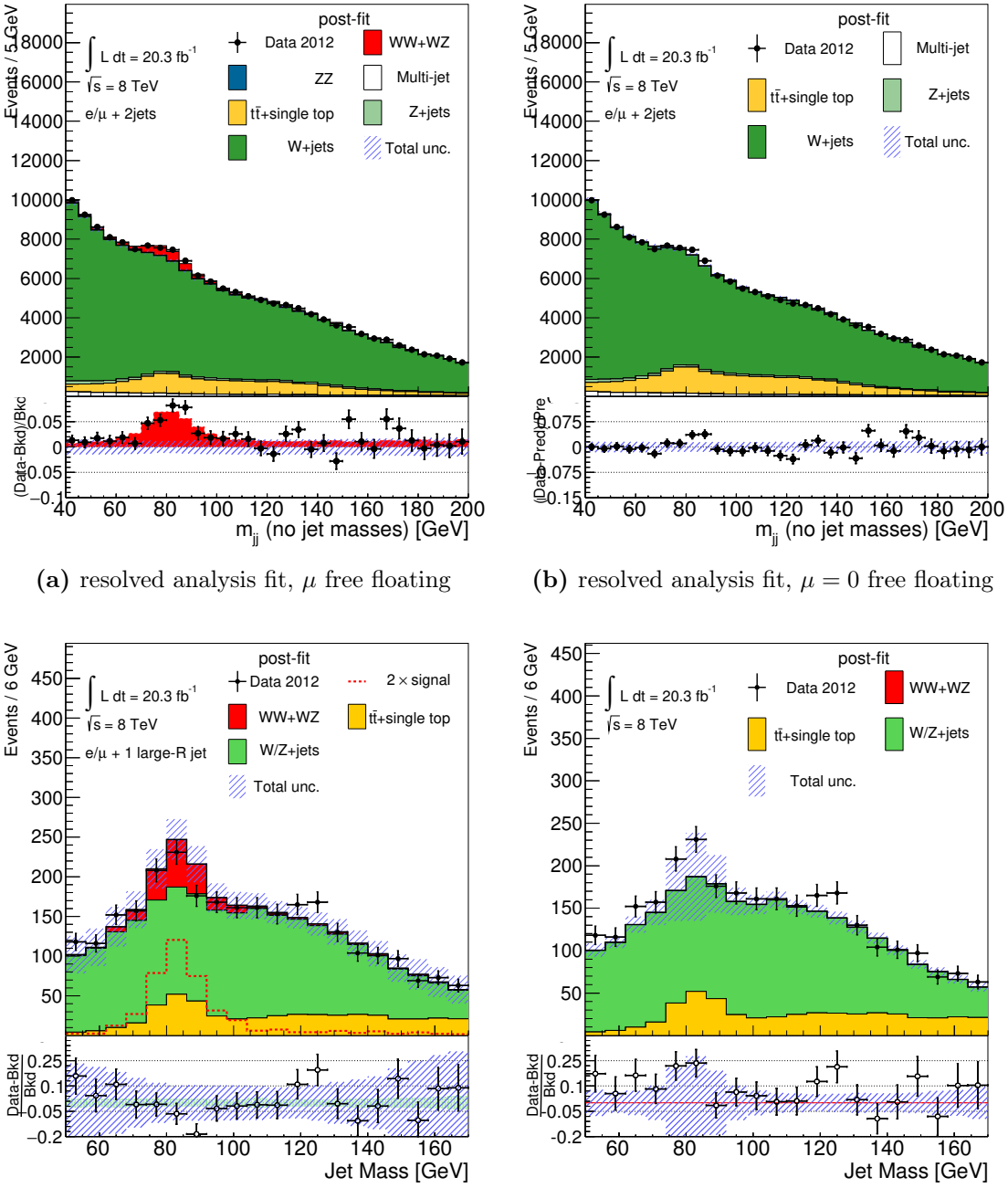

(a) resolved analysis fit, μ free floating

(b) resolved analysis fit, $\mu = 0$ free floating

(c) boosted analysis fit, μ free floating

(d) boosted analysis fit, $\mu = 0$

Figure 9.10.: Postfit distribution of the resolved analysis mass of the di-jet system, and the boosted analysis jet mass. Two fits are performed, an unconditional fit (μ free-floating) and a background-only fit ($\mu = 0$). The background-only fit is obtained by shifting all templates according to the best-fit values of all nuisance parameters and normalization factors. The uncertainties shown take into account both statistical uncertainties and systematic uncertainties from the fit.

the p_T of the large-radius jet in the boosted analysis. We use the TGClim package for the limit-setting procedure, previously used in other analyses [14]. Some technical details on the limit-setting procedure are given in Appendix C.

We apply an almost identical set of event selection criteria to that used in cross-section measurement, described in section 7.4. However, for the aTGC limit setting in the resolved analysis, we make an additional requirement that the dijet mass falls in the range $65 < m_{jj} < 95$ GeV. In the boosted analysis, we require that the large-radius jet mass falls in the range $60 < m_J < 100$ GeV.

Furthermore, in the boosted analysis, the W boson tagging requirement is no longer applied for events in which the large-radius jet p_T is greater than 500 GeV. The $D_2^{\beta=1}$ tagger is seen to lose efficiency for jets of higher transverse momentum. The greatest part of the sensitivity to aTGCs is expected to come from the bins of higher transverse momentum, so it is particularly important to have maximal sensitivity in these bins.

9.3.1. Treatment of Systematic Uncertainties

The same sources of systematic uncertainty affect aTGC limits as occur in the cross-section measurement, as described in section 8. Both shape and rate systematics are included. Once again, the systematic uncertainties are included as nuisance parameters. However, unlike the cross-section fit, in which each nuisance parameter represented a particular source of systematic uncertainty, in the aTGC fit each nuisance parameter represents the systematic uncertainty on one particular bin.

Let $\vec{\rho}$ be the vector of aTGC parameters (for example, $\rho_1 = \lambda$, $\rho_2 = \Delta g_1^Z$, $\rho_3 = \Delta\kappa_Z$) and $\vec{\alpha}$ be a vector of nuisance parameters, which will be described later. Then, the likelihood function is given by

$$L(\vec{\rho},\vec{\alpha}) = \prod_{i=1}^{m} Poisson(N^i_{\text{data}}, \mu^i(\vec{\rho},\vec{\alpha})) \times \frac{1}{(2\pi)^m}\exp\left(-\frac{1}{2}\vec{\alpha}\cdot C^{-1}\cdot\vec{\alpha}\right), \qquad (9.10)$$

where the product is over the bin number i and μ^i is the expected number of events in bin i:

$$\mu^i(\vec{\rho},\vec{\alpha}) = N^i_{\rm sig}(\vec{\rho})(1+\alpha_i) + N^i_{\rm bkg}(1+\alpha_{i+m})\,. \tag{9.11}$$

$N^i_{\rm sig}$ and $N^i_{\rm bkg}$ are the predicted number of signal and background events, respectively, in bin i. Thus if m is the number of bins, overall we have $2m$ nuisance parameters, α_i, describing the signal and background uncertainties in each bin. Each of the systematic uncertainties, defined by the α parameters, are allowed to vary within a Gaussian distribution, defined by defined by the covariance matrix C that appears in Eq. 9.10. The covariance matrix is given by

$$C_{i,j} = \langle \alpha_i, \alpha_j \rangle\,. \tag{9.12}$$

If we combine equations 9.11 and 9.12, C describes the systematic uncertainties on the signal and background in each bin, as well as the bin-to-bin correlations between these uncertainties, including correlations between signal and background. Therefore, C is able to describe both the normalization and shape systematics.

9.3.2. Evaluation of Limits

Following a similar approach to other analyses setting limits on triple gauge anomalous couplings [150], we find expected and observed 95% confidence intervals using a frequentist methodology.

Our test statistic is the profile-likelihood ratio, $\lambda(\rho)$, given by the ratio of the maximum likelihood for a given aTGC value, ρ, to the overall maximum likelihood, for any value of ρ. We scan over a variety of different values of ρ in order to find the observed value, $\lambda_{\rm obs}(\rho)$. $\lambda(\rho)$ is given by

$$\lambda(\rho) = \frac{L(N_{\rm data}|\rho,\hat{\hat{\alpha}})}{L(N_{\rm data}|\hat{\rho},\hat{\alpha})}\,, \tag{9.13}$$

where $\hat{\rho}$ and $\hat{\alpha}$ are the values of ρ and α, respectively, that simultaneously yield the overall maximum likelihood. $\hat{\hat{\alpha}}$ are the values of α that conditionally maximize the likelihood for the given value of ρ.

To find a frequentist p-value, we need to obtain the probability of obtaining a result at least as unlikely as the result observed. To estimate the probability of obtaining the observed result, we generate pseudo-data, in the form of many ($\sim 10,000$) "toy" datasets for each test-value of ρ, computing the profile-likelihood ratio $\lambda_{\text{toy}}(\rho)$ in each case,and comparing against the observed $\lambda_{\text{obs}}(\rho)$.

We generate these toy datasets by randomly drawing events from the probability density function. First, we take the mean value of $\hat{\hat{\alpha}}$, and allow Gaussian fluctuations, within the systematic uncertainties, of the nuisance parameters, α, around this value. We assume a Poisson distribution (with a mean determined from the values of ρ and α) to draw "observed events", N^i_{toy}, for each of these toy models.

Then, the p-value is given by the fraction of toy datasets that have a value of $\lambda_{\text{toy}}(\rho)$ less than the observed value of $\lambda_{\text{obs}}(\rho)$. We scan over ρ to determine the intervals for which the p-value $>= 5\%$. This defines the 95% confidence limits for ρ, the vector of aTGC parameters.

The fit using pseudo-data is very computationally expensive and so is only used in the determination of the final expected and observed limits. We use Asimov datasets, already explained in section 9.2, for the optimisation studies. The Asimov datasets were constructed using the Standard Model expectation (i.e. the sum of the signal and background Monte Carlo samples) in each bin. To set limits, we fit the Asimov datasets and find the interval corresponding to $\Delta(\ln L) = 1.92$.

Figure 9.11 show the p_T spectra used for the fit in the resolved and boosted channels, after the analysis selection. This includes both Monte Carlo and Asimov data, for the Standard Model hypothesis, and also the Monte Carlo simulated events for the signal selection with an aTGC of ${}^{c_{WWW}}/_{\Lambda^2} = 10$ TeV^{-2}. The Asimov data is identical to the Standard Model Monte Carlo, whilst the expected excess in events from a non-Standard Model aTGC is seen in the aTGC Monte Carlo.

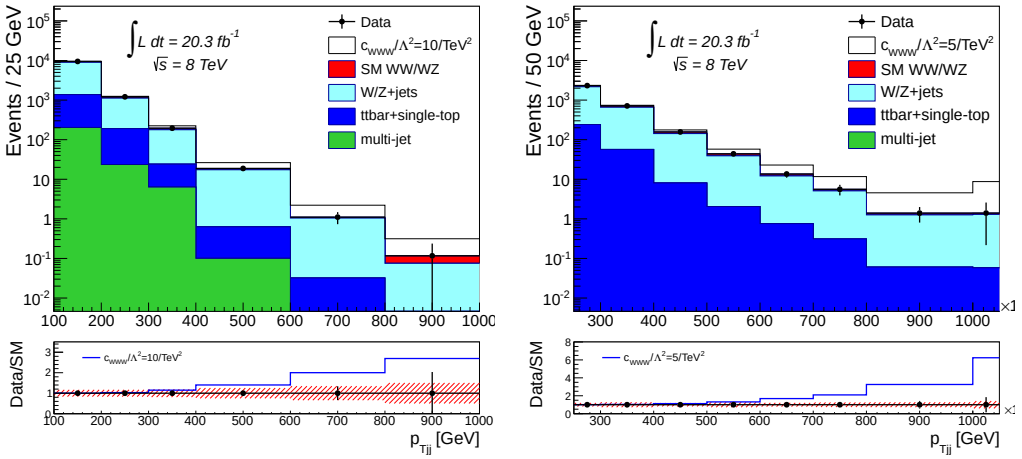

(a) resolved regime **(b)** boosted regime

Figure 9.11.: Expected p_{Tjj} distribution in the resolved channel and p_{TJ} distribution in the boosted channel. The data points represent the Asimov data. The expected signal in the presence of an aTGC of $c_{WWW}/\Lambda^2 = 10$ TeV^{-2} is shown for the resolved channel and $c_{WWW}/\Lambda^2 = 5$ TeV^{-2} for the boosted channel.

9.3.3. Reweighting of Monte Carlo Samples

For generating Monte Carlo samples with non-Standard Model aTGCs, we use the MC@NLO event generator, described in section 4.8.5. MC@NLO allows event-level reweighting of Monte Carlo simulated events to any arbitrary aTGC value [61, 112].

Including all possible triple gauge couplings, the most general form for the amplitude of W^+W^- production will take the form,

$$\mathcal{A} = \mathcal{A}_0 + \Delta g_1^Z \mathcal{A}_{gZ} + \Delta k_Z \mathcal{A}_{\kappa Z} + \lambda_Z \mathcal{A}_{\lambda Z} + \Delta g_1^\gamma \mathcal{A}_{g\gamma} + \Delta k_\gamma \mathcal{A}_{\kappa\gamma} + \lambda_\gamma \mathcal{A}_{\lambda\gamma}\,, \quad (9.14)$$

where the $\mathcal{A}_i$ are kinematics-dependent process amplitudes and $\mathcal{A}_0$ is the Standard Model total amplitude for WW production. The WZ amplitude has a similar form, except without the Δg_1^γ, Δk_γ and λ_γ terms. The cross-section is proportional to $|\mathcal{A}|^2$; we can therefore use this to make Monte Carlo predictions for any aTGC value by applying an appropriate event weight, w_{tot}. These weights will be proportional to $|\mathcal{A}^2|$:

$$
\begin{aligned}
w_{\text{tot}} = w_0 \;&+\; (\Delta g_1^Z)^2 w_1 + (\Delta k_Z)^2 w_2 + (\lambda_Z)^2 w_3 \\
&+\; (\Delta g_1^\gamma)^2 w_4 + (\Delta k_\gamma)^2 w_5 + (\lambda_\gamma)^2 w_6 \\
&+\; 2\Delta g_1^Z w_7 + 2\Delta k_Z w_8 + 2\lambda_Z w_9 \\
&+\; 2\Delta g_1^\gamma w_{10} + 2\Delta k_\gamma w_{11} + 2\lambda_\gamma w_{12} \\
&+\; 2\Delta g_1^\gamma \Delta k_Z w_{13} + 2\Delta k_Z \lambda_Z w_{14} + 2\Delta g_1^Z \Delta g_1^\gamma w_{15} \\
&+\; 2\Delta g_1^Z \Delta k_\gamma w_{16} + 2\Delta g_1^Z \lambda_\gamma w_{17} + 2\Delta k_Z \lambda_Z w_{18} \\
&+\; 2\Delta k_Z \Delta g_1^\gamma w_{19} + 2\Delta k_Z \Delta k_\gamma w_{20} + 2\Delta k_Z \lambda_\gamma w_{21} \\
&+\; 2\lambda_Z \Delta g_1^\gamma w_{22} + 2\lambda_Z \Delta k_\gamma w_{23} + 2\lambda_Z \lambda_\gamma w_{24} \\
&+\; 2\Delta g_1^\gamma \Delta k_\gamma w_{25} + 2\Delta g_1^\gamma \lambda_\gamma w_{26} + 2\Delta k_\gamma \lambda_\gamma w_{27}\,. \qquad (9.15)
\end{aligned}
$$

The MC@NLO generator allows us to store the 28 different (kinematics-dependent) weights, w_i (with $i = 0, 27$) in the data files for each event. We can then recalculate the w_{tot} for any event for any set aTGC parameters, allowing the sample to be reweighted to any chosen aTGC point.

9.3.4. Optimisation of Binning

A careful act of balancing is needed in choosing the optimal number of bins. Using a greater number of bins allows for a greater sensitivity to the aTGCs; however, if the binning is too fine then the computation time will rapidly increase, and the fitting machinery will fail to converge if there are bins in which the Monte Carlo predictions yield zero events. Extensive studies were performed for the optimal binning size, with results shown in figure 9.12. The largest possible number of bins for which the fit could converge was found to be 34. However, this number would be highly computationally intensive. It was found that the number of bins could be reduced to 11 without a significant loss of sensitivity. We use this number for the final analysis.

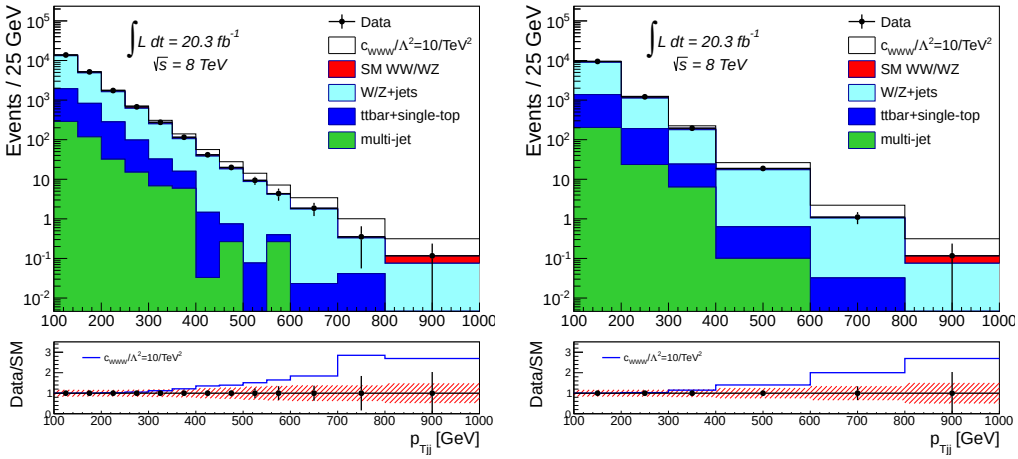

(a) 25 GeV bins **(b)** optimised bin sizes

Figure 9.12.: Expected $p_T jj$ distribution for the resolved regime in the signal region, for the sum of the muon and electron channels. Plot (a) shows a very fine binning, whereas (b) shows a binning optimized to have a small number of bins while still keeping good sensitivity to aTGCs. The data points represent the Asimov data. The expected signal in the presence of an aTGC of $c_{WWW}/\Lambda^2 = 10$ TeV^{-2} is shown.

9.3.5. Observed Limits on Triple Gauge Vertices

Figure 9.13 shows the data passing the event selection, alongside the Standard Model Monte Carlo simulated events for signal and background, as well as Monte Carlo simulated events with an aTGC parameter of $c_{WWW}/\Lambda^2 = 10$ TeV^{-2} for comparison.

Table 9.5 shows the observed and expected limits at confidence levels of 95%, for the three field theory parameters in the LEP scenario: c_{WWW}/Λ^2, c_W/Λ^2, and c_B/Λ^2, and Δg_1^Z, each calculated whilst holding the other two parameters at zero.

9.4. Summary

These results represent a significant improvement on the past measurement of the $WW + WZ$ production cross-section in the semileptonic channel, previously performed at a centre of mass energy of $\sqrt{s} = 7$ TeV [14]. In the resolved channel, the fiducial cross-section was measured to be $\sigma_{\text{fid}}(WW + WZ) = 219 \pm 61$ pb, where

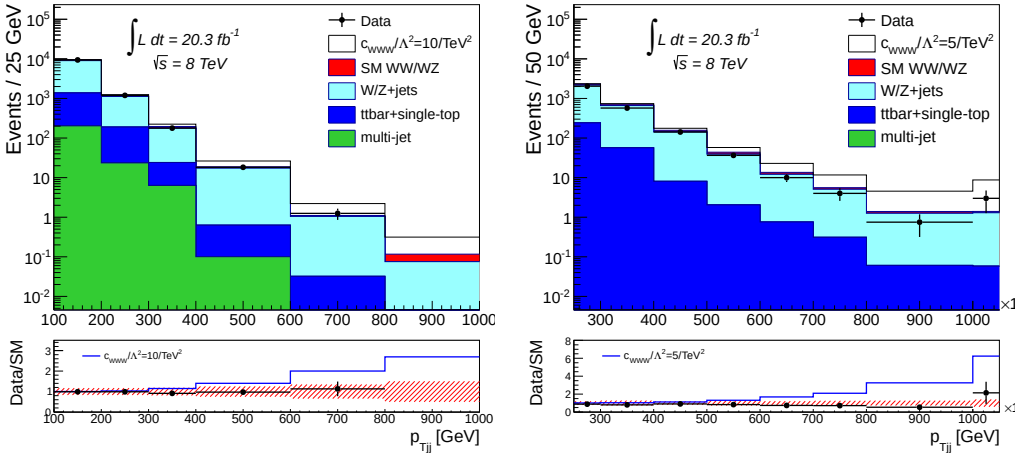

(a) resolved regime **(b)** boosted regime

Figure 9.13.: Distribution of p_{Tjj} in the resolved channel, and p_{TJ} in the boosted channel, for the data and Monte Carlo generated events. The expected signal in the presence of an aTGC of $c_{WWW}/\Lambda^2 = 10$ TeV^{-2} is shown for the resolved channel and $c_{WWW}/\Lambda^2 = 5$ TeV^{-2} for the boosted channel.

Table 9.5.: The observed and expected 95% confidence level limits on the field theory aTGC parameters c_{WWW}/Λ^2, c_W/Λ^2, and c_B/Λ^2, shown for the boosted and resolved channels. The limits on each parameter are calculated while fixing the other two parameters to zero. All limits are in units of TeV^{-2}.

	Resolved channel		**Boosted channel**	
Parameter	Observed Limit	Expected Limit	Observed Limit	Expected Limit
c_{WWW}/Λ^2	[-6.0, 6.0]	[-7.0, 6.9]	[-2.54, 2.52]	[-3.17, 3.10]
c_W/Λ^2	[-39, 46]	[-49, 55]	[-15.6, 17.2]	[-18.7, 22.0]
c_B/Λ^2	[-6.9, 12.1]	[-9.3, 13.4]	[-3.65, 4.94]	[-4.30, 6.09]

the observed significance of the signal is 4.45σ. This measurement is consistent with the MC@NLO prediction of the fiducial cross-section, of 225 ± 5.2 pb. In the boosted channel, the cross-section was measured to be 7.6 ± 4.9 pb, lower than the expected standard model cross section of 15.3 pb. The resolved channel contributed a significance of 4.45σ, while the boosted channel contributed a significance of 2.05σ.

The results also set new limits on the anomalous triple gauge couplings. The observed 95% CL limits on the anomalous triple gauge parameters are $-6.0 < {}^{c_{WWW}}/_{\Lambda^2} < 6.0$, $-39 < {}^{c_W}/_{\Lambda^2} < 46$ and $-6.9 < {}^{c_B}/_{\Lambda^2} < 12.1$ TeV^{-2} for the resolved analysis, and $-2.54 < {}^{c_{WWW}}/_{\Lambda^2} < 2.52$, $-15.6 < {}^{c_W}/_{\Lambda^2} < 17.2$ and $-3.65 < {}^{c_B}/_{\Lambda^2} < 4.94$ TeV^{-2}. Both mark a substantial improvement over the limits set by the comparable analysis at a centre of mass energy of $\sqrt{s} = 7$ TeV: $-9.5 < {}^{c_{WWW}}/_{\Lambda^2} < 9.6$, $-64 < {}^{c_W}/_{\Lambda^2} < 69$ and $-13 < {}^{c_B}/_{\Lambda^2} < 18$ TeV^{-2} [14]. The boosted regime improves on limits set by the analysis at $\sqrt{s} = 7$ TeV by around a factor of three, and improves on the limits set by the resolved regime by around a factor of two.

Table 9.6 shows the limits set on the aTGCs from the boosted analysis, compared against the observed limits from other recent results from the ATLAS experiment. The analysis provides the tightest limits on each of the aTGC parameters considered so far.

Table 9.6.: The observed and expected 95% confidence level limits on the field theory aTGC parameters ${}^{c_{WWW}}/_{\Lambda^2}$, ${}^{c_W}/_{\Lambda^2}$, and ${}^{c_B}/_{\Lambda^2}$, shown for the boosted analysis ($WV \to l\nu qq$, 8 TeV), and other recent ATLAS analyses ($WW \to 2l2\nu$, 8 TeV [12]; $WZ \to 3l\nu$, 8 TeV [13]; and $WV \to l\nu qq$, 7 TeV [14]). All limits are in units of TeV^{-2}.

Parameter	Limit	$\boldsymbol{WV \to l\nu qq}$, **8 TeV**	$WW \to 2l2\nu$, 8 TeV	$WZ \to 3l\nu$, 8 TeV	$WV \to l\nu qq$, 7 TeV
${}^{c_{WWW}}/_{\Lambda^2}$	expected	[-3.17, 3.10]	[-7.62, 7.38]	[-3.7, 7.6]	[-11.6, 11.5]
	observed	[-2.54, 2.52]	[-4.61, 4.60]	[-4.3, 6.8]	[-9.5, 9.6]
${}^{c_W}/_{\Lambda^2}$	expected	[-18.7, 22.0]	[-35.8, 38.4]	[-270, 180]	[-73,79.0]
	observed	[-15.6, 17.2]	[-20.9, 26.3]	[-320, 210]	[-64, 69]
${}^{c_B}/_{\Lambda^2}$	expected	[-4.30, 6.09]	[-12.58, 14.32]	[-3.9, 3.8]	[-13, 18]
	observed	[-3.65, 4.94]	[-5.87, 10.54]	[-3.9, 4.0]	[-17, 21]

Chapter 10.

Conclusions

The main focus of this thesis is an analysis, looking at the semileptonic decays of vector boson pairs, $WV \to l\nu jj$, at centre of mass energies of $\sqrt{s} = 8$ TeV. This analysis has two separate aims: to measure the diboson production cross-section and to search for anomalous triple gauge couplings. To do this, it considers two different regimes, described as the boosted and resolved, and considered very different jet physics for each topology. The thesis also presents a performance study for the trigger upgrade, which compares potential techniques to improve the performance of the jet trigger algorithms.

The performance study presented in chapter 6 provides important insights into the potential for partial scan to improve the algorithmic efficiency for the complex, high pile-up environment that the LHC will deliver throughout Run 2 and beyond. The study offers important information on efficiencies and algorithm timings to assess whether they could be adopted to improve the jet trigger performance at Run 2. Whilst the partial scan techniques were not ultimately adopted for Run 2, the studies improved our understanding and it is possible that partial scan or related ideas will become important for future upgrades.

The analysis presented in chapters 7, 8 and 9 is unique in several ways. Combining both a resolved and a boosted channel to study semileptonic decays, it provides improved measurements of the cross-section, more precise than any previously seen in this channel. It offers the potential for improved limits on anomalous triple gauge couplings, more sensitive than any so far produced in the semileptonic channel, and approximately three times that seen in a similar study at 7 TeV [14]. This powerfully

demonstrates the potential benefits of boosted analyses for studying anomalous couplings.

In particular, the analysis illustrates the potential of the rapidly developing field of jet substructure in boosted regimes. This was the first and only analysis to apply the 2012 recommendations of the boosted jet study described in [97], providing an innovative first application of energy-energy correlation functions as a tool for vector boson tagging. Cutting on the $D_2^{\beta=1}$ parameter was found to be superior to all previous techniques, and proved to be an effective for tagging W bosons in this analysis. These techniques for boosted analyses will prove even more important in Run 2; with the LHC now operating at the higher centre-of-mass energy of $\sqrt{s} = 13$ TeV, and with the intention to operate at even higher energies in the future, the field of jet substructure is likely to prove ever more important.

The measurements of the cross-section in the two channels were found to be consistent with the Standard Model predictions. Improved limits were set on aTGCs in both channels, and again no deviation from the Standard Model was found. Indeed, no deviation from this theory has yet been confirmed in any LHC analysis. Run 2 analyses are now underway, utilising new data at the higher centre-of-mass energies. This environment is more challenging in many ways, with higher levels of pile-up and higher jet multiplicities. Further-improved techniques will be needed to distinguish between signals and backgrounds in this richer and more complex physical environment; boosted analyses based upon jet substructure are likely to play a greater role in the future. These techniques will be vital for the search for new physics beyond the Standard Model.

Appendix A.

Monte Carlo Samples

Process	Dataset	Generator	$\sigma \cdot \mathrm{BR} \cdot \epsilon_f$ [pb]	N_{evt} [10^6]
$W \to e\nu(p_T > 0, \mathrm{bfilter})$	167740	Sherpa	154.38	15.00
$W \to e\nu(p_T > 0, \mathrm{cfilter/bveto})$	167741	Sherpa	591.62	10.00
$W \to e\nu(p_T > 0, \mathrm{cveto/bveto})$	167742	Sherpa	11324.49	49.87
$W \to \mu\nu(p_T > 0, \mathrm{bfilter})$	167743	Sherpa	154.43	14.99
$W \to \mu\nu(p_T > 0, \mathrm{cfilter/bveto})$	167744	Sherpa	513.12	9.99
$W \to \mu\nu(p_T > 0, \mathrm{cveto/bveto})$	167745	Sherpa	11404.48	49.78
$W \to \tau\nu(p_T > 0, \mathrm{bfilter})$	167746	Sherpa	154.38	14.96
$W \to \tau\nu(p_T > 0, \mathrm{cfilter/bveto})$	167747	Sherpa	557.10	9.99
$W \to \tau\nu(p_T > 0, \mathrm{cveto/bveto})$	167748	Sherpa	11360.17	49.88
$W \to e\nu(40 < p_T < 70, \mathrm{bfilter})$	180534	Sherpa	24.80	1.10
$W \to e\nu(40 < p_T < 70, \mathrm{cfilter/bveto})$	180535	Sherpa	123.34	0.90
$W \to e\nu(40 < p_T < 70, \mathrm{cveto/bveto})$	180536	Sherpa	570.00	16.93
$W \to \mu\nu(40 < p_T < 70, \mathrm{bfilter})$	180537	Sherpa	24.81	1.10
$W \to \mu\nu(40 < p_T < 70, \mathrm{cfilter/bveto})$	180538	Sherpa	119.03	0.90
$W \to \mu\nu(40 < p_T < 70, \mathrm{cveto/bveto})$	180539	Sherpa	574.57	16.95
$W \to \tau\nu(40 < p_T < 70, \mathrm{bfilter})$	180540	Sherpa	24.82	1.10
$W \to \tau\nu(40 < p_T < 70, \mathrm{cfilter/bveto})$	180541	Sherpa	121.47	0.89

$W \to \tau\nu(40 < p_T < 70, \text{cveto/bveto})$	180542	Sherpa	571.87	16.95
$W \to e\nu(70 < p_T < 140, \text{bfilter})$	167761	Sherpa	12.66	2.00
$W \to e\nu(70 < p_T < 140, \text{cfilter/bveto})$	167762	Sherpa	55.43	3.00
$W \to e\nu(70 < p_T < 140, \text{cveto/bveto})$	167763	Sherpa	207.49	15.00
$W \to \mu\nu(70 < p_T < 140, \text{bfilter})$	167764	Sherpa	12.66	2.00
$W \to \mu\nu(70 < p_T < 140, \text{cfilter/bveto})$	167765	Sherpa	53.76	3.00
$W \to \mu\nu(70 < p_T < 140, \text{cveto/bveto})$	167766	Sherpa	209.29	14.99
$W \to \tau\nu(70 < p_T < 140, \text{bfilter})$	167767	Sherpa	12.66	2.00
$W \to \tau\nu(70 < p_T < 140, \text{cfilter/bveto})$	167768	Sherpa	54.83	3.00
$W \to \tau\nu(70 < p_T < 140, \text{cveto/bveto})$	167769	Sherpa	208.02	15.00
$W \to e\nu(140 < p_T < 280, \text{bfilter})$	167770	Sherpa	2.16	5.00
$W \to e\nu(140 < p_T < 280, \text{cfilter/bveto})$	167771	Sherpa	7.61	2.00
$W \to e\nu(140 < p_T < 280, \text{cveto/bveto})$	167772	Sherpa	24.47	2.00
$W \to \mu\nu(140 < p_T < 280, \text{bfilter})$	167773	Sherpa	2.17	4.99
$W \to \mu\nu(140 < p_T < 280, \text{cfilter/bveto})$	167774	Sherpa	7.42	1.99
$W \to \mu\nu(140 < p_T < 280, \text{cveto/bveto})$	167775	Sherpa	24.70	1.99
$W \to \tau\nu(140 < p_T < 280, \text{bfilter})$	167776	Sherpa	2.17	4.00
$W \to \tau\nu(140 < p_T < 280, \text{cfilter/bveto})$	167777	Sherpa	7.54	2.00
$W \to \tau\nu(140 < p_T < 280, \text{cveto/bveto})$	167778	Sherpa	24.56	2.00
$W \to e\nu(280 < p_T < 500, \text{bfilter})$	167779	Sherpa	0.17	0.90
$W \to e\nu(280 < p_T < 500, \text{cfilter/bveto})$	167780	Sherpa	0.47	0.99
$W \to e\nu(280 < p_T < 500, \text{cveto/bveto})$	167781	Sherpa	1.38	2.49
$W \to \mu\nu(280 < p_T < 500, \text{bfilter})$	167782	Sherpa	0.17	0.90
$W \to \mu\nu(280 < p_T < 500, \text{cfilter/bveto})$	167783	Sherpa	0.46	1.00
$W \to \mu\nu(280 < p_T < 500, \text{cveto/bveto})$	167784	Sherpa	1.39	2.50
$W \to \tau\nu(280 < p_T < 500, \text{bfilter})$	167785	Sherpa	0.17	0.90
$W \to \tau\nu(280 < p_T < 500, \text{cfilter/bveto})$	167786	Sherpa	0.47	0.20
$W \to \tau\nu(280 < p_T < 500, \text{cveto/bveto})$	167787	Sherpa	1.38	0.50

$W \to e\nu(p_T > 500, \text{bfilter})$	167788	Sherpa	0.01	0.10
$W \to e\nu(p_T > 500, \text{cfilter/bveto})$	167789	Sherpa	0.03	0.01
$W \to e\nu(p_T > 500, \text{cveto/bveto})$	167790	Sherpa	0.07	0.01
$W \to \mu\nu(p_T > 500, \text{bfilter})$	167791	Sherpa	0.01	0.09
$W \to \mu\nu(p_T > 500, \text{cfilter/bveto})$	167792	Sherpa	0.03	0.61
$W \to \mu\nu(p_T > 500, \text{cveto/bveto})$	167793	Sherpa	0.07	1.05
$W \to \tau\nu(p_T > 500, \text{bfilter})$	167794	Sherpa	0.01	0.09
$W \to \tau\nu(p_T > 500, \text{cfilter/bveto})$	167795	Sherpa	0.03	0.01
$W \to \tau\nu(p_T > 500, \text{cveto/bveto})$	167796	Sherpa	0.07	0.05

Table A.2.: List of W+jets samples used in the analysis. l refers to e, μ, τ. σ refers to the channel cross-section, BR to its branching ratio and ϵ_f to the filter efficiency used in the process of generation. N_{evt} refers to the number of generated events in each sample.

Process	Dataset	Generator	$\sigma \cdot \text{BR} \cdot \epsilon_f$ [pb]	N_{evt} [10^6]
$Z \to ee(p_T > 0, \text{bfilter})$	167749	Sherpa	34.77	4.00
$Z \to ee(p_T > 0, \text{cfilter/bveto})$	167750	Sherpa	351.97	3.00
$Z \to ee(p_T > 0, \text{cveto/bveto})$	167751	Sherpa	856.14	4.98
$Z \to \mu\mu(p_T > 0, \text{bfilter})$	167752	Sherpa	34.76	4.00
$Z \to \mu\mu(p_T > 0, \text{cfilter/bveto})$	167753	Sherpa	352.58	3.00
$Z \to \mu\mu(p_T > 0, \text{cveto/bveto})$	167754	Sherpa	856.22	4.99
$Z \to \tau\tau(p_T > 0, \text{bfilter})$	167755	Sherpa	34.73	4.00
$Z \to \tau\tau(p_T > 0, \text{cfilter/bveto})$	167756	Sherpa	352.23	3.00
$Z \to \tau\tau(p_T > 0, \text{cveto/bveto})$	167757	Sherpa	856.32	4.98
$Z \to ee(70 < p_T < 140, \text{bfilter})$	167797	Sherpa	2.73	1.40
$Z \to ee(70 < p_T < 140, \text{cfilter/bveto})$	167798	Sherpa	11.72	1.00
$Z \to ee(70 < p_T < 140, \text{cveto/bveto})$	167799	Sherpa	18.58	2.00

$Z \to \mu\mu(70 < p_T < 140, \text{bfilter})$	167800	Sherpa	2.73	1.39
$Z \to \mu\mu(70 < p_T < 140, \text{cfilter/bveto})$	167801	Sherpa	11.70	1.00
$Z \to \mu\mu(70 < p_T < 140, \text{cveto/bveto})$	167802	Sherpa	18.57	2.00
$Z \to \tau\tau(70 < p_T < 140, \text{bfilter})$	167803	Sherpa	2.73	1.40
$Z \to \tau\tau(70 < p_T < 140, \text{cfilter/bveto})$	167804	Sherpa	11.73	1.00
$Z \to \tau\tau(70 < p_T < 140, \text{cveto/bveto})$	167805	Sherpa	18.58	2.00
$Z \to ee(140 < p_T < 280, \text{bfilter})$	167809	Sherpa	0.43	1.00
$Z \to ee(140 < p_T < 280, \text{cfilter/bveto})$	167810	Sherpa	1.65	0.40
$Z \to ee(140 < p_T < 280, \text{cveto/bveto})$	167811	Sherpa	2.39	0.60
$Z \to \mu\mu(140 < p_T < 280, \text{bfilter})$	167812	Sherpa	0.43	1.00
$Z \to \mu\mu(140 < p_T < 280, \text{cfilter/bveto})$	167813	Sherpa	1.65	0.40
$Z \to \mu\mu(140 < p_T < 280, \text{cveto/bveto})$	167814	Sherpa	2.38	0.60
$Z \to \tau\tau(140 < p_T < 280, \text{bfilter})$	167815	Sherpa	0.43	0.80
$Z \to \tau\tau(140 < p_T < 280, \text{cfilter/bveto})$	167816	Sherpa	1.65	0.40
$Z \to \tau\tau(140 < p_T < 280, \text{cveto/bveto})$	167817	Sherpa	2.38	0.60
$Z \to ee(280 < p_T < 500, \text{bfilter})$	167821	Sherpa	0.03	0.18
$Z \to ee(280 < p_T < 500, \text{cfilter/bveto})$	167822	Sherpa	0.10	0.55
$Z \to ee(280 < p_T < 500, \text{cveto/bveto})$	167823	Sherpa	0.14	0.55
$Z \to \mu\mu(280 < p_T < 500, \text{bfilter})$	167824	Sherpa	0.03	0.17
$Z \to \mu\mu(280 < p_T < 500, \text{cfilter/bveto})$	167825	Sherpa	0.10	0.55
$Z \to \mu\mu(280 < p_T < 500, \text{cveto/bveto})$	167826	Sherpa	0.14	0.55
$Z \to \tau\tau(280 < p_T < 500, \text{bfilter})$	167827	Sherpa	0.03	0.18
$Z \to \tau\tau(280 < p_T < 500, \text{cfilter/bveto})$	167828	Sherpa	0.10	0.55
$Z \to \tau\tau(280 < p_T < 500, \text{cveto/bveto})$	167829	Sherpa	0.14	0.55
$Z \to ee(p_T > 500, \text{bfilter})$	167833	Sherpa	0.00	0.09
$Z \to ee(p_T > 500, \text{cfilter/bveto})$	167834	Sherpa	0.01	0.06
$Z \to ee(p_T > 500, \text{cveto/bveto})$	167835	Sherpa	0.01	0.15
$Z \to \mu\mu(p_T > 500, \text{bfilter})$	167836	Sherpa	0.00	0.10

$Z \to \mu\mu(p_T > 500, \text{cfilter/bveto})$	167837	Sherpa	0.01	0.01
$Z \to \mu\mu(p_T > 500, \text{cveto/bveto})$	167838	Sherpa	0.01	0.01
$Z \to \tau\tau(p_T > 500, \text{bfilter})$	167839	Sherpa	0.00	0.09
$Z \to \tau\tau(p_T > 500, \text{cfilter/bveto})$	167840	Sherpa	0.01	0.06
$Z \to \tau\tau(p_T > 500, \text{cveto/bveto})$	167841	Sherpa	0.01	0.15

Table A.3.: List of Z+jets samples used in the analysis. l refers to e, μ, τ. σ refers to the channel cross-section, BR to its branching ratio and ϵ_f to the filter efficiency used in the process of generation. N_{evt} refers to the number of generated events in each sample.

	Process	Dataset	$\sigma \cdot \mathrm{BR} \cdot \epsilon_f$ [pb]	N_{evt} [10^6]
Reference WV samples				
Generator: MC@NLO				
Nominal WW	$qq \to WW$	185894	23.62	4.98
Nominal W^+Z	W^+Z	185895	4.47	1.00
Nominal W^-Z	W^-Z	185896	2.49	0.49
aTGC WW	$qq \to WW$ (aTGC, all decays)	185897	70.46	3.96
aTGC W^+Z	W^+Z (aTGC, all decays)	185898	19.60	0.98
aTGC W^-Z	W^-Z (aTGC, all decays)	185899	9.36	0.50
WV samples used for systematic evaluation				
Generator: Powheg+Pythia8				
Nominal WW	$qq \to WW$	181971	54.43	10.00
Nominal WZ	$WZ \to l\nu qq$	181970	4.87	10.00
	$WZ \to qqll$	181968	1.59	2.39
Generator: Sherpa				
Nominal WW	$qq \to WW \to e\nu qq$	183734	7.72	3.16
	$qq \to WW \to \mu\nu qq$	183736	7.74	3.16
	$qq \to WW \to \tau\nu qq$	183738	7.71	3.16
	$qq \to WW \to l\nu l\nu$	177997	5.61	0.40
Nominal WZ	$WZ \to e\nu qq$	183735	2.00	0.84
	$WZ \to \mu\nu qq$	183737	2.00	0.84
	$WZ \to \tau\nu qq$	183739	2.01	0.84
	$WZ \to qqee$	183585	1.54	0.18
	$WZ \to qq\mu\mu$	183587	1.54	0.18
	$WZ \to qq\tau\tau$	183589	1.54	0.18
	$WZ \to l\nu ll$	179974	10.23	2.70
	$WZ \to l\nu\nu\nu$	179975	1.47	0.40

Table A.1.: List of WW and WZ samples used in the analysis. Each channel refers to all W and Z decays unless the decays are explicitly specified. l refers to e, μ, τ. σ refers to the channel cross-section, BR to its branching ratio and ϵ_f to the filter efficiency used in the process of generation. N_{evt} refers to the number of generated events in each sample.

Process	Dataset	Generator	$\sigma \cdot \mathrm{BR} \cdot \epsilon_f$ [pb]	N_{evt} [10^6]
$t\bar{t}$(not all hadr.)	117050	Powheg+Pythia 6	137.32	15.00
single-top t-chan l^+	110090	Powheg+Pythia	18.39	4.99
single-top t-chan l^-	110091	Powheg+Pythia	9.96	5.00
single-top s-chan (lep)	110119	Powheg+Pythia	1.82	6.00
Wt	110140	Powheg+Pythia	22.36	1.00

Table A.4.: List of Monte Carlo $t\bar{t}$ and single-top samples used in the analysis. All cross-sections are normalised to the NNLO theoretical value. l refers to e, μ, τ. σ refers to the channel cross-section, BR to its branching ratio and ϵ_f to the filter efficiency used in the process of generation. N_{evt} refers to the number of generated events in each sample.

Appendix B.

Glossary of Statistical Terms

The following terms are used in the statistical fitting procedure, following definitions given in [151, 152].

- **Asimov dataset:** The pseudo-dataset which is taken as most representative of all the possible real datasets that could be obtained. A fit to an Asimov dataset generates expected values for each parameter. In practice, we build Asimov datasets from the nominal Monte Carlo predictions [1].
- **Confidence level:** The proportion of all possible samples that are expected to include the true value of a parameter. For example, a 95% confidence level implies that samples would contain the true value of the parameter 95% of the time. A more detailed discussion of confidence levels is given in Appendix C.
- **Likelihood:** The likelihood, L, of a set of parameters, θ, given outcomes, x, is the probability of those observed outcomes, given the set of parameters, i.e. $L(\theta|x) = P(x|\theta)$.
- **Maximum likelihood:** A method for estimating the set of parameters, for a given set of statistics, which makes the likelihood function a maximum. This maximises the "agreement" of the selected model with the observed data, and consequently maximises the probability of the observed data under the resulting distribution. A more detailed discussion is given in Appendix C.

[1] The term 'Asimov' dataset is inspired by 'Franchise', a short story by Isaac Asmiov, in which elections are held by selecting the single most representative voter to replace the entire electorate [153].

- **Nuisance parameter:** Parameters allowed to float in the fit, constrained by probability density functions. Nuisance parameters account for the different sources of systematic uncertainty, with normalisation uncertainties constrained by a log normal probability density, and shape uncertainties constrained by a Gaussian probability density.
- **p-value:** The probability to observe a given value, assuming that the null hypothesis is true. This is used widely in frequentist statistics, and does not given the probability that an alternative hypothesis is true. It is generally interpreted as an indication of the probability for the background to fluctuate to give the observed result, if there is zero contribution from the signal. A low p-value provides evidence to reject the null hypothesis.
- **Parameter of interest:** A parameter in the fit that we intend to measure; unlike the nuisance parameters, this is not constrained in the fit. In this analysis, the parameter of interest is the signal strength, μ.
- **Prefit:** The expected yield for each Monte Carlo sample in each bin, normalised to the theoretical cross-sections and integrated luminosity.
- **Postfit:** The expected yield for each Monte Carlo sample in the bin, after having run the fit. Monte Carlo yields are changed by the fit, which will vary the shape and normalisation, constrained by the nuisance parameters.
- **Pull:** The central value of a nuisance parameter, given after the fitting procedure as a shift from the prefit central value, and expressed as a fraction of the prefit uncertainty. A large value for the pull suggests a bias or changing in size of the error, implying that the uncertainty may have been over or under-estimated.

Appendix C.

Confidence Levels and Limit Setting

C.1. Likelihood Functions

The likelihood function for a single bin is given by the Poisson probability of observing n data events when we expect b background events, s signal events, and signal strength μ:

$$L(n|\mu, b) = \frac{(\mu s + b)^n}{n!} e^{-(\mu s+b)}\,, \tag{C.1}$$

and the likelihood across several bins is simply the product of the likelihood in each bin i:

$$L(\vec{n}|\mu, \vec{b}) = \prod_i \frac{(\mu s_i + b_i)_i^n}{n_i!} e^{-(\mu s_i+b_i)}\,. \tag{C.2}$$

To incorporate systematic uncertainties as Gaussian nuisance parameters, we multiply the likelihood function by the product of the Gaussians. For each systematic uncertainty j, θ_j is the systematic nuisance parameter; a value of $\theta_j = \pm 1$ corresponds to the full size of the up or down variation affecting the likelihood:

$$L(\vec{n},\vec{\theta}|\mu,\vec{b},\vec{\theta}) = \prod_i \frac{(\mu s_i + b_i)_i^n}{n_i!} e^{-(\mu s_i + b_i)} \prod_j \text{Gaus}(\theta_j^0 - \theta_j)\,, \tag{C.3}$$

where the central values of the nuisance parameters, θ_j^0, are generally fixed to zero; but we can vary them when running pseudo experiments.

For a test statistic, we use the profile-likelihood ratio, the ratio of the maximum likelihood for a given aTGC value, μ, to the overall maximum likelihood, for any value of μ; it is defined by

$$\lambda(\mu) = \frac{L(n|\mu,\hat{\hat{\theta}})}{L(n|\hat{\mu},\hat{\theta})}\,, \tag{C.4}$$

where $\hat{\mu}$ and $\hat{\theta}$ are the values of μ and θ, respectively, that simultaneously yield the overall maximum likelihood. $\hat{\hat{\theta}}$ are the values of θ that conditionally maximize the likelihood for the given value of μ.

We use the test statistic to calculate the frequentist p-value by running multiple pseudo-experiments that randomise the number of observed events as well as the central values of θ_j^0.

This procedure can be highly computationally demanding, requiring a huge number of pseudo-experiments to fully sample the space. To avoid this, we can "profile" the nuisance parameters. We fit the values of θ_j^0 to the data and μ. This provides a conservative approximation to the result that would have maximised the p-value, because by definition the data will give the result that maximises compatibility with the data. This technique allows us to run a far smaller number of pseudo-experiments in the construction of the test statistic distribution. We then integrate across the test statistic $\lambda(\mu)$ to find the p-value for this particular value of μ. For a given μ, if the p-value falls below a particular threshold (typically p=0.05), we declare this model for μ to be "excluded" [149].

C.2. Confidence Intervals for Setting Limits

Model-independent limits tell us the highest number of signal events which are compatible with data, at a set p-value threshold. To set model-independent limits, we consider one bin at a time, insert a signal size $s = 1$ and interatively increase μ until the desired p-value threshold is reached.

However, more often, we wish to set model-dependent limits. For this, we define the confidence level, CL_s. Suppose that for our experiment, we expect, from Monte Carlo estimations, s signal, and b background events, with s related to our parameter of interest, μ. We want to consider the $s + b$ hypothesis (in practice the hypothesis that the signal we are searching for does exist), against the background-only (null) hypothesis. Let n be our observed number of events for our test statistic; it will have some distribution, $f(n|s + b)$ under the $s + b$ hypothesis, and $f(n|b)$ under the background-only hypothesis.

Suppose we observe n^* actual events. The p-value for the $s + b$ hypothesis is defined as the probability that we would find a value of n with equal or less compatibility with the $s + b$ model relative to what we observe, n^*, in other words the probability of $n > n^*$, under the assumption of the $s + b$ hypothesis, i.e.

$$p_{s+b} = P(n \geq n^*|s + b) = \int_{n^*}^{\infty} f(n|s + b)dq\,. \tag{C.5}$$

Similarly, the p-value for the background-only hypothesis is defined as the probability to find $n < n*$ under the assumption of this hypothesis:

$$p_b = P(n \leq n^*|b) = \int_{-\infty}^{n^*} f(n|b)dq\,. \tag{C.6}$$

In the method known as CL_{s+b}, we carry out a statistical test of the $s + b$ hypothesis, based on the p-value, p_{s+b}. We regard signal model as excluded at a confidence level of $1 - \alpha$ if $p_{s+b} < \alpha$. We can construct a confidence interval at the confidence level $1 - \alpha$ for the signal process from those values not excluded. By

construction, the confidence interval will cover a range of values with a probability of at least 95%.

However, this leads to a problem when the sensitivity is low, i.e. the number of signal events is much lower than background, $s \ll b$. We may exclude the actual value of s with a probability of around α, corresponding to cases when there is a large downward fluctuation in s.

For example, let us consider the case where $n^* = 0$ events are observed. Then, we would find that $s + b \geq b$ is excluded altogether; this would exclude all possible values of $s \geq 0$. Such a result would be difficult to interpret: the experiment cannot easily distinguish small values of s from the null-hypothesis. It makes more sense to condition the probability that $n \leq n^*$ in the confidence interval, given that the real number of background events must be less than n^*; after all when the number of background events is small, it is more likely to produce an error (i.e. a confidence level that does not cover the true number of signal events). Thus we should not report an overall probability, but rather a conditional probability, given that we have an estimate of the number of background events in the sample.

To protect against excluding models to which we have little or no sensitivty, in the CL_s procedure, we exclude a signal model if we find:

$$CL_s \equiv \frac{p_{s+b}}{1 - p - b} < \alpha \,. \tag{C.7}$$

We can see from the definition that CL_s is always greater than the p-value p_{s+b}; hence the models we exclude by requiring $CL_s < \alpha$ are a subset of those excluded by demanding $p_{s+b} < \alpha$. In the limit of high μ, the set of models excluded by the CL_s approaches those excluded by $p_{s+b} < \alpha$. In this sense, the CL_s procedure is conservative. In terms of probabilities CL_s, is given by

$$P(n \leq n^* | n_b \leq n^*, s + b) = \frac{P(n \leq n^* | s + b)}{P(n_b \leq n^* | s + b)} = \frac{P(n \leq n^* | s + b)}{P(n \leq n^* | b)} \,. \tag{C.8}$$

This definition of a confidence level subtly differs from the standard statistical definition of a "confidence interval"; the stated confidence level does not exactly equal the coverage probability because the CL_s by design will always contain the zero value of the parameter of interest, and hence the coverage probability at this point is always 100%. This definition of CL_s avoids the undesirable property of confidence intervals of producing empty intervals with some fixed probability when the parameter value is zero. [154–156].

Colophon

This thesis was made in LaTeX 2_ε using the "hepthesis" class [157].

Bibliography

[1] H. W. Turnbull, *The correspondence of Isaac Newton. 2. 1676-1687.* Cambridge University Press, 1960.

[2] CERN, *The accelerator complex*, `http://public.web.cern.ch/public/en/research/AccelComplex-en.html`, 2012.

[3] J. Pequenao, *Computer generated image of the whole ATLAS detector*, `https://cds.cern.ch/record/1095924`, Mar, 2008.

[4] ATLAS Collaboration, G. Aad et al., *The ATLAS Experiment at the CERN Large Hadron Collider*, JINST **3** (2008) S08003.

[5] M. Cacciari, G. P. Salam, and G. Soyez, *The Anti-k(t) jet clustering algorithm*, JHEP **04** (2008) 063, `arXiv:0802.1189 [hep-ph]`.

[6] ATLAS Collaboration, *Performance of large-R jets and jet substructure reconstruction with the ATLAS detector*, Tech. Rep. ATLAS-CONF-2012-065, CERN, Geneva, Jul, 2012. `https://cds.cern.ch/record/1459530`.

[7] D. Krohn, J. Thaler, and L. Wang, *Jet Trimming*, JHEP **02** (2010) 084, `arXiv:0912.1342 [hep-ph]`.

[8] A. Tavares Delgado, *Performance of the ATLAS jet trigger: Partial scan of the Calorimeter* , Tech. Rep. ATL-COM-DAQ-2015-006, CERN, Geneva, Feb, 2015. `https://cds.cern.ch/record/1987584`.

[9] Particle Data Group Collaboration, K. A. Olive et al., *Review of Particle Physics*, Chin. Phys. **C38** (2014) 090001.

[10] ATLAS Collaboration, G. Aad et al., *Data-Quality Requirements and Event Cleaning for Jets and Missing Transverse Energy Reconstruction with the*

ATLAS Detector in Proton-Proton Collisions at a Center of Mass Energy $\sqrt{s} = 7$ *TeV*, Tech. Rep. ATLAS-CONF-2010-038, CERN, Geneva, 2010. https://cds.cern.ch/record/1277678.

[11] ATLAS Collaboration, G. Aad et al., *Electron reconstruction and identification efficiency measurements with the ATLAS detector using the 2011 LHC proton-proton collision data*, Eur. Phys. J. **C74** (2014) no. 7, 2941, arXiv:1404.2240 [hep-ex].

[12] ATLAS Collaboration, G. Aad et al., *Measurement of total and differential* W^+W^- *production cross sections in proton-proton collisions at* $\sqrt{s} = 8$ *TeV with the ATLAS detector and limits on anomalous triple-gauge-boson couplings*, arXiv:1603.01702 [hep-ex].

[13] ATLAS Collaboration, G. Aad et al., *Measurements of* $W^{\pm}Z$ *production cross sections in pp collisions at* $\sqrt{s} = 8$ *TeV with the ATLAS detector and limits on anomalous gauge boson self-couplings*, Phys. Rev. **D93** (2016) no. 9, 092004, arXiv:1603.02151 [hep-ex].

[14] ATLAS Collaboration, G. Aad et al., *Measurement of the* $WW + WZ$ *cross section and limits on anomalous triple gauge couplings using final states with one lepton, missing transverse momentum, and two jets with the ATLAS detector at* $\sqrt{\text{s}} = 7$ *TeV*, JHEP **01** (2015) 049, arXiv:1410.7238 [hep-ex].

[15] R. Feynman, *The Character of Physical Law*, M.I.T. paperback series (1967) . https://books.google.co.uk/books?id=Q9AxAAAACAAJ.

[16] D. Hanneke, S. Fogwell, and G. Gabrielse, *New Measurement of the Electron Magnetic Moment and the Fine Structure Constant*, Phys. Rev. Lett. **100** (2008) 120801, arXiv:0801.1134 [physics.atom-ph].

[17] S. Hawking, *A Brief History of Time*. Bantam Dell Publishing Group, 1988.

[18] ATLAS Collaboration, G. Aad et al., *Observation of a new particle in the search for the Standard Model Higgs boson with the ATLAS detector at the LHC*, Phys. Lett. **B716** (2012) 1–29, arXiv:1207.7214 [hep-ex].

[19] CMS Collaboration, S. Chatrchyan et al., *Observation of a new boson at a mass of 125 GeV with the CMS experiment at the LHC*, Phys. Lett. **B716** (2012) 30–61, arXiv:1207.7235 [hep-ex].

[20] E. Noether, *Invariant Variation Problems*, Gott. Nachr. **1918** (1918) 235–257, arXiv:physics/0503066 [physics]. [Transp. Theory Statist. Phys.1,186(1971)].

[21] S. Glashow, *Partial-symmetries of weak interactions*, Nucl. Phys. **22** (1961) 579–588.

[22] S. Weinberg, *A Model of Leptons*, Phys. Rev. Lett. **19 (21)** (1967) 1264–1266.

[23] A. Salam, *Elementary Particle Physics: Relativistic Groups and Analyticity, Eighth Nobel Symposium*, N. Svartholm, ed **367** (1968) .

[24] Gargamelle Neutrino Collaboration, F. J. Hasert et al., *Observation of Neutrino Like Interactions Without Muon Or Electron in the Gargamelle Neutrino Experiment*, Phys. Lett. **B46** (1973) 138–140.

[25] F. Englert and R. Brout, *Broken Symmetry and the Mass of Gauge Vector Mesons*, Phys. Rev. Lett. **13** (1964) 321–323.

[26] P. W. Higgs, *Broken symmetries, massless particles and gauge fields*, Phys. Lett. **12** (1964) 132–133.

[27] G. S. Guralnik, C. R. Hagen, and T. W. B. Kibble, *Global Conservation Laws and Massless Particles*, Phys. Rev. Lett. **13** (1964) 585–587.

[28] K. Hagiwara et al., *Probing the weak boson sector in* $e^+e^- \to W^+W^-$, Phys. Lett. **B, 282** (1987) 253–307.

[29] G. Gounaris, K. J.L., and R. Sekulin, *Trilinear gauge couplings in Physics at LEP2*, Report CERN 96-01 **1** (1996) 525.

[30] H. D. Politzer, *Reliable Perturbative Results for Strong Interactions?*, Phys. Rev. Lett. **30** (1973) 1346–1349.

[31] D. J. Gross and F. Wilczek, *Ultraviolet Behavior of Nonabelian Gauge Theories*, Phys. Rev. Lett. **30** (1973) 1343–1346.

[32] D. J. Gross and F. Wilczek, *Asymptotically free gauge theories. II*, Phys. Rev. D **9** (Feb, 1974) 980–993. http://link.aps.org/doi/10.1103/PhysRevD.9.980.

[33] K. G. Wilson, *Confinement of Quarks*, Phys. Rev. **D10** (1974) 2445–2459.

[34] R. Daniel, J. Davies, D. Mulvey, and D. Perkins, *Report by C. F. Powell at International Physics Conference, Copenhagen*, Phil. Mag. (1952) 753.

[35] G. Hanson et al., *Evidence for Jet Structure in Hadron Production by e+ e- Annihilation*, Phys. Rev. Lett. **35** (1975) 1609–1612.

[36] J. D. Bjorken, *Asymptotic Sum Rules at Infinite Momentum*, Phys. Rev. **179** (1969) 1547–1553.

[37] D. W. Duke and J. F. Owens, *Q**2 Dependent Parametrizations of Parton Distribution Functions*, Phys. Rev. **D30** (1984) 49–54.

[38] G. Miller et al., *Inelastic electron-Proton Scattering at Large Momentum Transfers*, Phys. Rev. **D5** (1972) 528.

[39] BCDMS Collaboration, A. C. Benvenuti et al., *A High Statistics Measurement of the Deuteron Structure Functions F2 (X, Q^2) and R From Deep Inelastic Muon Scattering at High Q^2*, Phys. Lett. **B237** (1990) 592.

[40] H1 Collaboration, T. Ahmed et al., *A Measurement of the proton structure function f2 (x, Q**2)*, Nucl. Phys. **B439** (1995) 471–502, arXiv:hep-ex/9503001 [hep-ex].

[41] H1 Collaboration, V. Andreev et al., *Measurement of inclusive ep cross sections at high Q^2 at $\sqrt{s} = 225$ and 252 GeV and of the longitudinal proton structure function F_L at HERA*, Eur. Phys. J. **C74** (2014) no. 4, 2814, arXiv:1312.4821 [hep-ex].

[42] V. N. Gribov and L. N. Lipatov, *Deep inelastic ep scattering in perturbation theory*, Sov. J. Nucl. Phys. **15** (1972) 438–450.

[43] G. Altarelli and G. Parisi, *Asymptotic Freedom in Parton Language*, Nucl. Phys. **B126** (1977) 298.

[44] Y. L. Dokshitzer, *Calculation of the Structure Functions for Deep Inelastic Scattering and e^+e^- Annihilation by Perturbation Theory in Quantum Chromodynamics*, Sov. Phys. JETP **46** (1977) 641–653.

[45] J. F. Donoghue, *The effective field theory treatment of quantum gravity*, AIP Conf. Proc. **1483** (2012) 73–94, arXiv:1209.3511 [gr-qc].

[46] M. Markevitch et al., *Direct constraints on the dark matter self-interaction cross-section from the merging galaxy cluster 1E0657-56*, Astrophys. J. **606** (2004) 819–824, arXiv:astro-ph/0309303 [astro-ph].

[47] G. Bertone, D. Hooper, and J. Silk, *Particle dark matter: Evidence, candidates and constraints*, Phys. Rept. **405** (2005) 279–390, arXiv:hep-ph/0404175 [hep-ph].

[48] P. J. E. Peebles and B. Ratra, *The cosmological constant and dark energy*, Rev. Mod. Phys. **75** (Apr, 2003) 559–606.

[49] O. Sawada and A. Sugamoto, eds., *Proceedings: Workshop on the Unified Theories and the Baryon Number in the Universe, Tsukuba, Japan, 13-14 Feb 1979*. 1979.

[50] J. A. Harvey, E. W. Kolb, D. B. Reiss, and S. Wolfram, *Calculation of Cosmological Baryon Asymmetry in Grand Unified Gauge Models*, Nucl. Phys. **B201** (1982) 16.

[51] A. D. Sakharov, *Violation of CP Invariance, c Asymmetry, and Baryon Asymmetry of the Universe*, Pisma Zh. Eksp. Teor. Fiz. **5** (1967) 32–35. [Usp. Fiz. Nauk161,61(1991)].

[52] H. Fritzsch and Z.-z. Xing, *Mass and flavor mixing schemes of quarks and leptons*, Prog. Part. Nucl. Phys. **45** (2000) 1–81, arXiv:hep-ph/9912358 [hep-ph].

[53] L. Susskind, *Dynamics of Spontaneous Symmetry Breaking in the Weinberg-Salam Theory*, Phys. Rev. **D20** (1979) 2619–2625.

[54] T. Mannel, *Theory and phenomenology of CP violation*, Nucl. Phys. Proc. Suppl. **167** (2007) 115–119. [,115(2007)].

[55] C. D. Froggatt and H. B. Nielsen, *Trying to understand the standard model parameters*, Surveys High Energ. Phys. **18** (2003) 55–75, arXiv:hep-ph/0308144 [hep-ph].

[56] J. Ellison and J. Wudka, *Study of Trilinear Gauge Boson Couplings at the Tevatron Collider*, Ann.Rev.Nucl.Part.Sci **48** (1998) 33–80, arXiv:9804322v2 [hep-ph].

[57] K. Hagiwara et al., *Low energy effects of new interactions in the electroweak boson sector*, Phys. Rev. **D48,5** (1993) 2182–2203.

[58] G. Gounaris et al., *Triple gauge boson couplings*, in *AGS / RHIC Users Annual Meeting Upton, New York, June 15-16,*. 1995. arXiv:hep-ph/9601233 [hep-ph]. http://alice.cern.ch/format/showfull?sysnb=0215385.

[59] K. Hagiwara, J. Woodside, and D. Zeppenfeld, *Measuring the WWZ coupling at the Fermilab Tevatron*, Phys. Rev. **D41,7** (1990) 2113–2119.

[60] E. Accomando and A. Kaiser, *Electroweak corrections and anomalous triple gauge-boson couplings in W^+W^- and $W^\pm Z$ production at the LHC*, Phys. Rev. **D73** (2005) 093006, arXiv:0511088 [hep-ph].

[61] L. Dixon, Z. Kunszt, and A. Signer, *Vector Boson Pair Production in Hadronic Collisions at $O(\alpha_s)$: Lepton Correlations and Anomalous Couplings*, Phys. Rev. **D60** (1999) 114037, arXiv:9907305 [hep-ph].

[62] C. Degrande, N. Greiner, W. Kilian, O. Mattelaer, H. Mebane, T. Stelzer, S. Willenbrock, and C. Zhang, *Effective Field Theory: A Modern Approach to Anomalous Couplings*, Annals Phys. **335** (2013) 21–32, arXiv:1205.4231 [hep-ph].

[63] CMS Collaboration, S. Chatrchyan et al., *Measurement of the sum of WW and WZ production with W+dijet events in pp collisions at $\sqrt{s} = 7$ TeV*, Eur. Phys. J. **C73** (2013) no. 2, 2283, arXiv:1210.7544 [hep-ex].

[64] CMS Collaboration, V. Khachatryan et al., *Measurement of the W^+W^- cross section in pp collisions at $\sqrt{s} = 8$ TeV and limits on anomalous gauge couplings*, arXiv:1507.03268 [hep-ex].

[65] O. S. Bruning, P. Collier, P. Lebrun, S. Myers, R. Ostojic, J. Poole, and P. Proudlock, *LHC Design Report Vol.1: The LHC Main Ring*, .

[66] S. Artz et al., *Upgrade of the ATLAS Central Trigger for LHC Run-2*, Tech. Rep. ATL-DAQ-PROC-2014-042, CERN, Geneva, Nov, 2014. https://cds.cern.ch/record/1969488.

[67] S. Yamamoto, *The Upgrade of the ATLAS First Level Calorimeter Trigger*, .

https://cds.cern.ch/record/2017813.

[68] ATLAS Collaboration, G. Aad et al., *Technical Design Report for the Phase-I Upgrade of the ATLAS TDAQ System*, Tech. Rep. CERN-LHCC-2013-018. ATLAS-TDR-023, CERN, Geneva, Sep, 2013. https://cds.cern.ch/record/1602235. Final version presented to December 2013 LHCC.

[69] V. Chang, G. Eilam, and R. C. Hwa, *Hadronization of Gluons in Quark and Gluon Jets*, Phys. Rev. **D24** (1981) 1818.

[70] B. R. Webber, *Fragmentation and hadronization*, Int. J. Mod. Phys. **A15S1** (2000) 577–606, arXiv:hep-ph/9912292 [hep-ph]. [,577(1999)].

[71] G. P. Salam, *Perturbative QCD for the LHC*, PoS **ICHEP2010** (2010) 556, arXiv:1103.1318 [hep-ph].

[72] J. E. Huth et al., *Research Directions for the Decade*, Proceedings of the Summer Study on High Energy Physics, Snowmass, Colorado (1990) .

[73] G. P. Salam, *Towards Jetography*, Eur. Phys. J. **C67** (2010) 637–686, arXiv:0906.1833 [hep-ph].

[74] G. P. Salam and G. Soyez, *A practical Seedless Infrared-Safe Cone jet algorithm*, JHEP **05** (2007) 086, arXiv:0704.0292 [hep-ph].

[75] M. Cacciari and G. P. Salam, *Dispelling the N^3 myth for the k_t jet-finder*, Phys. Lett. **B641** (2006) 57–61, arXiv:hep-ph/0512210 [hep-ph].

[76] M. Cacciari, G. P. Salam, and G. Soyez, *FastJet User Manual*, Eur. Phys. J. **C72** (2012) 1896, arXiv:1111.6097 [hep-ph].

[77] S. Catani, Y. L. Dokshitzer, M. H. Seymour, and B. R. Webber, *Longitudinally invariant K(t) clustering algorithms for hadron-hadron collisions*, Nucl. Phys. **B406** (1993) 187–224.

[78] Y. L. Dokshitzer, G. D. Leder, S. Moretti, and B. R. Webber, *Better jet clustering algorithms*, JHEP **08** (1997) 001, arXiv:hep-ph/9707323 [hep-ph].

[79] W. Lampl et al., *Calorimeter Clustering Algorithms: Description and*

Performance, Tech. Rep. ATL-LARG-PUB-2008-002.
ATL-COM-LARG-2008-003, CERN, Geneva, Apr, 2008.

[80] A. Abdesselam et al., *Boosted objects: A Probe of beyond the Standard Model physics*, Eur. Phys. J. **C71** (2011) 1661, arXiv:1012.5412 [hep-ph].

[81] A. Altheimer et al., *Jet Substructure at the Tevatron and LHC: New results, new tools, new benchmarks*, J. Phys. **G39** (2012) 063001, arXiv:1201.0008 [hep-ph].

[82] A. Altheimer et al., *Boosted objects and jet substructure at the LHC. Report of BOOST2012, held at IFIC Valencia, 23rd-27th of July 2012*, Eur. Phys. J. **C74** (2014) no. 3, 2792, arXiv:1311.2708 [hep-ex].

[83] ATLAS Collaboration, G. Aad et al., *Search for high-mass diboson resonances with boson-tagged jets in proton-proton collisions at $\sqrt{s} = 8$ TeV with the ATLAS detector*, JHEP **12** (2015) 055, arXiv:1506.00962 [hep-ex].

[84] ATLAS Collaboration, G. Aad et al., *Combination of searches for WW, WZ, and ZZ resonances in pp collisions at $\sqrt{s} = 8$ TeV with the ATLAS detector*, Phys. Lett. **B755** (2016) 285–305, arXiv:1512.05099 [hep-ex].

[85] J. M. Butterworth, B. E. Cox, and J. R. Forshaw, *WW scattering at the CERN LHC*, Phys. Rev. **D65** (2002) 096014, arXiv:hep-ph/0201098 [hep-ph].

[86] M. Dasgupta, A. Fregoso, S. Marzani, and G. P. Salam, *Towards an understanding of jet substructure*, JHEP **09** (2013) 029, arXiv:1307.0007 [hep-ph].

[87] C. Chen, *New approach to identifying boosted hadronically-decaying particle using jet substructure in its center-of-mass frame*, Phys. Rev. **D85** (2012) 034007, arXiv:1112.2567 [hep-ph].

[88] M. Cacciari and G. P. Salam, *Pileup subtraction using jet areas*, Phys. Lett. **B659** (2008) 119–126, arXiv:0707.1378 [hep-ph].

[89] S. D. Ellis, C. K. Vermilion, and J. R. Walsh, *Techniques for improved heavy particle searches with jet substructure*, Phys. Rev. **D80** (2009) 051501, arXiv:0903.5081 [hep-ph].

[90] S. D. Ellis, C. K. Vermilion, and J. R. Walsh, *Recombination Algorithms and Jet Substructure: Pruning as a Tool for Heavy Particle Searches*, Phys. Rev. **D81** (2010) 094023, arXiv:0912.0033 [hep-ph].

[91] J. M. Butterworth, A. R. Davison, M. Rubin, and G. P. Salam, *Jet substructure as a new Higgs search channel at the LHC*, Phys. Rev. Lett. **100** (2008) 242001, arXiv:0802.2470 [hep-ph].

[92] ATLAS Collaboration, D. W. Miller, *Jet substructure in ATLAS*, in *Particles and fields. Proceedings, Meeting of the Division of the American Physical Society, DPF 2011, Providence, USA, August 9-13, 2011*. 2011. arXiv:1110.1094 [hep-ex].

[93] D. Adams et al., *Towards an Understanding of the Correlations in Jet Substructure*, Eur. Phys. J. **C75** (2015) no. 9, 409, arXiv:1504.00679 [hep-ph].

[94] J. Thaler and K. Van Tilburg, *Identifying Boosted Objects with N-subjettiness*, JHEP **03** (2011) 015, arXiv:1011.2268 [hep-ph].

[95] A. J. Larkoski, G. P. Salam, and J. Thaler, *Energy Correlation Functions for Jet Substructure*, JHEP **06** (2013) 108, arXiv:1305.0007 [hep-ph].

[96] A. J. Larkoski, I. Moult, and D. Neill, *Power Counting to Better Jet Observables*, JHEP **12** (2014) 009, arXiv:1409.6298 [hep-ph].

[97] ATLAS Collaboration, G. Aad et al., *Identification of Boosted, Hadronically Decaying W Bosons and Comparisons with ATLAS Data Taken at* $\sqrt{s} = 8$ *TeV*, arXiv:1510.05821 [hep-ex].

[98] ATLAS Collaboration, G. Aad et al., *Performance of b-Jet Identification in the ATLAS Experiment*, JINST **11** (2016) no. 04, P04008, arXiv:1512.01094 [hep-ex].

[99] ATLAS Collaboration, G. Aad et al., *Measurement of the b-tag Efficiency in a Sample of Jets Containing Muons with 5* fb^{-1} *of Data from the ATLAS Detector*, Tech. Rep. ATLAS-CONF-2012-043, CERN, Geneva, Mar, 2012. http://cds.cern.ch/record/1435197.

[100] ATLAS Collaboration, G. Aad et al., *The ATLAS Simulation Infrastructure*,

Eur. Phys. J. **C70** (2010) 823–874, arXiv:1005.4568 [physics.ins-det].

[101] A. Papaefstathiou, *How-to: Write a parton-level Monte Carlo event generator*, arXiv:1412.4677 [hep-ph].

[102] GEANT4 Collaboration, S. Agostinelli et al., *GEANT4: A Simulation toolkit*, Nucl. Instrum. Meth. **A506** (2003) 250–303.

[103] T. Sjostrand, S. Mrenna, and P. Z. Skands, *A Brief Introduction to PYTHIA 8.1*, Comput. Phys. Commun. **178** (2008) 852–867, arXiv:0710.3820 [hep-ph].

[104] T. Sjostrand, *PYTHIA 8 Status Report*, in *Proceedings, workshop: HERA and the LHC workshop series on the implications of HERA for LHC physics*, pp. 726–732. 2008. arXiv:0809.0303 [hep-ph]. https://inspirehep.net/record/794180/files/arXiv:0809.0303.pdf.

[105] B. Andersson, G. Gustafson, G. Ingelman, and T. Sjostrand, *Parton Fragmentation and String Dynamics*, Phys. Rept. **97** (1983) 31–145.

[106] A. D. Martin, W. J. Stirling, R. S. Thorne, and G. Watt, *Parton distributions for the LHC*, Eur. Phys. J. **C63** (2009) 189–285, arXiv:0901.0002 [hep-ph].

[107] G. Corcella, I. G. Knowles, G. Marchesini, S. Moretti, K. Odagiri, P. Richardson, M. H. Seymour, and B. R. Webber, *HERWIG 6: An Event generator for hadron emission reactions with interfering gluons (including supersymmetric processes)*, JHEP **01** (2001) 010, arXiv:hep-ph/0011363 [hep-ph].

[108] M. Bahr et al., *Herwig++ Physics and Manual*, Eur. Phys. J. **C58** (2008) 639–707, arXiv:0803.0883 [hep-ph].

[109] M. L. Mangano, M. Moretti, F. Piccinini, R. Pittau, and A. D. Polosa, *ALPGEN, a generator for hard multiparton processes in hadronic collisions*, JHEP **07** (2003) 001, arXiv:hep-ph/0206293 [hep-ph].

[110] H.-L. Lai, M. Guzzi, J. Huston, Z. Li, P. M. Nadolsky, J. Pumplin, and C.-P. Yuan, *New parton distributions for collider physics*, Phys. Rev. **D82** (2010) 074024, arXiv:1007.2241 [hep-ph].

[111] T. Gleisberg, S. Hoeche, F. Krauss, M. Schonherr, S. Schumann, F. Siegert, and J. Winter, *Event generation with SHERPA 1.1*, JHEP **02** (2009) 007, arXiv:0811.4622 [hep-ph].

[112] S. Frixione, F. Stoeckli, P. Torrielli, B. R. Webber, and C. D. White, *The MC@NLO 4.0 Event Generator*, arXiv:1010.0819 [hep-ph].

[113] S. Frixione, F. Stoeckli, P. Torrielli, and B. R. Webber, *NLO QCD corrections in Herwig++ with MC@NLO*, JHEP **01** (2011) 053, arXiv:1010.0568 [hep-ph].

[114] P. Nason, *A New method for combining NLO QCD with shower Monte Carlo algorithms*, JHEP **11** (2004) 040, arXiv:hep-ph/0409146 [hep-ph].

[115] S. Frixione, P. Nason, and C. Oleari, *Matching NLO QCD computations with Parton Shower simulations: the POWHEG method*, JHEP **11** (2007) 070, arXiv:0709.2092 [hep-ph].

[116] S. Alioli, P. Nason, C. Oleari, and E. Re, *A general framework for implementing NLO calculations in shower Monte Carlo programs: the POWHEG BOX*, JHEP **06** (2010) 043, arXiv:1002.2581 [hep-ph].

[117] R. Mankel, *Pattern recognition and event reconstruction in particle physics experiments*, Rept. Prog. Phys. **67** (2004) 553, arXiv:physics/0402039 [physics].

[118] ATLAS Collaboration, G. Aad et al., *Jet energy scale and its systematic uncertainty for jets produced in proton-proton collisions at $\sqrt{s} = 7$ TeV and measured with the ATLAS detector*, Tech. Rep. ATLAS-CONF-2010-056, CERN, Geneva, 2010.

[119] ATLAS Collaboration, G. Aad et al., *Jet energy measurement with the ATLAS detector in proton-proton collisions at $\sqrt{s} = 7$ TeV*, Tech. Rep. CERN-PH-EP-2011-191, CERN, Geneva, 2011. arXiv:1112.6426 [hep-ex].

[120] ATLAS Collaboration, G. Aad et al., *Jet energy resolution and selection efficiency relative to track jets from in-situ techniques with the ATLAS Detector Using Proton-Proton Collisions at a Center of Mass Energy $\sqrt{s} = 7$ TeV*, Tech. Rep. ATLAS-CONF-2010-054, CERN, Geneva, 2010.

[121] ATLAS Collaboration, G. Aad et al., *Measurement of three-jet production cross-sections in pp collisions at 7 TeV centre-of-mass energy using the ATLAS detector*, Eur. Phys. J. **C75** (2015) no. 5, 228, arXiv:1411.1855 [hep-ex].

[122] ATLAS Collaboration, G. Aad et al., *Measurement of jet production in proton-proton collisions at 7 TeV centre-of-mass energy with the ATLAS Detector*, Tech. Rep. ATLAS-CONF-2010-050, CERN, Geneva, 2010.

[123] ATLAS Collaboration, G. Aad et al., *Expected electron performance in the ATLAS experiment*, Tech. Rep. ATL-PHYS-PUB-2011-006, CERN, Geneva, Apr, 2011. https://cds.cern.ch/record/1345327.

[124] ATLAS Collaboration, G. Aad et al., *Electron and photon energy calibration with the ATLAS detector using LHC Run 1 data*, Eur. Phys. J. **C74** (2014) no. 10, 3071, arXiv:1407.5063 [hep-ex].

[125] B. Resende, *Muon identification algorithms in ATLAS*, Tech. Rep. ATL-PHYS-PROC-2009-113, CERN, Geneva, Sep, 2009. https://cds.cern.ch/record/1209632.

[126] ATLAS Collaboration, G. Aad et al., *Measurement of the muon reconstruction performance of the ATLAS detector using 2011 and 2012 LHC protonâĂŞproton collision data*, Eur. Phys. J. **C74** (2014) no. 11, 3130, arXiv:1407.3935 [hep-ex].

[127] ATLAS Collaboration, G. Aad et al., *Expected performance of the ATLAS experiment: detector, trigger and physics*. CERN, Geneva, 2009. https://cds.cern.ch/record/1125884.

[128] ATLAS Collaboration, G. Aad et al., *Muon reconstruction efficiency and momentum resolution of the ATLAS experiment in proton-proton collisions at* $\sqrt{s}$ *= 7 TeV in 2010*, Eur. Phys. J. **C74** (2014) no. 9, 3034, arXiv:1404.4562 [hep-ex].

[129] ATLAS Collaboration, G. Aad et al., *Performance of Missing Transverse Momentum Reconstruction in ATLAS studied in Proton-Proton Collisions recorded in 2012 at 8 TeV*, Tech. Rep. ATLAS-CONF-2013-082, CERN, Geneva, Aug, 2013. https://cds.cern.ch/record/1570993.

[130] ATLAS Collaboration, S. Prince, *The updated ATLAS Jet Trigger for the LHC Run II*, in *Meeting of the APS Division of Particles and Fields (DPF 2015) Ann Arbor, Michigan, USA, August 4-8, 2015*. 2015. arXiv:1511.00972 [physics.ins-det]. https://inspirehep.net/record/1402596/files/arXiv:1511.00972.pdf.

[131] A. Tavares Delgado, *Design and performance of the ATLAS jet trigger system*, Tech. Rep. ATL-DAQ-PROC-2015-019, CERN, Geneva, May, 2015. https://cds.cern.ch/record/2018453.

[132] ATLAS Collaboration, *Performance of the ATLAS Jet Trigger in the Early sqrts=7 TeV Data*, Tech. Rep. ATLAS-CONF-2010-094, CERN, Geneva, Oct, 2010. https://cds.cern.ch/record/1299109.

[133] CMS Collaboration, *Measurement of WZ production rate*, Tech. Rep. CMS-PAS-SMP-12-006, CERN, Geneva, 2013. http://cds.cern.ch/record/1564318.

[134] J. Pumplin, D. R. Stump, J. Huston, H. L. Lai, P. M. Nadolsky, and W. K. Tung, *New generation of parton distributions with uncertainties from global QCD analysis*, JHEP **07** (2002) 012, arXiv:hep-ph/0201195 [hep-ph].

[135] M. Beneke, P. Falgari, S. Klein, and C. Schwinn, *Hadronic top-quark pair production with NNLL threshold resummation*, Nucl. Phys. **B855** (2012) 695–741, arXiv:1109.1536 [hep-ph].

[136] M. Cacciari, M. Czakon, M. Mangano, A. Mitov, and P. Nason, *Top-pair production at hadron colliders with next-to-next-to-leading logarithmic soft-gluon resummation*, Phys. Lett. **B710** (2012) 612–622, arXiv:1111.5869 [hep-ph].

[137] P. Baernreuther, M. Czakon, and A. Mitov, *Percent Level Precision Physics at the Tevatron: First Genuine NNLO QCD Corrections to $q\bar{q} \to t\bar{t} + X$*, Phys. Rev. Lett. **109** (2012) 132001, arXiv:1204.5201 [hep-ph].

[138] M. Czakon and A. Mitov, *NNLO corrections to top-pair production at hadron colliders: the all-fermionic scattering channels*, JHEP **12** (2012) 054, arXiv:1207.0236 [hep-ph].

[139] M. Czakon and A. Mitov, *NNLO corrections to top pair production at hadron colliders: the quark-gluon reaction*, JHEP **01** (2013) 080, arXiv:1210.6832 [hep-ph].

[140] M. Czakon, P. Fiedler, and A. Mitov, *Total Top-Quark Pair-Production Cross Section at Hadron Colliders Through $O(\alpha_S^4)$*, Phys. Rev. Lett. **110** (2013) 252004, arXiv:1303.6254 [hep-ph].

[141] M. Czakon and A. Mitov, *Top++: A Program for the Calculation of the Top-Pair Cross-Section at Hadron Colliders*, Comput. Phys. Commun. **185** (2014) 2930, arXiv:1112.5675 [hep-ph].

[142] M. Botje et al., *The PDF4LHC Working Group Interim Recommendations*, arXiv:1101.0538 [hep-ph].

[143] A. D. Martin, W. J. Stirling, R. S. Thorne, and G. Watt, *Uncertainties on alpha(S) in global PDF analyses and implications for predicted hadronic cross sections*, Eur. Phys. J. **C64** (2009) 653–680, arXiv:0905.3531 [hep-ph].

[144] J. Gao, M. Guzzi, J. Huston, H.-L. Lai, Z. Li, P. Nadolsky, J. Pumplin, D. Stump, and C. P. Yuan, *CT10 next-to-next-to-leading order global analysis of QCD*, Phys. Rev. **D89** (2014) no. 3, 033009, arXiv:1302.6246 [hep-ph].

[145] R. D. Ball et al., *Parton distributions with LHC data*, Nucl. Phys. **B867** (2013) 244–289, arXiv:1207.1303 [hep-ph].

[146] J. Friedman, *353QH Twice Smoothing Algorithm*, in *Proceedings of the CERN School of Computing, Norway, August 11-24*. 1974. http://www.slac.stanford.edu/cgi-wrap/getdoc/slac-r-176.pdf.

[147] G. Aad et al., *Track Reconstruction Efficiency in sqrt(s)=7 TeV Data for Tracks with pT > 100 MeV*, Tech. Rep. ATL-PHYS-INT-2011-001, CERN, Geneva, Jan, 2011. https://cds.cern.ch/record/1319318.

[148] ATLAS Collaboration, G. Aad et al., *Pile-up subtraction and suppression for jets in ATLAS*, Tech. Rep. ATLAS-CONF-2013-083, CERN, Geneva, Aug, 2013. https://cds.cern.ch/record/1570994.

[149] G. Cowan, K. Cranmer, E. Gross, and O. Vitells, *Asymptotic formulae for likelihood-based tests of new physics*, Eur. Phys. J. **C71** (2011) 1554,

arXiv:1007.1727 [physics.data-an]. [Erratum: Eur. Phys. J.C73,2501(2013)].

[150] ATLAS Collaboration, G. Aad et al., *Measurement of WZ production in proton-proton collisions at $\sqrt{s} = 7$ TeV with the ATLAS detector*, Eur. Phys. J. **C72** (2012) 2173, arXiv:1208.1390 [hep-ex].

[151] S. S. Wilks, *The Large-Sample Distribution of the Likelihood Ratio for Testing Composite Hypotheses*, Annals Math. Statist. **9** (1938) no. 1, 60–62.

[152] A. Wald, *Tests of Statistical Hypotheses Concerning Several Parameters When the Number of Observations is Large*, Transactions of the American Mathematical Society **54** (1943) no. 3, 426–482. http://www.jstor.org/stable/1990256.

[153] I. Asimov, *Franchise, in Isaac Asimov: The Complete Stories, Vol. 1.* Broadway Books, 1990.

[154] G. Zech, *Upper limits in experiments with background or measurement errors*, Nucl. Instrum. Methods Phys. Res., A **277** (Nov, 1988) 608. 6 p. https://cds.cern.ch/record/193135.

[155] B. Mistlberger and F. Dulat, *Limit setting procedures and theoretical uncertainties in Higgs boson searches*, arXiv:1204.3851 [hep-ph].

[156] E. Gross, *LHC statistics for pedestrians*, in *Statistical issues for LHC physics. Proceedings, Workshop, PHYSTAT-LHC, Geneva, Switzerland, June 27-29, 2007*, pp. 205–212. 2007. http://cds.cern.ch/record/1099994/files/p205.pdf.

[157] A. Buckley, *A class for typesetting academic theses*, 2010.